UNIVERSITÀ DEGLI STUDI DI TORINO

UniTo Ph.D. doctoral school

Doctorate in Pharmaceutical and Biomolecular Sciences – XXXIV cycle

Ph.D. Thesis

New anti-inflammatory agents for the treatment of chronic inflammatory diseases

In the search of NLRP3 inflammasome inhibitors

Simone Gastaldi

Tutor
prof. Massimo Bertinaria

Academic sector
CHIM/08

Academic Year 2020-2021

Contents

Chapter 1

Inflammasome general introduction

1.1 Inflammasomes

The inflammasomes are intracellular multimeric platforms that play a fundamental role in the activation of the innate immune system in response to a wide range of stimuli. The innate immune response is the first line of defense against pathogen invasion and maintains homeostasis in the body.[1] The inflammatory signalling cascade is activated upstream by the PRRs (Pattern Recognition Receptors). Those receptors are able to detect and process *non-self* molecules derived from microbes, called Pathogen- or Microbe-Associated Molecular Patterns (PAMPs or MAMPs, such as viral RNAs, microbial toxins, and bacterial surface components) as well as *endogenous host-derived* signalling molecules (DAMPs, Danger-Associated Molecular Patterns, such as uric acid crystals, ATP, aluminum adjuvant and β-amyloid peptide). DAMPs are involved in the so called *sterile* inflammation.[2] These innate immune processes bring the host inflammatory machineries to the site of infection or injury, and are responsible for the recruitment of additional immune cells such as lymphocytes to bridge innate and adaptive immunity.

Among the PRRs, nucleotide-binding domain and leucine-rich repeat receptors (NLRs) and absent in melanoma 2 (AIM2)-like receptors (ALRs) are responsible for inflammasomes assembly. Nowadays 22 human and 34 mouse NLRs have been identified. They can be divided into 4 subfamilies based on the type of N-terminal domain:

NLRA contain acidic transactivating domain (CIITA, Class II major histocompatibility complex transactivator)

NLRB contain a BIR (Baculovirus Inhibitor of apoptosis protein Repeatdomain)

NLRC the N-terminal domain is the caspase activation and recruitment domain (CARD). The receptors in this subfamily are NOD1-2 and NLRC3-5.

NLRP NLRs containing the pyrin domain(PYD). They are numbered 1-14.

A detailed scheme of the subdomains in the different isoforms is reported in figure 1.1. Only some isoforms are reported to be able to form inflammasome complexes. NLRP1 was

the first discovered by Martinon et al in 2002.[3] Years later, NLRP3, NLRC4, and AIM2 inflammasomes-mediated interleukin(IL)-1β were descibed.[4].

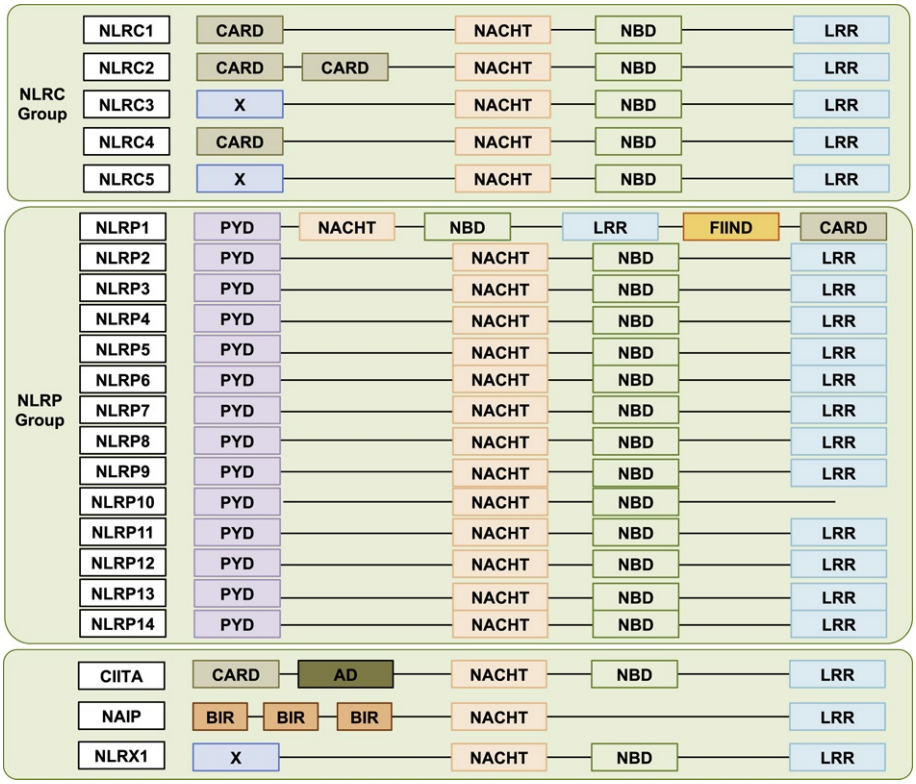

Figure 1.1: Schematic representation of NLR family members, including members of the NLRC and NLRP groups. Function to find domain (FIIND), Leucine-Rich Repeats (LRR), NAIP, CIITA, HET-E, and TP1-containing (NACHT) domain, Nucleotide-Binding Domain (NBD).

More recently NLRC1, NLRC2, NLRC3, NLRC5, NLRP6, NLRP12, have been shown to play a role as positive or negative regulators of immune signalling.[5] These inflammasomes have been reported to be able to form inflammasome supramolecular complexes and to activate caspase-1 (Casp-1). They all share the NACHT domain, but they are expressed in different cell types, in response to different stimuli, and interact with specific proteins in their own multimeric complexes.[6] The name of the NACHT domain (NAIP, CIITA, HET-E, and TP1-containing) comes from the name of the protein initially found to contain this feature. Table 1.1 highlights the physiological, structural and pathological aspects of the most studied inflammasomes. The biomolecular assembly, activation and dissolution of inflammasomes remains an emerging field of study. However, in the last years significant progress has been made in understanding inflammasomes and release of inflammatory mediators. NLRP3 inflammasome is probably the most studied among others inflammasomes.

Name	Expression site	Activation signals	Diseases	Structure
NLRP1 (NALP1)	Adaptive immune cells and tissues, non hematopoietic tissues	A/B toxins of *Bacillus anthracis*, *Toxoplasma gondii*, muramyl dipeptide	Vitiligo-associated multiple autoimmune disease, NAIAD, FKLC	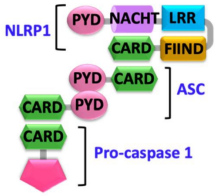
NLRP3 (Cryopyrin, NALP3, CIAS1)	Monocytes, neutrophils, dendritic cells, lymphocytes, osteoblasts, and epithelial cells	PAMPs, DAMPs (Monosodium urate, alum, silica, asbestos, K^+/Ca^{2+} efflux, ATP, ROS)	CAPS, MWS, NOMID, FCAS, CINCA Alzheimer's disease, type 2 diabetes, cancer, gout	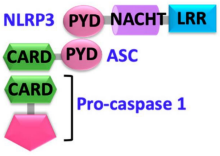
NLRC4 (IPAF)	Macrophage and intestinal epithelial cells	Bacteria, cytosolic flagellin	SCAN4, macrophage activation syndrome	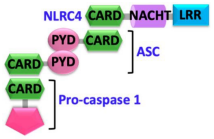
NLRP6	Cell of intestine and liver	Viral RNA, LTA of Gram-positive bacteria	Colitis and colitis-induced tumorigenesis	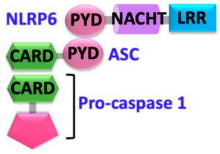
NLRP12	Neutrophils, eosinophils, monocytes, macrophages, and dendritic cells	Bacterial components	FCAS2	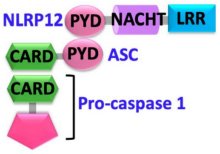

Table 1.1: Structural and functional details of most studied inflammasomes.[6]

1.2 Structural aspect of NLRP3 inflammasome

Increasing number of studies correlates NLRP3 inflammasome to host defence against pathogen, cancer, auto-inflammatory, neurodegenerative and metabolic diseases.[7] NLRP3 protein is a fundamental PRR for body homeostasis and is the sensor component of the inflammasome. The protein can be divided into three domains: LRR (C-terminal), NACHT and PYD (N-terminal).

The PYD domain has a significant role in the inflammasome assembly, it contains highly conserved hydrophobic and charged amino acid residues which establish interactions with

another inflammasome component, the apoptosis-associated speck-like protein containing a CARD (ASC) adaptor. The PYD domain of NLRP3 ($NLRP3^{PYD}$) structure consists of a six coiled α-helices structural fold, also known as *death fold*.[8] The structure reveals a six helices (α1-α6) and five connecting loops architecture. Among the others inflammasomes, NLRP4 and NLRP10 PYD demonstrates the higher structural similarity to $NLRP3^{PYD}$.[9,10] Published structure from Bae et al showed a disulphide bond between Cys-8 and Cys-108, which might be important for regulation of the activity of NALP3 by redox potential.[9] The crystal structure of $NLRP3^{PYD}$ reveals the presence of a symmetric dimer, whereas NMR, MALS (Multiangle light scattering), and SEC (Size-exclusion chromatography) show the coexistence of monomeric with higher-order oligomeric forms of $NLRP3^{PYD}$ in solution. The physiological relevance of the PYD dimer is still unclear.

LRR domains can be found in a variety of pattern recognition receptor proteins in the human innate system, because they provide a versatile binding scaffold for proteins and lipopeptides. Each LRR motif has 20-30 residues with a conserved 11-residues core sequence to assemble arc-shaped β-helical array with superstructure which can interact with several ligands. In NLRP3 structure there are 12 helices on the outer side and 13 β-strand on the concave side (See figure 1.2).

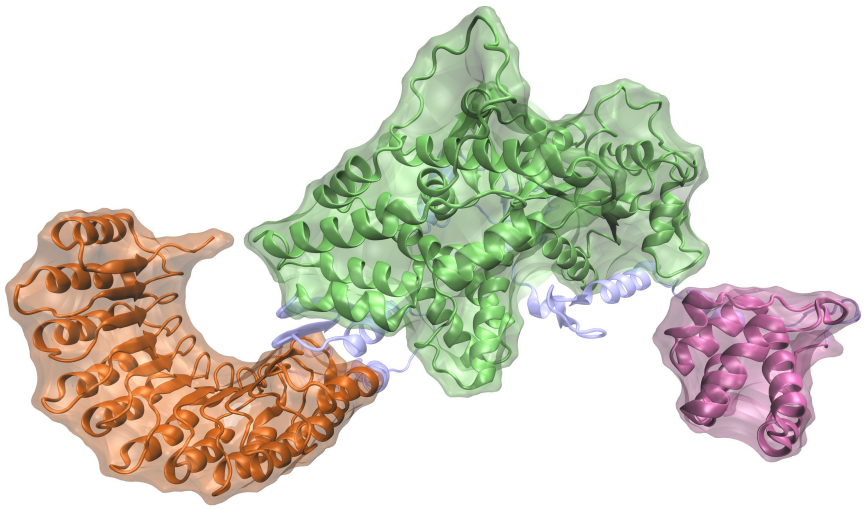

Figure 1.2: Representation of NLRP3 full-lenght model. Structure from AlphaFold.[11] PYD domain is coloured in mauve, NACHT domain in green, and LRR in orange.

In NLRP3 the domain is tought to contribute to autoregulation, protein-protein interaction and stimuli sensing. A cryo-EM structure has been recently acquired, showing a multimeric conformation of NLRP3 to form cages in its inactive form. These cages are mainly formed by interactions between the LRR curved surfaces in a *face-to-face* or *back-to-back* manner (figure 1.3).[12,13] The NLRP3 protein, similarly to others NLRs, belongs to the family of signal transduction ATPases with numerous domains (STAND) related to the AAA+ proteins. The NACHT domain contains 4 subdomains (figure 1.4): nucleotide-binding domain (NBD), helical domain 1 (HD1), winged-helix domain (WHD) and helical domain 2 (HD2).[14] The fish-specific NACHT associated (FISNA) domain is the terminal part of the

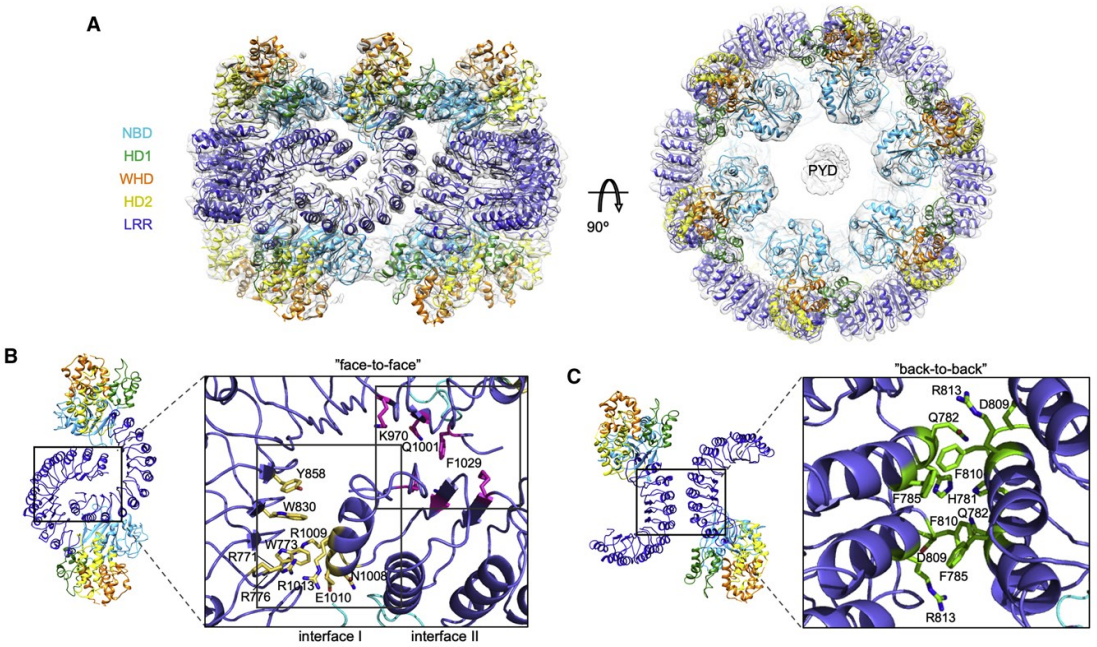

Figure 1.3: (A) Atomic model of the NLRP3 cage structure. NLRP3 domains are displayed with the color scheme in Figure 1A. (B and C) Overview and detailed views of *face-to-face* (B) and *back-to-back* (C) interaction interfaces. Residues used for mutagenesis are color-coded: green for *back-to-back* and yellow or magenta for *face-to-face* interfaces.[12]

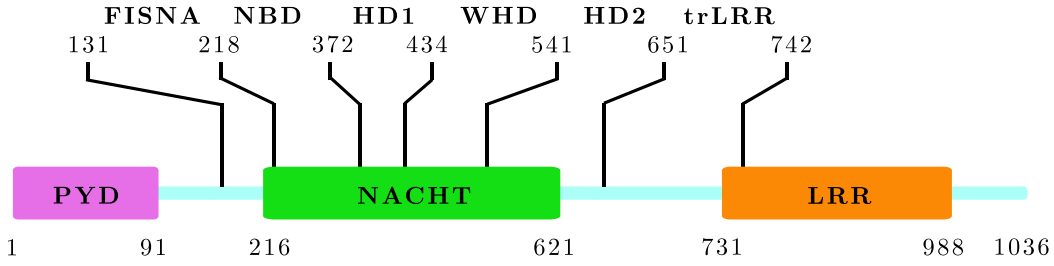

Figure 1.4: The 3 domains are reported on NRP3 sequence. The 6 subdomain are highlighted at the top.

PYD-NACHT linker and it is important for the correct placement of NLRP3^{PYD} to engage ASC. FISNA domain has been recently associated with the conformational change from the inactive close NLRP3 structure after decrease of K^+ intracellular concentration. The two polibasic sequences present in this region (KMKK^{132} and RKKYRKYVRSR^{145}) can interact with negatively charged lipids (phosphatidylinositol 4-phosphate, PtdIns4P)in the dispersed trans-Golgi network (TGN). Dispersed TGN enhances the displacement of the receptor to the centrosome, for full inflammasome activation. Double mutation of the two

polibasic sequences disrupts NLRP3 conformational changes and inflammasome activation. K^+ concentration influences the binding of NLRP3 to PtdIns4P.[15]

The NBD comprised of five parallel β-sheets (β1-β5) along with five α-helices (α1-α5), the HD1 exhibited four α-helices (α6-α9) and the C-terminal sub-domain, WHD consists of four α-helices (α10-α13) and two β-sheets (β6-β7). The NBD has the ATP-binding and hydrolysis properties. There are conserved motives in from AAA+ ATPases. Important structural features are the Walker A (ATPase specific P-loop) and the walker B motives (Mg^{2+} cation-binding site). Conserved sequence for walker A is GxxGxGK(T/S), where the lysine is directly interacting with γ-phosphate of ATP. In NLRP3 NACHT is located at K^{232}. The walker B has conserved acidic residue in hhhhDE motif (h stands for hydrophobic residues). The two acidic residues (in NLRP3: MDGF*DE*^{306}) coordinates the Mg^{2+} ion and the water molecule for phosphate hydrolysis (see Figure 1.5). A third region called

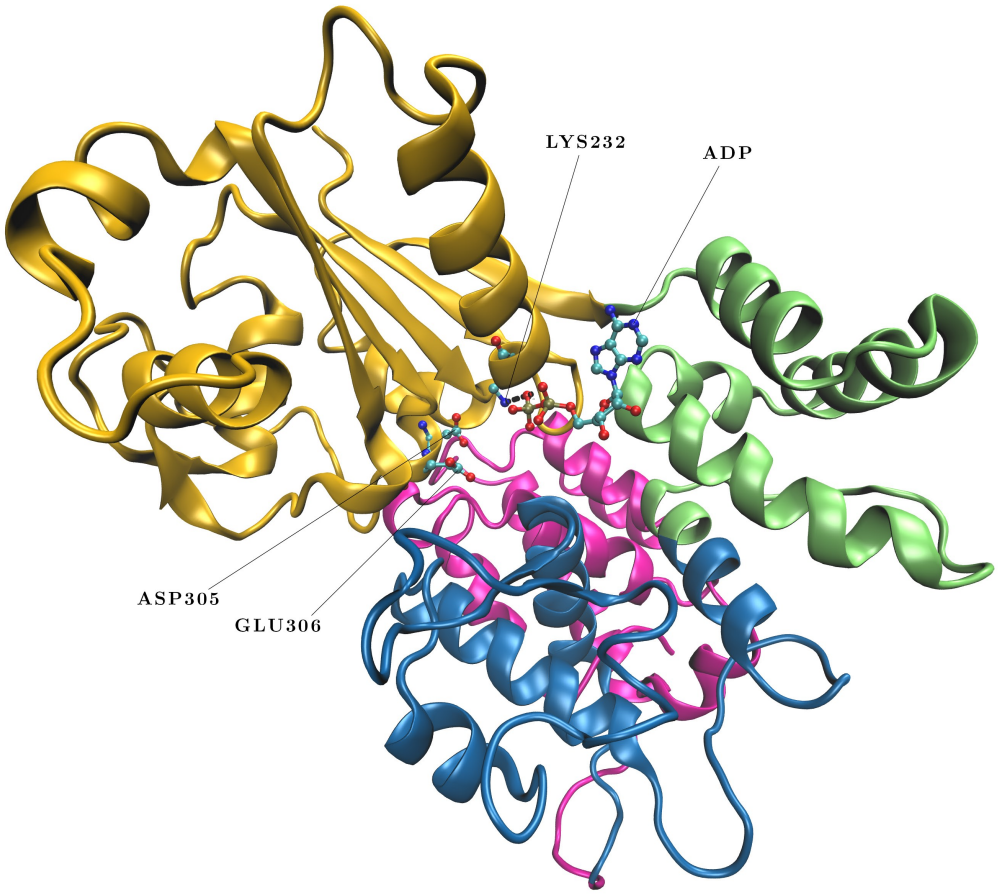

Figure 1.5: NACHT domain of NLRP3 (from residue 218 to 651). NBD in yellow, HD1 in green, WHD in blue and HD2 in magenta. The coordinates are from the crystal structure (PDB ID: 7alv). ADP molecules is shown in cyan, Asp305 and Glu306 are in Walker B, Lys 232 is in Walker A.

sensor 1 is important for the interaction between walker A and walker B and for the correct positioning of the ATP molecule. The moiety is hhhTTR (NLRP3: LLITTR^{351})

with the arginine residue interacting with phosphate group.[16] Studies on NLRC4, revealed that the switch from the inactive to the active conformation has a rigid body movement of approximately 90° of WHD-HD2-LRR module with respect to HD1 around the hinge region (between HD1 and WHD).[17] All the structures published in the closed conformation showed ADP molecule bound. It was previously reported about the ATP hydrolysis (after ADP to ATP transition) might be the cause behind the conformational change of NLRs, but nowadays this event seems not directly correlated with the activation mechanism.[18]

1.3 Molecular activation mechanism

The NLRP3 inflammasome is a critical component of the innate immune system. The activation of the inflammasome by PAMPs or DAMPs leads to the release of proinflammatory cytokines, recruitment of others immune system components and cell death. Since the inflammasome is activated by a variety of stimuli and agonists, the activation mechanism is extremely complex and regulated at different levels. Different cell types can have different regulation steps and can differ for the downstream effects. The NLRP3 inflammasome can be activated through three different mechanisms: canonical, noncanonical and alternative.

1.3.1 Canonical NLRP3 inflammasome activation

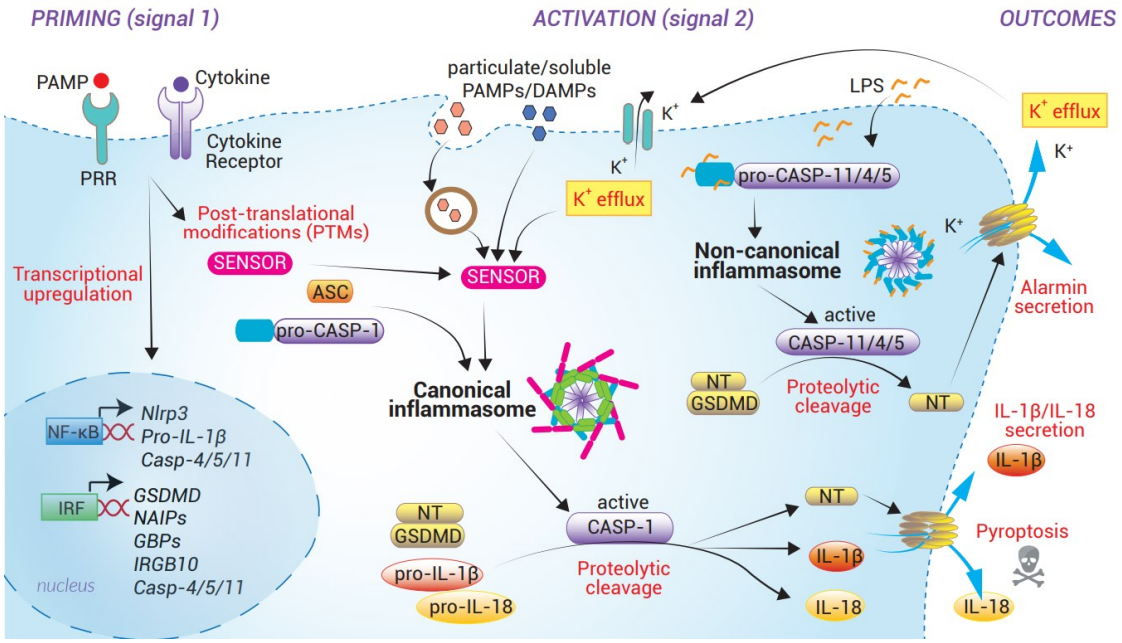

Figure 1.6: An overview on the NLRP3 inflammasome pathway. *Priming* and *activation* are two steps required by all inflammasomes for their assembly and mediated responses.

Priming

Inflammasome activation generally requires a two steps process: priming and activation. The overall process is summarised in figure 1.6. *Transcriptional priming* upregulates the expression of the inflammasome components, in particular of NLRP3, pro-caspase1 (pro-Casp1) and pro-IL-1β. In basal conditions, the concentration of these three proteins in the cytoplasm is not sufficient for full activation of the process in human monocytes and macrophages. The priming step in human cells is dependent on membrane signalling receptors: toll-like receptors (TLRs, e.g. TLR2, TLR4), tumor-necrosis factor receptor (TNFR), or cytokine receptors (IL-1β receptors, IL-1R1) which downstream activate the inducible nuclear transcriptor factor NF-κB.[19] After activation, NF-κB can translocate into the nucleus and promote the transcription of the pro-inflammatory genes.

During infection conditions, different bacterial components such as Pam3CysK4, Poly(I:C), lipopolysaccharides (LPS) and R848 can engage respectively TLR -2,-3,-4 and -7. In absence of an infection, NF-κB activation can also occur. For example IL-1α (an alarmin secreted by damaged cells) can bind its receptor (IL-1R1) and activate MyD88 and downstream NF-κB. Also IL-1β is an inducer of IL-1R1-mediated NF-κB activation. Since IL-1β is one of the final effector of the inflammasome activation, a positive autoregulatory loop is created. Similarly, TNF-α acts through its receptor to prime NLRP3 for activation in macrophages, but independently of MyD88.[20] Figure 1.7 reports an overview of the pathogen-related and sterile stimuli for *nlrp3* gene expression. Upstream NF-κB, regulatory proteins such as TIR-domain-containing adapter-inducing interferon-β (TRIF), interleukin-1 receptor-associated kinase (IRAK) -1 and -4, and the inhibitors of NF-κB kinase complexes (IKKs), are involved in the signalling pathway according to specific stimuli.[19]

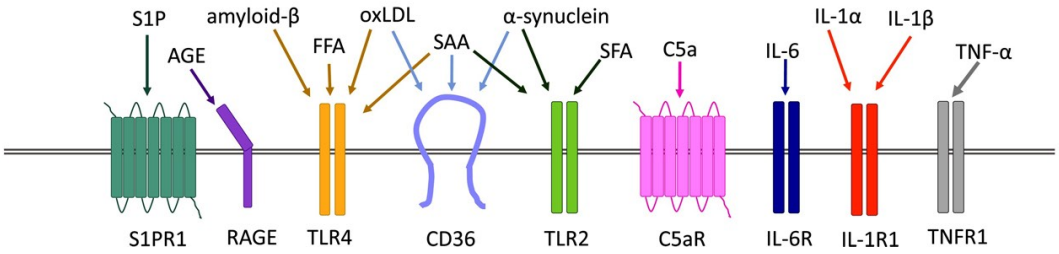

Figure 1.7: NLRP3 priming stimuli act upon a wide variety of cell surface receptors, with the same stimuli being able to target different receptors. Sterile stimuli and bacterial stimuli are reported above the receptors. Sphingosine-1-phosphate (S1P) receptor 1 (S1PR1), advanced glycation end product (AGE), receptor for AGEs (RAGE), free fatty acid (FFA), saturated fatty acid (SFA), oxidised low density lipoprotein (oxLDL), serum amyloid A (SAA), cluster of differentiation 36 (CD36), complement component 5a (C5a) receptor (C5aR).

While *transcriptional priming* relies on the NF-κB, two other priming steps have been described so far: the *post-transcriptional priming* and the *post-translational priming*.[20] Post-transcriptional regulation includes alternative splicing, non-coding RNAs (miRNA).[21]

The alternative pre-mRNA splicing is an important but less studied mechanism of inflammasome regulation. During alternative splicing, introns are removed and some protein coding exons can be excluded from the assembled mature mRNAs allowing for the generation of various mature mRNAs from the same DNA template. Increasing evidences correlates this phenomenon to the complexity of immune response and development of some diseases.[22] An example of alternative splicing is the regulation of the exon 5 in *nlrp3* gene. This variant lose the ability to interact with NIMA-related kinase 7 (NEK7) an to form active inflammasome. Another regulation step is through methylation and acetylation. For example, following Mycobacterium tuberculosis infection, the promoter region of the human NLRP3 gene is de-methylated, increasing NLRP3 expression and enhancing inflammasome activation.[23] microRNAs (miRNA) are negative feedback mediators of the innate immune system by targeting a range of signalling molecules downstream of TLR4. For example miR-223 has been described to suppress NLRP3 expression by binding to a conserved site in the $3'$ untranslated region of NLRP3, resulting in decreased inflammasome assembly.

Once expressed, NLRP3 protein is subjected to others regulatory steps driven by *post-translational* mechanism, influencing protein folding, stability, localisation and interaction with other proteins. The most relevant mechanisms are the phosphorylation and ubiquitination at specific positions. These aspects will be discussed in section 1.4 (regulation of NLRP3 inflammasome).

Molecular activation

NLRP3 inflammasome can be activated by a wide range of stimuli (PAMPs and DAMPs). It is unlikely a direct interaction with these activators, due to biochemical dissimilarity. To date, it is widely accepted that PAMPs and DAMPs induce multiple molecular and cellular events, including ion fluxes (such as K^+ efflux, Cl^- efflux, Na^+ influx, and Ca^{2+} mobilization), mitochondrial dysfunction, release of reactive oxygen species (ROS) and of mitochondrial DNA (mtDNA), lysosomal disruption and trans-Golgi disassembly. All the stimuli converge toward the sensor protein, in this case NLRP3.[19]

K^+ efflux was connected to IL-1β before the discovery of inflammasomes. K^+ efflux is sufficient but not strictly necessary for NLRP3 activation, and high extracellular K^+ concentration can block the inflammasome activation. Studies have identified some small chemical compounds, such as GB111-NH_2, imiquimod, and CL097, which are able to activate NLRP3 independently of potassium efflux. Additionally mouse macrophages with mutant NLRP3 (mutation R258W) found in Muckle-Wells syndrome, activate inflammasome upon LPS stimulation, independently of potassium concetration. These evidences also suggest that intracellular K^+ decrease may cause NLRP3 conformational changes that can be similarly induced by those small molecules, NLRP3-activating mutations, or signals from the alternative inflammasome pathway.[24] Very recently the NLRP3 conformational changes from the *close* and inactive to the *open* active conformation has been measured using a Bioluminescence Resonance Energy Transfer assay(BRET). The linker and FISNA domain have been identified as possible key structure in NLRP3 able to sense the K^+ efflux (see chapter 1.2, FISNA section).[15]

The role of Ca^{2+} mobilization in NLRP3 inflammasome activation remains controversial. Experiments with Ca^{2+} releasers did not show all the same results, and it is not

clear why ion flux activates NLRP3 in certain settings but not in others. Evidences of links between Ca^{2+} concentration and inflammasome activation were found in treatment with BAPTA-AM, a Ca^{2+} chelator, able to inhibit IL-1β release.[25] It was hypothesised that Ca^{2+} directly regulates NLRP3 inflammasome activation, as an increase of Ca^{2+} can promote interaction between NLRP3 and ASC in cell lysates of macrophages. However, NLRP3 inflammasome can be activated in macrophages that were incubated with Ca^{2+}-free medium, which suggests that at least the extracellular pool of Ca^{2+} is not required for NLRP3 inflammasome activation.[26] In conclusion, calcium mobilization might not be essential for activation, but it could be involved in the regulation of NLRP3 inflammasome activation under certain conditions.

The role of ROS and mitochondria in NLRP3 inflammasome activation is not well understood and is a topic of long-standing debate.[27] Studies on crystal structure of NLPR3 PYD have found a high conserved disulphide bond between Cys-8 and Cys-108 suggesting that regulation of disulphide bond formation by ROS, induces conformational changes, which might have a critical role for inflammasome activation.[9] Main sources for intracellular ROS are NADPH oxidase, respiratory mitochondrial function (mtROS), nicotinamide adenine dinucleotide phosphate oxidases (NOX), xanthine oxidase, oxygenase. Furthermore, ROS accumulation can induce TRPM2-mediated calcium influx. Direct connection between ROS and NLRP3 activation were also found in TXNIP, this protein can bound full-length NLRP3 and its NACHT domain. TXNIP dissociates from thioredoxin (TRX) and binds NLRP3 upon excess ROS production and regulates NLRP3 inflammasome activation. During ER stress, the ER stress sensors IRE1α and PERK upregulate TXNIP transcription and inhibit TXNIP mRNA degradation by reducing miR-17. Recent findings described the role of mitochondria as scaffolds for the assembly of the NLRP3 inflammasome. Mitochondrial molecules (mitochondrial antiviral-signalling protein (MAVS), mitofusin 2, and cardiolipin) associate with NLRP3 in response to NLRP3 activating stimuli. MAVS-NLRP3 interaction is required for NLRP3 inflammasome activation induced by soluble stimuli, such as ATP, nigericin, and poly (I:C), but not by particulate stimuli, such as silica, alum, and MSU.[19] However, further studies are required for clarifying the role of ROS and mitochondria in NLRP3 inflammasome activation.

In addition to ROS and potassium efflux, lysosome rupture plays a key role in NLRP3 activation. Crystalline and particulate structures, as MSU, β-amyloid, cholesterol crystals, silica, asbestos, alum, and CPPD are phagocytised causing lysosomal membrane damage and the release into the cytosol of cathepsin B, a cysteine protease of the papain family.[28] However, cytosolic release of cathepsins and particulate may also trigger K^+ efflux. Treatment with CA-074-Me, a cathepsin inhibitor, was found to partially inhibit NLRP3 activation. Cathepsin-B ablation is not effective in inhibiting NLRP3 activation, probably because of compensation by others redundant lysosomal cathepsins, instead CA-074-Me has off-target effect and is also able to inhibit other cathepsins.[29] Moreover, it is known that lysosomes have high concentration of calcium, and rupture-induced release may trigger ER calcium-induced calcium release and NLRP3 activation involving also Ca^{2+} channel.

1.3.2 IL-1β maturation and pyroptosis

The full inflammasome structure consists of a supramolecular complex composed by NLRP3, ASC (the adaptor) and the casp-1 (the effector). The biochemical explanation of the

NLRP3 activation by various stimuli is an emerging topic. Very recently, some structures of the inactive form have been published, contributing to the mechanistic information of NLRP3 activation.[12,13,30] The protein in the resting and inactive conformation is present in solution in a closed conformation in a double-ring cage assembly (see figure 1.8) that is primarily membrane localized on various membranous organelles (from plasmic reticulum to mitochondria and Golgi).[31] The cages are not able to nucleate ASC filament formation.

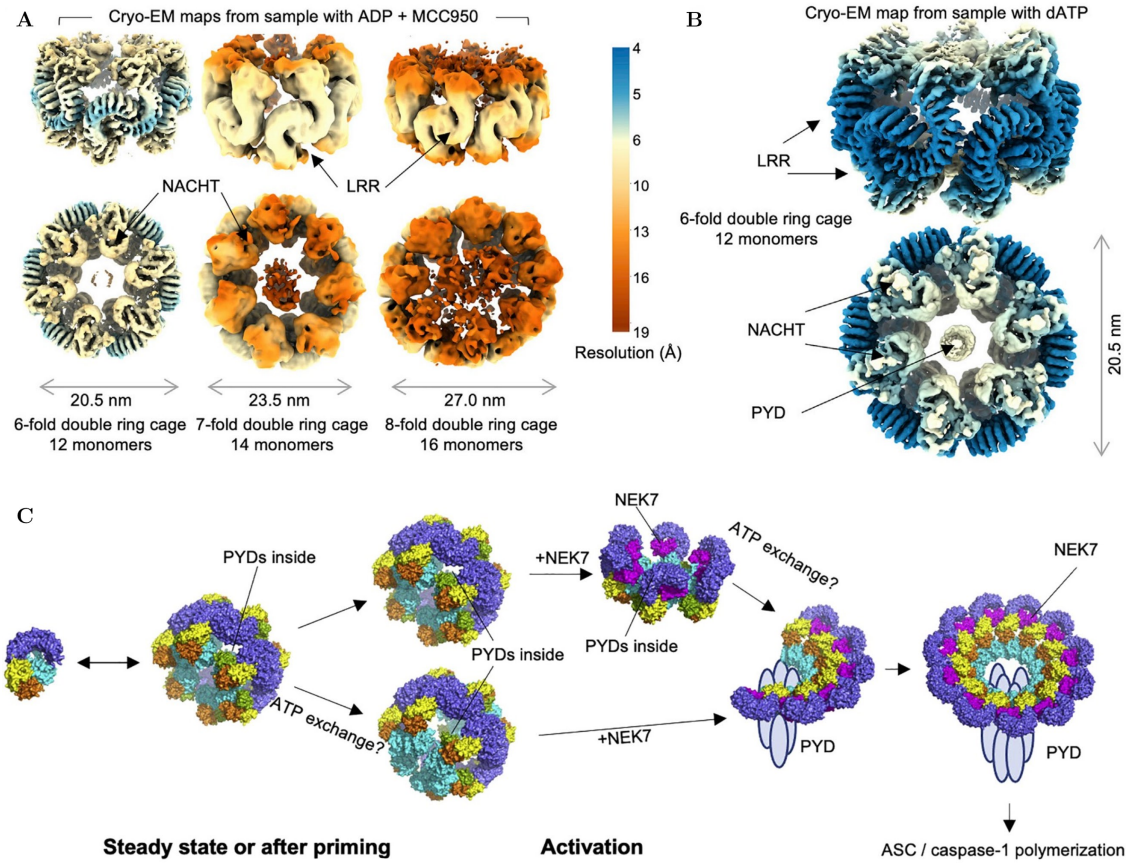

Figure 1.8: Cryo-EM maps of NLRP3 cage species purified in presence of ADP and MCC950 (A) or dATP (B). Maps are colored by resolution.[12] (C) NLRP3 activation model. Proposed structural rearrangements of NLRP3 in the course of NLRP3 activation. In a resting state, NLRP3 exists presumably in both monomeric and double-ring cage forms. Upon activation, NLRP3 gets transported to centrosome, with either "closed" (top) or "open" (bottom) NACHT domains. At centrosome, the double-ring cages get disrupted by NEK7 leading to a partial and then full NLRP3 oligomerization in a form of an active inflammasome complex.

Upon inflammasome stimulation, NLRP3 colocalise to the centrosome and engages NEK7. The interaction with NEK7 generates smaller NLRP3 oligomers species, but it is not sufficient for NLRP3 activation. NEK7 was reported to licences the activation of NLRP3.[14]

Another suggested trigger could be the exchange of ADP to ATP. NLRP3 has been suggested to have ATPase activity,[32] though the exact role of ATP hydrolysis in NLRP3 inflammasome activation remains unclear, and additional effectors may be required for nucleotide exchange. Structural understanding of inflammasome activation is largely based on snapshots of active and inactive states that reveal the conformational changes required for activation yet do not elucidate the sequence of events.[33] NLRP3 activation models rely on the activated structure of NLRC4: in the conformational change of NBD–HD1 subdomain, locate NEK7 at the oligomerisation interface mediating interaction with adjacent NLRP3.

The oligomerisation of active NLRP3 is the first step in the assembly of the inflammasome machinery. The NLRP3 active oligomer is able to induce the formation of a long filament of ASC (ASC speck). ASC has two subdomain, PYD and CARD. ASC^{PYD} can interact with $NLRP3^{PYD}$ and with other ASC^{PYD} domains. Specifically, the interactions between ASC-ASC and ASC-NLRP3 share the same two binding interfaces, found on opposite side: one involves α-1, α-4 and N- terminal α-5 helices and the other α-2, α-3 and C-terminal α-5 helices. The two opposite binding surfaces allow ASC self-association in a AB–BA–AB moiety. It was demonstrated that NLRP3 increases ASC-ASC aggregation, confirming the fundamental role of ASC self-association to form a helical fibril, containing six PYD repeats per turn, described via cryo-electron microscopy and also known as ASC speck (figure 1.9).[34,35] Unlike traditional signalling pathways in which protein molecules

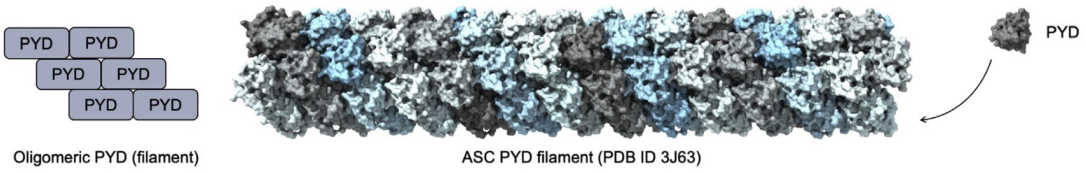

Figure 1.9: Polymerization of ASC^{PYD} forms a helical filament.

form interactions as monomers, dimers, or oligomers, the innate immune system forms higher-order protein complexes for signal transduction. These higher-order complexes are often assembled through homotypic domain-domain interactions into large specks as signalling hubs. Because of the high cooperativity, these higher-order assemblies have a characteristic threshold or all-or-none signalling behaviour in innate immune responses. The supramolecular ASC filament, exposing the CARD domain of the monomers to the cytosol is a platform for pro-casp-1 binding. The pro-caspase recruitment occurs through $pro\text{-}casp\text{-}1^{CARD}$ and ASC^{CARD} interactions. The pro-casp-1 is the inactive zymogen produced by the cells and consists of one prodomain (or propeptide) CARD (1–119) that interacts with upstream adaptor proteins and a catalytic domain consisting of subunits p20 (120–297) and p10 (317–404).[6,36] Mature casp-1 consist of tetramer of two large subunits of approximatively 20 kDa, surrounding two small subunits of approximately 10 kDa. In the active site the conserved QACXG pentapeptide where C is the nucleophilic cysteine is present.[37] During pro-casp-1 activation, the zymogen is cleaved after a critical Asp residue, generating both large and small subunits. The cleavage is the results of an autoproteolytic activity of the caspase, induced by proximity and dimerisation on the ASC surface. Activated caspase

proteolytically processes pro-IL-1β and pro-IL-18. The mature cytokines, once released, initiate downstream signalling events leading to the transcription of many proinflammatory and antiviral genes. Inflammatory caspase activation can also lead to pyroptotic cell death characterized by spillage of cellular contents.

The connection of pyroptosis and innate immunity is receiving an increasing interest from the scientific community. This form of cell death was originally deemed to be apoptosis because some of its characteristics were similar to apoptosis, such as caspase-dependency, DNA damage, and nuclear condensation. Afterward, this form of death was observed to be different from apoptosis. In 2001, D'Souza et al. coined the term of pyroptosis, which comes from the Greek roots pyro (fire/fever) and ptosis (to-sis, falling), to describe pro-inflammatory programmed cell death.[38] During the process, activated casp-1 (or casp-11/4/5) cleaves the Gasdermin-D (GSDMD) on a long loop, after the Asp of the sequence FLTD^{275}.[39] The generated N-terminal domain (GSDMD-NT) undergoes a conformational change, oligomerises in circular assemblies bearing 31 to 34 units. Three interface regions have been identified for the assembly of the circular structure, on the GSDMD-NT. These structures have hydrophobic residues with high affinity to plasma membranes. The insertion of the circular assembly in the membrane generates a pore measuring an average inner diameter of 215 Å (figure 1.10).[40,41] The activation of the GSDMD occurs in a two-

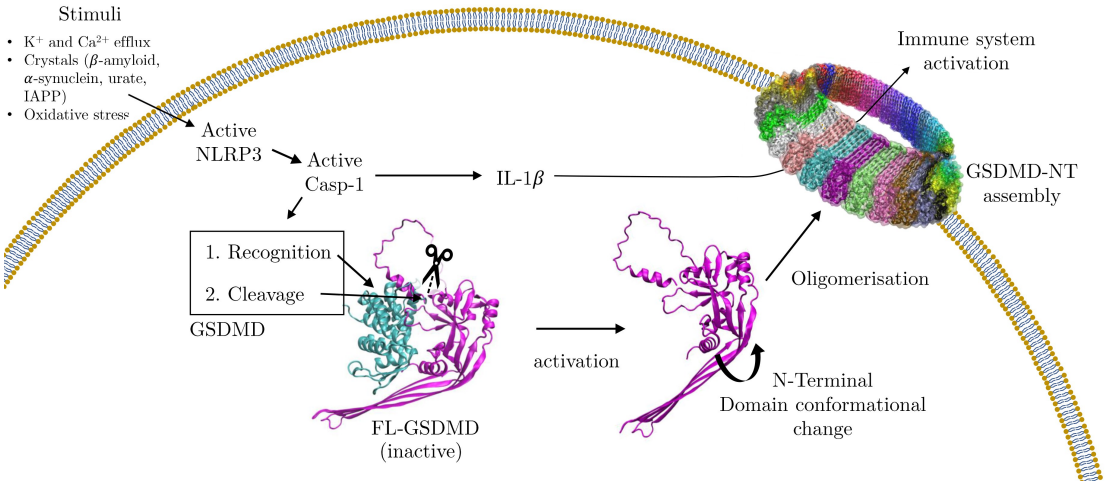

Figure 1.10: Activation of GSDMD induced by casp-1. Cleavage on a specific residue on GSDMD loop triggers activation, conformational change and oligomerisation of the N-terminal domain to form large circular pores in the cell membrane.

step process. A first critic recognition between casp-1 and GSDMD C-terminal domain (GSDMD-CT) is driven by an hydrophobic site. The complex has a 2:2 stoichiometry and is assembled in a highly similar manner as caspase-11/4-GSDMD-CT complexes. The protruding βIII/βIII' sheet at the caspase-1 dimer interface interacts strongly with the hydrophobic groove of GSDMD-CT. Trp294 and Ile318 of caspase-1 contact Val364, Leu367, Leu308 and Leu304 on the GSDMD-CT side (crystal structure PDBID: 6KN0). Caspase-1

I318N mutants, while undergoing normal autoprocessing, were defective in mediating GSDMD cleavage and pyroptosis in inflammasome-activated macrophages. The same results is obtained with V364A and L367A double-mutation or L367A L304A L308A triple mutation on the GSDMD side, demonstrating the fundamental role of the recognition step in the cleavage process of GSDMD and the hotspots involved.[42]

The second step is the cleavage at Asp275 of the GSDMD, removing the inhibitory 22 kDa C-terminal domain from the cytotoxic 31 kDa N-terminal fragment. The C-terminal and the N-terminal domain interacts each others with a 2,200 $Å^2$ of solvent accessible surface area, buried within the domain interface of hGSDMD, to form the auto-inhibited conformation. Residues participating in the NT-CT interfaces are conserved among gasdermin family members. In crystal structure (PDBID: 6N9O), the β1-β2 loop contributes to the majority of the interface. In particular, two aromatic residues in the middle of the β1-β2 loop (F49 and W50) dock onto a hydrophobic pocket formed by residues L290, E293, Y373, A377, C467, and A471 from the α5, α7, α8, and α13 helices. Most of these residues are conserved among gasdermin family members. Mutants of this region disrupt the auto-inhibition of the GSDMD-CT and induce the cytotoxic effect of the GSDMD-NT domain even without the casp-1 cleavage.[41] The recognition step brings the complex in the correct conformation for the cleavage. The proximity of the casp-1 catalytic site with the loop of the GSDMD allow the FLDT sequence to bind, allowing the cleavage by the proteasic serine.

Recently, pyroptosis has been redefined as gasdermin-mediated programmed cell death. Many other proteins from the gasdermin family are tightly connected and activated by caspases or different pathway. The genes that encode the proteins of the gasdermin family are highly conserved in vertebrates. There are six genes in humans (*GSDMA*, *GSDMB*, *GSDMC*, *GSDMD*, *GSDME*, and *DFNB59*). GSDMA3, GSDMB, and GSDME, can also be cleaved and induce pyroptosis like GSDMD, while the cleavage of GSDME by caspase-3 facilitates chemotherapy drug-induced pyroptosis in tumor cells.[43]

1.3.3 Different NLRP3 inflammasome activation mechanisms

The overall scenario of NLRP3 activation and interaction with the variety of stimuli is not completely elucidated. Potassium efflux seems to play a central role in the inflammasome activation, even if the molecular activation events are not completely understood. Historically, a K^+- and a TLR4-independent mechanism of inflammasome activation have been described in addition to direct NLRP3 activation. These are respectively the alternative and the non-canonical inflammasome pathway (figure 1.11).

Noncanonical NLRP3 inflammasome activation is strictly correlated with gram-negative infection or in vitro LPS stimulation. LPS is a ligand of TLR4 receptor, which trigger NF-κB mediated NLRP3 and pro-IL-1β priming. Studies on TLR4-deficient mice, showed only partial abrogation of NLRP3 activation but no priming activity, suggesting a different signalling pathway triggered by cytosolic LPS.[44] Non-canonical inflammasome represents an additional defense, against pathogens that have evolved to bypass cell surface TLR4. Gram-negative bacteria secrete LPS-loaded outer-membrane vesicles (OMVs), delivering LPS into the host cytosol. Murine caspase-11 or human caspase-4 and caspase-5 can be activated by direct binding of the hexa- and penta-acylated lipid A moiety of LPS, secreted

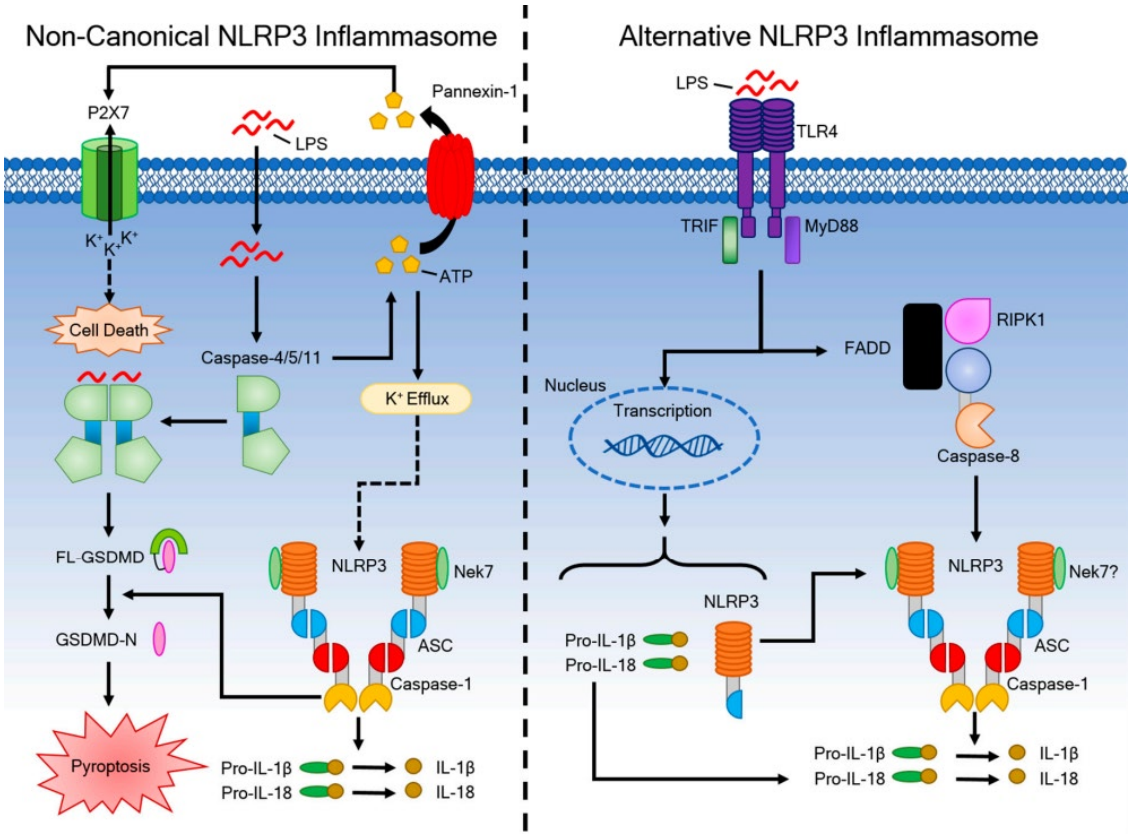

Figure 1.11: Mechanism of Activation for the Non-Canonical and Alternative NLRP3 Inflammasome Pathways. Non-canonical NLRP3 inflammasome activation (left) is induced by LPS internalization into the cytosol by transfection or infection. Caspase-11/4/5 induces pyroptosis through the cleavage of GSDMD. This process also activates pannexin-1 through caspase-11 to release ATP and induce K^+ efflux, which drives NLRP3 inflammasome assembly and release of IL-1β. The alternative NLRP3 inflammasome (right) is activated in human monocytes in response to LPS and requires receptor-interacting serine/threonine-protein kinase 1 (RIPK1), FADD, and caspase-8 for its activation. This pathway is K^+ efflux independent and does not induce pyroptosis.[19]

by certain gram-negative bacteria (E. coli, S. flexneri, S. typhimurium) via its CARD domain. In contrast to murine casp-11, human casp-4 is expressed in the cells in basal condition and the priming is not required for full inflammasome activation in human cells.[45] Caspases-4/5/11 induce pyroptosis through the processing of GSDMD, and pannexin-1, which is a protein channel that releases ATP from the cell. GSDMD cleavage generates its N-terminal fragment which has affinity for phosphatidylinositol phosphate of the inner plasma membrane, its oligomerisation forms pores inducing cell swelling, osmotic lysis and release of cytosolic contents in the extracellular space. Extracellular ATP released through pannexin-1 can activate P2X7 receptors (P2X7R, an ATP-gated cation selective channel

that opens a pore that triggers K^+ efflux. The non-canonical activation is inhibited by oxidized phospholipid 1-palmitoyl-2-arachidonoyl-sn-glycero-3-phosphorylcholine (oxPAPC), by caspase-4/11 binding and competition with LPS. OxPAPC inhibits the related LPS-induced pyroptosis.[46]

The alternative NLRP3 inflammasome activation escapes the classical two-step activation process (priming and activation). This mechanism has been observed in human monocyte, where LPS stimulation per se is able to activate caspase-1-dependent IL-1β maturation and secretion. This mechanism is completely absent from murine peripheral blood mononuclear cells. Murine bone-marrow-derived macro-phages and immortalized murine macrophages failed to secrete IL-1β in response to LPS treatment in the absence of additional nigericin stimulation. The alternative pathway for NLRP3 inflammasome activation is induced by TLR4, a membrane receptor activated by extracellular LPS. Downstream the signalling pathway proceed trough TRIF and the activation of the RIPK1 (Receptor-interacting serine/threonine-protein kinase 1)-FADD (fas-associated protein with death domain)-casp8 axis, resulting in casp-8 catalytic activity upstream of NLRP3. The interaction mode of NLRP3 and casp-8 is not known, because NLRP3 does not undergo direct casp-8 cleavage and an intermediate protein might be required. Is important to remember that the alternative mode of activation does not induce pyroptosis. Indeed, this pathway allows the cell to respond with a gradual release of IL-1β without committing to non-reversible cell death. In this setting, cell activation and effector function are separated and pro-inflammatory IL-1β signalling can be distinct to pyroptosis-associated effector functions in human monocytes.[47] How IL-1β can be released without lytic cell death remains to be verified. Unconventional secretory pathway might involve threading of IL-1β into early stage phagophores and the autophagy machinery.[48,49]

1.4 Regulation of NLRP3 inflammasome

Given the critical need to control a potentially harmful process and the number of danger signals converging on NLRP3, it is not surprising that numerous NLRP3 regulatory proteins have been discovered. The steps of the process for the NLRP3 inflammasome could be summarised in: epigenetic regulations, transcriptional regulations, degradation, post-translational modulations, interaction with other protein regulators, charge state in solution, subcellular localisation, 3D conformational changes and assembly into supramolecular quaternary structure. Only the main aspect of this complex scenario will be briefly described below.

Phosphorylation

Considering the limited expression level of NLRP3 in quiescent macrophages, the priming step has initially been demonstrated as a prerequisite for NLRP3 transcription. NF-κB can be activated by TLR signalling, and upregulate the expression of NLRP3, as well as pro-IL-1β.[50] However, emerging evidence indicates that a rapid priming within 30 min is sufficient for the activation of NLRP3 inflammasome, suggesting that rather than transcription, another layer of regulation may be more essential for the priming of NLRP3 inflammasome. Inhibitors targeting IKK or its downstream pathway shows little effects on LPS/ATP-induced caspase-1 activation in THP-1 cells, while the inhibitors acting upstream of the

IKK complex indeed blocks both NF-κB and inflammasome activation.[51] This study suggested that TGF-β-activated kinase 1 (TAK1), the mitogen-activated protein kinase kinase kinase (MAPKKK), or other TLR signalling-related kinase(s), may phosphorylate NLRP3 or other inflammasome components, which serves as a rapid but essential step for NLRP3 priming. In line with this hypothesis, both IKKα and IKKi have been described to play an important role in ASC phosphorylation. The dual phosphorylation of Ser16 and Ser193 of ASC by IKKα negatively regulates the binding of ASC to NLRP3 by sequestering ASC into the nucleus. In contrast, IKKi/IKKε can bind with ASC and phosphorylate Ser58 site during LPS-induced priming, which facilitates the translocation of ASC from the nucleus to the perinuclear region.[52]

Besides IKK/NF-κB signalling, MAPKKK-MAPKK-MAPK cascade is another crucial pathway involved in the TLR signalling. As the MAPK cascade can be rapidly activated via either Myeloid differentiation primary response protein 88 (MyD88) or TRIF, two adaptors downstream of TLRs, several groups investigated the potential role of different MAPKs in NLRP3 inflammasome activation.[50]

Phospho-proteomics analysis on NLRP3 identified several phosphorylation sites, ranging from the N-terminal PYD to the C-terminal LRR region. In human NLRP3 the most important sites are S5 (S3 in mouse), S198 (S194 in mouse), S295 (S291 in mouse), Y861 (Y859 in mouse). Dephosphorylation by protein phosphatase 2 A (PP2A) at S5 located in the N-terminus PYD regulates the interaction of NLRP3 and ASC. It was found that a phosphomimetic mutant of S5 that creates a negative charge completely attenuates NLRP3 activation by disturbing the interaction between NLRP3 and ASC.[53] Similar results were obtained from the phosphorylation of S295 by protein kinase A (PKA) and protein kinase D (PKD). In addition, dephosphorylation of Y861 by $PTPN_22$ allows NLRP3 activation and subsequent IL-1β secretion. The absence of $PTPN_22$ in cells results in increased NLRP3 phosphorylation, which abolishes inflammasome assembly and reduces IL-1β secretion. Another kinase, Jun N-terminal kinase1 (JNK1), has been shown to phosphorylate S198, providing a critical priming signal for NLRP3 self-association. The phosphorylation/dephosphorylation interplay has been associated with the cryopyrin-associated periodic syndrome (CAPS), as it has been shown to be coupled to impaired phosphorylation at the S194 site in mouse. Hence, the inhibition of NLRP3 phosphorylation/dephosphorylation processes is a potential pharmaceutical target for the treatment of NLRP3-associated diseases.[54]

Ubiquitination

Ubiquitination and deubiquitination events are crucial for NLRP3 inflammasome regulation and involve a series of enzymatic steps mediated by ubiquitin-activating enzyme. Deubiquitination is required for complete inflammasome activation, because it controls NLRP3 levels by the proteasome or autophagy degradation pathways. Lopez-Castejon et al. first reported that NLRP3 is ubiquitinated and inhibition of its deubiquitination by a deubiquitinase (DUBs) inhibitor b-AP15 blocks NLRP3 inflammasome activation.[55] The post-translational modification of proteins by ubiquitin constitutes a delicate equilibrium between the addition and the removal of this 8.5 kDa molecule from its targets. Addition of ubiquitin to its substrate is mediated by the sequential activation of E1-E2-E3enzymes. First, the E1 ubiquitin-activating enzyme and ubiquitin form a thioester bond that is then

transferred to an E2 ubiquitin-conjugating enzyme forming an ubiquitin-thioester intermediate that is finally transferred to the substrate protein by an E3 ubiquitin ligase. The ubiquitin system presents a great level of complexity compared to other PTMs. Ubiquitin is conjugated to lysine (K) residues in its substrate by its C-terminal G75 and G76 residues.[56]

Direct targets of ubiquitination in inflammasome pathway are NLRP3 itself, ASC and casp-1. TRIM31 (Tripartite motif containing 31, a protein with E3 ubiquitin-protein ligase functionality) has been shown to directly bind to NLRP3, inducing K48 poly-Ub and leading to proteasomal-mediated degradation of the NLRP3.[56] The SCF-FBXL2 E3 ligase is an anti-inflammatory system that binds at the W73 site and targets K689 for ubiquitin ligation and proteasomal degradation of NLRP3. In response to LPS exposure, an elevated level of FBXO3 (F-box O3), another E3 ligase, inhibits FBXL2 (promoting FBXL2 proteosomal degradation) with a final effect of NLRP3 expression level increase in cells. A small molecule, BC-1215, acts as an inhibitor for FBXO3 and reduces the secretion of mature IL-1β and IL-18.[57] It has been shown that cigarette smoke induces NLRP3 ubiquitination leading to its proteasomal degradation. Other E3 ligases involved in the dopamine signalling and NLRP3 modulation are the PARKIN, studied in polymicrobial sepsis, and MARCH7 able to mediate K48 ubiquitination and NLRP3 degradation by autophagy.[54]

Another mechanism independent from protein degradation where E3s are involved, is preventing NLRP3 inflammasome activation by holding the NLRP3 in an inactive state. The most recent E3 ligase linked to this mechanism is Cullin. This work showed that upon inflammasome priming, Cullin1 binds to and ubiquitinates NLRP3, maintaining it in an inactive state. After the activating signal (e.g. extracellular ATP) the cullin1 is dissociated from NLRP3, allowing it to form active inflammasome. A novel ligase reported in literature is the Pellino2. This E3 ligase plays a dual role in NLRP3 regulation. First, it interacts with NLRP3 during the LPS-priming phase facilitating NLRP3 K63 polyubiquitination, a step required for consequent inflammasome activation upon signal 2. In addition, the authors found that Pellino2 also ubiquitinates IRAK1 and limits its interaction with NLRP3 and consequently the ability of IRAK1 to inhibit NLRP3. In Pellino2-deficient macrophages, this effect is lost, and IRAK1 mediates its inhibitory effect on NLRP3 activation.[58]

DUBs also contribute to NLRP3 inflammasome activation. Involvement of DUBs as positive regulators of NLRP3 inflammasome was first identified when different DUB inhibitors G5, PR619, bAP15 and WP1130 were shown to block NLRP3-induced caspase-1 activation and IL-1b release. BRCC3, a JAB1/MPN/Mov34 (JAMM) domain-containing Zn^{2+} metalloprotease, is reported to directly interact with NLRP3, and its presence is required for appropriate NLRP3 inflammasome formation. BRCC3, in combination with the protein ABRO1 (Abraxas brother 1), forms the cytosolic BRISC complex and deubiquitinates the LRR domain of NLRP3 by specifically cleaving the K63-linked polyubiquitin chain.[19]

SUMOylation and nitrosylation

Several types of post-translational modulations, including SUMOylation and nitrosylation, are also involved in the regulation of NLRP3 inflammasome activation. Previous studies showed that nitric oxide (NO) and S-nitrosylation of NLRP3 inhibit inflammasome

assembly and IL-1 production during mycobacterial infection and LPS stimulation. However, whether nitrosylation is required for NLRP3 priming or feedback regulation after NLRP3 inflammasome activation remains to be fully characterized. In addition, NLRP3 SUMOylation plays either a positive or negative role in NLRP3 inflammasome activation depending on the context. NLRP3 SUMOylation by the small ubiquitin-like modifier (SUMO) E3 ligase MAPL (MUL1) restrains activation of the NLRP3 inflammasome, suggesting that SUMO conjugation of NLRP3 at multiple sites is a fundamental negative regulator of innate immune signalling. However, another study showed that SUMOylation of NLRP3 at K204 by SUMO1 facilitates ASC oligomerisation and NLRP3 inflammasome activation. Additional studies are needed to understand how multiple post-translational modulations pathways are selected and coordinated for the priming/licensing of NLRP3 and its oligomerisation.[59]

Chapter 2

NLRP3-related pathologies

The NLRP3 inflammasome complex formation and activation has been widely studied in a number of diseases. NLRP3 inflammasome is strictly involved in physiological activation and regulation of the innate immune system. It takes part in the first response to microbe and pathogen infection and restores homeostasis when activated in response to infection. Misregulation, overactivation, ageing or others pathological conditions lead to stimuli accumulation, and NLRP3 activation turns from beneficious to deleterious effects. Overactivation of NLRP3 is involved in several pathologies and diseases, including: a series of hereditary rare diseases known as CAPS,[60] atherosclerotic plaque progression and instability in atherosclerotic patients and animal models,[61,62] metabolic diseases involving oxidized low-density lipoprotein and cholesterol crystals which triggers NLRP3 inflammasome activation,[63] macrophage and animal model of type 2 diabetes and diabetic retinopathy,[64] gout stimulated by uric acid accumulation and monosodium urate crystals,[65] inflammatory bowel disease, including ulcerative colitis and Crohn's disease,[66] Amyloid β in Alzheimer's disease,[67] a role in initiation and development of cerebral and myocardial ischemic diseases,[68] contribution to progression of multiple sclerosis,[69] extracellular α-synuclein in Parkinson's disease,[70] obesity and functional abnormality of adipocytes caused by FFAs-induced inflammation,[71] chronic obstructive pulmonary disease,[72] non-alcoholic fatty liver disease,[73] and many others.

For further description, the most studied diseases has been categorised into CAPS, Metabolic disorders, and central nervous system (CNS) diseases.

2.1 CAPS

In the early 2000s, before the discovery of NLRP3 inflammasome, germline mutations in *nlrp3* gene, coding for a protein called cryopyrin, have been implicated in two autosomal dominant disorders: FCAS and MWS. Furthermore, *nlrp3* mutations were also identified in NOMID (also named CINCA). All these disorders caused by *nlrp3* gain-of-function mutations are now collectively known as Cryopyrin-Associated Periodic Syndromes (CAPS) and are part of the spectrum of the same systemic autoinflammatory condition. Cardinal clinical signs are fever, urticaria-like rash, arthralgia, sensorineural deafness and possibly amyloid A amyloidosis. Most of the mutations identified in CAPS patients are missense

variants located in the NACHT domain of NLRP3. However, mutations involving the same amino acid residue can be associated with either a severe form of the disease or a mild phenotype. The proposed underlying mechanism leading to inflammasome activation suggests that several mutations in the NACHT domain of the protein prevent the NLRP3 repression by ubiquitination and PKA. Recently a second mechanism has been observed in MWS phenotype macrophages, where NEK7 associates and activates NLRP3 even in absence of K^+ efflux as standard stimulus.[74]

2.2 Peripheral diseases and metabolic disorders

IBD is a chronic gastrointestinal inflammatory disease that affects the entire gastrointestinal tract and the colon. Two of the most common types of IBD include ulcerative colitis and Crohn's disease. Abnormal activation of NLRP3 inflammasome induce chronic colitis. The NLRP3-R779C variant is associated with the development of very-early-onset IBD in children younger than 6 years old. This NLRP3-R779C missense variant enhances NLRP3 inflammasome activation and pyroptotic death of macrophages. Similar gain-of-function mutation of NLPR3 D305N maintains NLRP3 in the active conformation associated with autoinflammation in adult patients. NLRP3 inflammasome activation in monocytes mediates systemic inflammation induced by Western diet feeding and promotes the progression of inflammatory diseases, including IBD. Intestinal microbiota plays an essential role in the control of intestinal pathogenesis and maintaining tissue homeostasis. NLRP3 serves as the central node in the interplay between intestinal microbiota and inflammatory response. Activation of the NLRP3 inflammasome reshapes the composition of intestinal microbiota; whereas metabolites of intestinal bacteria such as short chain fatty acids, ameliorate G protein-coupled receptors-triggered NLRP3 activation.[75] NLRP3 inflammasome is also associated with IBD-related diseases, such as primary sclerosing cholangitis and colon cancer.

More recent studies have suggested that the NLRP3 inflammasome is also an unexpected sensor for metabolic danger and stress. The NLRP3 inflammasome has been attributed to the development of many major metabolic diseases including atherosclerosis, non-alcoholic fatty liver disease (NAFLD), gout, type 2 diabetes and obesity induced insulin resistance.[76]

Atherosclerosis is a disease characterized by the deposition of fatty substances and cholesterol on the inner walls of arteries forming plaques and infiltration of immune cells into the atherosclerotic lesion. Although the precise mechanism and pathophysiology of atherosclerosis still remains incompletely understood, the progression of atherosclerosis is closely linked to dyslipidemia, obesity related factors, smoking, diabetes, Western-style diet, lack of exercise, and chronic immune-driven inflammatory conditions. NLRP3 links metabolic disturbances and inflammation. These danger signals comprise crystalline cholesterol, calcium precipitates, extracellular matrix component, ATP, as well as modified host molecules like oxidized LDL. Inflammasome activation induces secretion of pro-inflammatory and atherogenic cytokines like IL-1β and IL-18, which contributes to the vascular inflammatory response driving atherosclerosis development and progression.[77]

Non-alcoholic fatty liver disease (NAFLD) is the most common liver disease. Non-alcoholic steatohepatitis (NASH) is a type of NAFLD, characterized by inflammation and liver cell damage, along with fatty liver. Over-nutrition, complicated by certain health

conditions including insulin resistance, obesity, metabolic syndrome, and type 2 diabetes, makes NAFLD more likely to develop into NASH. Excessive hepatic levels of lipotoxic lipids, such as ceramides, diacylglycerols and free fatty acids, have been suggested as key molecules promoting progression of NAFLD to NASH. The pathology leads to hepatic steatosis, inflammation, and fibrogenesis.[76]

Gout is an inflammatory arthritis caused by precipitation of mono-sodium urate (MSU) in articular joints and other tissues that is characterised by abrupt, self-limiting attacks of joint inflammation (So, 2008). Uric acid is the end product of the purine degradation pathway. When there is too much uric acid in the blood, it can start to form crystals in joints and under the skin, causing gout. MSU crystals are recognized by the pattern recognition receptors of the innate immune system, such as the TLRs, and are phagocytosed by macrophages. Intracellular MSU crystals act as a 'danger' signal activating the NLRP3 inflammasome to induce inflammatory response both in vitro and in vivo. The response of macrophages to stimulation by MSU is also dependent on the inflammasome components ASC and caspase-1.[78]

Chronic inflammation associated with obesity has been shown to contribute to the development of insulin resistance and Type 2 diabetes. Evidence suggests NLRP3 and IL-1β play an important role. Obesity causes an increase of lipotoxic lipids, mitochondrial dysfunction, ROS, and ATP from necrotic adipocytes. These danger signals activate NLRP3 inflammasome and the secretion of inflammatory cytokines like IL-1β. This can prevent adipocyte differentiation and insulin signalling, leading to the development of insulin resistance.[79] In type 2 diabetes, IL-1β has been proposed to be a critical player in the loss of β cell mass. Patients receiving IL-1β antagonists showed improved glycemic control and β cell mass.

2.3 CNS diseases

Neuro-inflammation is a necessary response for eliminating invading pathogens, clearing damaged cells or debris, and promoting tissue repair in the central nervous system (CNS). However, uncontrolled neuro-inflammation has been identified as a causative factor of multiple neurological diseases. Microglia are the prominent innate immune cells that drive neuro-inflammation. Other CNS resident cell types like astrocytes, neurons, as well as infiltrating macrophages also express inflammasomes. Upon NLRP3 activation, the maturation of IL-1β and IL-18 and induction of pyroptotic cell death is triggered. High levels of IL-1β and IL-18 have been confirmed in the cerebrospinal fluid, brain tissue and plasma of patients with CNS infections, traumatic brain injury, Alzheimer's disease (AD), multiple sclerosis and Parkinson's disease (PD).[80]

In the case of chronic sterile inflammation, aggregated and misfolded proteins such as fibrillar amyloid-β and α-synuclein are resistant to lysosomal degradation. The accumulation of protein or aberrant protein deposition causes endosomal rupture, which leads to NLRP3 inflammasome activation.

AD is the most prevalent neurodegenerative disorder and the most studied with respect to inflammasome activation. Indeed, increasing number of studies have found a clear association between the microglia-mediated immune response and AD progression. AD is

characterized by the accumulation and deposition of amyloid-β (Aβ and by the intraneuronal formation of neurofibrillary tangles (NFTs) consisting of hyperphosphorylated tau proteins, both of which are danger signals and are known to activate microglia cells. Aβ is generated by sequential processing of two proteases and is usually removed from the brain by transport into the CSF, the blood vessels and local degradation by microglia. If the Aβ concentration rises above a critical threshold, oligomers and fibrils form and deposit in so-called senile plaques. At this stage, Aβ, and in particular its oligomeric or fibrillar forms, act as a danger-associated molecular pattern (DAMP) and are able to cause inflammasome activation.[81] In human AD brains, caspase-1 activity was strongly increased when compared with non-demented and age-matched controls. Similar condition has been found in patients suffering from mild cognitive impairment due to AD and from early-onset AD patients, suggesting that NLRP3 inflammasome activation represents an early event rather than a late pathogenic event. Both fibrillar and soluble Aβ demonstrated able to induce NLRP3-mediated IL-1β production. Another feature of inflammasome activation is the formation of ASC specks, which represent multimer NLRP3 complexes. Those ASC specks can be found in activated microglial cells and in the extracellular space, when microglial cells undergo pyroptosis. Once released, ASC specks bind rapidly to Aβ peptides, thereby increasing their propensity to aggregate in a time-dependent and concentration-dependent manner. ASC-bound Aβ was identified in brain samples from APP/PS1 mice and human AD cases. These findings suggest the involvement of the NLRP3-dependent pyroptosis in the earliest stage of Aβ deposition and progression of the disease.[82]

Similar to Aβ, fibrillar forms of α-Syn increased monocytic and microglial IL-1β release in a caspase-1-mediated fashion. This process requires the phagocytic uptake of α-Syn, ROS production, cathepsin B activation and ultimately NLRP3 inflammasome activation. TLR2 and Myd88 may be involved in the signalling pathway for microglial inflammasome activation.[83] α-Syn inflammasome activation may be only one axis of a mutual interaction. Recently, it has been shown that inflammasome activation through classical stimuli, including nigericin, paraquat, aluminium crystals, LPS or menadione, directly leads to α-Syn truncation through caspase-1-mediated cleavage. This truncation increased the propensity of α-Syn to aggregate and increased neuronal toxicity. In turn, neuronal loss was reduced by caspase-1 inhibition. This process can contributes to neuronal death through high cytokine levels and increased aggregated α-Syn. In support of a neuroprotective effect of inflammasome inhibition in PD, the phenolic flavonoid baicalein was found to reduce inflammasome activation and apoptosis in the rat substantia nigra dopaminergic system.[80]

Multiple sclerosis (MS) is a neurodegenerative disease of the CNS characterized by auto-immune driven inflammation. The study of inflammasomes in MS is focused on the peripheral immune response that enters the CNS through a compromised blood-brain barrier during MS pathology. Caspase-1 and IL-1β are present in MS plaques. These proteins are also elevated in peripheral blood mononuclear cells of MS patients. ASC and caspase-1 are suggested potential biomarkers for MS onset.[84] NLRP3 inflammasome activation has been studied in experimental autoimmune encephalomyelitis (EAE) rodent models of MS. Mice deficient in NLRP3, ASC, and caspase-1 were protected from developing EAE. Moreover, NLRP3 inhibition by MCC950 suppressed IL-1β production and attenuated EAE severity in mice.

Experimental, epidemiological, genetic and epigenetic data provided evidence for a role of innate immune mechanisms for neurodegenerative disease. Inflammasomes are able

to influence the initiation, persistence and chronicity of innate immunity. Modulation of inflammasome activity in models of AD, PD and other neurodegenerative disease suggests a potential therapeutic role for substances that can effectively inhibit this immune signalling mechanism.[80]

Chapter 3

Designing inflammasome inhibitors

3.1 Reported inhibition strategies

NLRP3 is the most deeply researched, probably the most poorly understood, and undoubtedly the most perplexing member in the family of inflammasome protein complexes. The strong inflammatory potential of NLRP3, as well as its role in diseases, makes it an attractive drug target. Various therapeutic approaches have been attempted to reach this goal, including blockage of TLR receptors, P2X7 receptor, NF-κB, caspase-1, IL-1β and IL-18, as well as NLRP3 itself. Recent fruitful progress has been made to block IL-1β signalling or specifically inhibit NLRP3 inflammasome activation. Nowadays, about a dozen of companies have programs dedicated to stopping NLRP3 or related inflammasome proteins, and three of them have been recently acquired by big pharma (Tab. 3.1).

3.1.1 Biologics against interleukin signalling

Therapeutic targeting of IL-1 family cytokines, and IL-1β in particular, has gained significant attention due to its central role in a range of autoinflammatory diseases. Therapies targeting NLRP3-dependent cytokines are already approved for therapeutic use; however, they have notable disadvantages relative to direct NLRP3 antagonists. Unfortunately, to date there are no NLRP3 antagonists approved for clinical use. Anakinra is a nonglycosylated recombinant version of human IL-1Ra (IL-1 Receptor a), and functions as a competitive inhibitor of both IL-1α and IL-1β for binding to IL-1R1. It has a good safety profile, but its short half-life of 4-6 hours makes daily subcutaneous injections necessary to maintain high target engagement levels. Anakinra was initially approved for the treatment of rheumatoid arthritis with methotrexate in patients that failed treatment on methotrexate alone, but these patients are nowadays prioritized to TNF-blocking agents. Anakinra is nowadays primarily used to treat CAPS and colchicine-resistant FMF (figure 3.1).[85]

Canakinumab is a human monoclonal antibody with an extended half-life of 26 days that specifically binds and neutralizes IL-1β. It has been approved by the FDA for the treatment of CAPS. Canakinumab is also being used for treating autoinflammatory diseases such as

Phase	**Company**	**Activity target**
Phase II	Olatec Therapeutics	Small-molecule NLRP3 inhibitors
	GlaxoSmithKline	recombinant human IL-18-neutralizing antibody
Phase I	Bristol-Myers Squibb	NLRP3 activators for cancer immunotherapy acquired from IFM Therapeutics
	Novartis	Small-molecule NLRP3 inhibitors acquired from IFM Therapeutics and developed in-house
Preclinical	Ardan ImmunoPharma	Small-molecule activators and inhibitors of the TMEM176B ion channel, which is an inhibitor of the inflammasome
	Genentech	NLRP3 inhibitors acquired from Jecure Therapeutics
	IFM Therapeutics	Small-molecule inhibitors of the NLRP1, NLRP6, NLRP10, and NLRC4 inflammasomes; small-molecule activators of the AIM2 inflammasome for cancer immunotherapy
	Inflammasome Therapeutics	Small-molecule inflammasome inhibitors
	NodThera	Small-molecule NLRP3 inhibitors expected to begin clinical studies this year
	Quench Bio	Small-molecule gasdermin-D inhibitors
	Ventus Therapeutics	Small-molecule inhibitors of innate immune system proteins, including inflammasomes
	ZyVersa Therapeutics	Antibody inhibitors of the inflammasome protein ASC

Table 3.1: Interest of the industry on the inflammasome pharmacological modulation. While NLRP3 is a hot target for drug designers, companies are taking a wide range of strategies to tackle the inflammasome.

FMF, TNF receptor-associated periodic syndrome and hyperimmunoglobulin D syndrome. canakinumab was evaluated in the Canakinumab Anti-inflammatory Thrombosis Outcome Study (CANTOS) (ClinicalTrials.gov Identifier: NCT01327846). High sensitivity CRP measurements are approved as a clinical biomarker of cardiovascular risk, and CANTOS was designed to evaluate the therapeutic potential of canakinumab in reducing the risk of cardiovascular events and secondary stroke in this cohort.[86]

A third clinically approved IL-1-targeted therapy for the treatment of CAPS is rilonacept or IL-1 Trap. Rilonacept is a human dimeric fusion protein consisting of the extracellular domains of IL-1R1 and IL-1RAcP fused to the Fc fragment of IgG. It functions as a soluble decoy receptor that prevents binding of both IL-1α and IL-1β to the IL-1R1 (figure 3.1). This chimeric protein has a half-life of approximately 1 week. On the IL-18 side, a regulatory mechanism that is being exploited for diagnosis and therapy of patients is the

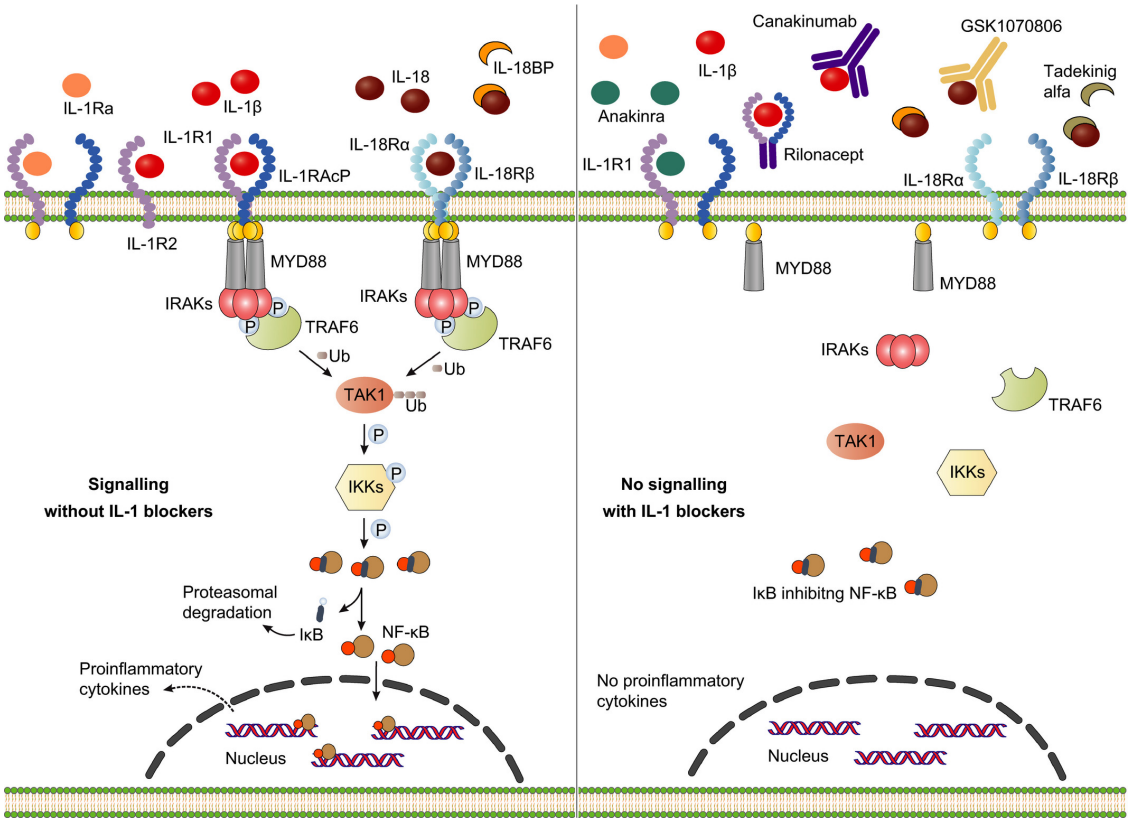

Figure 3.1: IL-1 and IL-18 signalling and its modulation by therapeutic agents: (*Left*) Engagement of IL-1 and IL-18 receptors by IL-1α, IL-1β, and IL-18, respectively, leads to the cytosolic recruitment of MyD88, IRAK kinases IRAK1/2/4, which associate with the E3-ubiquitin ligase TRAF6. This allows the activation of IKKs. In turn, IKKs phosphorylate and degrade IκB, inducing the upregulation of NF-κB target genes and the release of pro-inflammatory cytokines. (*Right*) Three biologic agents targeting IL-1 signalling have been approved by the FDA. As a recombinant form of the IL-1Ra, anakinra competes with IL-1β and IL-1α. Canakinumab, a human anti-IL-1β monoclonal antibody that specifically binds and neutralizes IL-1β. Rilonacept is a soluble decoy receptor, which consists of the extracellular domains of IL-1R1 and IL-1RAcP, and binds and neutralizes both IL-1β and IL-1α. In clinical phases, The recombinant IL-18BP, tadekinig alfa, and the human anti-IL-18 monoclonal antibody, GSK1070806, bind to IL-18 and inhibit the interaction of IL-18 to its cell surface receptors.[86]

neutralization of IL-18 by the natural IL-18 binding protein (IL-18BP), which precludes binding of IL-18 to its cognate receptors (figure 3.1). Given that the expression ratio of IL-18 and IL-18BP is often disturbed in inflammatory diseases, circulating levels of IL-18BP-unbound IL-18 (free IL-18) have been proposed as a biomarker for disease activity in adult onset Still's disease and systemic-onset juvenile idiopathic arthritis.[87] Moreover,

a recombinant version of human IL-18BP named tadekinig alfa demonstrated a favorable safety profile with early signs of efficacy in a recent phase II clinical trial of patients with adult onset Still's disease (ClinicalTrials.gov Identifier: NCT02398435). GSK1070806 is another biologic that was developed to neutralize IL-18-mediated inflammation. It is a recombinant human IL-18-neutralizing antibody with an extended half-life in circulation. It is currently being tested in a phase 2 clinical study for the treatment of patients with moderate to severe Crohn's disease (ClinicalTrials.gov Identifier: NCT03681067).

Protein-based products, like IL-1β- and IL-18-based biologics, request frequent subcutaneous injections. More importantly, chronic suppression of a key arm of the innate immune system inevitably comes with an increased risk for serious infections. Additional adverse events that are associated with chronic IL-1β inhibition include neutropenia, low platelet counts, headaches, abdominal pain, diarrhea, urticarial lesions, and inflammation at the site of injection.[86] Therapies acting upstream of IL-1β secretion might show an improved safety and efficacy profile because selective inflammasome inhibition would still allow IL-1β-driven host defense through non-targeted inflammasomes.

3.1.2 NLRP3 transcription and licensing inhibition

Inhibition of NLRP3 can be achieved by limiting TLR-mediated and TNF-mediated increases in NLRP3 expression; however, this approach is not ideal as it lacks specificity and is likely to produce many off-target effects. Aberrant TLR signalling is implicated in certain auto-inflammatory diseases, and inhibitors of interleukin-1 receptor-associated kinase 4 (IRAK4), a kinase essential for TLR-mediated activation of NF-κB, are already in development. A class of N-acyl 2-aminobenzimidazole derivatives and Imidazo[1,2-a]pyridine derivatives were identified from an high throughput screening of a small in-house molecular database followed by classical hit optimisation.[88,89] Inhibition of NLRP3 transcription pathway is reported is some of the first non-selective identified inflammasome inhibitors, such as sulforaphane, BAY 11-7082, parthenolide and isoliquiritigenin. Bay 11–7082, along with several structurally related vinyl sulfone compounds, and BOT-4-one (figure 3.3), were discovered via screening NF-κB inhibitors.

Multiple studies have established E3 ligases and DUBs as viable targets for novel anti-inflammatory proteins and small molecules. Evidences highlighted a number of E3 ligases and a DUB that critically regulate the protein constituents of the inflammasome, and inflammasome activation relies on adequate protein abundance of NLRs and ASC. Destabilizing inflammasome constituents by targeting ubiquitination is therefore a rational approach in inhibiting the inflammasome. One study has validated this approach. The small-molecule inhibitor BC-1215 (figure 3.4) was developed to inhibit the pro-inflammatory E3 ligase subunit, FBXO3, which ubiquitinates and degrades another E3 ligase component, FBXL2. NLRP3 is ubiquitinated by FBXL2 and degraded at the proteasome. Treatment with BC-1215 inhibits inflammasome activity by decreasing NLRP3 abundance. Analogs of BC-1215 also inhibit FBXO3 and have been shown to inhibit IL-1β secretion and tissue damage in sepsis mouse models including cecal puncture and ligation, bacterial-induced

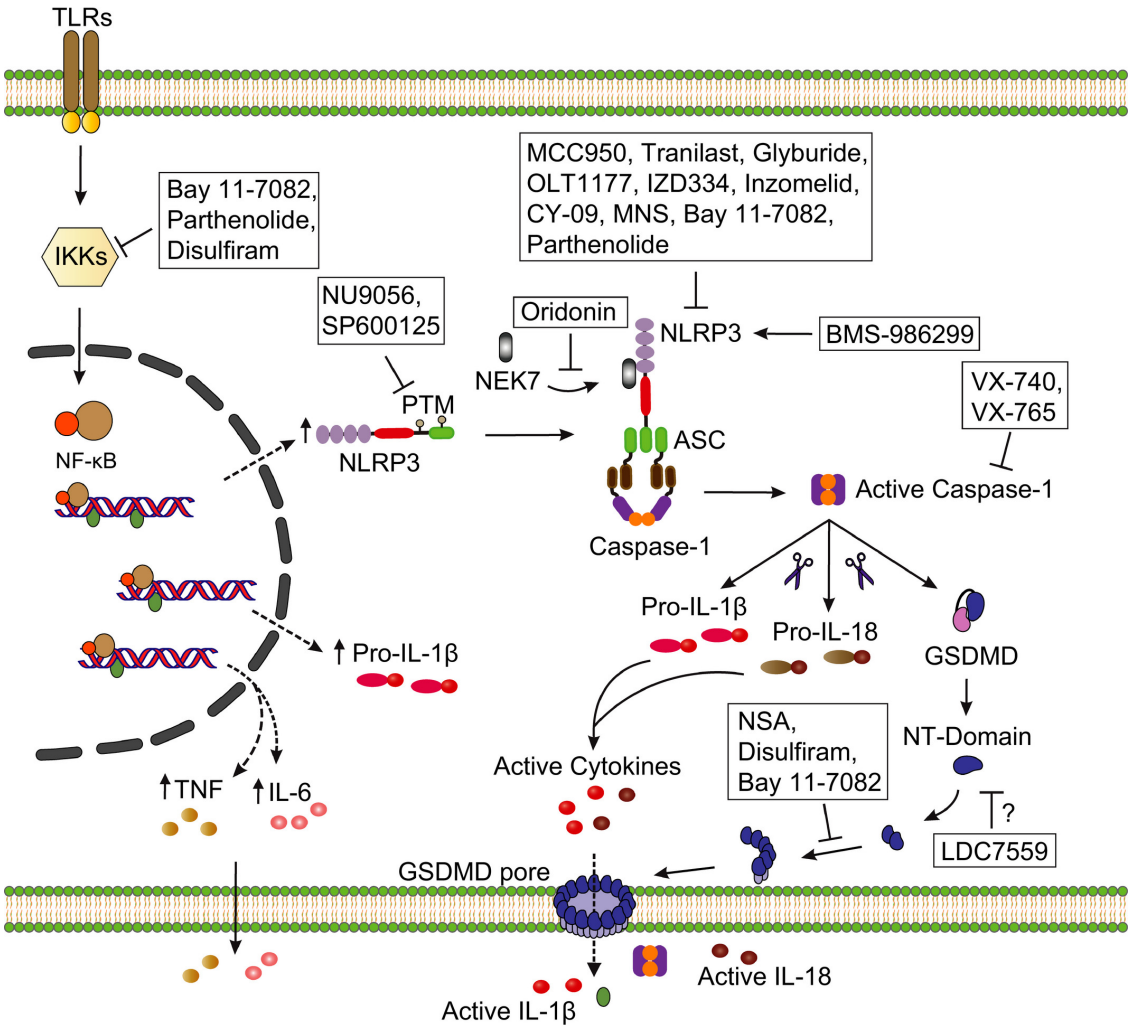

Figure 3.2: Pharmacological targeting of inflammasomes. Small molecule compounds such as Bay 11-7082, parthenolide, and disulfiram were shown to inhibit inflammasome signalling at several levels, including the priming step. Small molecules were also shown to inhibit NLRP3 (acetylation- or phosporilation-dependent activation) at the post-translational level. Other small molecules directly inhibit NLRP3 inflammasome activation. Blocking inflammasome signalling by targeting caspase-1 or GSDMD are alternative strategies currently being explored.[86]

pneumonia and H1N1 infection. Although BC-1215 also inhibits TRAFs and is not specific to the inflammasome, these studies serves as a proof of concept for therapeutic targeting of the inflammasome through inhibition of the ubiquitin machinery.[90] 3,5-bis((4-nitrophenyl)methylene)-1,1-dioxide,tetrahydro-4H-thiopyran-4-one (also known as G5, figure 3.4), a pan DUB inhibitor, was initially identified in a screening for compounds that

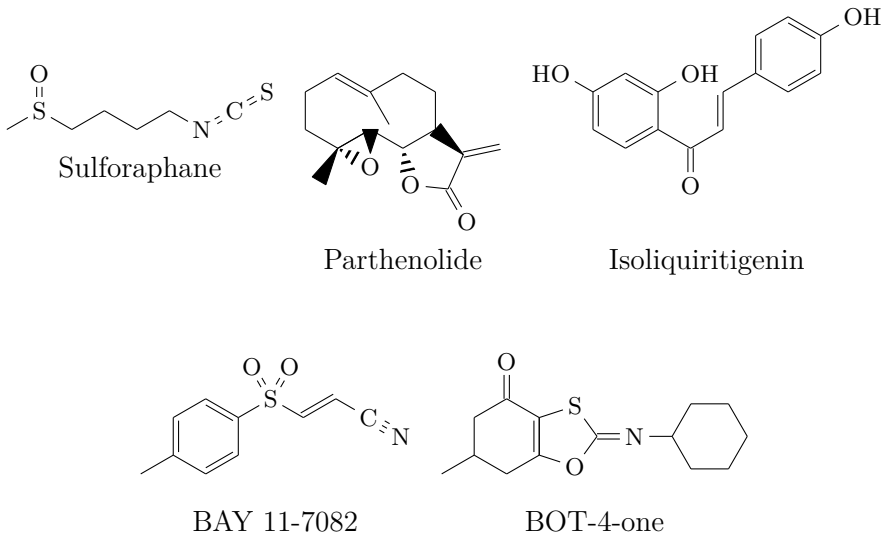

Figure 3.3: Non-selective NLRP3 inflammasome inhibitors.

are able to trigger caspase and induce apoptosis. It was later shown to specifically inhibit NLRP3 inflammasome activation but not AIM2 or NLRC4 inflammasome.[91] A recent study identified ML323 (figure 3.4) as a novel NLRP3 inflammasome inhibitor. The study reported that UAF1/USP1 is a deubiquitinase complex that eliminates the K48-linked polyubiquitination of NLRP3. As K48-linked ubiquitination is related with protein degradation, the UAF1/USP1 complex stabilizes the degradation of NLRP3, which increases cellular NLRP3 levels and promotes NLRP3 inflammasome activation. Since ML323 has an inhibitory effect on the UAF1/USP1 complex, its use keeps NLRP3 in check at the cellular level and prevents NLRP3 inflammasome activation. Moreover, the use of ML323 in folic acid-induced acute tubular necrosis (ATN) inhibited NLRP3 inflammasome-mediated inflammation.[92,93]

Acetylation plays a crucial role in NLRP3 inflammasome activation. KAT5 (also known as Tip60), belongs to MYST family of histone acetyltransferase and is involved in inflammasome post-translational modulation. KAT5 inhibitor-NU9056 exhibited a robust inhibitory effect on NLRP3 inflammasome both in vitro and in vivo, blocking NLRP3 acetylation.[94]

Targeting the JNK pathway has long been considered as a strategy for treatment of inflammatory disease. SP600125, a selective and potent antrapyrazolone inhibitor of JNK1 (Jun N-terminal kinase-1, figure 3.5), 2 and 3, was first identified and characterized as a JNK inhibitor in a high-throughput biochemical screening. JNK1 mediated S194 phosphorylation, an essential priming step required for NLRP3 self-association. Recently, SP600125 was reported to inhibit nigericin-induced caspase-1 cleavage and IL-1β maturation.[95]

The Syk-Pyk2 pathway has been shown to be involved in the phosphorylation regulation of NLRP3 inflammasome. Syk deletion or pharmacological inhibition with R406 (figure 3.5), a potent and selective Syk inhibitor, can completely block the production of IL-1β in response to fungal stimulation (Candida albicans). Another recent study also indicated that R406 was able to diminish ASC oligomerization through inhibition of ASC phosphorylation in ATP-or nigericin-induced NLRP3 inflammasome activation model. In addition to R406,

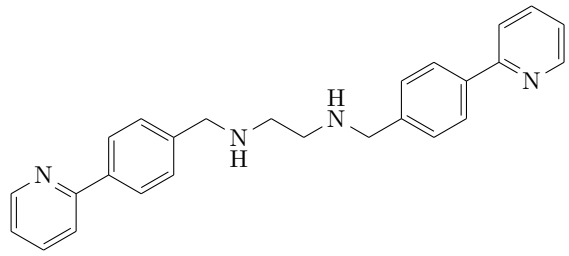

BC-1215

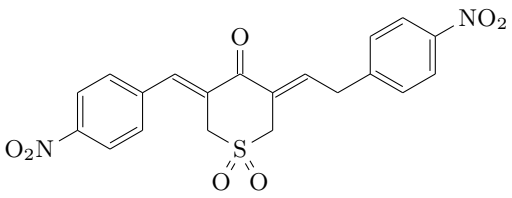

G5

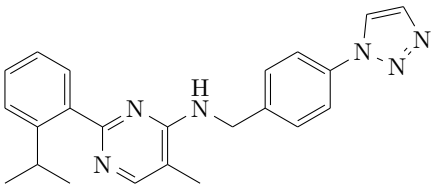

ML323

Figure 3.4: Inhibitors active towards NLRP3 ubiquitination state in post-translational modulation.

the Syk inhibitor piceatannol (figure 3.5) was also shown to inhibit IL-1β maturation and secretion stimulated by hemozoin in THP-1 macrophages. Proline-rich tyrosine kinase 2 (Pyk2), which is downstream of Syk, was shown to directly phosphorylate ASC at Tyr146 and promote ASC oligomerization, effects that were prevented by PF-431396 (Pyk2/FAK dual inhibitor, figure 3.5).[96,91]

As a key modulator downstream of B cell receptor signalling pathway, Bruton's tyrosine kinase (BTK) is emerging as a promising drug target in B cell malignancies and autoimmune disorders. The FDA-approved first-in-class BTK inhibitor ibrutinib is now used for mantle cell lymphoma, Waldenstrom's macroglobulinaemia and chronic lymphocytic leukemia. Two groups have recently shown that BTK is critical modulator of NLRP3 inflammasome activation. Pharmacological inhibition of BTK by ibrutinib or CGI1746 precludes caspase-1 cleavage and IL-1β maturation, without changing the expression level of either pro-capase-1 or pro-IL-1β. Due to potential off-target effects, irreversible covalent BTK inhibitors, such as ibrutinib, are not approved by FDA for long-term treatment of autoimmune disorders. Thus, the increasing number of reversible BTK inhibitors, such as CGI1746 (figure 3.5), holds promise for the IL-1β-driven inflammatory diseases.[97,91]

Inhibition of ATP-mediated activation of the P2X purinoceptor 7 (P2X7) is a possible mechanism to prevent NLRP3-dependent inflammatory diseases specifically triggered by high concentrations of ATP. However, inhibitors of P2X7 have thus far demonstrated little impact on auto-inflammatory diseases. This is believed to be due to lack of activity against the receptor, however, the development of more potent and selective compounds might afford better results in the future.[98]

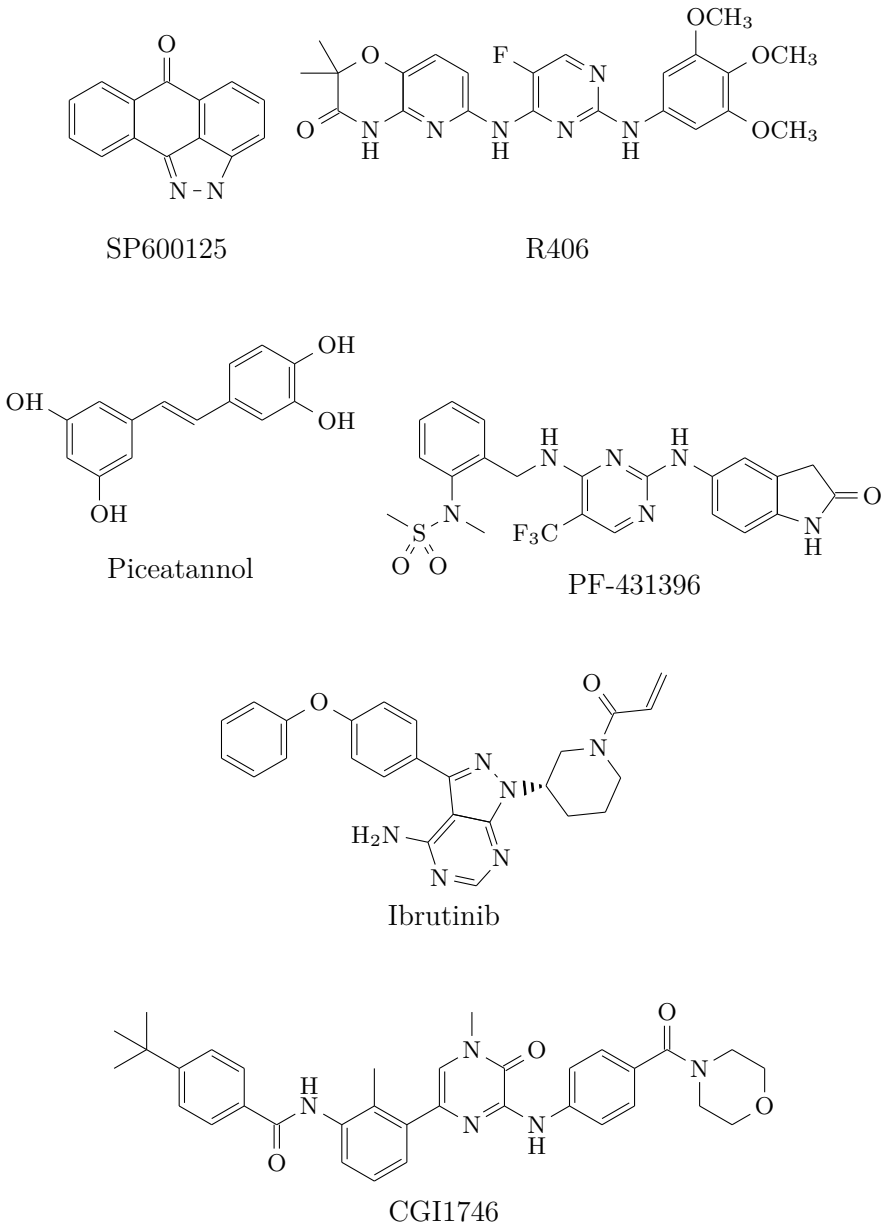

Figure 3.5: NLRP3 inhibitors active toward acetylation in post-translational modulation.

Lysosomal disruption-mediated NLRP3 activation is a common pattern in several diseases and thus represents an interesting intervention point. Unfortunately, the only currently identified components of this pathway are cathepsins, which are vital to many functions within the cell. Consequently, inhibiting these proteases would be expected to cause side effects. Ideally, lysosomal disruption could be inhibited by simply preventing uptake of the crystalline material or by inhibiting potassium efflux following lysosomal damage. One example compound is Ca-076Me, a cathepsin B inhibitor.[99] However, this approach requires further research before translation into clinic.[98]

3.1.3 Small-molecules for direct NLRP3 inhibition

Most inhibitors of the NLRP3 pathway were obtained from phenotypic screening, and development of these compounds has been hampered by an inability to directly identify their molecular targets. This is because the NLRP3 activation pathway remains relatively undefined in some aspect. Rational design of a direct antagonist of NLRP3 is also a challenge, the 3D structure has been only recently published.[12,30] NLRP3 structure has opened up avenues for the rational design of NLRP3 modulators.

The first major discovery in the field of NLRP3 inhibitors dates back to 2001 when a set of sulfonylurea derivatives were identified as capable of inhibiting IL-1β release form human monocytes. These compounds, structurally related to the insulin secretagogue glyburide, were named CRIDs. Structural modulation of glyburide analogues allowed the identification of a compound originally described as CP456,773 or CRID3 and lately renamed MCC-950 (figure 3.6).[100,101]

Extensive studies were performed in order to elucidate the mechanism of action and to identify the binding site of MCC950. Different biochemical and biophysical approaches have led to the shared hypothesis that MCC-950 binds to the Walker B domain of the NLRP3 protein, next to the ATP-binding site, inducing an inactive state of the protein which then is not able to revert to an active state. Regardless of its mechanism of action, the identification of MCC-950 as a potent and selective NLRP3 inhibitor sparkled great research activity around its chemical scaffold. This compound was used both as pharmacological tool for investigating the physiological and pathophysiological role of NLRP3 and as a structural template for the development of new di-arylsulfonylurea and di-arylsulfonylurea-like NLRP3 inhibitors.[102,103] A large series of di-arylsulfonylurea analogues of MCC-950 was generated and patented.[104] In their work, authors selected MCC-7840 (figure 3.6), with an IC_{50} of 13 nM in the IL-1β assay in mouse BMDMs, as the most attracting MCC-950 analogue according to PK properties. The sulfonylurea scaffold was further exploited for the generation of more water-soluble compounds. One selected compound (example 4, figure 3.6) showed better PK properties than previously developed sulfonylureas. Isosteric replacement of one oxygen atom of the sulfonylurea with a NH group furnished a series of novel sulfoximineureas structurally related to MCC-7840, two structural examples are represented by sulfoximine derivatives 3 and 27(figure 3.6).[105] Studies confirm that the area of the molecule occupied by the tricyclic submoiety of MCC-950 can undergo structural modulation and ring replacement. Researchers at Nodthera further explored the sulfonylurea moiety through the synthesis of a large library of compounds. Compound 1L with an IC_{50} of 0.074 µM was the most active of the series.[106] Another sulfonylurea derivative, NP3-146 (figure 3.6) very similar to MCC-950, was developed by Dekker and colleagues at the Novartis Institute for Biomedical Research. This compound was co-crystallized with the NACHT domain of NLRP3 in complex with ADP and allowed to define the binding site and the main contacts of MCC-950-like sulfonylurea derivatives.[30]

The crystal showed a binding pocket formed by the four subdomains of the NACHT domain, namely NBD, HD1, WHD1, and HD2. This inhibitor stabilizes the NLRP3 in an inactive conformation and does not allow the ADP-ATP exchange which is needed for conformational activation of the NLRP3 protein.

Another groups of active NLRP3 inhibitors share the benzensulfonamide group. The first compound of the series was JC-21 (figure 3.7), a synthetic intermediate used in the

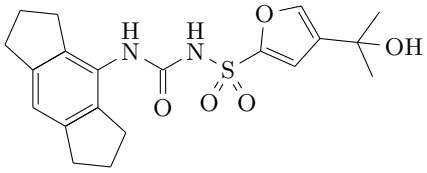

MCC-950

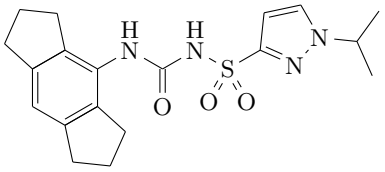

MCC-7840

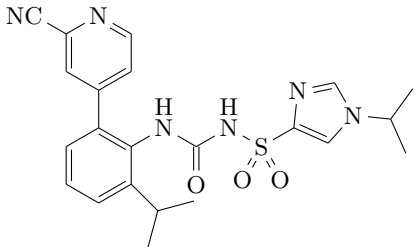

Example 4

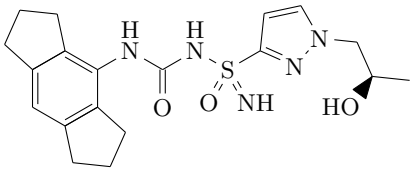

Derivative 3

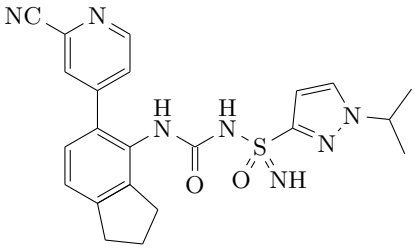

Derivative 27

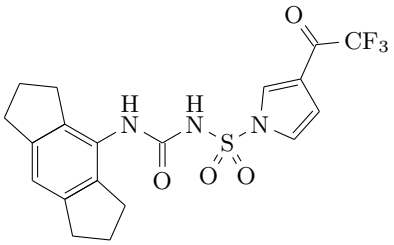

Compound 1L

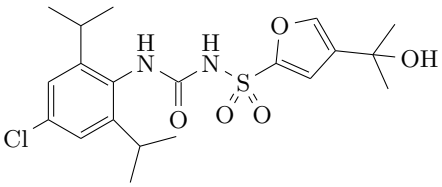

NP3-146

Figure 3.6: Direct NLRP3 inhibitors: structures of MCC-950 analogues.

preparation of glyburide. JC-21 proved able to decrease the IL-1β released from murine macrophages J774A.1 stimulated with LPS/ATP, cholesterol crystals or sodium monurate, and ASC aggregation in immortalized adult murine cardiomyocytes HL-1.[107] The structure of the lead compound JC-21 has been extensively modulated by Zhang and coworkers in order to obtain more potent NLRP3 inhibitors and to draw the SAR for NLRP3 inflammasome inhibition. A new hit compound, JC-124, was identified and its chemical scaffold extensively modulated in its molecular features giving rise to the more potent compounds

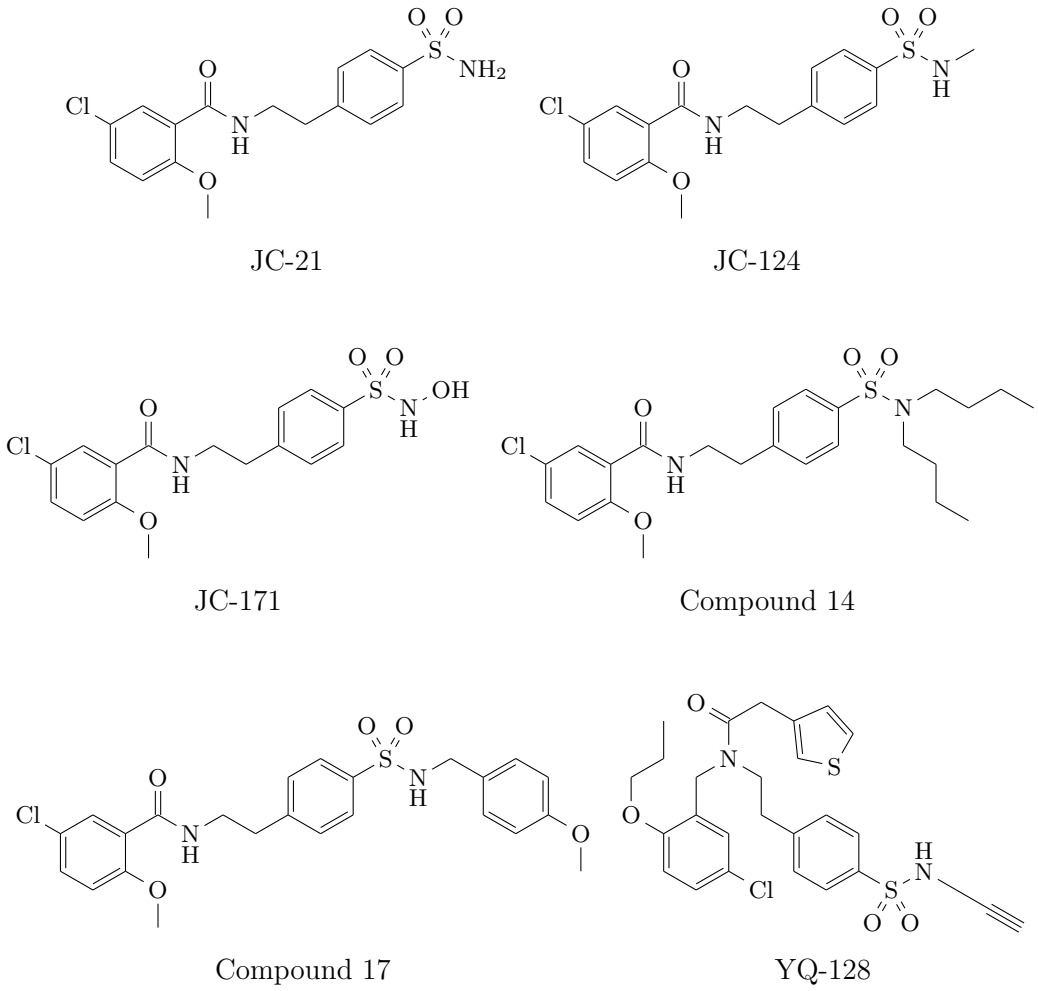

Figure 3.7: Direct NLRP3 inhibitors: structures of benzenesulfonamide-based analogues.

14 and 17 (figure 3.7), with about 6-7 fold the potency of JC-124. These compounds are selective for NLRP3 with no inhibition of the priming step and of AIM2 and NLRC4 inflammasomes.[108] JC-124 was also tested in an Alzheimer's disease model using APP TgCRND8 transgenic mice. Administration of the test compound for four weeks resulted in a reduction in amyloid-β deposition, microglia activation and a decrease in oxidative stress.[109] Another compound, JC-171 (figure 3.7), was designed as the putative hydroxylated metabolite of JC-21 and has a higher polarity than the parent derivative. This sulfonamide derivative was able to prevent the recruitment of ASC to NLRP3, thereby inhibiting the formation of ASC-NLRP3 complex. The in vivo effects of JC-171 were verified in two models of inflammation: systemic inflammation triggered by LPS and the experimental autoimmune encephalomyelitis (EAE) model of central nervous system inflammation, a commonly used animal model of multiple sclerosis. In both these models, JC-171 was shown to decrease the inflammatory response by inhibiting plasma levels of IL-1β and the induction of IL-17-producing T-helper cells.[110] Finally, from a second-generation sulfonamide derivatives SAR study on JC-124 analogues, the compound YQ-128 (figure 3.7) was

developed. YQ-128 proved selective NLRP3 inhibition of IL-1β release with submicromolar potency.[111]

Another compound, CY-09 (figure 3.8), was identified as a novel reversible inhibitor of the NLRP3 inflammasome that acts as a competitive inhibitor of nucleotide binding to the central NLRP3 NACHT domain with an IC50 of 5 µM. This compound showed specific inhibition of NLRP3 inflammasome activation without impeding NLRC4 and AIM2 inflammasome activity. Importantly, CY-09 binds to the Walker A motif of the NATCH domain and blocks NLRP3 oligomerization and ASC recruitment in the activation step. CY-09 was shown to limit NLRP3 inflammasome activation in pre-clinical disease models of CAPS and reverse metabolic disorders in diabetic mice by inhibition of NLRP3-dependent inflammation. Further, CY-09 is active ex vivo in cells from healthy human donors, and can suppress the pre-activated NLRP3 inflammasome in isolated synovial fluid cells from gouty patients.[112] A series of modulation for SAR elucidation has been developed. The SAR exploration of 2-thioxothiazolidin-4-one scaffold revealed that the one carbon spacer between phenyl ring and thiazolidinone core, the thioxo group, 4-carboxyl group on the second benzene ring, and 3-trifluoromethylphenyl group were key structural features for achieving both potent inhibitory activity and selectivity against NLRP3. In particular, the one carbon spacer demonstrated essential for the abrogation of the inhibition of Cystic fibrosis transmembrane conductance regulator.[113]

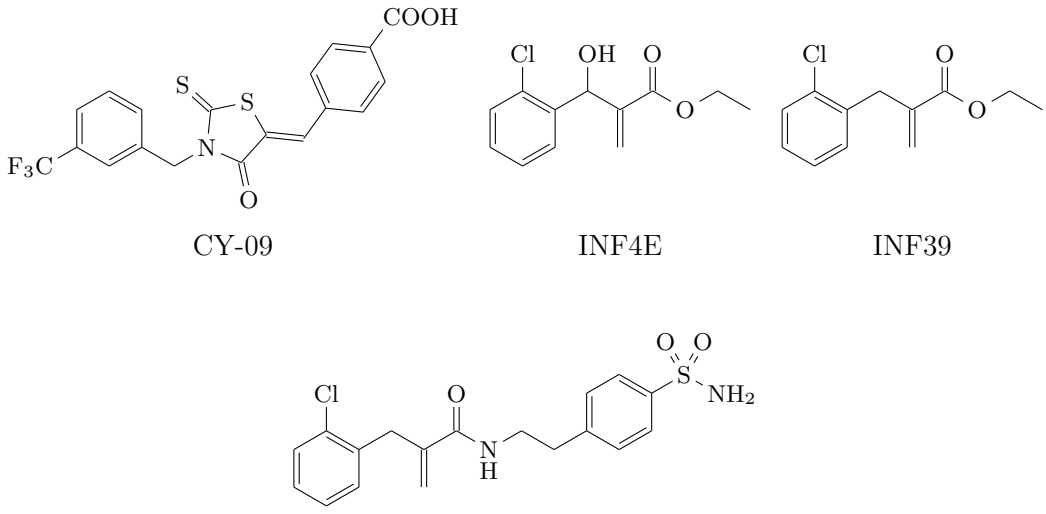

CY-09 INF4E INF39

INF58

Figure 3.8: Structures of direct NLRP3 inhibitors: CY-09, acrylates and acrylamides.

In our group, we previously described a series of electrophilic warheads designed to irreversibly inhibit the NLRP3 ATP-binding domain. INF4E (figure 3.8) demonstrates able to block NLRP3-dependent pyroptosis of THP-1 cells stimulated with LPS and either ATP or nigericin in a conc- and time-dependent manner in the submicromolar range.[114] The irreversible effect could be attributed to covalent-irreversible binding to nucleophilic residues of the target protein. In a second generation of compounds, the reactivity was modulated generating two series of compounds. This allowed the elucidation of SAR for

the acrylic acid derivatives. We found that both the elimination of the hydroxyl group at the benzylic position and the use of the acrylamide moiety instead of the acrylate ester reduced the reactivity and toxicity of the lead compound. Using this approach two groups of acrylates and acrylamides, with the hit compounds respectively INF39 and INF58, were obtained (figure 3.8).[115,116] These acrylic acid derivatives proved able to covalently inhibit NLRP3 activation without any detected binding to albumine. INF39 irreversibly dampened the conformational changes of YFP-NLRP3-Luc receptor expressed in HEK293 cells measured through bioluminescence resonance energy transfer (BRET) technique. INF39 also showed a certain ability to interfere with NF-κB signalling, being able to reduce the gene expression of TNF-α, IL-6 and IL-1β, thus it can be considered a multi-target drug that inhibits two closely related inflammatory pathways.

Until now, a small amount of research has been devoted to the de novo design of NLRP3 inhibitors. This was mainly due to the lack of the crystal structure of the NLRP3 sensor protein which has hindered structure-based drug design. The recently elucidated crystal structure of the NACHT domain of NLRP3 promises to open a new race towards NLRP3 inhibitors based on novel chemotypes.

3.1.4 Downstream NLRP3: casp-1 and GSDMs

Caspase-1 is the protease that matures IL-1β and it is the common denominator of all canonical inflammasome pathways. Development of clinical-grade molecules that selectively inhibit caspase-1 protease activity has been a focal effort of the pharmaceutical industry for many years. An electrophilic warhead that reacts with and inhibits Cys285 is therefore one of the strategies used by reversible (aldehyde-containing) and non-reversible (ketone-based) tetrapeptide inhibitors to inhibit caspase-1.[86] Nonetheless, due to their toxic by-products, poor stability, solubility and selectivity, tetrapeptide-based inhibitors are not suitable for therapeutic application. Fully synthetic peptide-mimetic prodrugs such VX-740 (pralnacasan) and VX-765 (belnacasan) were generated to overcome the toxicity and low bioavailability issues associated with peptidic caspase inhibitors (figure 3.9).[117] These prodrugs are metabolically converted in the cytosol by esterase activity to, respectively, VRT-18858 and VRT-043198, both of which act as reversible inhibitors of caspase-1 and the related inflammatory caspases 4 and 5. However, a phase 2 clinical trial with VX-740 in rheumatoid arthritis patients was discontinued after hepatotoxicity was observed in long-term follow-up animal studies. VX-765 reduces acute seizures and chronic epileptic activity in two mouse models of epilepsy, and it significantly suppressed the production of inflammatory mediators in models of rheumatoid arthritis and skin inflammation, and it was also tested in mouse model of Alzheimer's disease where it was able to inhibit amyloid beta deposition and neuroinflammation.[118] Problems in clinical trials with caspase inhibitors have spurred investigators to refocus efforts on inhibiting inflammasome sensors that act upstream of caspase-1, and more recently, on targeting the pyroptosis effector GSDMD.

The soluble inactive full-length of GSDM-D is formed by 2 domains, the C-terminal auto-inhibitory domain and the N-terminal pore-forming domain connected by a flexible interdomain linker. Activated caspases can cleave the linker, allowing the GSDMD-N to translocate into the inner plasma membrane. Very recently GSDMD became an attractive target for inflammasome and pyroptosis inhibition. Preventing GSDMD activation

in peripheral myeloid cells was recently shown to protect mice from neuroinflammation and demyelination in the EAE model of multiple sclerosis.[119] Molecules have already been reported to inhibit GSDMD-mediated pore formation. The alkylating compound necrosulfonamide (figure 3.9) binds directly to full-length GSDMD via Cys191, thereby preventing GSDMD-N dimers from assembling higher order oligomers that drive pyroptotic pore formation and cell lysis.[120] Disulfiram was recently discovered in a screen for inhibitors of GSDMD using a fluorogenic liposome leakage assay (figure 3.9). The molecule inhibited GSDMD by covalently modifying the GSDMD Cys191. Disulfiram was shown to inhibit pyroptosis in human and murine myeloid cells with µM potency, and it prevented secretion of IL-1β from these cells.[121] Finally, LDC7559 (figure 3.9) emerged as a direct inhibitor of GSDMD from a small molecule screen for inhibitors of phorbol ester-induced NETosis in human neutrophils.[122] Differently from disulfiram, NSA inhibits GSDMD through covalent modification of Cys191, the mechanism of action of LDC7559 is unclear. Other findings suggest that it may lack activity on recombinant GSDMD in the liposome leakage assay.[121] Concluding, GSDMD is an attractive novel target to modulate pathological inflammation driven by pyroptosis, including the release of inflammasome-dependent cytokines and DAMPs.

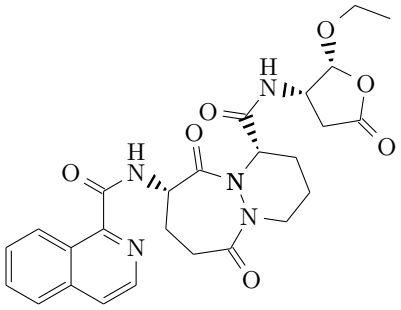

pralnacasan

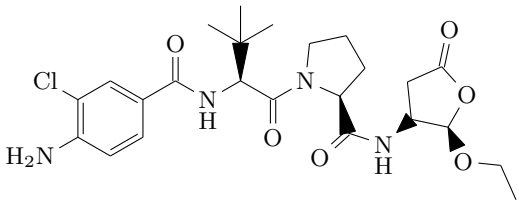

belnacasan

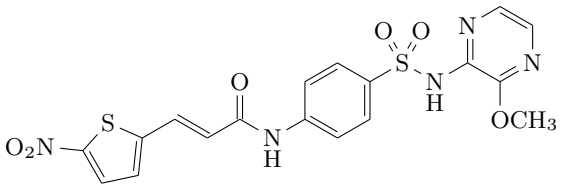

necrosulfonamide

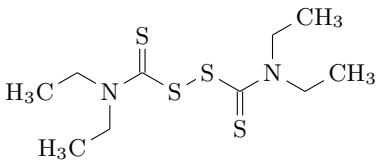

disulfiram

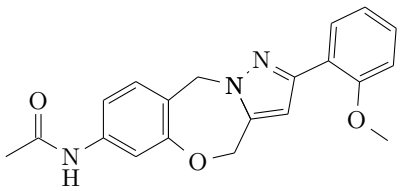

LDC7559

Figure 3.9: Caspase-1 and GSDM-D inhibitors.

Chapter 4

Aim of the thesis

Despite the well-established protective role, uncontrolled or protracted inflammation is thought to exert detrimental effect, by exacerbating underlying pathological processes and promoting the onset of new disorders. The aberrant activation of NLRP3 inflammasome is involved in the onset and progression of a wide range of human diseases. Among them auto-inflammatory, autoimmune, cardiovascular, neurodegenerative and metabolic diseases are the most studied. At present there are few inhibitors available, a concerted research effort toward the discovery of small molecules able to block NLRP3 activation is being performed both by industry and academia. These efforts have enabled the discovery of interesting compounds, some of which are now in clinical development. In recent years some aspects of the molecular activation mechanism have been explained. The publication of some NLRP3 structures will drive the design of new chemical entities able to interact with NLRP3. Among the inflammasome interacting network, the attention of medicinal chemist focused on some regulatory and/or effector protein as new tool for inflammasome modulation. We reported the post-translational modulators and the gasdermin family as the most promising alternative drug target.

In this PhD thesis for the modulation of the inflammasome pathway, we focused our attention on different molecular strategies. We started from a pharmaco-chemical hybridization strategy based on known molecule to design our benzo[d]imidazole-2-one compounds series. Activity data drove the development of the more advanced piperidinamide group of compounds, followed by the replacement of the central core with a more complex range of heterocycles. New study on the gasdermin-D were also conducted to investigate a possible new strategy for inhibiting its activation and the involvement in the pyroptotic cell death. To better describe the rational of the molecular design we divided our work in 5 sections. The synthesised compounds were characterised in preliminary in vitro pharmacological assay for the potential inhibition of NLRP3-dependent IL-1β release and pyroptotic cell death in differentiated THP-1 cells.

4.1 Playing around the benzimidazole scaffold

In previous studies, the research team of Prof. Bertinaria discovered that α,β-unsaturated Michael acceptor are common pharmacophores of both direct and multi-target NLRP3

inhibitors. Based on this observation a library of electrophilic warheads was developed to explore the possibility of obtaining new compounds able to interfere with the NLRP3 inflammasome signalling. INF4E showed the best activity within this series of warheads. It was tested on PMA-differentiated and LPS-primed THP-1 cells, at concentration of 10 µM, pyroptosis was triggered by ATP (5 mM), and LDH activity was measured in collected supernatant by a colorimetric assay.[114] Pyroptosis inhibition tested at 10 µM, was found to be 80.9 ± 5.7 %, with a cytotoxic concentration (TC_{50}) of 65.0 ± 5 µM measured in HK-2 cells by the MTT assay.[116] In order to reduce the cytotoxicity, INF4E was modulated developing INF39, by tuning down the reactivity of the Michael acceptor moiety and the cytotoxicity related to the benzylic hydroxy-group (Figure 4.1). INF39

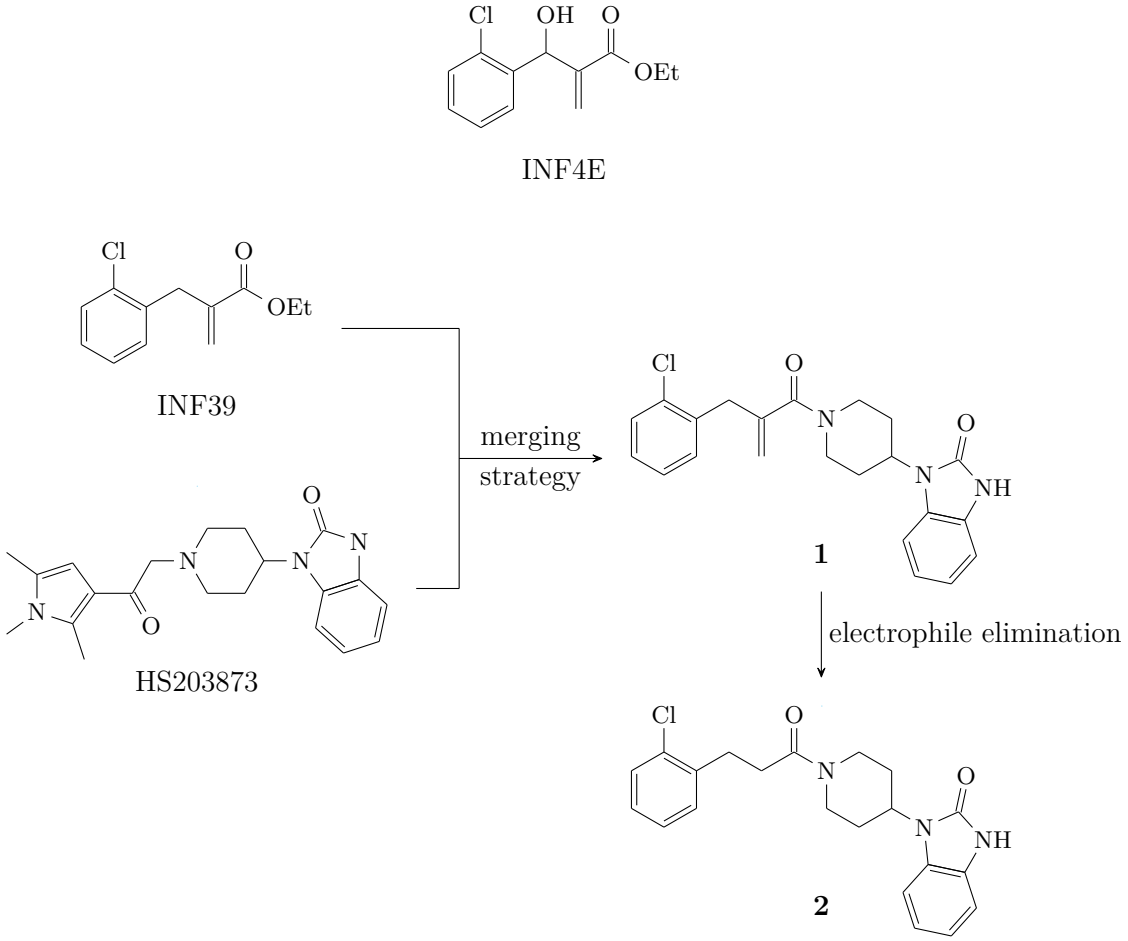

Figure 4.1: Structure of compounds INF4E, INF39, HS203873 and rational design of compounds **1** and **2**

was able to decrease pyroptotic cell death of LPS/ATP-stimulated THP-1 cells by 33.6 ± 7.1 % at 10 µM showing no relevant cytotoxicity up to 100 µM, owing to its reduced reactivity. In addition, INF39 proved able to prevent DNBS-induced colitis in vivo after oral administration in mice at both 50 and 25 mg/kg.[116] A recent report demonstrated that

INF39 is also able to inhibit the NEK7–NLRP3 interaction attenuating NLRP3 assembly in macrophages.[123] A benzo[d]imidazole-2-one derivative, HS203873, was identified in a fluorescent-linked enzyme chemoproteomic assay (FLECS). HS203873 was able to bind to NLRP3 and its ability to inhibit NLRP3 activation and IL-1β release in differentiated THP-1 cells was confirmed.[124] To develop new molecular scaffolds with NLRP3 inhibition potential, we applied a pharmacophore-hybridisation strategy. The strategy was based on the merging of two molecular probes: the acrylate INF39 and HS203873, to obtain compound **1**, bearing an electrophilic acrylamide substructure and still able to inhibit pyroptotic cell death and IL-1β release in human macrophages. We decided to focus on non-electrophilic compounds, to obtain non-covalent NLRP3 inhibitors. For this reason compound **2** was synthesised (Figure 4.1). Since **2** showed reduced activity, we further modulated this scaffold to design more active non-covalent compounds able to block NLRP3 inflammasome. Four different modulations have been designed to obtain four series of compounds (A-D), their structures are reported in figure 4.2. The modulation of the aliphatic chain linking the 2-chlorobenzene moiety to the piperidine ring was the first strategy adopted (A). The different distance of the lipophilic 2-chlorophenyl ring and the HBA amide has a fundamental role in the target interaction.

A

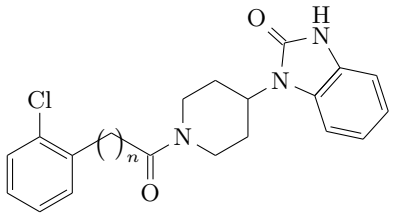

2 n = 2
3 n = 1
4 n = 0

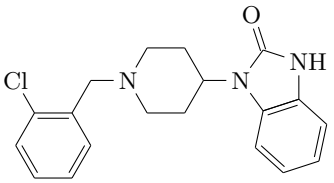

5

B

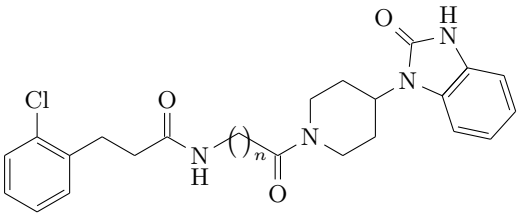

6 n = 1
7 n = 2
8 n = 3

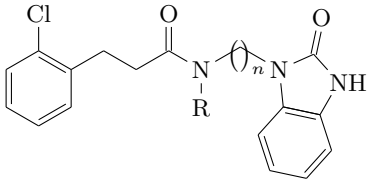

9 n = 2, R = H
10 n = 3, R = H
11 n = 3, R = CH_3

Figure 4.2 continue on next page.

C

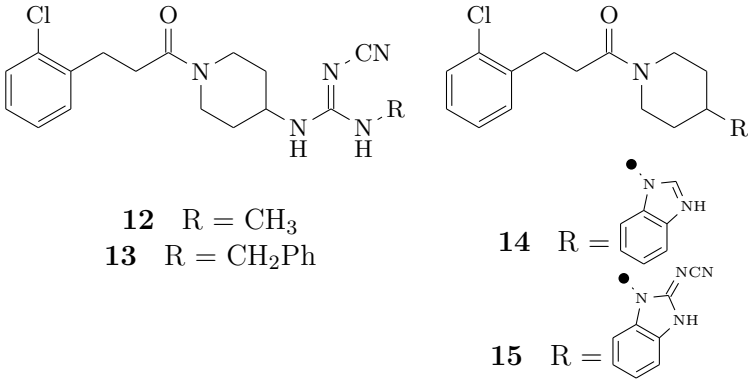

12 R = CH_3
13 R = CH_2Ph
14 R =
15 R =

D

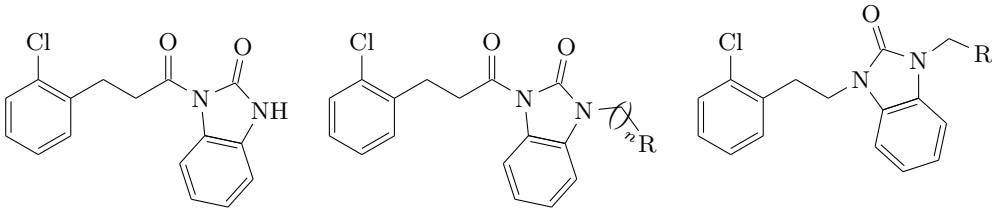

16

17 n = 1, R = COOEt
18 n = 2, R = COOEt
19 n = 1, R = COOH
20 n = 2, R = COOH
21 n = 1, R = tetrazole

22 R = COOEt
23 R = COOH

Figure 4.2: Chemical structure of designed compounds. (A) Modulation of the aliphatic chain linking the 2-chlorobenzene moiety to the piperidine ring (**2**, **3**, **4** and **5**); (B) Modulation of the amide substituent and of the benzoimidazol-2-one linker (**6**, **7**, **8**, **9**, **10** and **11**); (C) Replacement of the benzimidazol-2-one moiety with urea-like substructures (**12**, **13**, **14** and **15**); (D) Elimination of the piperidine ring and benzoimidazol-2-one functionalization (**16**, **17**, **18**, **19**, **20**, **21**, **22** and **23**).

Compounds **3** and **4** showed a reduced distance compared to the reference **2**. Once verified that the two carbon atom spacer was critical for NLRP3 inhibition, a two methylene chain was used in the design of the next series of compounds. In the second group (B), compounds **6**, **7** and **8** showed a different aminoacidic substitution on the amide, and **9**, **10** and **11** bear the modulation of the benzimidazol-2-one linker, where the use of an alkyl chain in place of the piperidine allowed the generation of more flexible molecules compared to reference compound **2**. Isosteric substitutions of the ureidic submoiety of the benzimidazol-2-one were explored (C). Cyanoguanidines **12** and **13** and the cyclic **14** and **15** replaced the benzimidazol-2-one ring. Finally, compounds showing the elimination of the piperidine ring (**16**) and the benzoimidazol-2-one functionalization (**17**, **18**, **19**, **20** and

21) were synthesised (D). This modulation increases the hydrogen bond-forming network in the central part of the molecules, in a similar fashion compared to the sulfanylureidic structure in MCC-950.

4.2 The piperidinamide sub-moiety

The results from the benzimidazol-2-one series encouraged further investigations on the molecular modulation of **2**. Compounds with terminal polar or acidic moiety showed a promising activity profile on pyroptotic cell death, IL-1β release in differentiated THP-1 cells and cytotoxicity in THP-1 cells. In particular, compound **13**, bearing the polar substituted cyanoguanidine group in the *east* terminal, and compound **19**, with the acid acetate moiety, afforded a pyroptosis decrease of 45.0 ± 8.8 % and 36.4 ± 11.1 %, and an IL-1β release inhibition of 25.2 ± 4.9 % and 21.1 ± 3.1 % at 10 µM in THP-1 cells without any undesired cytotoxic effect at the active concentration. Therefore, we decided to design a series of compounds bearing an acidic functionality on the position R_1 (see figure 4.3), on the piperidine. In a second time we added on R position (Figure 4.3), on the aliphatic chain linking the 2-chlorobenzene moiety to the piperidine ring, another lipophilic group connected through an appropriate spacer.

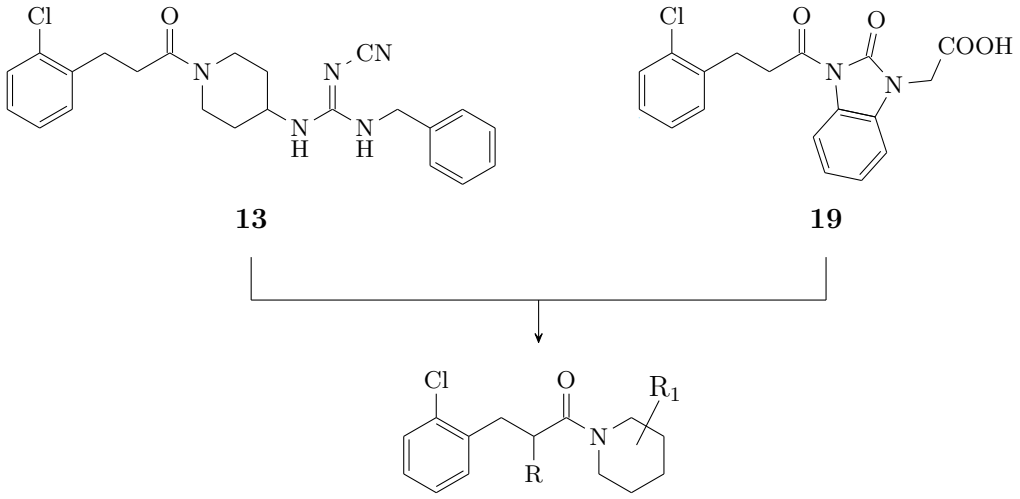

Figure 4.3: Piperidinamide series general structure I. A terminal acidic of polar group on position R_1 was introduced.

The designed modulation of structure I are detailed in figure 4.4. A series of modulated compounds was generated from the reference compounds **25** and **27**. Both esters and corresponding carboxylic acids were designed. Esters behave as prodrugs, since cellular esterases are able to rapidly generate carboxylic acid group from the ethyl ester in this class of compounds. The non-cleavable amidic derivatives were also synthesised to assess whether the presence of a polar and non acidic-group could influence the activity. The

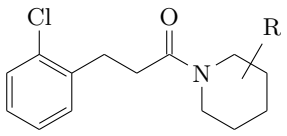

24 R = 4-COOEt
25 R = 4-COOH
26 R = 3-COOEt
27 R = 3-COOH
28 R = 3-$CONH_2$

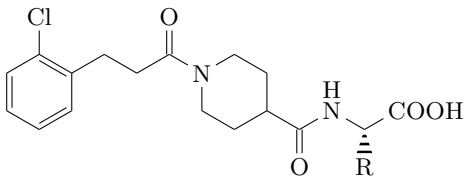

29 R = CH_3
30 R = CH_2Ph

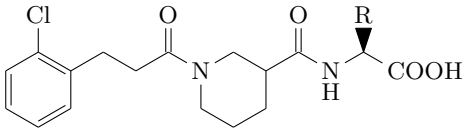

31 R = H
32 R = CH_3

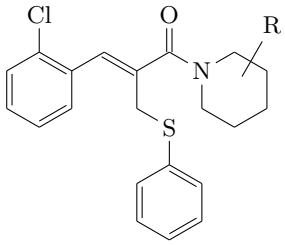

33 R = 4-COOEt
34 R = 4-COOH
35 R = 3-COOEt
36 R = 3-COOH
37 R = 3-$CONH_2$

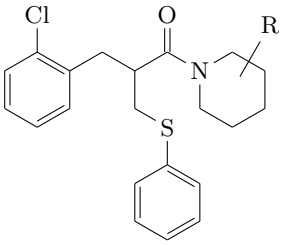

38 R = 4-COOEt
39 R = 3-COOEt

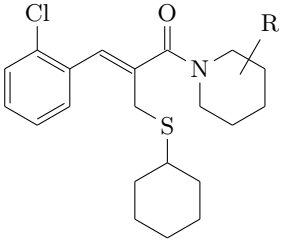

40 R = 4-COOEt
41 R = 3-COOEt

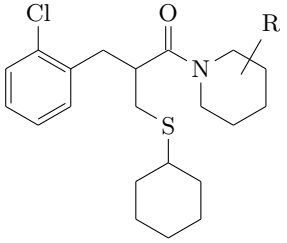

42 R = 4-COOEt
43 R = 3-COOEt

Figure 4.4: Designed compounds of the piperidinamide series: **24**–**43**.

carboxilic acid of the reference compounds was then derivatised by coupling with a selected aminoacid. In position 4 of the piperidine ring L-alanine and L-phenylalanine were used (Respectively in **29** and **30**). The 3-COOH was coupled with glycine and L-alanine (**31** and **32**). Those modulation extended the southern region of the overall structure of the

compounds. The substituents were designed with the α-position with different hindrance. More interesting derivatives were synthesised with the α-β-unsaturated carbonyl linker (**33**, **34**, **35**, **36**, **37**, **40** and **41**; Figure 4.3) and with the saturated equivalent (**38**, **39**, **42** and **43**). The compounds **38**, **39**, **40**, **41**, **42** and **43** were synthesised only as ethyl ester prodrug, since in the cellular screening assay this is the favourite form, probably due to improve cell permeability reasons. In the R- position of structure I (Figure 4.3), the aliphatic linker was branched with the thiophenol (**33**, **34**, **35**, **36**, **37**, **38** and **39**) and with the cyclohexylthio group (**40**, **41**, **42** and **43**). The unsaturated compounds showed a negligible of reactivity toward thioles, because the α-β-unsaturated amide are less reactive compared to esters, and the α-substituion also contribute to the low reactivity of the functionality. For this reason the α-β-unsaturated functionality among this group of compounds has to be considered as a different 3D geometry rather than conferring a covalent mechanism of binding to the target.

4.3 Central heterocyclic replacement

To develop this new series of compounds, a classical ligand-based approach was adopted. From the structure of many published NLRP3 inhibitors, a general three-portion pharmacophore has been identified (see figure 4.5). The west-terminal is tipically a substituted aromatic ring endowed with high lipophilicity, the central core has extensive HBA and/or HBD properties, and the east-terminal part has polar or acidic group. At the west-terminal

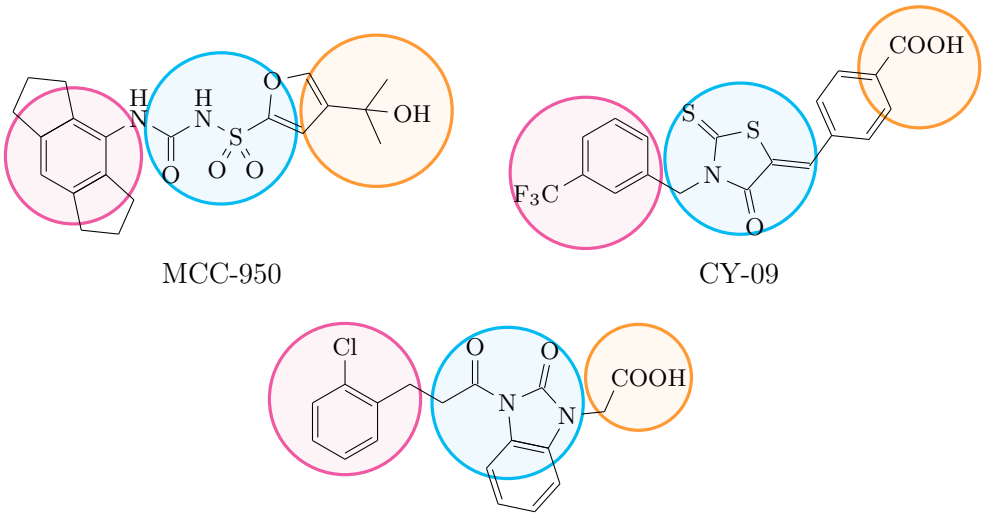

Figure 4.5: Common pharmacophore features in known NLRP3 inhibitors. West-lipophilic terminal is coloured in magenta, central hydrogen bond-forming units in cyan and east-terminal polar moiety in orange.

position, in our previous work, we successfully used the lipophilic 2-chlorobenzyl substructure. We identified this moiety from a series of compounds with different halogen substitutions on the phenyl ring and different heterocycles. The mono-chloro substitution at

ortho position of the benzene ring, demonstrated the best properties among a series of substituted acrylate derivatives.[114,116] The central core with hydrogen bond acceptor and/or donor properties, rich in heteroatoms, usually is represented by sulfonamidic, amidic, ester or ureidic moieties. The east-terminal polar region appears to accomodate various substitutions, as evidenced from the modulation of MCC-950.[106] In the search for new bioactive compounds, we decided to investigate the modulation of the three different portions, replacing these moieties with other substructures to achieve greater NLRP3 inhibition. In particular, we focused our design on the central core of the molecules, fundamental in correct placement into the binding site in the protein and for the metabolic stability of the compounds. On the basis of the aforementioned observations, different heterocycle derivatives were synthesised. We designed 5-membered ring with appropriate electronic properties: 1,2,4-oxadiazoles, 1,2,4-oxadiazol-2-ones, and 1,3,4-thiadiazoles (figure 4.6).

In the 1,2,4-oxadiazole series (figure 4.6, A), the molecules were designed with a 3-substituted phenyl ring. The trifluoromethyl substitution, was selected for similarity to CY-09, a potent NLRP3 inhibitor. The central core is represented by a 1,2,4-oxadiazole differently substituted in order to test whether the electronic density and the substituent position affect the anti-pyroptotic and the IL-1β inhibition ability. The 1,2,4-oxadiazole ring shows amide-like properties and geometry, acting as HBA. The phenyl and the oxadiazole rings are connected through a methylene chain. The selected substituent was a second phenyl ring with a *para*-carboxylic acid functionality (**45**) or the ester prodrugs (**44**, **46** and **47**), easily cleaved by cellular or plasma esterases. The direct conjugation of these substituted aromatic rings to the oxadiazole confers rigidity and planarity to the designed molecules.

In the second series (figure 4.6, B) of 1,2,4-oxadiazol-2-one derivatives, the 2-chlorophenyl moiety is retained, this part of the molecule is linked to the central core through a methylene chain. The selected heterocycle is a carbamate-like moiety that acts as non-classical amide isostere. The nitrogen of the cyclic carbamate was derivatised with an acetate group. The acetate was synthesised as free carboxylic acid (**48**), ethyl ester (**49**) as hydrolysable prodrug, and t-butyl ester (**50**). **50** later was designed to obtain an ester non-cleavable by the plasma and cellular eserases to examine its effect on the pharmacokinetics of the molecule. We designed **52** as analogue to compound **44**. In compound **52** a benzyl spacer was introduced between the acidic functionality and the central HBA ring. Also compound **53** bearing the methoxyphenyl group is similar to **53** but the substituent on the east-terminal is polar but non-acidic and non-hydrolysable in physiological conditions.

Finally the 1,3,4-thiadiazole was used in the central core replacement strategy (figure 4.6, C). In particular, 2-amino-1,3,4-thiadiazole behaves as urea mimicker, thus conferring to the obtained molecules an acilurea-like substructrure well represented in several compounds active on the NLRP3 inflammasome pathway. For similarity to compound **35**, which demonstrated a good activity profile in preventing NLRP3-dependent pyroptotic cell death and IL-1β release, we designed **54** bearing the ethyl nipecotate in east-terminal position. Non-cyclic analogues endowed with greater flexibility in the part bearing the acidic functionality were also synthesised. Compounds **55** and **56** were obtained by joining the N-Methyl and N-benzyl ethyl glycinate to position 5 of the central 1,3,4-thiadiazole ring, respectively. All the modulations can cover a wide chemical space around this backbone and could be useful to understand important structure-activity relationships in NLRP3 inhibition.

A

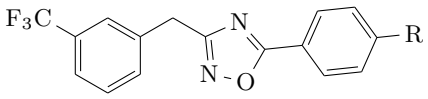

44 R = COOMe
45 R = COOH

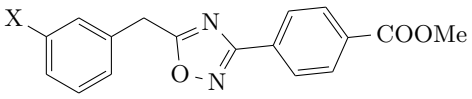

46 X = Cl
47 X = CF_3

B

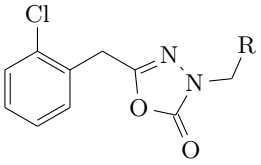

48 R = COOEt
49 R = COOH
50 R = COO-t-Bu
51 R = Tetrazole

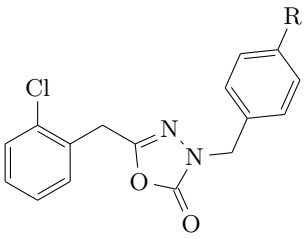

52 R = COOEt
53 R = OMe

C

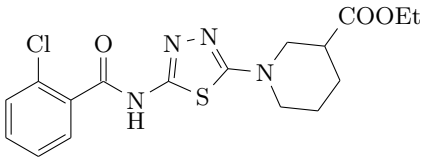

54

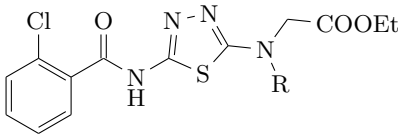

55 R = CH_3
56 R = Benzyl

Figure 4.6: Series of modulation on the central core of the molecules. (A) 1,2,4-oxadiazoles, (B) 1,2,4-oxadiazol-2-ones, and (C) 1,3,4-thiadiazoles.

4.4 Towards Gasdermin inhibition

Recent findings described the activation and the involvement of gasdermin family in the inflammasome pathway and cell death. Among gasdermins, Gasdermin-D is the most related to inflammasome and pyroptosis in human cells. Its mechanism of activation is described in chapter 1.3.2. There are a few inhibitors reported for gasdermin-D (necrosulfonamide, disulfiram, LDC7559, figure 3.9). None of these compounds have a clear target on the protein GSDMD, and they are reported to covalently bind Cys residues located in the N-terminal part of the protein. Up to date, no reference inhibitor has been identified for this protein, and the discovery of a new small-molecule able to interfere with the GSDMD

signalling would be essential for a better pharmacological and clinical study of gasdermin family. For these reasons, we decided to study a possible strategy for GSDMD inhibition. The published 3D structures are focused on the C-terminal domain and they miss all the loops in the structures, including the fundamental linker between C- and N-terminal domain involved in protein activation by casp-1. However, a crystal structure of Caspase-1 in complex with GSDMD-CT has been recently published by Ding and co-workers.[42] They identified a two-step process in the GSDMD activation. Initially the casp-1 recognises the GSDMD through an hydrophobic exosite located on the C-terminal domain. The second step, possible only after the correct placement occurred in step one, is the activating linker cleavage at the specific FLTD peptide sequence in the catalytic site of caspase-1, not far away from the recognition site. The cleavage, remove the auto-inhibitory C-terminal domain from the active N-terminal domain of GMSMD. We decided to focus our efforts on the C-terminal domain, bearing the described fundamental regulatory and recognition functions. We decided to study GSDMD behaviour in solution and the interaction with possible ligand using nuclear magnetic resonance techniques. NMR is a powerful technique to obtain atomic-resolution and dynamic details of a protein in solution. The protein was successfully expressed in high yields using natural abundance and ^{15}N and ^{13}C isotopic labelling schemes. For the complete assignment of all the resonances in the protein, and for dynamic studies, the following 2D and 3D spectra were acquired: ^{15}N-HSQC, ^{15}N-NOESY-HSQC, HNCACB, CC(CO)NH, (H)CC(CO)NH, ^{1}H-^{15}N-Het correlation exchanging spectra, ^{15}N-HSQC-T1 measurment, ^{15}N-HSQC-T2 measurement, and Het-NOE relaxation measurement. In the meanwhile, we studied the exosite of GSDMD-CT, focusing on possible strategies for small-molecule targeting. Ding and co-worker, identified from a series of mutants the hotspots in the Casp-1 GSDMD-CT recognition site. Mutation on I318 and W294 or the cognate four hydrophobic residues in GSDMD (L304, L308, V367, and G307; see figure 4.7) confirmed the importance of the hydrophobic interaction for caspase-1 recognition of GSDMD. Mutants were defective in mediating GSDMD cleavage and pyroptosis in inflammasome-activated macrophages. These findings strongly suggest the GSDMD exosite as a potential drug target to interfere with pyroptosis-related diseases.[42] The first strategy was to mimic the grey filament in figure 4.7, synthesising the pentapetide VWFKD (**57**). Peptide **57** includes W^{294}, facing the exosite in the protein-protein interaction. A second strategy was to optimise the GSDMD-CT structure using molecular dynamics simulations. From the trajectory the most representative conformation has been used for a virtual screening on a library of commercially available small-molecules. The library was optimised for drug-like and protein-protein inhibitors-like properties. An extensive manual selection of the chemical scaffold and analysis of the binding poses allowed us to identify an initial dozen of hit compounds. Particular attention was given to chemical diversity of the molecules, to cover a wider chemical space. The compound screened for binding affinity towards the GSDMD-CT, using NMR techniques. These strategies includes ligand-observed experiment, such as saturation-transfer difference (STD), Water-Ligand Observed via Gradient SpectroscopY (waterLOGSY), diffusion experiments; and protein-observed experiments such as the ^{15}N-HSQC chemical shift perturbation titration. NMR screening allows detection of binders in a wide range of affinity, including low-affinity binders as expected from this proof-of-concept small series of compounds.

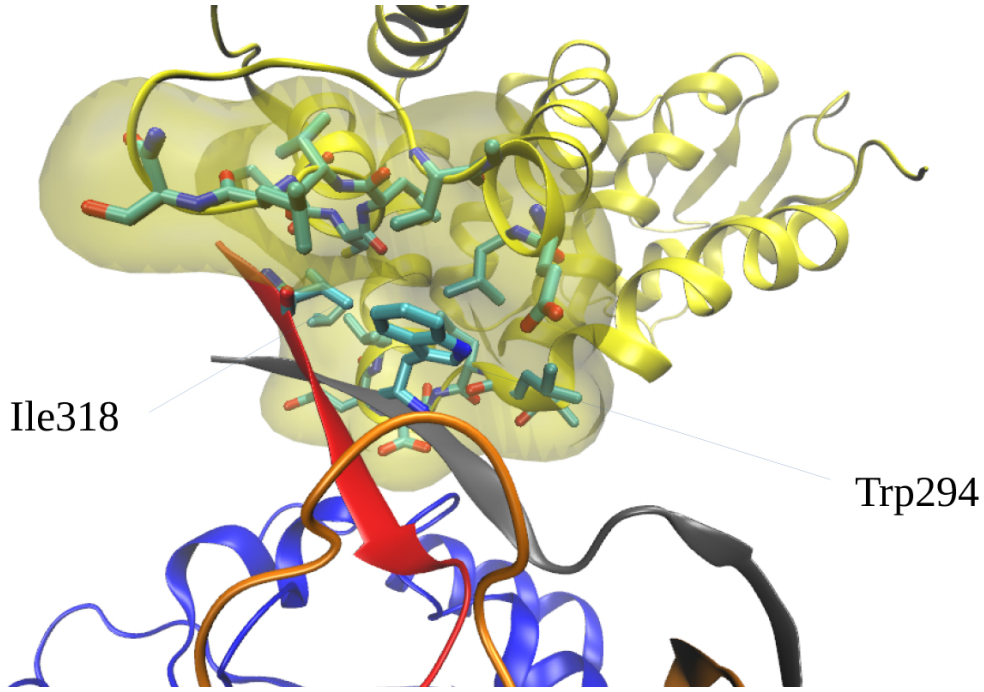

Figure 4.7: Representation of the contact between C-terminal domain (represented in yellow), and the casp-1 (dimer of 2 pairs of p20/p10 subunits. P20 is in grey, p10 in red). The hotspots for the interaction are: on GSDMD side L304, L308, V367, and G307; on casp-1 side two filament contact the GSDMD-CT exosite, conserved amino acids are I318 and W294.[42] Yellow fog highlights the exosite on GSDMD-CT.

Chapter 5

Synthetic strategies

5.1 Benzimidazole derivatives

For the synthesis of the benzimidazole derivative series, compounds **2**, **3** and **4** were obtained according to figure 5.1, by coupling of the appropriate carboxylic acid with commercially available 1-(piperidin-4-yl)-2,3-dihydro-1,3-benzodiazol-2-one (**81**). Carbonyldiimidazole (CDI) in CH_2Cl_2 was used to promote the amide bond formation. Derivative **5**, lacking the amide function, was obtained in high yield by alkylation of 2-chlorobenzyl bromide with **81** in basic medium (triethylamine, TEA) in acetonitrile (ACN) as reaction solvent. The reference compound **1** was synthesised by the reaction of p-chlorobenzyl bromide with tert-butyl diethylphosphonoacetate in the presence of sodium hydride to give the intermediate phosphonate **85** and then reacted with formaldehyde in basic aqueous solution to yield compound **86**. After the deprotection of t-butyl ester with trifluoroacetic acid (TFA) 10% in CH_2Cl_2, the resulting acid was coupled with commercially available 1-(piperidin-4-yl)-2,3-dihydro-1,3-benzodiazol-2-one (**81**) using hydroxybenzotriazole (HOBt) and N,N,N',N'-Tetramethyl-O-(1H-benzotriazol-1-yl)uronium hexafluorophosphate (HBTU) as the activating agents and diisopropylethylamine (DIPEA) as the base to yield **1** in 23% overall yield.

The second series of benzimidazolone derivatives (**6**, **7** and **8**), bearing a spacer between the amide group and the piperidine ring, was synthesised using the synthetic approaches depicted in figure 5.2. The commercially available 2-chlorophenyl propionic acid (**82**) was converted into its O-hydroxysuccinimide ester **82a** using dicyclohexylcarbodiimide (DCC) and N-hydroxysuccinimide (NHS) and then reacted with the aminoesters **93** and **94** to afford the intermediates **87** and **88**, which were hydrolysed in basic medium (NaOH 2.5 M) to give the acids **89** and **90**. These acids were coupled with **81** using HOBt, HBTU and DIPEA to give the desired derivatives **6** and **8**.

The synthesis of **7** was attained with a slightly different procedure (figure 5.2). The piperidine derivative **81** was first coupled with Boc-protected β-alanine using HBTU/HOBt /DIPEA as activating agents. The tert-butyl protected intermediate **91** was cleaved in 10% TFA in CH_2Cl_2 to afford the free amine **92**, which was subsequently coupled with hydroxysuccinimide ester **82a**, under the previously described conditions to afford **7** in 36% overall yield.

Compounds formally derived by the opening of the piperidine ring, were synthesised

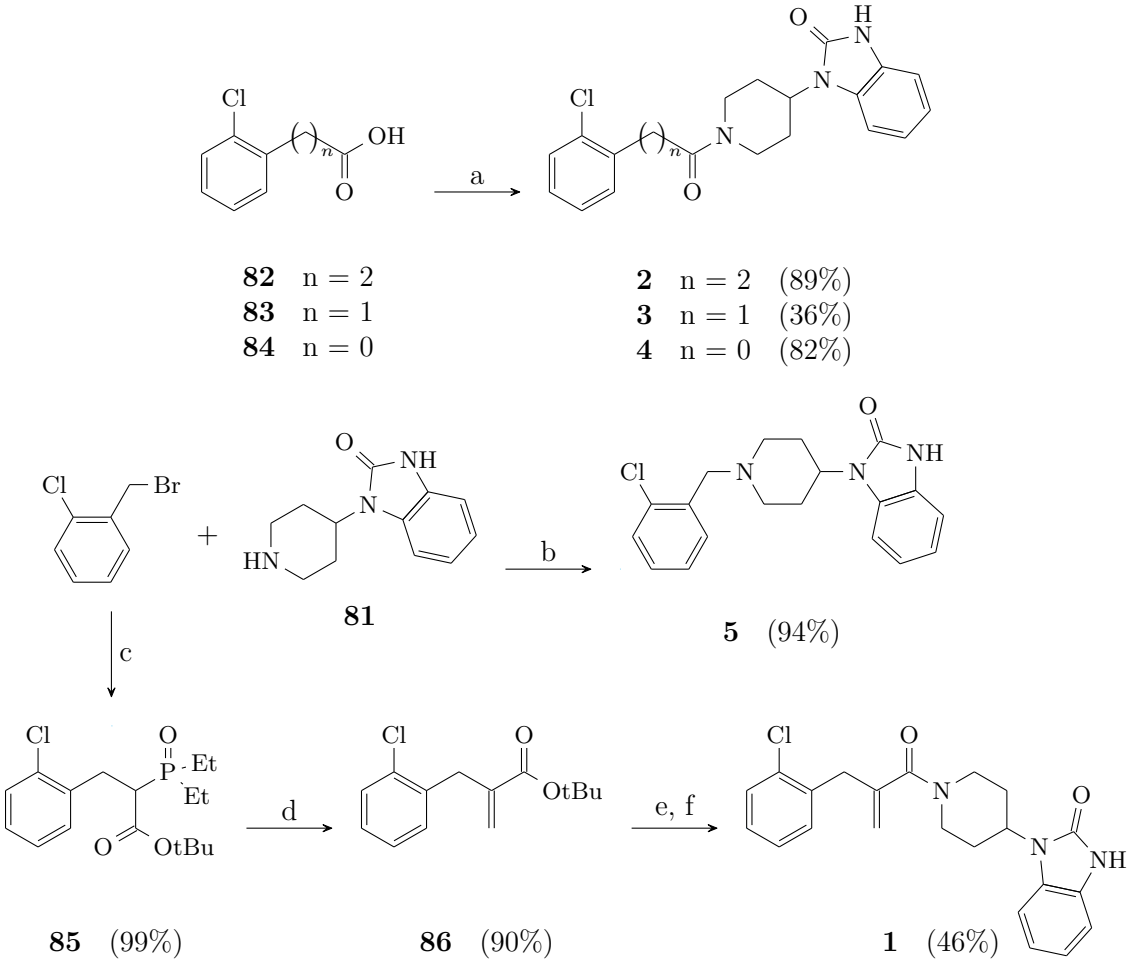

Figure 5.1: Reagents and conditions: (a) CDI (1 eq), CH_2Cl_2, rt, 30 min; **81** (1 eq), rt, 16 h. (b) **81** (1 eq), TEA (1 eq) in ACN 2 h. (c) NaH (1 eq), tert-butyl diethylphosphonoacetate (1.2 eq) in DMF 0°C to rt, 2 h; (d) paraformaldehyde (15 eq), K_2CO_3 (2 eq) in water, 12 h; (e) TFA/DCM 10%, 18 h; (f) **81** (1.1 eq), HBTU (1.5 eq), HOBt (0.1 eq), DIPEA (3 eq) in DMF, 18 h.

according to figure 5.3. The aminoalkylbenzimidazol-2-one derivatives **101** and **102** were obtained through a nucleophilic substitution of the fluorine atom on 1-fluoro-2-nitrobenzene using the Boc-protected alkylamines **95** and **96** to afford nitrobenzene derivatives **97** and **98**. Catalytic hydrogenation over Pd/C 10% allowed the reduction of the nitro group to afford aniline derivatives **99** and **100**, which were cyclised using CDI to afford benzimidazolone derivatives **101** and **102** in good overall yields. Deprotection with TFA 10% in CH_2Cl_2 afforded the free amines **103** and **104**, which were reacted with the activated ester **82a** in DIPEA/DMF to afford the final compounds **9** and **10**. To obtain the N-methyl substituted derivative **11**, a different approach was used. The benzimidazol-2-one was converted into the intermediate **105** by protection with di-tert-butyldicarbonate and

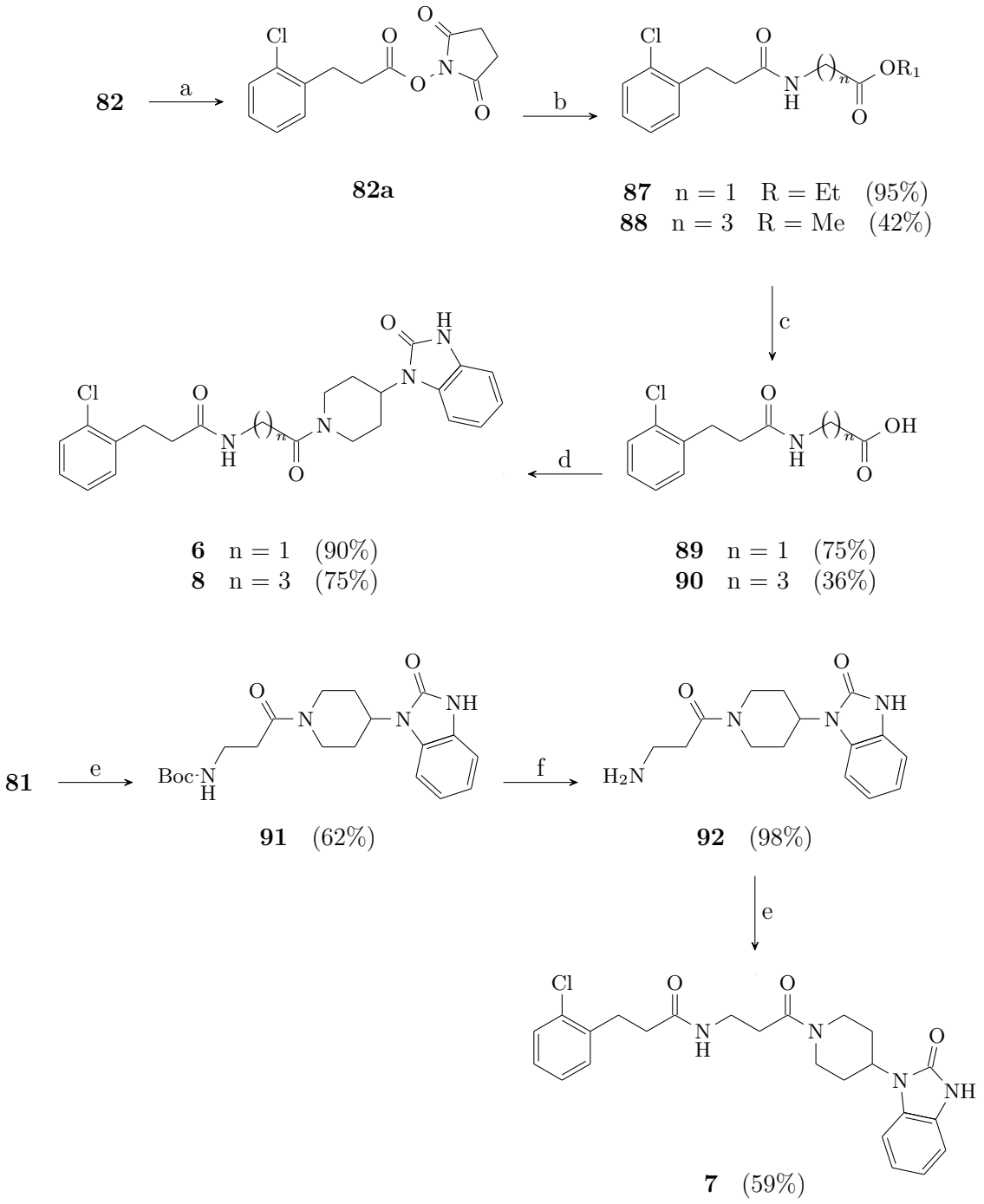

Figure 5.2: Reagents and conditions: (a) DCC (1 eq), NHS (1.5 eq), THF, 0 °C to rt, 18 h. (b) R-NH_2(1.1 eq), Et_3N (3 eq), CH_2Cl_2, rt, 18 h. (c) NaOH 2.5 M (2.5 eq), EtOH or MeOH, rt, 18 h. (d) HBTU (1.5 eq), HOBt (0.15 eq), DIPEA (3 eq), DMF, rt, 18 h. (e) HBTU (1.5 eq), HOBt (0.15 eq), DIPEA (3 eq), DMF, rt, 18 h. (f) TFA/DCM 10%, rt, 18 h.

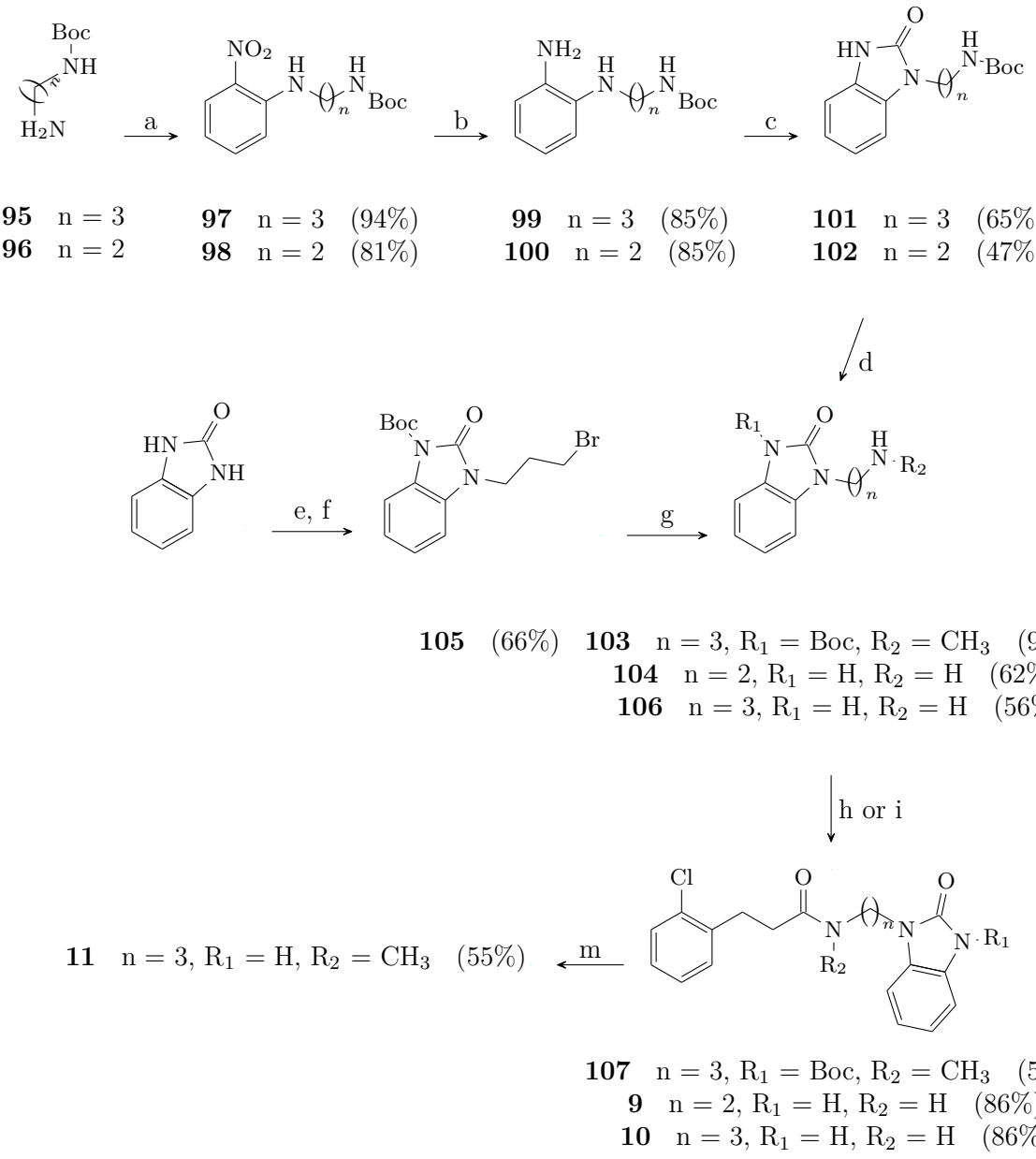

95 n = 3
96 n = 2

97 n = 3 (94%)
98 n = 2 (81%)

99 n = 3 (85%)
100 n = 2 (85%)

101 n = 3 (65%)
102 n = 2 (47%)

105 (66%)

103 n = 3, R_1 = Boc, R_2 = CH_3 (97%)
104 n = 2, R_1 = H, R_2 = H (62%)
106 n = 3, R_1 = H, R_2 = H (56%)

11 n = 3, R_1 = H, R_2 = CH_3 (55%)

107 n = 3, R_1 = Boc, R_2 = CH_3 (56%)
9 n = 2, R_1 = H, R_2 = H (86%)
10 n = 3, R_1 = H, R_2 = H (86%)

Figure 5.3: Reagents and conditions: (a) 1-fluoro-2-nitrobenzene (1 eq), **95** or **96** (1.1 eq), K_2CO_3 (2.2 eq), DMF, N_2, 70°C, 18 h. (b) Pd/C (0.1 eq), H_2, THF, rt, 18 h. (c) CDI (1.1 eq), THF, rt, 18 h. (d) TFA/DCM 10% (10 eq), rt, 4 h. (e) 1,3-dihydro-2H-benzo[d]imidazol-2-one (1 eq), Boc_2O (1 eq), NaH (1.1 eq), dry DMF, 0°C to rt, 18 h. (f) $Br(CH_2)_3Br$ (10 eq), K_2CO_3 (5 eq), KI (0.1 eq), ACN, rt 18 h. (g) Methylamine 40% aq (20 eq), THF, rt, 1 h. (h) CDI (1 eq), DCM, rt, 30 min; **82** (1 eq), rt, 18 h. (i) **82a** (1 eq), DIPEA (1.5 eq), DMF, rt, 18 h. (m) TFA/DCM 10% (10 eq), rt, 18 h.

subsequent alkylation with excess 1,3-dibromopropane. Nucleophilic substitution of the bromine with aqueous methylamine afforded **106**, which, in its turn, was coupled with **82** using CDI to afford the protected intermediate **107**. The usual deprotection with TFA 10% in CH_2Cl_2 gave the desired **11** in modest yield.

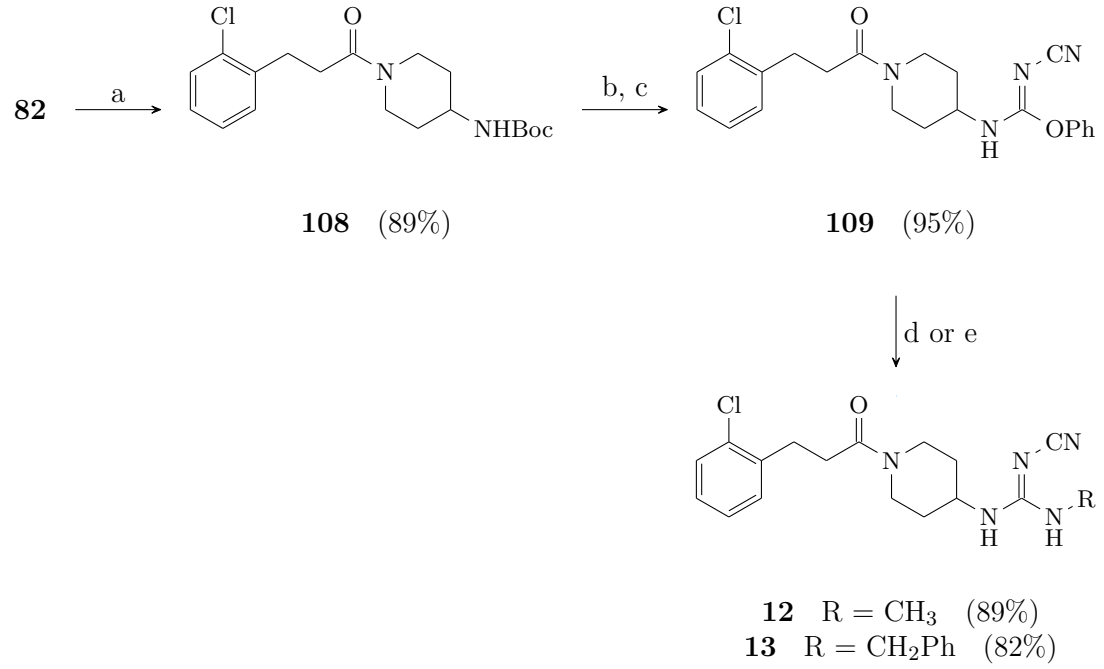

Figure 5.4: Reagents and conditions: (a) $SOCl_2$ (2.5 eq), DMF (0.1 eq), DCM, rt, 2 h; t-butyl piperidin-4-ylcarbamate (1.1 eq), DIPEA (2 eq), DCM, rt, 3 h. (b) TFA/DCM 10% (10 eq), rt, 18 h. (c) diphenyl cyanocarbonimidate (1.1 eq), DCM, rt, 3 h. (d) methylamine (33% in EtOH, 20 eq), rt, 3 h. (e) benzylamine (5 eq), iPrOH, rt, 18 h.

Compounds **12** and **13**, bearing a cyanoguanidine residue in place of the imidazole-2-one ring, were obtained in high yield according to the pathway described in figure 5.4. The acid **82** was converted into the corresponding acyl chloride using $SOCl_2/DMF$ at room temperature and immediately reacted with commercially available tert-butyl piperidin-4-yl carbamate to give **108** in nearly quantitative yield. The amino group was deprotected and reacted with diphenyl cyanocarbonimidate to afford the O-phenylisourea derivative **109**. Displacement of the phenoxy group using excess methylamine or benzylamine afforded the final compounds **12** and **13**, respectively.

Compounds bearing the benzimidazole and the cyclic cyanoguanidine moieties at the terminal position, were synthesised using tert-butyl 4-((methylsulfonyl)oxy)piperidine-1-carboxylate (**110**) as the starting material (figure 5.5). Compound **110** was subjected to a nucleophilic substitution using benzimidazole/K_2CO_3 in DMF at 100°C to give **111**, albeit in poor yield. Deprotection and subsequent coupling with the preformed activated ester **82a** afforded the desired **14**. To obtain **15**, the synthesis of the intermediate **113**

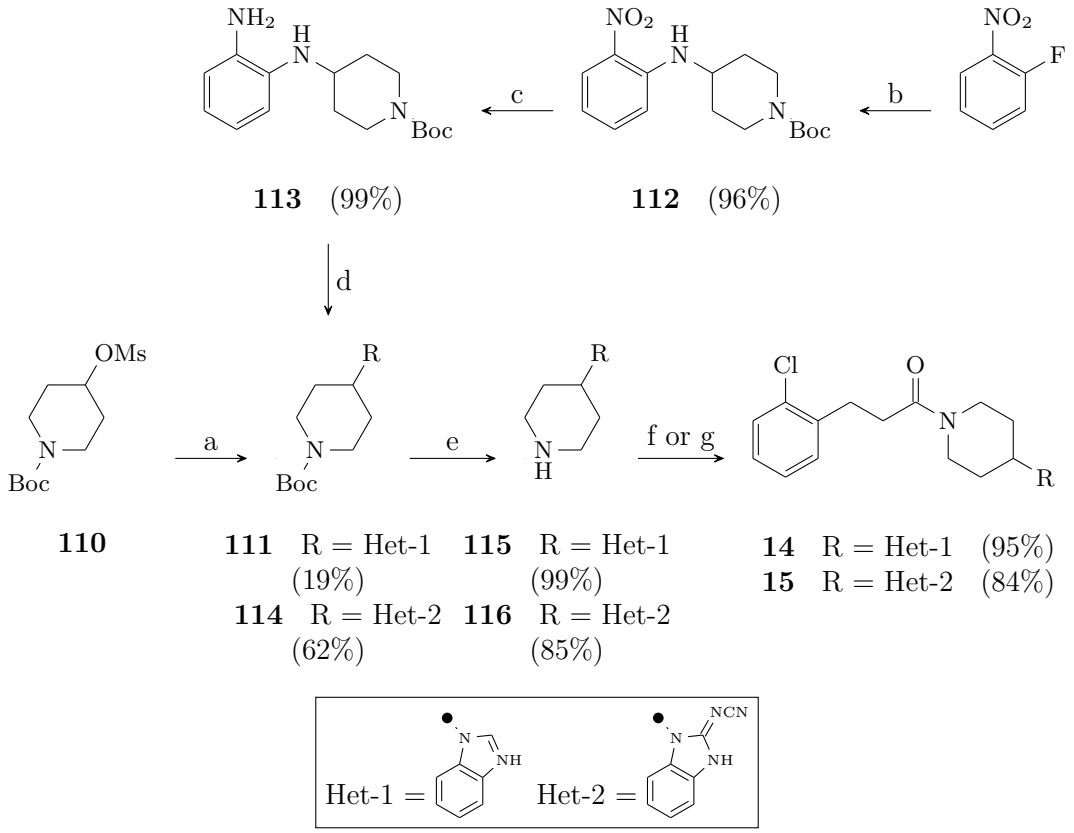

Figure 5.5: Reagents and conditions: (a) benzimidazole (1 eq), K_2CO_3 (2 eq), DMF, 100°C, 18 h. (b) t-bu 4-aminopiperidine-1-carboxylate (1.4 eq), K_2CO_3 (2.2 eq), DMF, N_2, 70°C, 18 h. (c) Pd/C (0.1 eq), H_2, THF, rt, 18 h. (d) diphenyl cyanocarbonimidate (1 eq), DIPEA (2 eq), ACN, N_2, reflux, 18 h. (e) TFA/DCM 10% (10 eq), rt, 18 h. (f) **82a** (1 eq), DIPEA (3 eq), DMF, rt, 18 h. (g) **82** (1 eq), CDI (1 eq), DIPEA (5 eq), DCM, rt, 30 min; rt, 18 h.

was needed. This intermediate was obtained through nucleophilic aromatic substitution of the tert-butyl piperidin-4-ylcarbamate on 1-fluoro-2-nitrobenzene to give **112** followed by catalytic hydrogenation of the nitro group to give the substituted benzendiamine derivative **113** in 95% yield over two steps. Cyclization of **113** with diphenyl cyanocarbonimidate afforded tert-butyl 4-(2-(cyanoimino)-2,3-dihydro-1H-benzo[d]imidazol-1-yl)piperidine-1-carboxylate (**114**). Finally, Boc-deprotection and CDI-mediated coupling with the acid **82** afforded the desired **15**.

The series of compounds **16**–**21** was designed with the 3-(2-chlorophenyl)-propanoyl moiety directly linked to the benzimidazol-2-one group, to generate an acyl-urea substructure. Compounds were synthesised according to figure 5.6. The synthesis started from the deprotonation of the 1,3-dihydro-2H-benzo[d]imidazol-2-one, which was achieved with sodium hydride and its reaction with the in-situ-generated 3-(2-chlorophenyl)-propanoyl

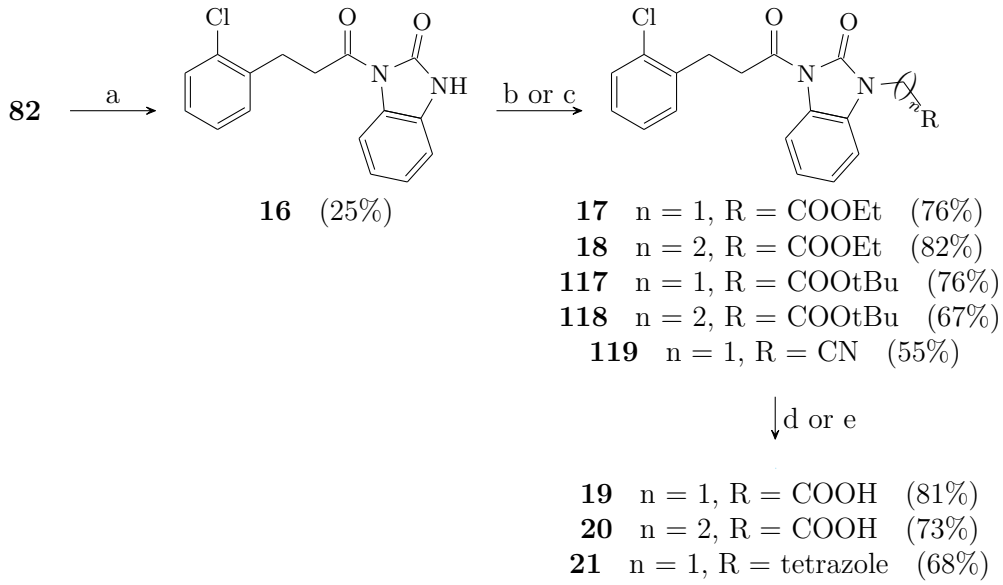

Figure 5.6: Reagents and conditions: (a) I. 29 (1 eq), $SOCl_2$, 85°C, 1 h; benzo[d]imidazole-2-one (1 eq), NaH 60% (1 eq), dry THF, nitrogen atmosphere, rt, 1 h; dry DMF, rt, 3 h. (b) DBU (2 eq), ethyl or t-Bu bromoacetate or bromoacetonitrile (2.5 eq), THF, rt, 18 h. (c) DBU (2 eq), ethyl or t-Bu acrylate (solvent), rt, 18 h. (d) NaN_3 (3 eq), NH_4Cl, DMF, 120°C, 2 h. (e) TFA (10 eq), DCM, rt, 18 h.

chloride. By this procedure, we were able to isolate compound **16** in low yield (25%). Compound **16** was then reacted with 1,8-diazabicyclo[5.4.0]undec-7-ene (DBU) and alkylated with the appropriate α-bromo carbonyl derivative (ethyl 2-bromoacetate, tert-butyl 2-bromoacetate or 2-bromoacetonitrile) to give the final compound **17**, the tert-butyl-protected intermediate **117** and the nitrile **118**, respectively. The intermediate **117** was deprotected in TFA 10% to afford the desired acetic acid derivative **19**, while the nitrile was reacted with sodium azide and NH_4Cl to furnish the tetrazole isostere **21**. The same alkylation using bromo-derivatives bearing a longer alkyl chain gave only trace amounts of the desired N-alkylated compounds, therefore compound **16** was alkylated using ethyl or tert-butyl acrylate, in a Michael reaction, to afford **18** and the protected intermediate **119**. The latter was hydrolysed to give the desired **20** in reasonable yield.

Finally, compounds **22** and **23** were synthesised according to figure 5.7. Nucleophilic aromatic substitution with 2-(2-chlorophenyl)ethylamine on 1-fluoro-2-nitrobenzene, followed by reduction and cyclization were performed using the same synthetic steps as described above to afford the intermediate 1-(2-chlorophenethyl)-1,3-dihydro-2H-benzo[d] imidazol-2-one (**122**). This intermediate was alkylated in good yields using ethyl 2-bromoacetate and tert-butyl 2-bromoacetate in basic medium (DBU) to afford **22** and **123**, respectively. The latter was then hydrolysed in DCM/TFA 10% to afford the desired acetic acid derivative **23**.

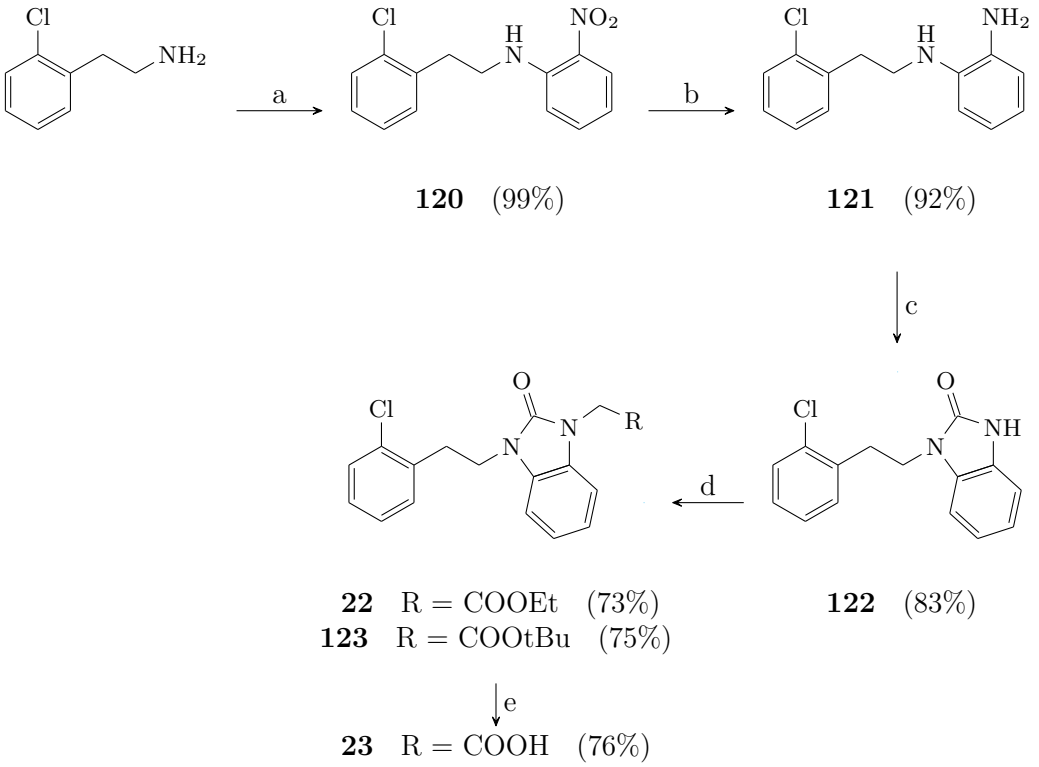

Figure 5.7: Reagents and conditions: (a) 2-(2-Chlorophenyl)ethylamine (1.3 eq), 1-Fluoro-2-nitrobenzene (1 eq), K_2CO_3 (2 eq), DMF, N_2, 70°C, 18 h. (b) Pd/C (10%mol), H_2, THF, rt, 16 h. (c) CDI (2 eq), DCM, rt, 18 h. (d) DBU (2 eq), ethyl or t-Bu bromoacetate (2.5 eq), THF, rt, 18 h. (e) TFA (10 eq), DCM, rt, 18 h.

5.2 Piperidinamide derivatives

The piperidinamide derivatives can be divided in two subgroups: those bearing a linear carbon linker between the piperidine and the phenyl rings and those bearing a branched alkyl linker. The linear ones were synthesised according to the scheme in figure 5.8 from the 2-chlorophenyl propanoic acid (**82**). The coupling of the acid with the ethyl isonipecotate, ethyl nipecotate and 4-piperidinecarboxamide gave respectively the compounds **24**, **26** and **28** in good yields. The hydrolysis of the ethyl esters in the corresponding acid derivatives (**25** and **27**) and subsequent coupling with HBTU/HOBt/DIPEA conditions, afforded compounds **124**–**127**. The coupled aminoacids are protected as tert-butyl or benzyl esters. The protecting groups were removed in classical conditions to yield the final compounds **29**–**32**.

For the synthesis of unsaturated derivatives described in figure 5.9, **128** was synthesised by the Morita-Baylis-Hillman reaction between the aldehyde and the tert-butyl acrylate in presence of 1,4-diazabicyclo[2.2.2]ottane (DABCO). The reaction was kept at room temperature, however, it has very long reaction times (seven days). The MBH adduct was

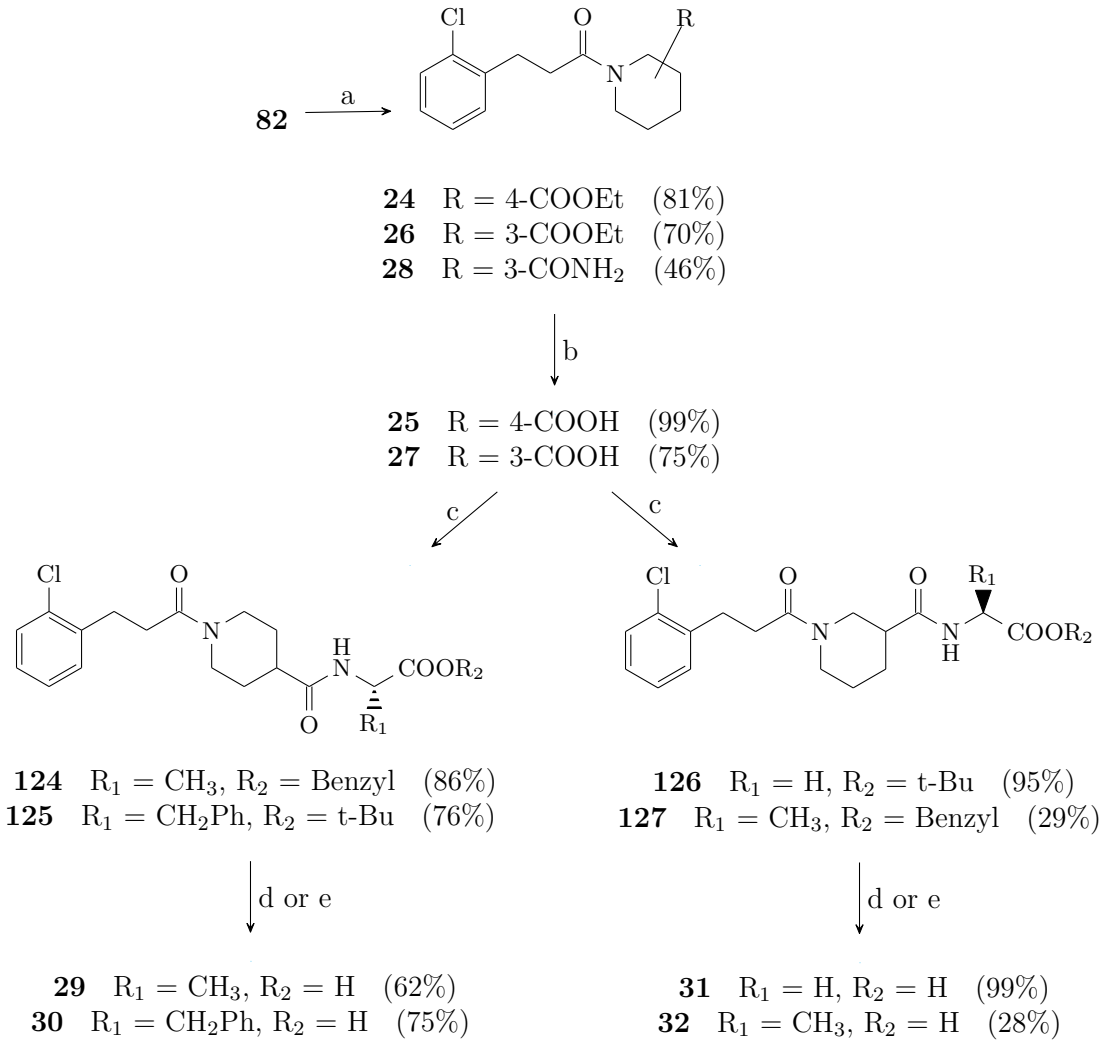

Figure 5.8: Reagents and conditions: (a) CDI (1 eq), DCM, rt, 30 min; substituted piperidine (1 eq) rt, 18 h. (b) NaOH 2.5 M (2.5 eq), EtOH, rt, 18 h. (c) aminoacid (1.1 eq), HBTU (1.5 eq), HOBt (0.1 eq), DIPEA (3 eq) in DMF, 18 h. (d) TFA (10 eq), DCM, rt, 18 h. (e) Pd/C (0.1 eq), H_2, MeOH, rt, 18 h.

acetylated to **129** using acetic anhydride in dichloromethane. In turn, compound **129** was reacted with an appropriate thiole (thiophenol or cyclohexylmercaptane) in presence of a base (triethylamine or DBU). DBU is required to speed-up the reaction of cyclohexylmercaptane with the conjugated electophilic double bond, by deprotonating the less acidic thiole. The reactions were conducted in oxygen-free atmosphere, to reduce the side-oxidation of the thioles into useless disulfur derivatives. The 1-3-conjugated nucleophilic substitution yielded compounds **130** and **131**. Deprotection of tert-butyl ester and subsequent coupling with the appropriate piperidine derivatives allowed the production of the

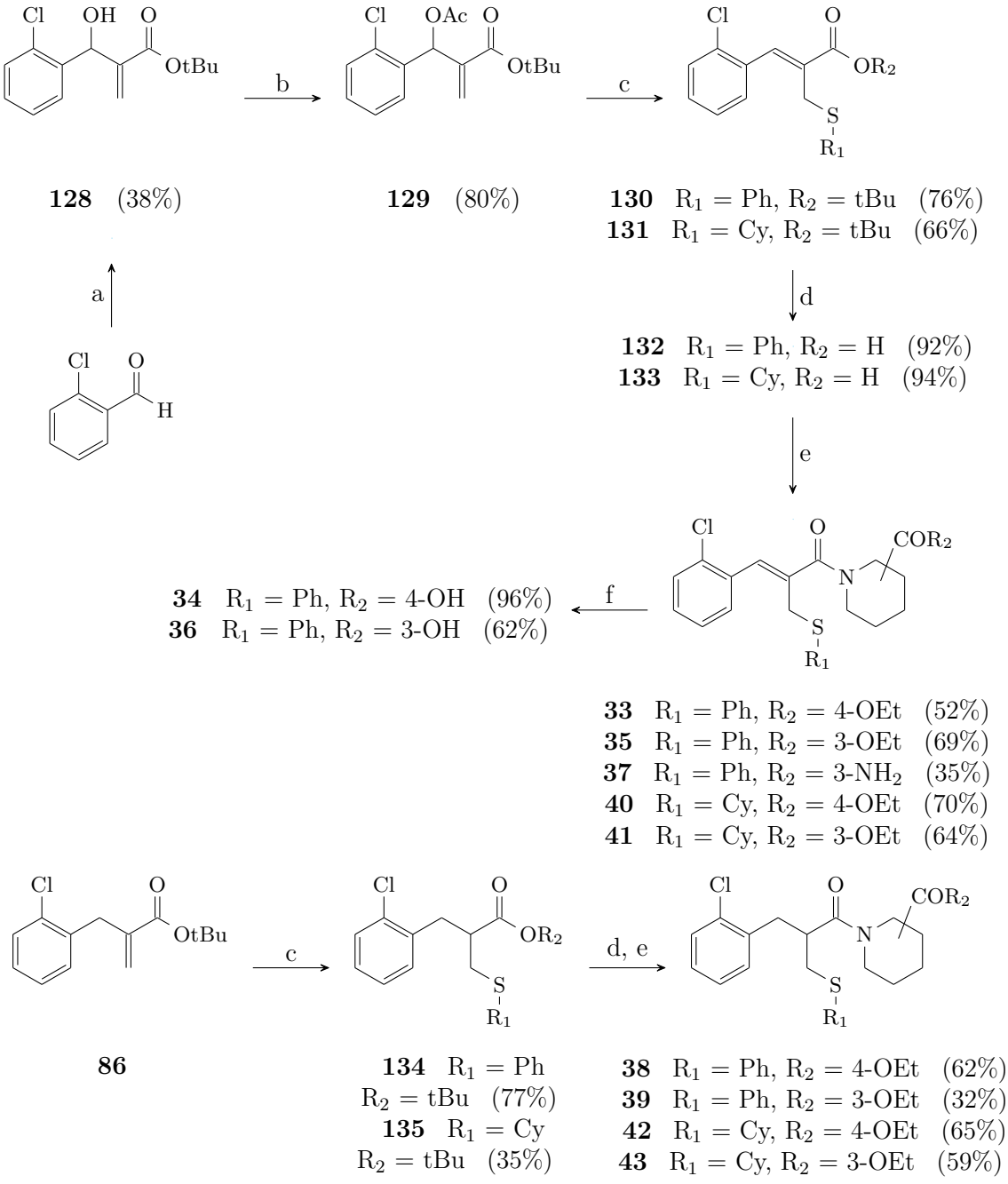

Figure 5.9: Ph=*phenyl*, Cy=*cycloexyl*.
Reagents and conditions: (a) 2-chlorobenzaldehyde (1 eq), t-Bu acrylate (3 eq), DABCO (1 eq), $ACN{:}H_2O$ (9:1), rt, 7 d. (b) acetic anhydride (1.2eq), DMAP (0.2 eq), DCM, rt, 4 h. (c) appropriate thiole (1.1 eq), DBU (1.2 eq), DCM, rt, N_2, 30 min to 18 h. (d) TFA (10 eq), DCM, rt, 18 h. (e) cyclic amine (1.1 eq), HBTU (1.5 eq), HOBt (0.1 eq), DIPEA (3 eq) in DMF, 18 h. (f) NaOH 2.5 M (2.5 eq), EtOH, rt, 18 h.

desired compounds. Ethyl isonipecotate was coupled to produce **33** and **40**, the use of ethyl nipecotate gave **35** and **41** and finally 4-piperidinecarboxamide was used to obtain **37**. Only the ethyl esters bearing the unsaturated linker were cleaved in basic medium to produce the free carboxylic acid analogues in position 4 and 3 of the piperidine ring, respectively **34** and **36**.

The adopted synthetic pathway for saturated compounds **38**, **39**, **42** and **43** (see figure 5.9) started from previously described compound **86**.[125] A thio-Michael reaction was used to combine **86** with thiophenol and cyclohexylmercaptane, producing respectively **134** and **135**. Tert-butyl esters were cleaved in typical conditions (solution of TFA 10% in DCM) and directly coupled with the appropriate ethyl isonipecotate or ethyl nipecotate to produce the the saturated piperidinamide derivatives in overall good yields (**38**, **39**, **42** and **43**).

5.3 Central heterocycle derivatives

In the central heterocycle modulation, the 1,2,4-oxadiazoles were synthesised according to figure 5.10. The synthesis of compounds **44** and **45** required the production of the intermediate methyl 4-(N'-hydroxycarbamimidoyl)benzoate (**138**) which was obtained by

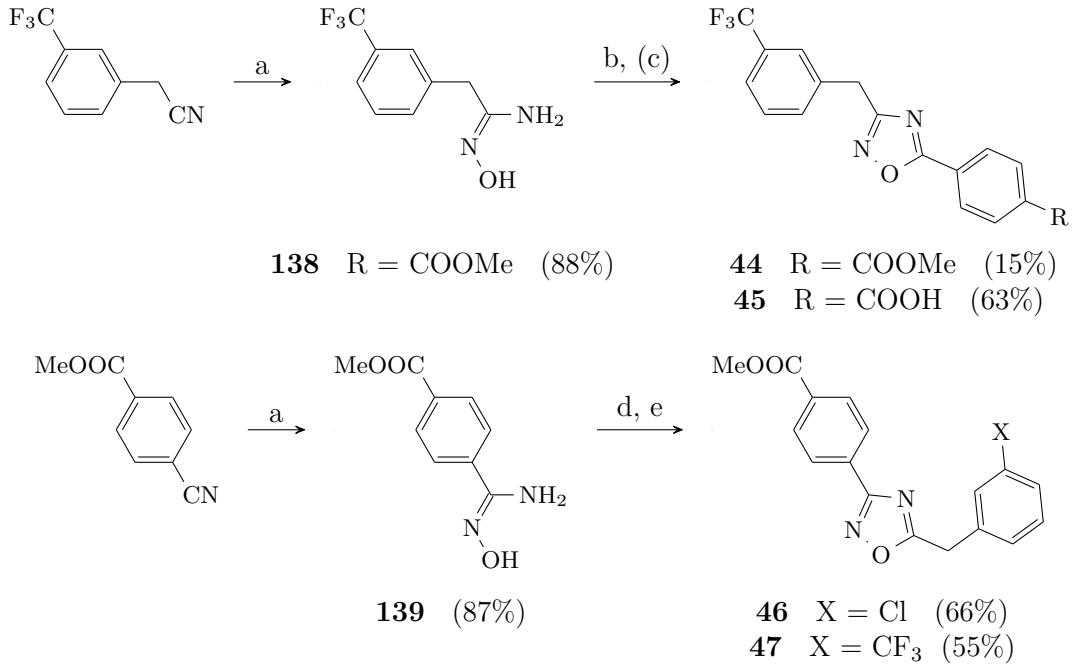

138 R = COOMe (88%)

44 R = COOMe (15%)
45 R = COOH (63%)

139 (87%)

46 X = Cl (66%)
47 X = CF_3 (55%)

Figure 5.10: Reagents and conditions: (a) hydroxylamine hydrochloride (2.2 eq), TEA (2.3 eq), EtOH 96%, 75°C, 5h. (b) PTSA (0.1 eq), dry toluene, reflux, 18h. (c) LiOH (5 eq), THF, rt, 18h. (d) appropriate phenyl acetic acid (1.1 eq), CDI (1.1 eq), THF, rt, 3h. (e) Acetic acid, 118°C, 18h.

heating a mixture of commercially available 3-trifluoromethylphenyl acetonitrile and hydroxylamine in EtOH for 3 h. The resulting hydroxyimidamine (**138**) was then reacted with methyl-4-formyl benzoate in the presence of a catalytic amount of p-toluenesulfonic acid (PTSA) to afford **44** in low yield (15%). **45** was then obtained from **44** by basic hydrolysis using an aqueous solution of LiOH in THF. Since **44** was obtained in low yield using the above reported reaction conditions, a different synthetic pathway was pursued for the synthesis of the 1,2,4-oxadiazole ring in compound **47**. In this case, the cyclization was carried out in a two-step procedure. The coupling agent CDI activates the 2-(3-(trifluoromethyl)phenyl)acetic acid, which undergoes the hydroxyimidamide (**139**) attack, causing the intern cyclization, under acid conditions, obtaining **47**. The same procedure was adopted for the synthesis of **46**, using 2-(3-chlorophenyl)acetic acid as coupling partner of the hydroxyimidamide **139**.

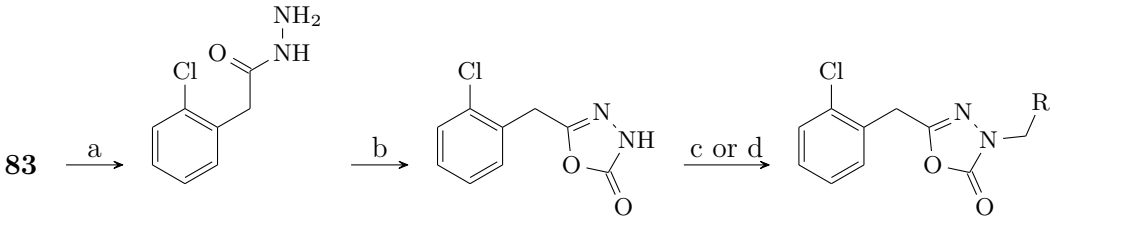

Figure 5.11: Reagents and conditions: (a) CDI (1.1 eq), $NH_2NH_2 \cdot H_2O$ (1.5 eq), THF, rt, 18h. (b) CDI (1.1 eq), dry THF, rt, 18 h. (c) 6 (1 eq), DBU (1.5 eq), ethyl 2-bromoacetate, or t-Bu 2-bromoacetate, or 2-bromoacetonitrile, or ethyl (4-bromomethyl) benzoate (2 eq), THF, rt, 18 h. (d) DIAD (1.5 eq), 4-methoxybenzyl alcohol (1 eq), PPh_3 (1.5 eq), THF, 0°C to rt, 4h. (e) TFA (10 eq), DCM, rt, 18 h. (e) TFA (10 eq), DCM, rt, 18 h. (f) NaN_3 (1.5 eq), NH_4Cl (1 eq), DMF, rt, 2h.

For the synthesis of 1,2,4-oxadiazol-2-ones (**48**–**53**, figure 5.11), 2-Chloro- phenylacetic acid was converted into the hydrazide intermediate **140** using hydrazine and CDI as the coupling agent. This intermediate was then cyclized to obtain 5-(2-chlorobenzyl)-1,3,4-oxadiazol-2(3H)-one (**141**) through the use of another equivalent of CDI. The 1,3,4-oxadiazol-2(3H)-one ring was then functionalised with various substituents. The presence of an acid hydrogen on the ring (predicted pKa of 6.34, calculated using Advanced Chemistry Development ACD/Labs Software V11.02) allowed the formation of a new C-N bond by using either the DBU-mediated nucleophilic substitution, leading to compounds **48**, **50**,

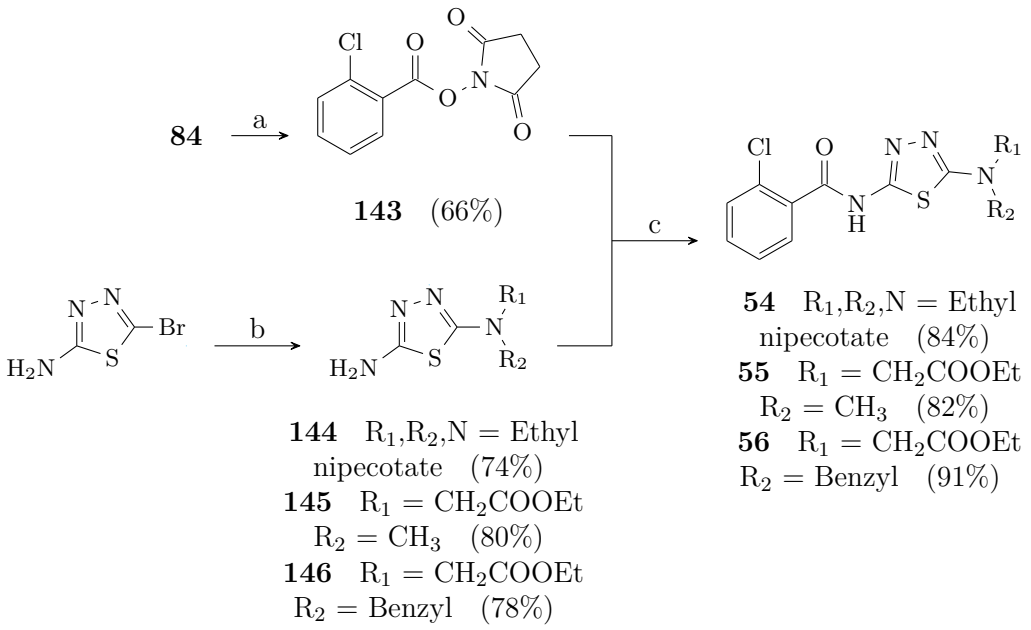

Figure 5.12: Reagents and conditions: (a) DCC (1 eq), NHS (1.5 eq), THF, 0°C to rt, 18 h. (b) ethyl nipecotate (1.1 eq), DIPEA (5 eq), DMF, 80°C, 2h. (c) **143** (1 eq), DIPEA (1 eq), DMF, 100°C, 18 h.

52 and **142**. The electrophilic reagents were respectively methyl 2-bromo-acetate, t-butyl 2-bromo-acetate, 2-bromoacetonitrile and ethyl (4-bromomethyl)- benzoate. The intermediate **142** was cyclised using the click reaction between the nitrile and sodium azide, in presence of ammonium chloride in DMF to give **51** in high yields. The hydrolysis of the tert-butyl ester of **50** gave compound **49**. We observed that it was not possible to obtain compound **49** by basic hydrolysis of the ethyl ester derivative **48**, owing to decomposition of the heterocycle under these conditions. Analogously, the acidic nitrogen of 1,3,4-oxadiazol-2(3H)-one ring was involved in the Mitsunobu reaction, leading to compound **53**.

Finally, the synthesis of the 1,3,4-thiadiazoles was obtained according to figure 5.12. The first reaction is a nucleophilic aromatic substitution by different amines on 2-bromo-5-amino-1,3,4-thiadiazole. The reaction was performed by heating the mixture at 80°C in DMF for 2 h, in presence of DIPEA as base. We reacted ethyl nipecotate, ethyl N-methylglycinate and ethyl N-benzylglycinate to obtain the substituted thiadiazole intermediate, respectively **144**, **145** and **146** in good yields. The aromatic amines were then reacted at 100°C with the activated NHS ester **143** prepared from 2-chlorobenzoic acid and NHS, using dicyclohexyl carbodiimide (DCC). This procedure led to the efficient preparation of the desired compounds **54**, **55** and **56**.

Chapter 6

Results and discussion

6.1 Biological evaluation

For the development of NLRP3 inhibitors, different modulations were performed and three series of compounds were synthesised. The compounds were tested in a first screening for their ability to inhibit pyroptotic cell death using the methods developed in the laboratory of Cancer Pharmacogenomics at the Department of Drug Science and Technology of the University of Turin.[125] Lactate dehydrogenase (LDH) extracellular concentration was measured to quantify the ATP-stimulated pyroptotic cell death of human macrophages. The day preceding each experiment THP-1 cells were plated and differentiated into macrophages by treatment with phorbol myristate acetate (PMA; 50 nM; 24 h). Differentiated cells were primed with lipopolysaccharide (LPS; 10 µg/mL; 4 h) in serum-free medium and then treated with either vehicle alone or test compound (10 µM; 1 h). The cell death was triggered with ATP (5 mM), and the pyroptotic cell death was evaluated after 1.5 h by measuring the LDH released in the cell supernatants. Data are expressed as a percent of pyroptosis decrease vs vehicle alone. Most of the compounds were also tested for the ability to inhibit the release of IL-1β, to confirm the interaction with the inflammasome pathway. In a parallel experiment, IL-1β was quantified by ELISA assay on the supernatants obtained using the same procedure described for LDH quantification in THP-1 cells. Results are expressed as % inhibition of IL-1β release versus vehicle-treated cells Also the cytotoxicity of the compounds was evaluated, to know possible undesired toxic effect on cells and animal models. The cytotoxicity of the synthesised compounds was evaluated by MTT assay. THP-1 cells were exposed to increasing concentrations (0.1–100 µM) of each compound, and cell viability was measured at 72 h using the MTT assay. The results are expressed as TC_{50}. Analysis of the obtained results is reported in the following sections, for each series of compounds.

6.1.1 Benzimidazole derivatives

The compounds from the modulation of the benzimidazol-2-one scaffold were evaluated for their NLRP3 inhibitory activity by measuring their ability to prevent NLRP3-dependent pyroptosis, to inhibit IL-1β release, and cytotoxicity at the tested concentration in differentiated THP-1 cells. Results are reported in table 6.1.

Compound	Pyroptosis decrease[a] % inhibition at 10 µM	IL-1β inhibition[b] % inhibition at 10 µM	Cytotoxicity[c] TC_{50} (µM)
1	24.9 ± 6.3[d]	14.4 ± 5.0	32.9 ± 19.0
2	14.9 ± 5.8	10.3 ± 5.8	64.1 ± 4.7
3	30.8 ± 9.8[d]	15.9 ± 5.5	65.7 ± 1.0
4	NA	NT	80.9 ± 3.2
5	NA	NT	72.6 ± 3.3
6	35.0 ± 6.9[d]	21.0 ± 3.2[d]	61.7 ± 1.0
7	34.5 ± 5.2[d]	17.8 ± 7.5	62.4 ± 13.3
8	32.2 ± 10.6[d]	NT	86.3 ± 5.1
9	39.2 ± 6.6[d]	20.3 ± 1.3[d]	87.1 ± 1.9
10	NA	NT	> 100
11	NA	NT	76.8 ± 3.2
12	15.7 ± 9.1	19.0 ± 0.4	> 100
13	45.0 ± 8.8[e]	25.2 ± 4.9[d]	85.7 ± 5.6
14	NA	NT	92.6 ± 4.0
15	NA	NT	83.4 ± 0.8
16	37.7 ± 7.6[d]	14.9 ± 8.8	77.3 ± 3.7
17	25.1 ± 4.0[d]	24.2 ± 11.2	95.4 ± 1.1
18	24.4 ± 6.8	13.8 ± 5.4	57.6 ± 3.2
19	36.4 ± 11.1[d]	21.1 ± 3.1	> 100
20	NA	NT	80.1 ± 1.4
21	26.2 ± 1.6[d]	< 10	> 100
22	NA	NT	92.8 ± 2.1
23	26.3 ± 3.5[d]	13.9 ± 16.4	62.4 ± 1.2
MCC950	42.5 ± 0.9[e]	37.6 ± 6.0	> 100

Table 6.1: Inhibitory effect of synthesised compounds on pyroptotic cell death, IL-1β release in differentiated THP-1 cells and cytotoxicity in THP-1 cells. [a]Pyroptosis of differentiated THP-1 cells was triggered using LPS/ATP. Data are reported as the % inhibitionof pyroptosis of cells treated with 10 µM conc of test compound vs vehicle-treated cells. Data are the mean ± SEM of three to five experiments run in triplicate. [b]IL-1β inhibition was measured in the cell supernatants form the same experiments. Data are reported as % inhibition ± SEM of three to five experiments run in triplicate. [c] Cytotoxicity was determined after 72 h treatment of THP-1 cells with increasing conc (0.1–100 µM) of test compounds. Data are reported as TC50 ± SEM of three experiments. [d] $p < 0.05$ vs. vehicle treated cells (t-student); [e] $p < 0.01$ vs. vehicle treated cells (t-student); NA = not active at 10 µM; NT = not tested.

Analysis of the obtained results showed that by merging the structure of INF39 with the 1-(piperidin-4-yl)-2,3-dihydro-1,3-benzoimidazol-2-one moiety present in HS-203873, to obtain **1**, a compound able to prevent pyroptosis (24.9 ± 6.3%) and IL-1β release (19.4 ± 0.4%) at 10 µM was generated. When the electrophilic substructure was eliminated

(compound **2**), the anti-pyroptotic activity dropped down to 14.9 ± 5.8% inhibition ($p = 0.198$); however, the effect of compound **2** appeared to be concentration-dependent as the pyroptosis inhibition increased to 29.1 ± 4.8% ($p < 0.05$) at 50 µM. In order to understand whether it was possible to restore/increase the activity, the structure of **2** was modulated.

We first modulated the carbon chain linker used to conjugate the 2-chlorobenzene moiety to the piperidine ring by synthesising three compounds (derivatives **3**–**5**, figure 4.2). Among these compounds, only derivative **3**, bearing an acetamide bridge, showed an anti-pyroptotic activity (table 6.1). Further shortening of the linker (**4**) or elimination of the carbonyl group (**5**) led to inactive compounds at the tested concentration of 10 µM. When the 1-(piperidin-4-yl)-2,3-dihydro-1,3-benzodiazol-2-one moiety was conjugated with 2-chlorophenylacetamide through a spacer (derivatives **6**–**8**, figure 4.2), two compounds showed the ability to prevent about 35% of pyroptotic cell death and to decrease IL-1β by approximately 18–21% (compounds **6** and **7**; figure 4.2, table 6.1).

Compound **2** was also modulated by opening the piperidine ring linking the benzimidazole-2-one to the phenylacetamido moiety in order to check whether the increase of flexibility could improve the interaction with the putative target. To this aim, compounds **9**–**11** (figure 4.2) were synthesised. Results showed that only compound **9** maintained the anti-pyroptotic activity (39.2 ± 6.6% inhibition) and the IL-1β inhibition (20.3 ± 1.3%), while **10** and **11** were inactive at 10 µM. To understand the role played by the benzimidazole-2-one substructure, compounds **12**–**15** (figure 5.4) were synthesised. The replacement of benzimidaz-
ol-2-one with a benzimidazole afforded an inactive compound (derivative **14**, 4.2). The use of a cyanoguanidine group in place of the ureidic moiety present in the benzoimidazol-2-one ring gave encouraging results. Compounds **12** and **13**, bearing a methyl- and benzyl-substituted cyanoguanidine residue at the terminal position were able to inhibit both NLRP3-dependent pyroptosis and IL-1β release in LPS/ATP-treated macrophages. Surprisingly, compound **15**, bearing the di-substituted cyanoguanidine constrained into a 1,3-dihydro-2H-benzo[d]imidazol-2-ylidene)cyanamide was inactive (table 6.1).

Finally, derivatives **16**–**23** (figure 4.2) were synthesised. In these series of compounds the piperidine ring moiety were removed, and the benzoimidazol-2-one structure was directly linked to the 2-chlorophenyl substructure through a propanoyl or an ethyl linker. In this series of compounds, the benzimidazol-2-one ring was substituted with an acidic group or with an ethyl ester, used as the carboxylic acid prodrug, at the terminal nitrogen. The biological results showed that the 1-(3-(2-chlorophenyl)propanoyl)-1,3-dihydro-2H-benzmidazol-2-one scaffold could be the minimal requirement for NLRP3 inhibition (compound **16**: 37.7 ± 7.6% pyroptosis reduction; 14.9 ± 8.8% IL-1β inhibition). When this scaffold was functionalised with an acetic acid residue (**19**) or a tetrazol-5-yl-methyl residue (**21**), two active compounds were obtained. Interestingly, the conversion of **19** into the corresponding ethyl ester **17** maintained the activity as well as the removal of the carbonyl group in compound **23**. When the carboxylic group was further spaced apart from the benzoimidazol-2-one ring, the activity was suppressed (derivative **20**). It is difficult to rationalize the behaviour of compounds **18** and **22**. All the synthesised compounds did not show relevant toxicity in THP-1 cells (table 6.1), with the partial exception of compound **1** (TC_{50} 32.9 ± 19 µM), possibly because of the electrophilic character of this derivative.

From the preliminary screening, compounds **6**, **9**, **13** and **19** (one from each series) were selected for further biological evaluation. The anti-pyroptotic effect of the selected

compounds was determined in human macrophages using increasing concentrations (0.1–50 µM) of test compounds (figure 6.1). In these conditions, **6**, **9**, **13** and **19** showed a concentration-dependent inhibition of NLRP3-mediated pyroptosis with a maximal inhibition ranging between 40 and 60%. Interestingly, compounds **9**, **13** and **19** maintained a significant ability to inhibit pyroptosis down to 1 µM (approx. 20–30% inhibition).

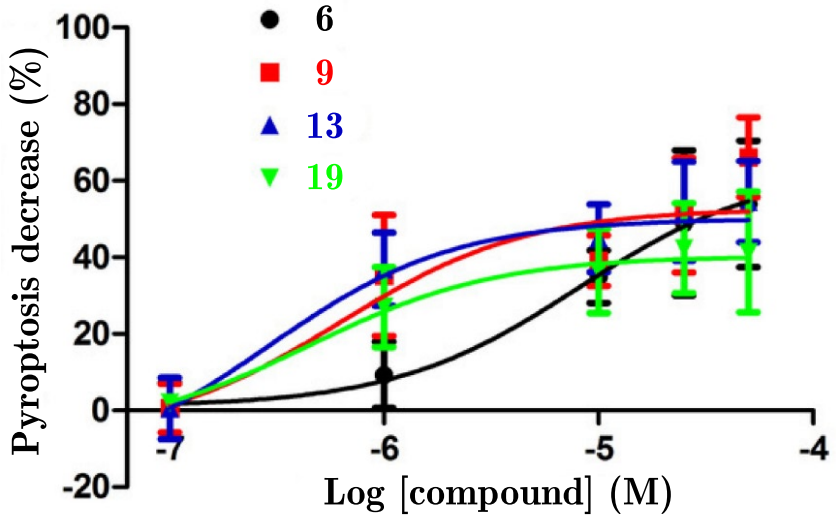

Figure 6.1: Concentration-response curves for the effects of compounds **6**, **9**, **13** and **19** on the ATP-triggered cell death of differentiated THP-1 cells. PMA-differentiated and LPS-primed THP-1 cells were pre-treated with vehicle alone or indicated compound. Each compound was added at increasing concentrations (0.1–50 µM) 1 h before exposure to ATP (5 mM; 90 min). LDH activity was measured in the collected supernatant by a colorimetric assay. Data are expressed as decrease of cell death vs. vehicle alone and are the mean ± SEM of at least three experiments run in triplicate.

6.1.2 Piperidinamide derivatives

The compounds from the modulation of the piperidinamide scaffold were evaluated at fixed concentration (10 µM) for the inhibition of NLRP3-dependent pyroptosis, IL-1β release, and cytotoxicity in differentiated THP-1 cells. The obtained results are reported in table 6.2. the structures of this series of compounds are reported in figure 4.4

Among the parent compounds **24** and **26**, bearing the ablation of the benzimidazol-2-one ring and the insertion of an ester functionality, only **26** was able to prevent the pyroptosis by 32.92 ± 3.39%. The substitution in position 3 of the piperidine ring (**26**) demonstrated a promising inhibitory activity at 10 µM. Considering its relative low molecular weight, the structure could be differently functionalised to reach further interaction and increase the potency of the molecule. From the hydrolysis of the ethyl ester, the acidic derivatives **25** and **27** were obtained. These compounds measured an antipyroptotic effect

Compound	Pyroptosis decrease[a] % inhibition at 10 µM	IL-1β inhibition[b] % inhibition at 10 µM	Cytotoxicity[c] TC_{50} (µM)
24	11.0 ± 9.0	NT	> 100
25	< 10	NT	> 100
26	32.9 ± 3.4[d]	38.0 ± 7.5	> 100
27	40.4 ± 11.9[e]	40.5 ± 5.5	> 100
28	22.7 ± 10.3	13.2 ± 1.1	> 100
29	11.4 ± 6.2	< 10	74.3 ± 1.5
30	< 10	NT	> 100
31	22.8 ± 7.09	24.4 ± 8.2	> 100
32	< 10	< 10	> 100
33	13.8 ± 7.1	NT	>100
34	< 10	NT	>100
35	45.2 ± 7.2[e]	17.4 ± 6.6 [d]	94.2 ± 6.8
36	20.1 ± 9.8 [d]	< 10	>100
37	NA	NT	89.7 ± 8.8
38	NA	NT	94.6 ± 4.0
39	NA	NT	86.9 ± 4.0
40	NA	NT	33.7 ± 5.33
41	NA	NT	86.3 ± 3.0
42	NA	NT	85.9 ± 2.0
43	62.2 ± 9.8[e]	44.6 ± 5.4	59.4 ± 2.2

Table 6.2: Inhibitory effect of synthesised compounds on pyroptotic cell death, IL-1β release in differentiated THP-1 cells and cytotoxicity in THP-1 cells. [a]Pyroptosis of differentiated THP-1 cells was triggered using LPS/ATP. Data are reported as the % inhibitionof pyroptosis of cells treated with 10 µM conc of test compound vs vehicle-treated cells. Data are the mean ± SEM of three to five experiments run in triplicate. [b]IL-1β inhibition was measured in the cell supernatants form the same experiments. Data are reported as % inhibition ± SEM of three to five experiments run in triplicate. [c] Cytotoxicity was determined after 72 h treatment of THP-1 cells with increasing conc (0.1–100 µM) of test compounds. Data are reported as TC50 ± SEM of three experiments. [d] $p < 0.05$ vs. vehicle treated cells (t-student); [e] $p < 0.01$ vs. vehicle treated cells (t-student); NA = not active at 10 µM; NT = not tested.

similar to that of their corresponding ester analogues, and **27** (pyroptosis reduction: 40.41 ± 11.86%; IL-1β inhibition: 40.53 ± 5.51%) confirmed the position 3- as the preferred for further modulations. This hydrolysis easily occurs in physiological conditions, and for this reason the ester analogues were considered as prodrugs. The piperidine-3-carboxyamide **28**, devoid of acidic properties revealed a reduced activity profile, compared to the corresponding ester or acid at the tested concentration of 10 µM (pyroptosis reduction: 22.7 ± 10.3%; IL-1β inhibition: 13.24 ± 1.14%).

The functionalisation of **25** with alanine or phenylalanine (**29** and **30**) did not show

significant improvements in the antipyroptotic activity. Similarly, the alanine derivatives in position 3 of the piperidine ring, **32** revealed inactive, compared to **27**. Interestingly, compound **31**, with the similar glycine derivatisation, the ability to inhibit the pyroptotic cell death and the IL-1β-release was only slightly reduced, and the compound measured a mild potency (pyroptosis reduction: 22.77 ± 7.09 %; IL-1β inhibition: 24,35 ± 8.17 %).

Finally, derivatives **33**–**43** where synthesised from the insertion of a sulphur-containing side chain. These compounds were synthesised with phenylthio group (**42** and **43**) and the piperidine functionalised in position 4 and 3, respectively; or with the cyclohexylthio side chain (**38** and **39**). The saturation of the linker between the amide and the 2-chlorophenyl ring, abrogated the antipyroptotic activity in derivatives **38**, **39** and **42**, except for compound **43**. Compound **43** bearing the 3-carboxypiperidine and the phenylthio substituents, reduced the pyroptotic cell death in THP-1 cells by 62.2 ± 9.8% and reduced the IL-1β release by 44.6 ± 5.4% at the concentration of 10 µM used in the preliminary screening. The main problem of the compound was a certain degree of cytotoxicity (TC_{50} = 59.4 ± 2.2 µM). From the series of α-β unsaturated derivatives, compound **33** and **40** bearing the 4-carboxypiperidine and the phenylthio substituent, measured a low potency in antipyroptotic effect (13.8 ± 7.1%). Similarly, cyclohexylthio analogue **40** was inactive in the tested conditions. Once again, the most promising compounds were identified from the 3-carboxypiperidine derivatives. On the side-chain position, the favourite phenylthio substituent was adopted for compounds **35**, **36** and **37**. The ethyl ester **35** showed a better efficacy compared to the free carboxylic acid analogue **36** (45.2 ± 7.2% and 20.1 ± 9.8%) and demostrated the ability to inhibit the IL-1β release by 17.4 ± 6.6% on ATP-stimulated THP-1 cells at 10 µM dose. Surprisingly the carboxyamide analogue **37** proved inactive, confirming the hypothesis on the importance of an acidic functionality on the piperidinamide scaffold. The cyclohexylthio analogues **40** and **41** were inactive at the tested doses in our assay.

Compound **35** was then tested *in vivo* in an experimental murine model of dextrane sodium sulphate(DSS)-induced colitis. Compound **35** demonstrated a good efficacy in overall intestinal inflammation reduction. Oral administration of 25 mg/kg/die or 50 mg/kg/die of **35** determined an improvement of systemic and tissue parameters related to colitis (figure 6.2). Parameters were evaluated on the mice after 9 day of treatment (4 groups: vehicle, DSS, DSS+25 mg/kg **35**, DSS+50 mg/kg **35**).Furthermore, **35** reduced the animal body weight loss and spleen weight increase, significantly reducing the disease activity index (DAI), IL-1β and myeloperoxidases (MPO) levels in colonic tissues. Myeloperoxidases are index of inflammatory cells infiltration to the tissue (figure 6.2).

Compound **35** was also tested in a mice model with accelerated spontaneous senescence (SAMP8). SAMP8 mice are used as neurodegenerative diseases model such as the mild cognitive impairment (MCI), that usually evolves in Alzheimer's disease. Chronic administration (2 month) of compound **35** (oral administration of 50 mg/kg/die) to SAMP8 mice, starting at the age of four month, before the symptoms onset, significantly prevents the cognitive impairment evaluated by the Morris Water Maze (MWM) test. The test relies on distal cues to navigate from start locations around the perimeter of an open swimming arena to locate a submerged escape platform. After 8 weeks of treatment, an initial training test period of 8 days was performed to assess spatial learning of the mice across repeated trials and reference memory. Escape latency is recorded during this phase (figure 6.3, A). On the ninth day, the platform was removed: the number of target crossing and number of

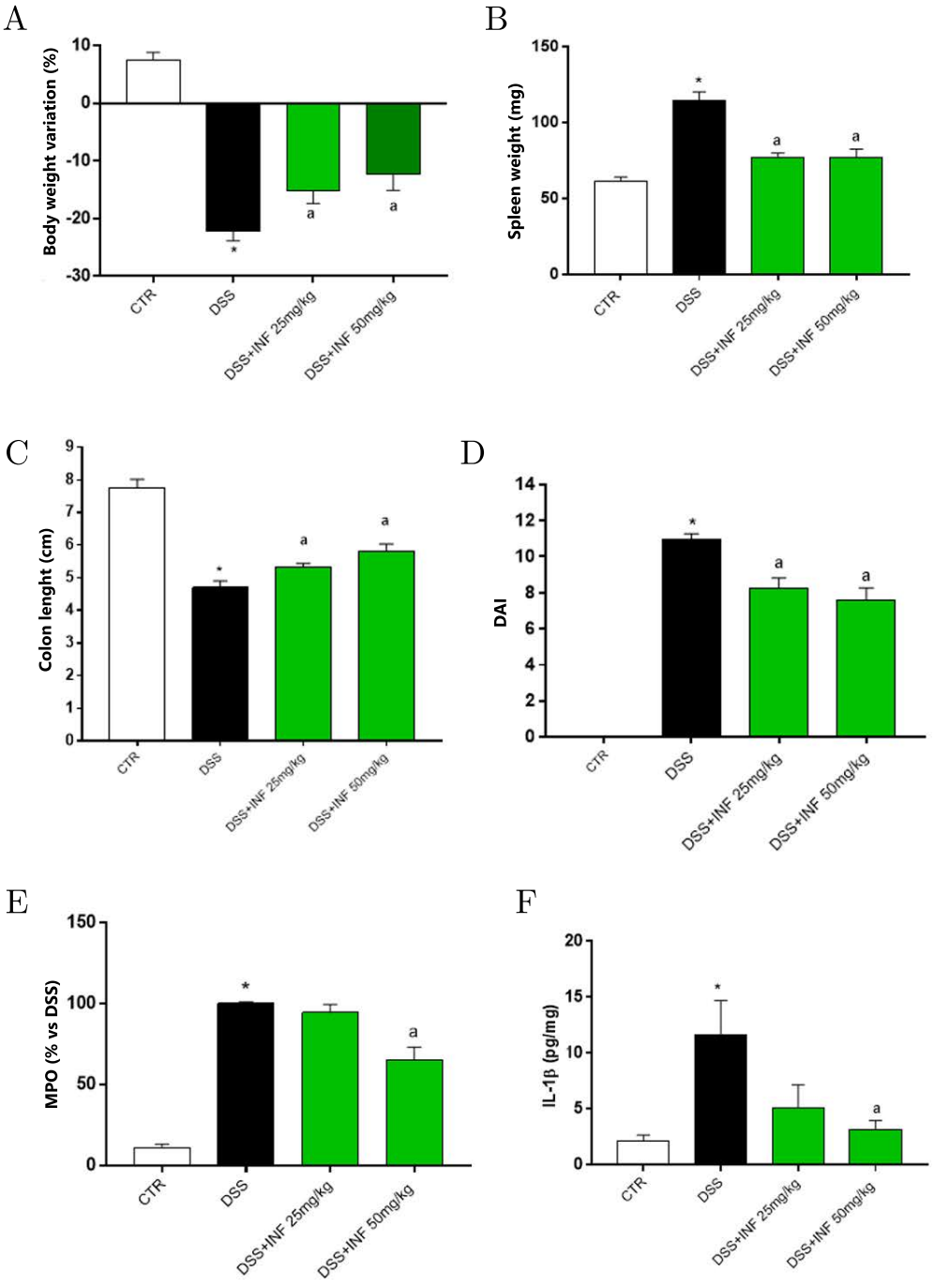

Figure 6.2: Effect of the treatment with **35** at the daily dose of 25 and 50 mg/kg on DSS-induced colitis mice model: (A) body weight variation, (B) spleen weight, (C) colon lenght, (D) disease activity index (DAI), (E) colonic myeloperoxidases, (F) colonic IL-1β level. $^{*}P<0.05$ vs control (CTR) and $^{a}P<0.05$ vs DSS.

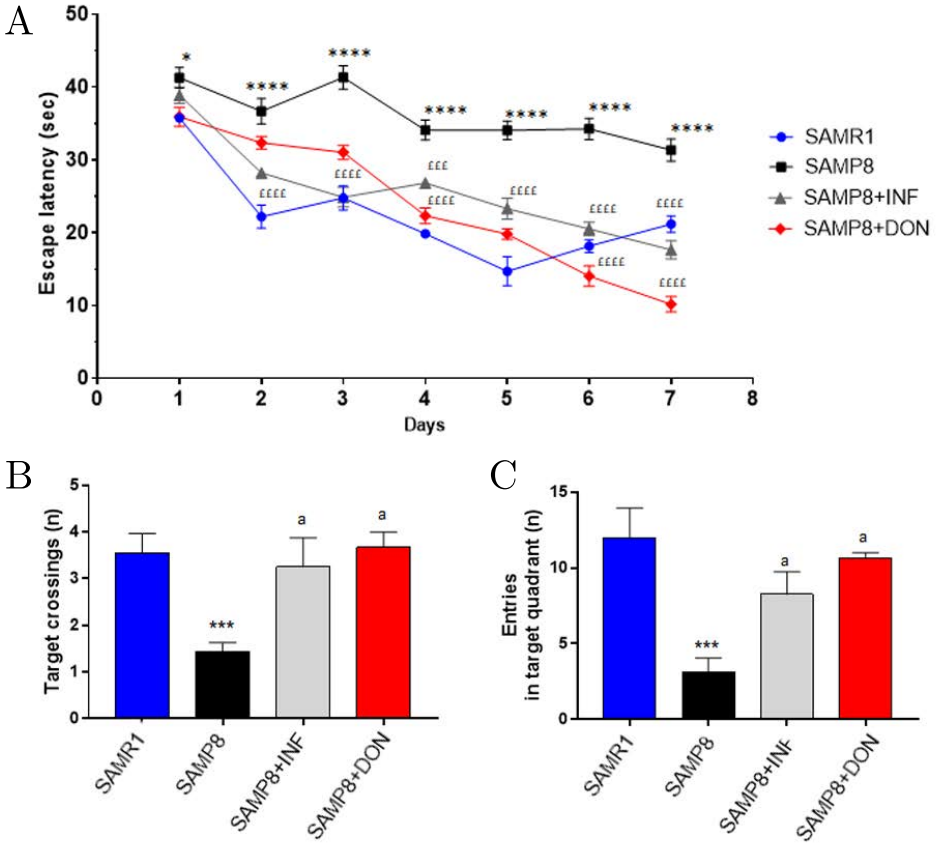

Figure 6.3: Effect of the treatment with **35** at the daily dose of 50 mg/kg or donepezil (3 mg/kg) after 8 weeks of treatment in the Morris Water Maze test on: (A) escape latency in the training phase (days 1–8), (B) number of target crossing, (C) entries in target quadrant. B and C are measured on day 9, in absence of the platform. *P<0.01 vs SAMR1; ***P<0.001 vs SAMR1; ****P<0.0001 vs SAMR1; $^{£££}$P<0.001 vs SAMP8; $^{££££}$P<0.0001 vs SAMP8; ^{a}P<0.05 vs SAMP8

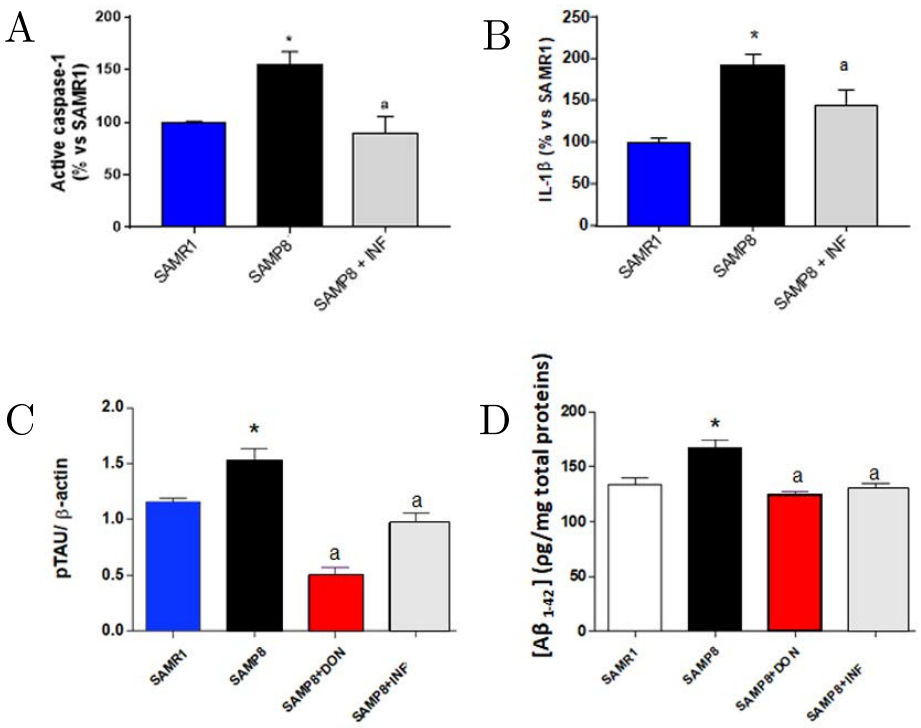

Figure 6.4: Effect of the treatment of SAMP8 mice with **35** at the daily dose of 50 mg/kg or donepezil (3 mg/kg) in brain tissue: (A) cleaved caspase-1 levels, (B) IL-1β level, (C) pTAU protein expression, (D) amiloid $\beta_{1\text{-}42}$ deposition. $^{*}P<0.05$ vs control (CTR) and $^{a}P<0.05$ vs DSS.

target entrance where the platform was present in the training phase are evaluated.[126] Mice were also treated with donepezil (3mg/kg, 8 weeks), drug approved for Alzheimer's disease therapy. Control experiment were performed on healthy SAMR1 mice (figure 6.4). SAMP8 mice treated with **35** maintain cognitive functions in Morris Water Maze test comparable to control SAMR1 mice and to the donepezil-treated mice (see figure 6.3). Donepezil binds and reversibly inactivates the cholinesterases, increasing acetylcholine concentrations at cholinergic synapses. However, it has been reported an effect of donepezil on amiloid β deposition and pTAU protein expression. In our assay the results were in accordance to literature.[127,128,129] Furthermore, **35** reduces the active caspase-1 and the central IL-1β levels in the brain to basal concentration found in control SAMR1 mice. It reduces also the expression of p-tau protein (Alzheimer's disease markers) and the accumulation of amiloid $\beta_{1\text{-}42}$ in brain tissue with an effect comparable to donepezil treatment at its therapeutic dose (see figure 6.4).

6.1.3 Central heterocycle derivatives

The same experiments described before, were also used to screen the antipyroptotic activity, the inhibition of IL-1β release and the cytotoxicity on ATP-stimulated inflammasome activation on differentiated THP-1 of the compounds bearing the heterocyclic core reported in figure 4.6 at 10 µM. The obtained results are reported in table 6.3.

Among the synthesised 1,2,4-oxadiazole derivatives (**44**–**47**), only compound **44** measured a good antipyroptotic activity at 10 µM (46.3 ± 17.3%) but, surprisingly, it was not able to hamper IL-1β release in the same THP-1 cellular system. The hydrolysis of the terminal methyl ester (**45**) resulted in a significant activity reduction in preventing ATP-induced inflammasome-mediated pyroptotic cell death (14.2 ± 2.08%). The reversed central heterocycle (**47**) was also inactive in our assay.

The results obtained for compounds **48**–**56** are collected in table 6.3. Compound **48** bearing a ethyl acetate terminal derivatisation, measured a good inhibition of ATP-induced inflammasome-mediated pyroptotic cell death and IL-1β release in THP-1 cells (77.4 ± 6.4% pyroptosis reduction; 28.7 ± 4.3% IL-1β inhibition at 10 µM) with no relevant cytotoxic effect at the active concentration (TC_{50}=75.6 ± 1.1). The free carboxylic acid analogue **49**, showed a reduced, but still remarkable, antipyroptotic effect at 10 µM (33.2 ± 2.3%). In accordance with the hypothesis of in vivo hydrolysis and activation of the ethyl ester prodrug, we tested the t-butyl ester derivative **50**, uncleavable in physiological condition. As expected, this compound was inactive at the tested concentration (10 µM), confirming the importance of the presence of the free carboxylic acid form. The replacement of the acidic group with the more lipophilic classical bioisostere tetrazole reduced the antipyroptotic effect to 20.2 ± 15.5% at 10 µM. Analogously, the insertion of a phenyl ring between the heterocycle and the carboxy group yielded **52**, with reduced potency (pyroptosis reduction: 17.7 ± 6.4% at 10 µM) compared to the hit compound **48**. The replacement of the carboxy group in **52** with a non-hydrolysable methoxy substituent abrogated the antipyroptotic activity of compound **53**.

Finally, the amide-like heterocycle 1,3,4-thiadiazole was adopted for the synthesis of derivatives **54**, **55** and **56**. Compound **54**, bearing a close replacement of the amidic core of **26** with the new heterocycle, maintained the ability to inhibit the NLRP3-dependent pyroptotic cell death in THP-1 cells at tested concentration of 10 µM (38.4 ± 14.9%).

Compound	Pyroptosis decrease[a] % inhibition at 10 µM	IL-1β inhibition[b] % inhibition at 10 µM	Cytotoxicity[c] TC_{50} (µM)
44	46.3 ± 17.3[d]	< 10	> 100
45	14.2 ± 2.1	NT	27.3 ± 1.3
46	NA	NT	> 100
47	< 10	NT	94.5 ± 1.1
48	77.4 ± 6.4[e]	28.7 ± 4.3	75.6 ± 1.2
49	33.2 ± 2.3[d]	NT	94.6 ± 1.2
50	< 10	NT	98.9 ± 15.0
51	20.2 ± 15.5	NT	> 100
52	17.7 ± 6.4	NT	> 100
53	11.4 ± 3.8	NT	64.8 ± 5.6
54	38.4 ± 14.9	22.4 ± 9.5	79.7 ± 7.0
55	25.7 ± 5.8	20.7 ± 12.6	96.1 ± 4.0
56	73.6 ± 6.9[e]	49.0 ± 12.4	91.6 ± 14.5

Table 6.3: Inhibitory effect of synthesised compounds on pyroptotic cell death, IL-1β release in differentiated THP-1 cells and cytotoxicity in THP-1 cells. [a]Pyroptosis of differentiated THP-1 cells was triggered using LPS/ATP. Data are reported as the % inhibitionof pyroptosis of cells treated with 10 µM conc of test compound vs vehicle-treated cells. Data are the mean ± SEM of three to five experiments run in triplicate. [b]IL–1β inhibition was measured in the cell supernatants form the same experiments. Data are reported as % inhibition ± SEM of three to five experiments run in triplicate. [c] Cytotoxicity was determined after 72 h treatment of THP-1 cells with increasing conc (0.1–100 µM) of test compounds. Data are reported as TC50 ± SEM of three experiments. [d] $p < 0.05$ vs. vehicle treated cells (t-student); [e] $p < 0.01$ vs. vehicle treated cells (t-student); NA = not active at 10 µM; NT = not tested.

Keeping the east-terminal carboxy group, the ring-opening strategy led to compound **55** with mild antipyroptotic activity at 10 µM (25.7 ± 5.8%). A lipophilic benzyl substituent on the eastern nitrogen was inserted in compound **56**. This modulation significantly increased the potency of the derivative toward the inhibition of pyroptotic cell death and IL-1β release from THP-1 cells. Compound **56** also measured a favourable absence of cytotoxicity at the tested doses (TC_{50} = 91.6 ± 14.5 µM) confirming this derivative as one of the most promising from this work.

6.2 GSDMD-CT characterisation

The C-terminal domain of Gasdermin-D was expressed from the plasmid pET-SUMO-hGSDMD (Addgene, plasmid n 111559, 6.5) with designed mutations. In particular, the N-Terimal domain (aminoacids 1–274) were deleted and a sequence ENLYFQG was inserted between the SUMO tag and the GSDMD-CT coding dna. The sequence ENLYFQG is recognised by the TEV protease, used to cleave the His-SUMO tag during the purification

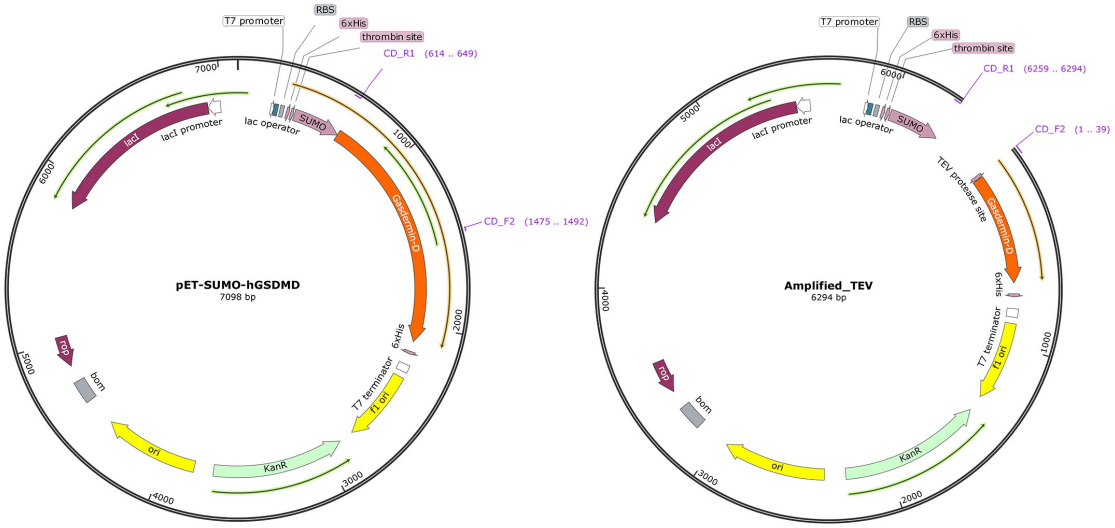


```
hGSDMD/1-484      1 MGSAFERVVRRVVQELDHGGEFIPVTSLQSSTGFQPYCLVVRKPSSSWFWKPRYKCVNLSIKDILEPDAAEPDVQ  75
CT_domain/1-210     ----------------------------------------------------------------------------

hGSDMD/1-484     76 RGRSFHFYDAMDGQIQGSVELAAPGQAKIAGGAAVSDSSSTSMNVYSLSVDPNTWQTLLHERHLRQPEHKVLQQL 150
CT_domain/1-210     ----------------------------------------------------------------------------

hGSDMD/1-484    151 RSRGDNVYVVTEVLQTQKEVEVTRTHKREGSGRFSLPGATCLQGEGQGHLSQKKTVTIPSGSTLAFRVAQLVIDS 225
CT_domain/1-210     ----------------------------------------------------------------------------

hGSDMD/1-484    226 DLDVLLFPDKKQRTFQPPATGHKRSTSEGAWPQLPSGLSMMRCLHNFLTDGVPAEGAFTEDFQGLRAEVETISKE 300
CT_domain/1-210   1 ------------------------------------------------GGVPAEGAFTEDFQGLRAEVETISKE  26

hGSDMD/1-484    301 LELLDRELCQLLLEGLEGVLRDQLALRALEEALEQGQSLGPVEPLDGPAGAVLECLVLSSGMLVPELAIPVVYLL 375
CT_domain/1-210  27 LELLDRELCQLLLEGLEGVLRDQLALRALEEALEQGQSLGPVEPLDGPAGAVLECLVLSSGMLVPELAIPVVYLL 101

hGSDMD/1-484    376 GALTMLSETQHKLLAEALESQTLLGPLELVGSLLEQSAPWQERSTMSLPPGLLGNSWGEGAPAWVLLDECGLELG 450
CT_domain/1-210 102 GALTMLSETQHKLLAEALESQTLLGPLELVGSLLEQSAPWQERSTMSLPPGLLGNSWGEGAPAWVLLDECGLELG 176

hGSDMD/1-484    451 EDTPHVCWEPQAQGRMCALYASLALLSGLSQEPH                                        484
CT_domain/1-210 177 EDTPHVCWEPQAQGRMCALYASLALLSGLSQEPH                                        210
```

Figure 6.5: At the top the original plasmid with the designed primers for mutations: forward primer (CD_F2, 5′-gaa aac ctg tat ttt cag ggc ggg gtc cct gcg gag ggg-3) and reverse primer (CD_R1, 5′-acc acc aat ctg ttc tct gtg agc ctc aat aat atc-3′) allowed the deletion of the N-terminal domain and the insertion of TEV site. The resulting plasmid is schematically reported on the top right.

step. GSDMD-CT with 210 aminoacids was numbered in this work from 1 to 210. The first genuine residue G276 correspond to internal numbering 2 while the terminal H484 correspond to position 210 (See aligment in figure 6.5).

The mutations were performed using PCR with the designed primers and Q5 Site-Directed Mutagenesis Kit (New English Biolabs Inc.) for the amplification and competent cells. The nucleotide sequence coding for the His-Sumo-Tev-GSDMD(CT) portion of DNA was sequenced using T7 promoters to confirm the correct mutation and DNA composition. The plasmid was successfully transformed into BL-21 competent cell grown in LB media at 37°C. The plasmid bears the kanamycin-resistance gene, and the bacteria were grown in presence of this antibiotic, to selectively grow bacteria with the plasmid. The optical

density (OD) was measured upon reaching a value around 0.8. At this point the buckets were cooled to 20°C and the protein expression was triggered by IPTG (isopropyl β-D-1-thiogalactopyranoside) solution and shaked overnight. For the expression of isotopic labelled protein required for protein NMR spectroscopy, a different strategy was adopted after reaching OD around 0.8. The cells were harvested by gentle centrifugation (5 min at 5000 rpm) and resuspended in fresh M9 media. M9 media is composed by salts (Mg^{2+}, Ca^{2+}), vitamins, micronutrients, the appropriate antibiotic, ammonium chloride as source of nitrogen, and glucose as carbon-source. For protein labelling, ammonium chloride and/or glucose were selectively replaced by the ^{15}N or ^{13}C labelled version of the reagent.[130] The harvesting-resuspension procedure was repeated to wash residue of LB from the cells. Usually, cells from 4 litres of LB colture with appropriate OD, were washed and merged into 1 litre of M9 media. The cells were grown in shaker for 1 hour and the protein expression induced with the same IPTG solution at 20°C overnight. The next day, cells were harvested for the purification step.

First, cells were lysed using a combination of lysozyme and triton 100x for cell wall and cell membrane rupture and freeze-thawing physical strategy. The solvent used in the purification step is the FF6 buffer, containing phosphate buffer (20 mM, pH 7.4), NaCl (500 mM) and NaN_3 (0.02%). The mixture was snap-frozen in liquid nitrogen and thawed to facilitate cell breaking. To reduce the mixture viscosity DNAase was added. High-speed centrifugation (2 h, 9000 rpm, 4°C) allowed the separation of the cellular component from the clear solution containing proteins. GSDMD-CT purification was performed using HIS-tag affinity chromatography. The mixture was eluted through His-Trap (GE Healthcare) fast flow 5 mL column containing Ni^{2+} were the His-Sumo-GSDMD-CT was linked to the column. The elution with FF6 buffer containing imidazole (500 mM) allowed the collection of the protein with a few aspecific binder proteins. An intermediate step of incubation with TEV proteases, followed by dialysis of the solution in fresh FF6 imidazole-free buffer allowed the cleavage of the HIS-SUMO fragment from the GSDMD-CT and the removal of imidazole from the buffer. The so obtained mixture underwent a second His-Trap column to remove aspecific binders from the GSDMD-CT (without HIS-tag, removed by TEV cleavage) that does not interact with the column. Expression yields were 43 mg/L, 21 mg/L, and 11 mg/L of colture respectively for unlabelled, ^{15}N, and $^{15}N^{13}C$-double labelled proteins.

To investigate protein folding and stability, UV and circular dichroism (CD) spectra were acquired at 23°C (Chirascan CD spectrometer, Applied Photophysics Ltd) and in a thermal ramp up to 94°C (See figure 6.6). CD measures the differential absorption of circularly polarized light as a function of the wavelength of the beam. CD spectra of proteins in the region of near-UV (180-240 nm) is influenced by secondary structure in the protein. In general, the CD signal at 215 nm indicates the sheet content and the signal at 208 nm and 222 nm are used to calculate the helical content, and the resulting spectra can be treated as a sum of three components: α-helical, β-sheet, and random coil contributions. Monitoring the CD at 222 nm of a protein as a function of temperature or chemical denaturant yields important information on protein stability allowing to compute the melting point (59.0 ± 0.2°C). CD plots reported in figure 6.6 highlight a good protein folding into expected α-helices secondary structure. Furthermore, the protein behaviour at higher temperature and the partial recover of the secondary structure after heating at 90°C, indicate a good overall stability of the protein at temperature above 23°C.

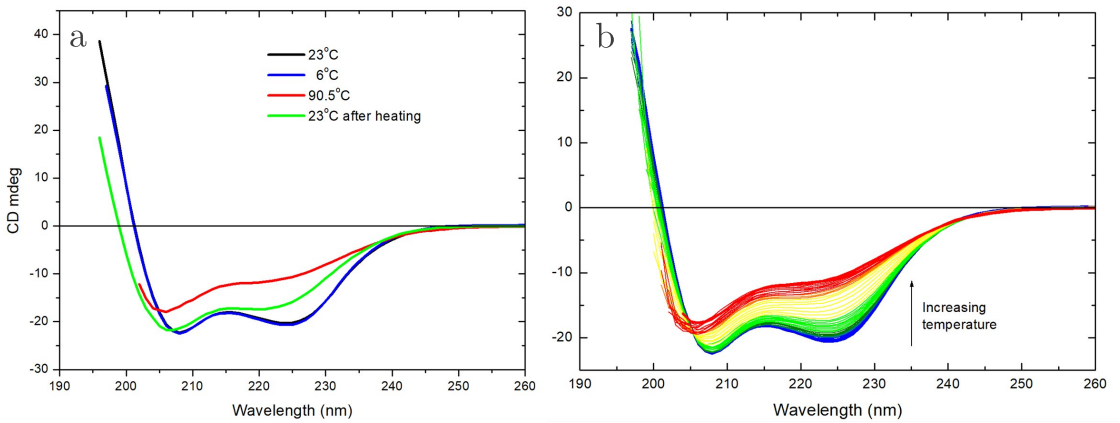

Figure 6.6: CD spectra of GSDMD-CT acquired at protein concentration 0.3 mg/mL, in 20 mM phosphate buffer, 50 m M NaCl, 0.02% NaN_3, pH 7, with 0.5 mm pathlenght. (a) Cd spectra acquired at different temperature. The green line is the signal at 23°C after heating to high temperature (91°C) and showed a partial reversible conformation of the protein after heating. (b) CD signal over temperature ramping. The protein demonstrates a good tolerance to higher temperature.

For NMR purposes, the buffer was changed with the NMR buffer using size exchange chromatography (Clarion P25, Sorbtech Inc.), The NMR buffer is composed by phosphate buffer (20 mM), NaCl (50 mM), and NaN_3 (0.02%). When needed, the anti-oxidant DTT was added in a concentration of 2 mM. The samples were concentrated (Vivaspin 20 MWCO 5000, Cytiva) up to 0.8-1 mM concentration without observing any precipitation. The volume for the Shigemi NMR tube was around 300 µL. The spectra were acquired at 35°C to reduce the line broadening caused by the high molecular weight (22 kDa is on the edge of the stuctural protein NMR sensitivity). We successfully acquired all the spectra usually required for backbone and side chain assignment: 2D: ^{1}H-^{15}N-HSQC; 3D HNCACB, (H)C(CCO)NH, H(CCCO)NH, ^{15}N and ^{13}C resolved 3D NOESY-HSQCs. Spectra were phased using TopSpin 4.4.1 (Bruker) and assigned in CCPN analysis 2.4.[131]

In ^{1}H-^{15}N-HSQC experiment, magnetization is transferred from hydrogen to attached ^{15}N nuclei via the J-coupling.[132] The chemical shift is evolved on the nitrogen and the magnetisation is then transferred back to the hydrogen for detection. The scheme of magnetisation evolution during the experiment is reported in figure 6.10 This is the most standard experiment and shows all H-N correlations and represent the fingerprint of the protein. Mainly these are the backbone amide groups, but Trp side-chain Nε-Hε groups and Asn/Gln side-chain Nδ-Hδ/Nε-Hε groups are also detected. The acquired spectrum is reported in figure 6.7.

The HSQC experiment roughly plots one NH peaks each residue in the protein. In GSDMD-CT (210 aminoacids) spectrum (figure 6.7) we found 621 peaks. We excludeed the presence of impurity in our sample and we recorded a particular NMR sequence to investigate possible dynamics in solution causing the peaks multiplying. In the exchange experiments an initial excitation of the proton is followed by indirect frequency labelling.

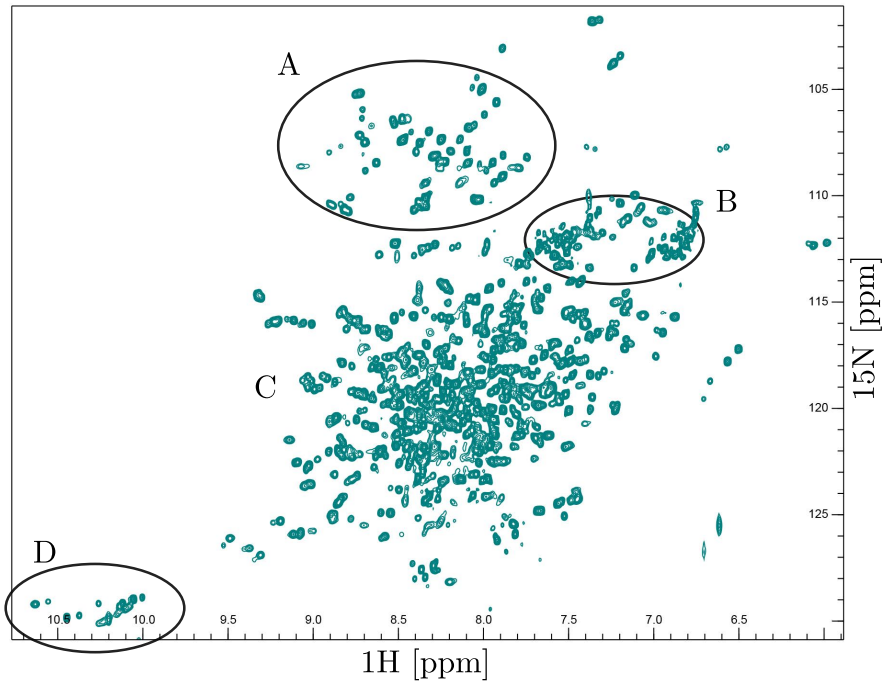

Figure 6.7: ^{15}N spectrum of the GSDMD-CT domain. Peaks are plotted in cyan. In a typical folded protein spectrum different regions appears in the HSCQ peaks: A) Glycine region, B) Asn and Gln side chain NH_2, there are logically 2 peaks on the same nitrogen chemical shift, but different hydrogen ppm values. C) NH crosspeaks from most of the residues of the protein. For folded protein peaks are spread in the center of the spectrum. D) Tryptophan side chain nitrogens.

Subsequently, magnetization is transferred to the nitrogen, where magnetization is rotated onto the z-axis, where it can lasts longer during mixing time. Nitrogen Z-magnetization (Nz) is then allowed to exchange during a mixing time T. Then, Nz is rotated onto the xy-plane and transferred back to the proton where it is detected. These experiments are recorded as simple NOESY-like 2D spectra with two proton axes or as pseudo-3D spectra where the third axis is the mixing time.[133] We found 2s as the optimum mixing time, meaning a very slow conformational exchange. Most of the peaks are present in both conformation A and B, and some of them located in a less crowded area, were also identified in conformation C and D. The chemical shift distance between the conformations is not constant among the residues. For this reason some of the peaks of conformers B, C, and D are easily identified, but in other case they collapse in a single peaks and their discrimination is not easy. $\Delta\delta$ is greater around some specific residues. In particular we identified some higher value around specific prolines in the sequence. P4, P180, P140 (and P150 in the unassigned region) could play a pivotal role in conformational exchange regulation. Prolines have *cis-trans* isomers in exchange with slow kinetics compatible to our observation. Further studies are now running to determine the importance of *cis-trans* equilibrium on GSDMD-CT structure. This peculiarity of the proteins has been found also

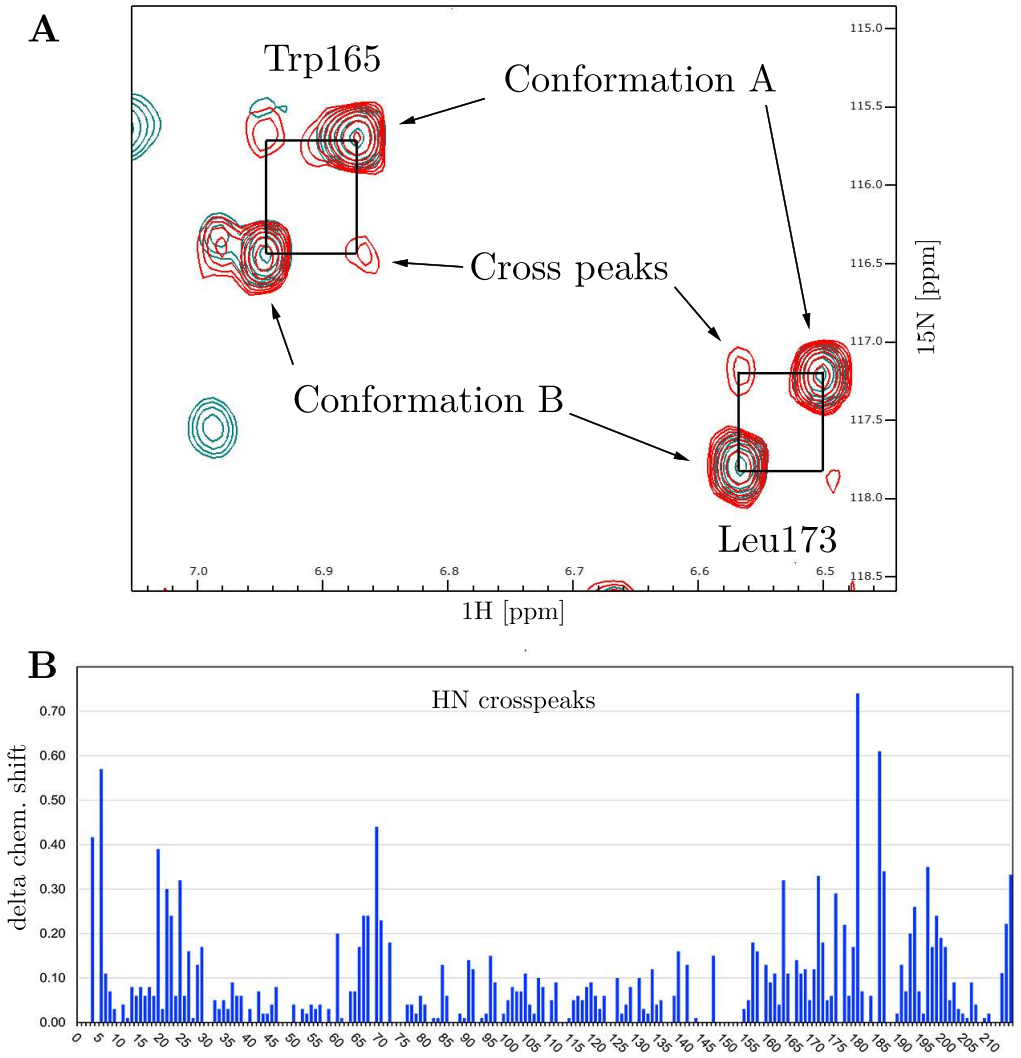

Figure 6.8: A) focus on the superimposition of the classical ^{15}N-HSQC (in cyan) and the ^{1}H-^{15}N heteronuclar correlation exchange spectra with a delay of 2s (in red). Cross peaks are generated if the two conformations are interconverting with an exchange rate matching the delay of the sequence (2s, in this case). B) the distance in chemical shift between different conformers. For residues with more than two conformers the value was calculated for the two most distant conformers.

in all the other spectra, and made the assignment more complicated, but more than 95% of the residue in conformation A and 80% of conformation B were successfully assigned.

The HNCACB spectrum is part of the standard and fundamental set of experiment needed for backbone assignment. Usually each strip should contain four peaks: the Cα, and Cβ from the same residue as the NH group ($C\alpha_i$ and $C\beta_i$) which are stronger, and the Cα and Cβ from the preceding residue ($C\alpha_{i-1}$ and $C\beta_{i-1}$) which are weaker (figure 6.9). In

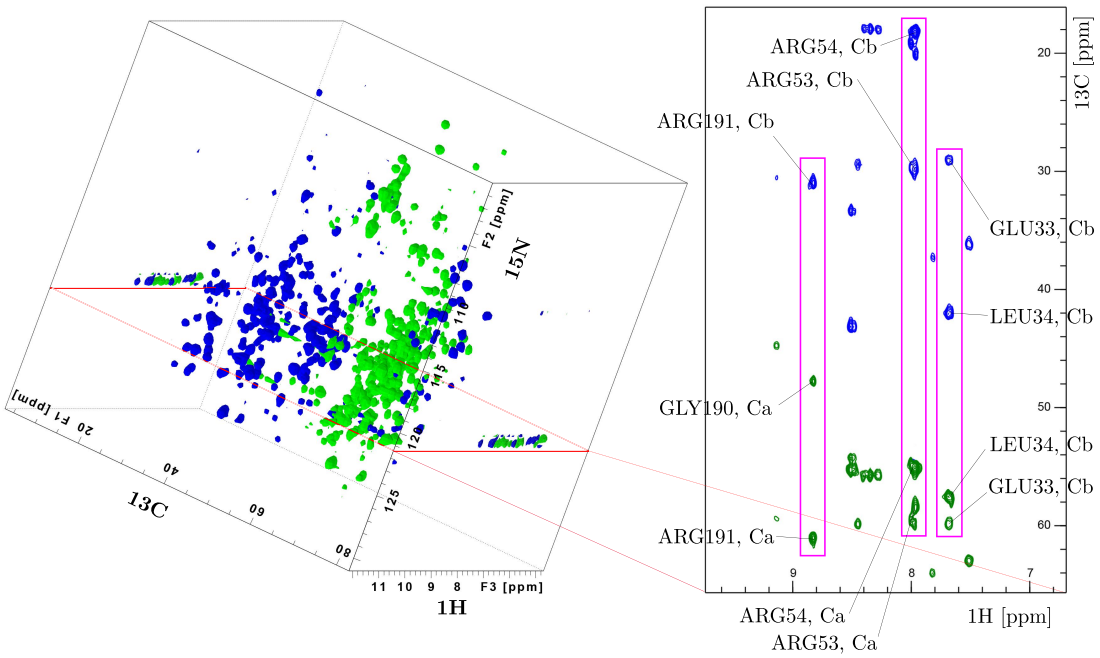

Figure 6.9: The 3D representation of the HNCACB spectrum of GSDMD-CT is reported on the left. During the elaboration of the spectrum, slices on the nitrogen plane are evaluated. On the right hand side, the 121.56 ppm nitrogen plane is reported. The peptidic nitrogens of three residues have been found with this nitrogen chemical shift. Three strips are highlighted with magenta rectangles. Different N-*H* chemical shifts spread the strips on the x axes. On each strips is possible to find the cross peaks at the carbon chemical shift corresponding to the atom reported on the tags, cross peaks with lower intensity are referred to the preceding residue in the protein.

addition, Cα peaks are negative, while the Cβ are positive, or vice verse depending on the phasing. During the experiment, the magnetisation is transferred from ^{1}Hα and ^{1}Hβ to ^{13}Cα and ^{13}Cβ, respectively, and then from ^{13}Cβ to ^{13}Cα. From here it is transferred first to ^{15}NH and then to ^{1}HN for detection (see figure 6.10). Transfer form $C\alpha_{i-1}$ can occur both to $^{15}N_{i-1}$ and $^{15}N_{i}$, or viewed the other way, magnetisation is transferred to $^{15}N_{i}$ from both $^{13}C\alpha_{i}$ and $^{13}C\alpha_{i-1}$. Thus for each NH group there are two Cα and Cβ peaks visible. The chemical shift is evolved simultaneously on ^{13}Cα and ^{13}Cβ, so these appear in one dimension. The chemical shifts evolved in the other two dimensions are ^{15}NH and ^{1}HN.[134]

Another experiment, H(CCCO)NH (and the carbon equivalent (H)C(CCO)NH) is a useful spectrum for obtaining hydrogen side-chain assignments. In each NH strip, the hydrogen chemical shifts from the whole side chain of the previous residue are visible. Magnetisation is transferred from the side-chain hydrogen nuclei to their attached ^{13}C nuclei. Then isotropic ^{13}C mixing is used to transfer magnetisation between the carbon nuclei. From here, magnetisation is transferred to the carbonyl carbon, onto the amide nitrogen and finally the amide hydrogen for detection (figure 6.10). The chemical shift is

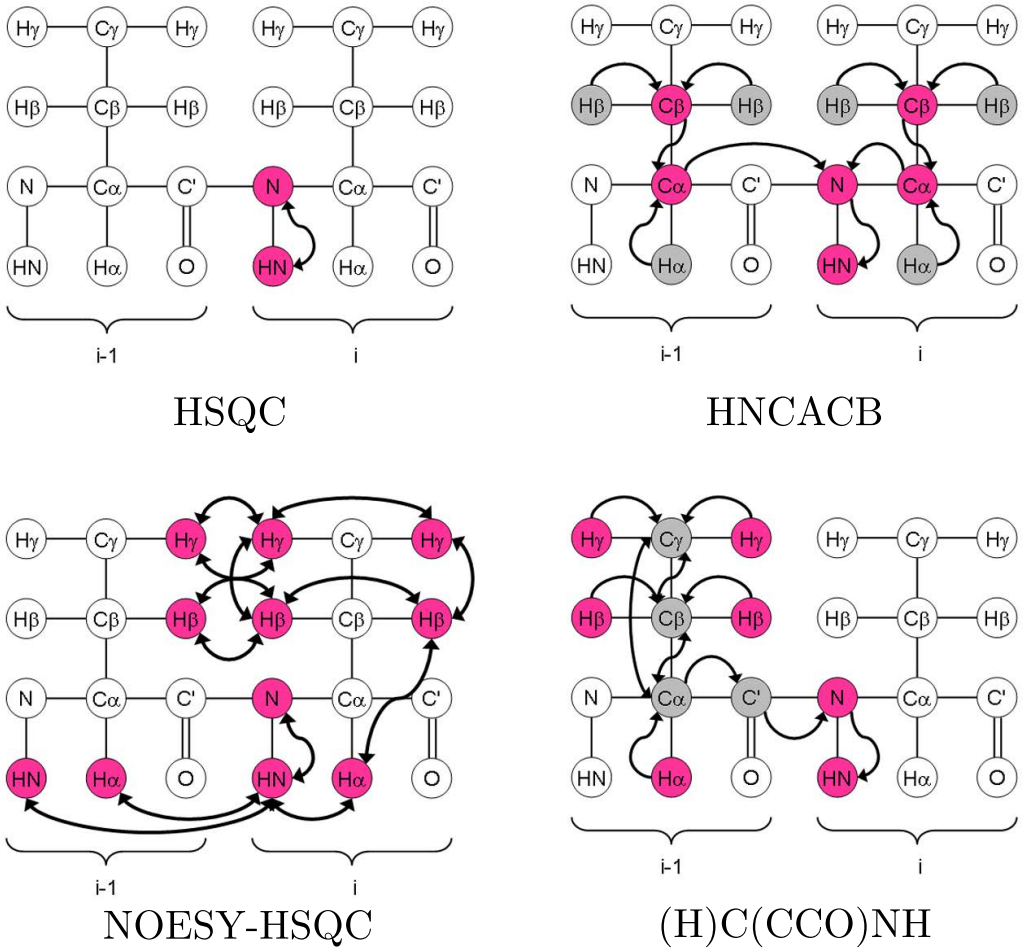

Figure 6.10: Scheme of the evolution of the magnetisation during the NMR experiments. In pink the nuclei detected in the NMR sequences.

evolved simultaneously on all side-chain hydrogen nuclei, as well as on the amide nitrogen and hydrogen nuclei, resulting in a three-dimensional spectrum with one nitrogen and two hydrogen dimensions.[135]

The ^{15}N-NOESY-HSQC was used to help assignment, and this spectrum can be usually used to obtain restraints for structure calculations. In the spectra, each strip contains NOEs from one NH group to all other hydrogen atoms close by. Magnetisation is exchanged between all neighbour hydrogens using the NOE. Then the magnetisation is transferred to ^{15}N nuclei and back to ^{1}H for detection (figure 6.10).[136]

6.3 In the search for GSDMD-CT binders

Recently, Gasdermin-D has received increasing attention from the scientific community. Many aspect has been described, but no successfully inhibitory strategy has been found. Some binders of the N-terminal domains have been reported, but their efficacy in inhibiting GSDMD-mediated effects is controversial. Our C-terminal-based strategy could be a novel approach to identify possible binders of this subunit, as a starting point for the development of new inhibitors of GSDMD activation acting on the recognition step between caspase-1 and GSDMD.

We started from the published crystal structure (PDB code: 6KN0) of the C-terminal domain in complex with Casp-1. Before conducting a MD simulation, we kept only the structure of GSDMD-CT and evaluated any inconsistencies such as the protonation state of every residues: this is important for amino acids with electrically charged side chain like Histidine, Lysine, Arginine, Aspartic Acid and Glutammic Acid. Furthermore, N- and C-terminal has missing residues, and they were capped (to suppress the teminal charge) avoiding artifical strong interaction between termini, which might not reflect the behaviour in solution of the full-length protein. The last pdb adjustment consist in modelling the missing part of the crystallographic structure as usually happen in flexible loops, Hence, we used Modeler 9.25[137] in order to obtain a prediction for missing loops structures by aligning the sequence UniProtKB - P57764 (GSDMD-human) with the C-terminal FASTA sequence (amino acids range: 275–484), in addition an artificial G274 (deriving from TEV cleavage, see paragraph 6.2) was added, to have the same structure expressed in the laboratory. Modeler method predicts the positions of all nonhydrogen atoms of a given loop in a fixed environment by optimizing a scoring or "energy" function. Bonds, angles, some dihedral angles, and improper dihedral angles are restrained by the corresponding terms in the CHARMM22 potential function.[138] The mainchain and sidechain dihedral angles as well as non-bonded atom pairs are restrained by statistical potentials. The energy function is optimized by a combination of conjugate gradients and molecular dynamics with simulated annealing. The loop modeling method first takes the generated model, and selects all standard residues around gaps in the alignment for additional loop modeling. An initial loop conformation is then generated by simply positioning the atoms of the loop with uniform spacing on the line that connects the mainchain carbonyl oxygen and amide nitrogen atoms of the N- and C-terminal anchor regions respectively. Next, a number of loop models are generated, each takes the initial loop conformation and randomizes it by $\pm$ 5 Å in each of the Cartesian directions. The model is then optimized thoroughly twice, firstly considering only the loop atoms and secondly with these atoms "feeling" the rest of the system. The loop optimization relies on an atomistic distance-dependent statistical potential of mean force for non-bond interactions. This loop optimization is fundamental in order to conduct a Molecular Dynamics (MD) simulation because of the need for a continuous structure.

In order to perform our MD simulations we used the MD program Gromacs-2021 and CHARM36 force fields.[139,140] The protein was solvated within a cubic box of the transferable intermolecular potential with a three-points (TIP3P) water model allowing a minimum of 10 Å marginal distance between protein and each side of the 3D box.[141] Under periodic boundary conditions implementation, the protein residues were assigned for their standard ionization states at physiological conditions (pH 7.0), and the whole complexes were

neutralized via sufficient numbers of K^+ and Cl^- ions added via Monte-Carlo ion-placing method.[142] The MD simulation was conducted over three stages and $1000 kJ/molnm^2$ force constant was used for restraining all heavy atoms and preserving original protein folding. The first stage involved initial optimization of each system geometry using 5000 iterations (5 ps) with the steepest descent algorithm. The subsequent step involved system two-staged equilibration where the system was conditioned for 100000 iterations (100 ps) at each stage. The first equilibration stage was proceeded under constant Number of particles, Volume, and Temperature (NVT) ensemble guided by the Berendsen temperature coupling method for regulating the temperature within the 3D box.[143] Subsequently, the second equilibration stage was performed under a constant Number of particles, Pressure, and Temperature (NPT) ensemble at 1 atm and 303.15 K guided by using the Parrinello-Rahman barostat.[144] Finally, the MD simulations were run for 100 ns under constant pressure (NPT ensemble) and long-range electrostatic interactions were computed using Particle Mesh Ewald (PME) algorithm.[145] Adopting such a highly accurate and rapid algorithm for treating long-range Coulomb interactions to achieve stable nanosecond trajectories within highly polar biomolecules like proteins. However, the implemented linear constraint LINCS method was used to constrain all covalent bond lengths, including hydrogens, allowing an integration time step size of 2 fs.[146] The non-bounded interactions, Coulomb (electrostatic potential), and Lennard Jones (Pauli repulsion and hydrophobic/van der Waals attractions) interactions were truncated at 10 Å using the Verlet cut-off scheme.[147] Obtained trajectories were analysed using the GROMACS built-in tools and Visual Molecular Dynamics 1.9.3 (VMD) package (the University of Illinois at Urbana-Champaign, USA) to visualise the results.

We identified from the simulation 5 centroids, using the GROMACS gmx cluster tool. The centroids represent the mean structure in a cluster of frame structures grouped by a given RMSD. The cutoff was 1.2 Å. From the 5 middle structures of the clusters, we selected the 3 most populated and we used the generated PDBs for virtual screening. Docking was carried out using GOLD 2021 2.0.[148] Binding sites were defined as the residues with at least one heavy atom within 10 Å from the peptide sequence of casp-1 contacting GSDMD-CT. No water was present in any binding site. The default docking protocol was applied and the top 3 pose in the ranking saved. The scoring function was ChemPLP. ChemPLP is the most recently introduced scoring function. This treats neutral and repulsive contacts with a piecewise linear potential (PLP). This simple potential has both an attractive and repulsive part for neutral contacts and solely a repulsive part for anti-complementary contacts. The Chemscore hydrogen bonding term is used for hydrogen bonds and the Chemscore internal energy term is also used.[149] We selected a library of commercially available compounds. The compounds were selected based on focused library of protein-protein interaction inhibitiors (iPPI) developed by Otava and Life Chemicals. Among the Otava libraries, we selected a combination of 2 focused library. These libraries were filtered by Lipinski rules but taking into account higher MW and LogP of known PPI inhibitors, MW constraints were set between 300 and 700 Da and LogP was set between 1 and 6. Number of hydrogen bond acceptors is between 0 and 10 and number of hydrogen bond donors is from 0 to 5.

iPPI Tree Library (Otava) with 1211 compounds was designed by the company with decision tree algorithm based on several molecular shape and functional group descriptors. This algorithm provides efficient partitioning between PPI inhibitors and non-PPI inhibitors.

iPPI Bayesian Library (Otava) with 2637 compounds was prepared using Bayesian modeling (ECFP6 and FCFP6 fingerprints) based on known active PPI inhibitors (IC50<100 nM) taken from TIMBAL database. A number of physico-chemical descriptors (MW, HBD, HBA, LOGP, RB, number of Rings) have been considered in each model. Final compound selection was carried out with Bayesian similarity score cut-off. Compounds with reactive groups were removed from the library.

PPI Targeted Libraries (Life Chemicals) by Receptor-based Approach. To cover relevant chemical space that includes peptidomimetic molecules, the library was not made compliant with Lipinski's Rule of Five. Each screening subset contains drug-like screening compounds free of PAINS (Pan-Assay Interference Compounds), toxic, and reactive groups that are potential PPI binders. The PPI-related molecular targets included in the company-evaluation were BCL-2, MDM2–p53, LFA1–ICAM1, αIIbβ3, IAP, BET Bromodomain, BRD9.

The poses of top-ranked compound in the virtual screening performed on the 3 clusters were manually analysed. Evaluation of the binding pose and the presence of a molecule in more than a centroids allowed to have a pool of structures for further refinement. At this preliminary step of the project compounds were filtered in order to investigate wider chemical space, so among groups of similar molecules only one were picked.

The selection of 24 compounds allowed the optimisation of the binding pose via MD, where also the dynamics and the persistence of the binding were evaluated. Simulations were run using the same parameters described before. The CHARMM force field parameters for the investigated ligands were automatically generated using the CHARMM General Force Field (CGenFF) program (ParamChem project; https://cgenff.umaryland.edu).[150] Trajectories were analysed using VMD, and the fluctuation (RMSF) is reported in scheme 6.11 under the structure of selected molecules.

Under the condition of the molecular dynamics simulations, some of the compounds confirmed the interaction with the target over the simulation time. From the Otava compounds we selected **58**, **59**, **60**, **61**, **62**, **63**, **64**, **65**, **66**, **67** and **68**, while from Life Chemicals catalogue we identified **70**, **71**, **72**, **73** and **74**. We decided to keep the peptide **57** as the reference compound for the experiments setup. To experimentally confirm the binding of the compounds and the GSDMD-CT, we performed 2 different NMR-based experiments. NMR is a powerful technique for probing and characterizing protein–ligand interactions. On the first hand, the faster approach were ligand-observed NMR sequences, were the ^{1}H spectra of the ligand is acquired in particular conditions and the signal intensity influenced by the presence of the protein in solution. These experiments do not require labelled protein. On the other hand, protein-observed experiment was acquired for some of the compounds. For this NMR sequence, ^{15}N-labelled protein is needed.

6.3.1 ligand-observed NMR screening

NMR spectroscopy detects and reveals protein-ligand interactions with a large range of affinities (10^{-9}–10^{-3} M), and is widely used in pharmaceutical research to identify hits from compound library screening in drug discovery. These experiments are based on the observation on the ligand spectra of different effects. Most common experiments rely

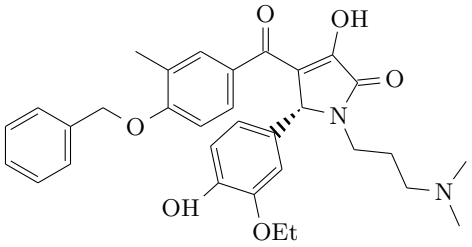

75
MW: 544.6
RMSF: 70

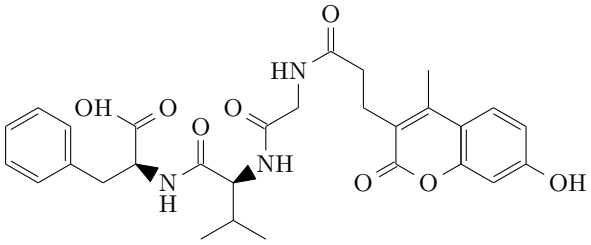

74
MW: 551.6
RMSF: 3.4

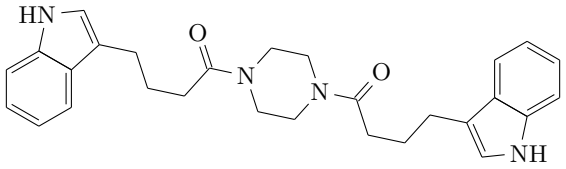

58
MW: 456.6
RMSF: 3.7

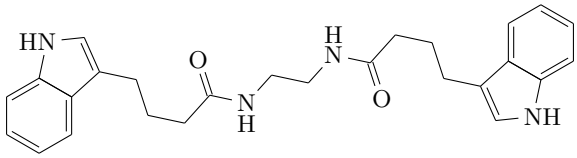

59
MW: 430.6
RMSF: 3.9

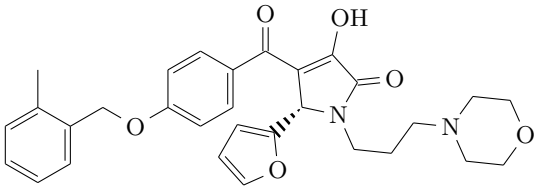

60
MW: 516.6
RMSF: 6.3

Figure 6.11 continues on next page.

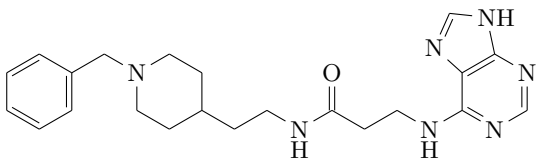

76
MW: 407.5
RMSF: 18.4

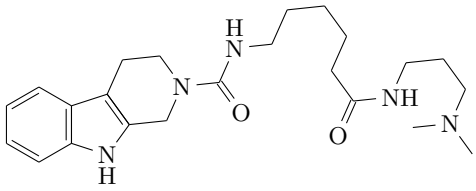

61
MW: 413.6
RMSF: 6.7

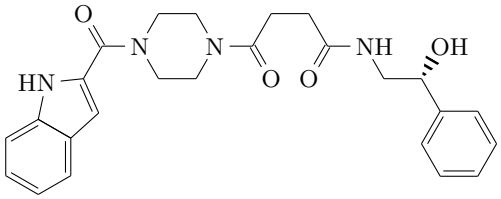

62
MW: 448.5
RMSF: 14

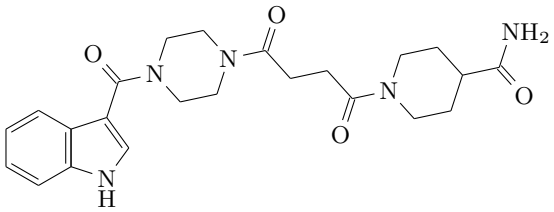

63
MW: 439.5
RMSF: 5.3

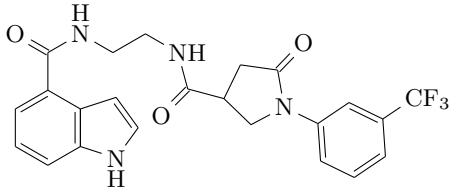

64
MW: 458.4
RMSF: 1.9

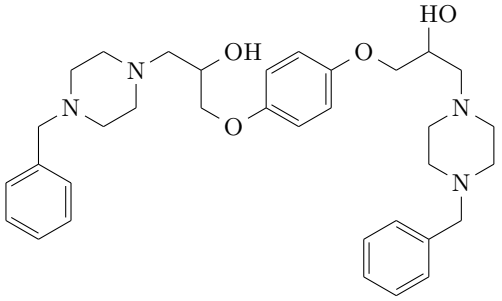

65
MW: 574.8
RMSF: 3.7

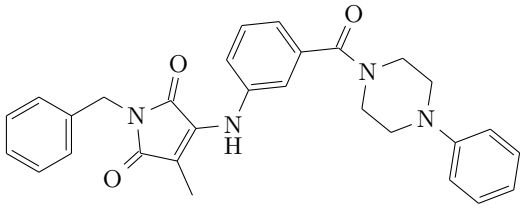

77
MW: 480.6
RMSF: 5.3

Figure 6.11 continues on next page.

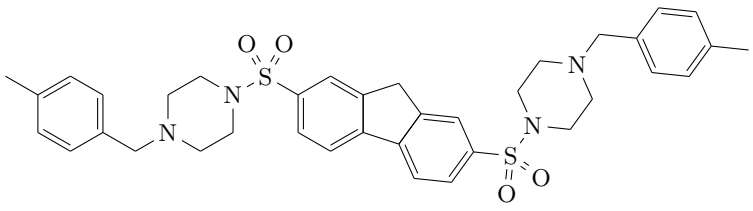

66
MW: 670.9
RMSF: 2.7

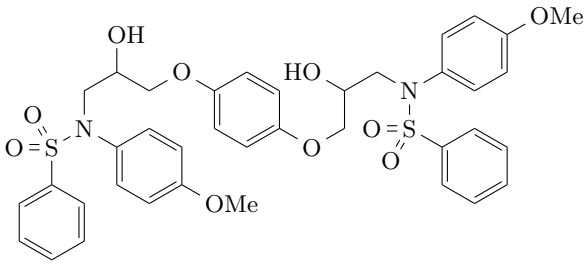

67
MW: 776.9
RMSF: 3.9

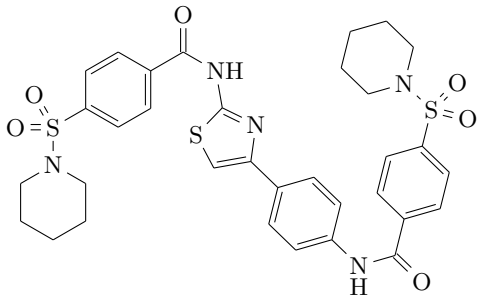

69
MW: 693.9
RMSF: 2.1

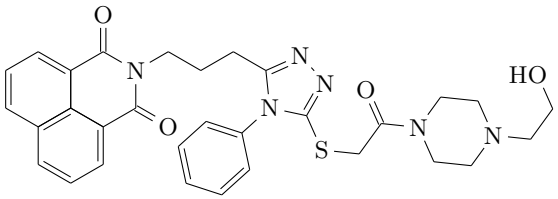

78
MW: 584.7
RMSF: 9.1

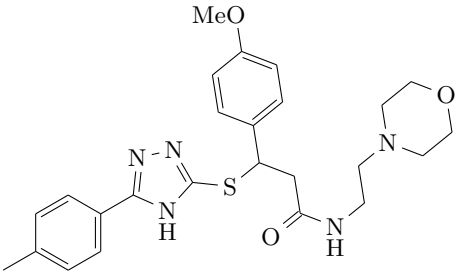

70
MW: 481.6
RMSF: 5.8

Figure 6.11 continues on next page.

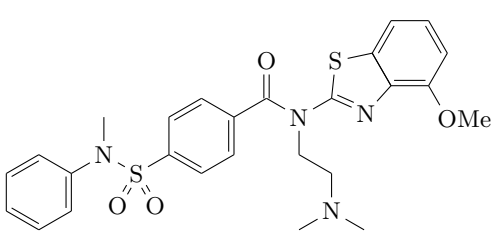

71
MW: 524.7
RMSF: 1.9

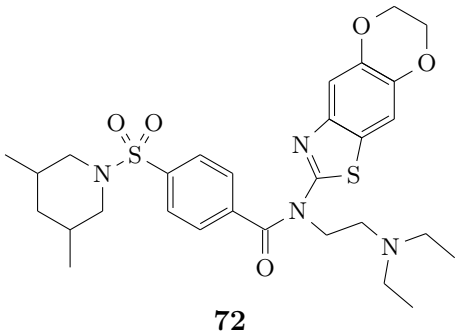

72
MW: 586.7
RMSF: 3.2

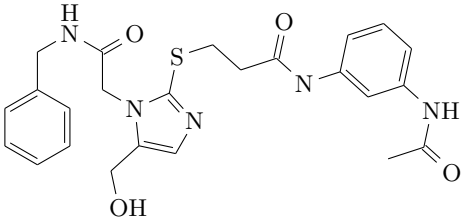

79
MW: 467.5
RMSF: 9

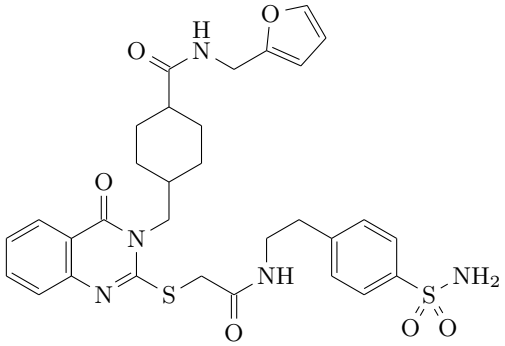

73
MW: 637.8
RMSF: 7.3

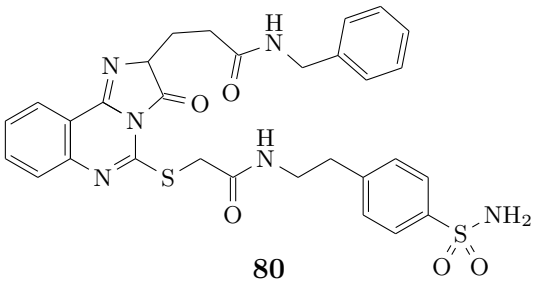

80
MW: 618.7
RMSF: 6.3

Figure 6.11: Chemical structures of compounds selected for MD complex stability evaluation.

on intermolecular magnetization transfer. In this class of experiments we highlight saturation transfer difference (STD) spectroscopy and water–ligand observed via gradient spectroscopy (WaterLOGSY) experiment. STD experiments are based on magnetization exchange from the protein-bound state to the free state of the ligand. The method consists in applying radio-frequency irradiation to selectively saturate the protein NMR signals. The saturation then spreads within the protein via the NOE and spin diffusion. In the presence of a ligand and under fast exchange conditions, the saturation will also spread to the ligand through intermolecular NOEs. Spectra are recorded with and without saturation of the protein protons. In the case of saturation *on resonance*, the signals of the compounds that bind to the protein will be saturated (and thus attenuated). By subtracting the spectrum corresponding to the receptor saturation *off resonance*, one observes only the signals of the binders, whereas the signals of the protein, non-binders, buffer, and other components are ideally subtracted.[151]

WaterLOGSY is based on the NOESY experiment, and implies transfer of magnetization via a intermolecular NOE and spin diffusion. In the experiment, the bulk water magnetization is excited and transferred during the NOESY mixing time to the bound ligand via different mechanisms. Binders interact with water via water–ligand–protein or protein–ligand complexes, whose rotational correlation times yield negative cross-relaxation rates and exhibit a negative NOE with water. By contrast, small molecules that only interact with bulk water (non-binders) will experience much faster tumbling, which translates into a positive NOE. Therefore, opposite signs for signals from free versus protein-bound ligands are observed in a WaterLOGSY spectrum, which enables one to easily discriminate binders and non-binders.[152]

In relaxation-based NMR method, the different T_2 is used to evaluate possible binding to the protein. T_2 relaxation times of large biomolecules are much shorter than those of small-molecules. Usually two spectra are measured and compared, one with CPMG spin-lock time of 10 ms (relaxation delay) and one with a CPMG spin-lock time of 200 ms. Fragments that bind can be identified from a comparison of the spectra: ligand signals of binders are weaker in the presence of the protein with longer delay.[153]

Among the described sequences, we identified STD as the most suitable in our system. The experiments were carried out at two different protein, ligand and DMSO concentration, according to the solubility of the tested compounds. Compounds were solubilised in DMSO and diluted to the desired concentration with NMR buffer. From the compounds selected with the virtual screening, a few were discarded due to solubility issue. The samples were prepared using the classical protein-ligand ratio of 1:50. Results are reported in table 6.4. Data were obtained comparing the intensity of the significant peaks between the on-resonance and off-resonance spectra. The score were calculated using the formula 6.1:

$$STDscore = \frac{I_{off} - I_{on}}{I_{off}} \cdot 100 \tag{6.1}$$

Were I_{off} is the intensity of a single peak in the off-resonance spectrum and I_{on} the intensity in the on-resonance spectrum.

The spectra elaboration represented a critical step in the process. To avoid artefacts the on-resonance spectra were manually phased and a python script written in topspin was used to copy the same phasing parameters to the corresponding off-resonance spectra. An example of spectra is reported in figure 6.12 for **71**. On the 0–2 ppm part of the

Name	Conditions	STD Score	Control
57	a	2.94	0.38
74	a	2.31	0.53
58	b	6.95	1.22
59	b	5.73	0.52
60	b	2.29	0.50
61	a	6.76	0.60
62	b	1.60	0.19
63	a	2.11	0.27
64	b	1.91	0.20
65	b	1.81	0.27
66	b	3.72	1.20
69	b	4.80	1.13
70	a	13.00	0.78
71	b	10.15	0.55
72	b	5.13	0.64
73	b	4.24	0.40
ctrl	a	1.71	0.19

Table 6.4: List of the STD scores representing the reduction in peak intensities during protein saturation (STD experiment, 2s saturation). Sample conditions: Group a) Ligand 1 mM, protein 50 µM, phosphate buffer 460.8 µL, D_2O 60 µL, 1% DMSO. Group b) Ligand 0.5 mM, protein 25 µM, phosphate buffer 534 µL, D_2O 60 µL, 10% DMSO.

spectra the presence of the protein on the background causes the misalignment of the baseline between off- and on- resonance conditions (saturation of the protein reduces its signal intensity), causing possible artefacts in the peak intensity evaluations. Peaks in this region were carefully and manually edited to avoid false positives. Control experiments were important to check possible direct and undesired saturation of the ligands. Ideally, in the absence of the protein off- and on-resonance should not vary peaks intensity.

Surprisingly, peptide **57** did not showed significant STD effect in the tested condition. From the screening, we decided to set the significant threshold around 5% of signal reduction. Compounds **58**, **59**, **61**, **70**, **71** and **72** were selected as possible binders. In particular, **70** and **71** measured the higher STD effect of respectively 13 and 10.15%. Compounds over the threshold were selected for the chemical shift titration described in the next chapter, for the identification of the aminoacids on the protein involved in the putative binding.

6.3.2 protein-observed NMR titrations

In protein-observed methods, the most typical parameter (and the easiest) to follow is the chemical shift. Chemical shift perturbations of the protein resonances observed upon ligand addition are identified to localize the ligand binding site. This enables one to immediately distinguish specific from non-specific binding. This approach requires the complete

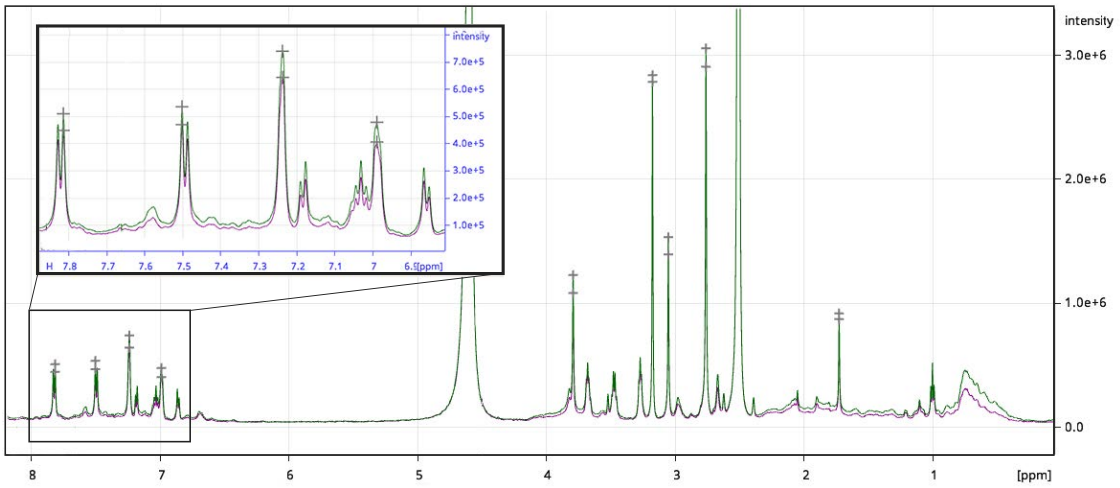

Figure 6.12: Superimposition of the spectra acquired for **71**. The off-resonance spectrum is reported in green, while the on-resonance in magenta. Peak heights are marked with the grey cross.

assignment of protein resonances. A series of ^{15}N-HSQC spectra have been acquired with increasing concentration of the ligand. We selected the peptide **57**, the best performing compounds from the STD screening (**58**, **59**, **61**, **69**, **70** and **71**), and the non binder control **147**. For the titration, protein concentration (135 µM), DMSO (10%) and pH (7.2) were accurately kept constant over the different sample, to avoid chemical shift drift caused by those aspecific factors. We used the cross-dilution strategy, adding to the protein dissolved in the buffer a solution of the ligand in DMSO, and in a second sample, the same amount of pure DMSO (0 mM and 2 mM ligand concentration). After acquisition of the NMR spectra, we mixed the two starting solution in appropriate ratio to obtain 0.5 and 1.5 mM ligand solution together with the protein. The spectra were acquired and elaborated to superimpose the 4 spectra with different ligand concentrations. Most of the peaks (see figure 6.14) did not change their chemical shifts. From a first visual inspection is possible to note the shift of some selected peaks. A better evaluation has been carried out by calculating the chemical shift perturbation factor (CSP) of each identified peak in the spectra using the formula 6.2.

$$CSP_i = \sqrt{(\Delta\delta_{Hi})^2 + \alpha(\Delta\delta_{Ni})^2} \tag{6.2}$$

where α denotes the relative weighting of chemical shift changes of the ^{15}N nuclei relative to the ^{1}H nuclei, by convention set to 0.14, and $\Delta\delta_{Hi}$ and $\Delta\delta_{Ni}$ denote the observed changes of the proton and nitrogen chemical shifts for residue i, respectively.[154] The result are represented in figure 6.13. Compounds **61** and **70** induced a higher perturbation of the chemical shift when incubated with the protein in the HSQC spectra. These shifts are related to an interaction between the ligand and the protein in solution. The higher CSP for **70** are Gly62 and Val90, wich are located on the surface of GSDMD-CT, in the hydrophobic site involved in the recognition step of casp-1 GSDMD, before the activating cleavage. These encouraging preliminary results have to be validated with point mutagenesis of

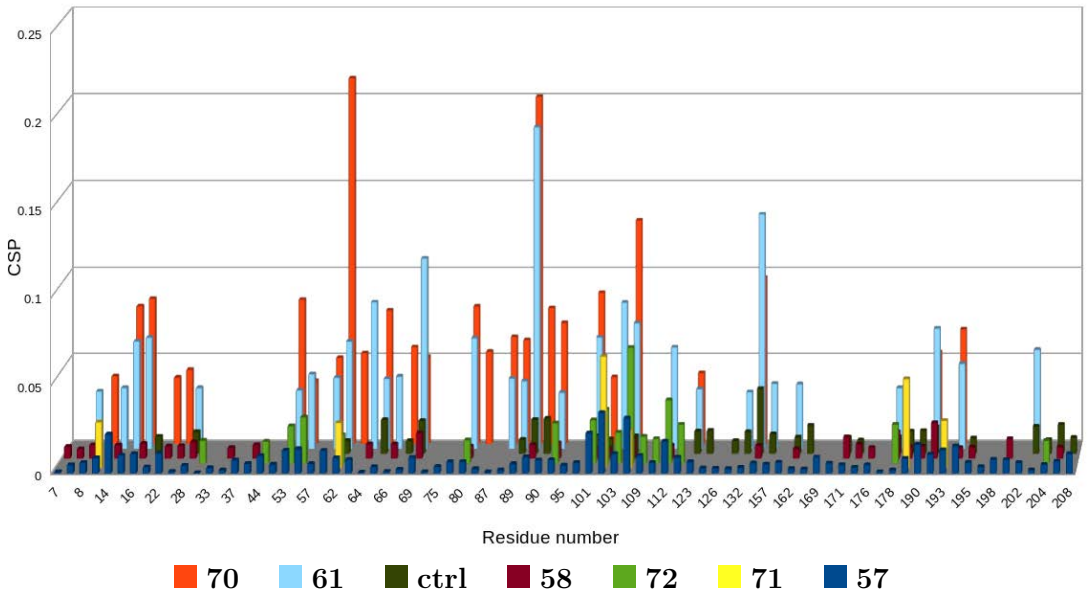

Figure 6.13: The histograms represent the hemical shift perturbations for each experiment recorded incubating the protein with a different compound. The experiments are represented using different colours.

selected residue and reacquisition of STDs and chemical shift perturbation analysis.

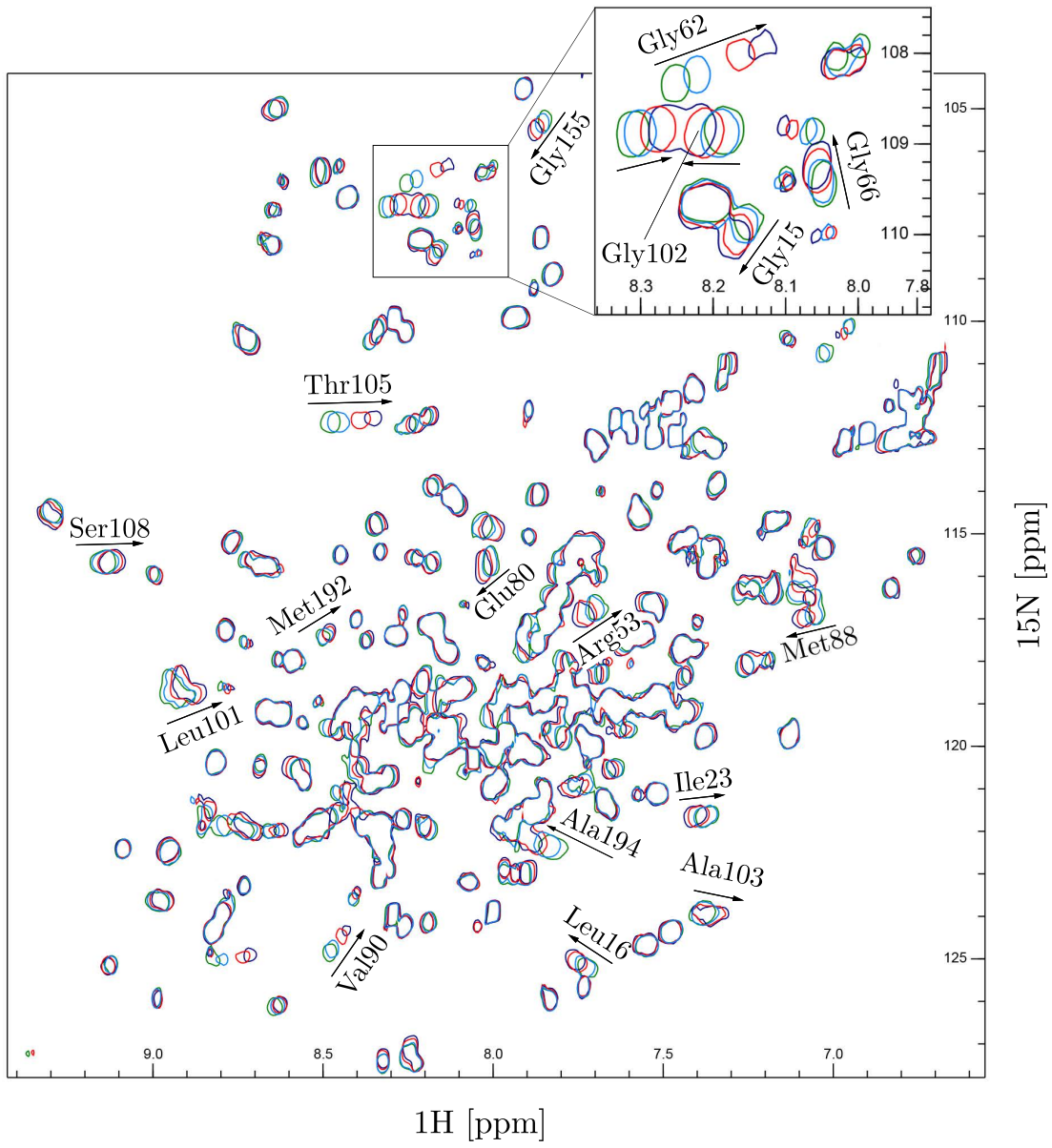

Figure 6.14: ^{15}N-HSQC of GSDMD-CT with compound **70** at increasing concentration. Green, light blue, red, and blue correspond to 0, 0.5, 1.5, and 2 mM concentration of the ligand.

Chapter 7

Conclusions

Through the synthesis of three series of derivatives, we investigated different strategy for inflammasome inhibition. From the new benzimidazol scaffold, compounds **6**, **9**, **13** and **19** were identified as promising molecular scaffold, measuring a concentration-dependent inhibition of NLRP3-mediated pyroptosis. From the piperidinamide derivatives, **26** and its derivative **35** (and the respective free carboxylic acid analogues, **24** and **36**) demonstrated a reduction of the pyroptotic cell death in the range of 30-45% at the dose of 10 µM. In particular compound **35** was selected for *in vivo* characterisation, in a mice model of inflammatory bowel disease and mild cognitive impairment. In our conditions, **35** at the oral dose of 25 and 50 mg/kg/die significantly prevented the inflammatory effects induced by colitis in mice. Furthermore, **35** prevents the cognitive decline decreases the typical markers related to neurodegenerative disease in mice model of mild cognitive impairment at the dose of 50 mg/kg. Pharmacokinetics studies are actually running to fully characterise the compound. When the central core of the molecules was replaced with an heterocycle an interesting series of molecules was synthesised. Among them **48** and **56** measured the highest inhibition of NLRP3-mediated pyroptotic cell death of the presented compounds (>70% inhibition at 10 µM). Compound **48** is currently under evaluation for the ADME profile and in *in vivo* activity towards high fat diet-induced metaflammation (metabolic-inflammation) in mice, leading to cardiovascular diseases.

During the PhD project, new studies on gasdermin-D protein were initiated. The expression and characterisation of the GSDMD-CT via solution NMR, allowed to record the main 2D and 3D spectra for the complete assignment of the protein resonances. Protein dynamics in solution were then investigated. We are focusing on the proline *cis-trans* isomers and its possible structural involvement. In particular, point mutation has been designed for the replacement of the specific Prolines. Furthermore, the proof-of-concept ligand screening identified compounds **61** and **70** able to reduce the STD signals and influence the protein resonances in the chemical shift perturbation titrations. These compounds need further analysis to be confirmed as possible binders, estimation of affinity using NMR (and MST/ITC), the validation of binding site with point mutants. Finally, the validation of the inhibitory activity using an enzymatic assay will be implemented in future work.

Chapter 8

Material and methods

8.1 Chemistry

All the reactions were monitored by Thin Layer chromatography (TLC) on Merck 60 F254 (0.25 mm) plates, which were visualised by UV inspection (254 nm) and/or by spraying KMnO4 (0.5 g in 100 mL 0.1 N NaOH). Na_2SO_4 was used as drying agent for the organic phases. Flash chromatography (FC) purifications were performed using silica gel Merck with 60 mesh particles. Unless otherwise specified, all reagents were used as received without further purification. Dichloromethane was dried over P_2O_5 and freshly distilled under nitrogen prior to use. DMF was stored over 3 Å molecular sieves. Anhydrous THF was freshly distilled under nitrogen from Na/benzophenone ketyl. ^{1}H and ^{13}C-NMR spectra were registered on JEOL ECZR600 spectrometer, at 600 and 151 MHz. Coupling constants (J) are given in Hertz (Hz) and chemical shifts (δ) are given in ppm, calibrated to solvent signal as internal standard. Following abbreviations are used to describe multiplicities: s= singlet, d = doublet, t = triplet, q = quadruplet, m = multiplet and br= broad signal. The following abbreviations are used to identify exact proton: ArH = Aromatic proton, BzImH= benzimidazolone ring, Pip = piperidine. ESI-mass spectra were recorded on a Waters Micromass Quattro Micro equipped with an ESI source. Melting points were measured with a capillary apparatus (Buchi 540). The purity of the final compounds was determined by RP-HPLC. Analyses were performed with a HP1100 chromatograph system (Agilent Technologies, Palo Alto, CA, USA) equipped with a quaternary pump (G1311A), a membrane degasser (G1379A) and a diode-array detector (DAD) (G1315B) integrated into the HP1100 system. Data analyses were processed using a HP ChemStation system (Agilent Technologies). The analytical column was a LiChrospher 100 C18-e (250 × 4.6 mm, 5 µm) (Merck KGaA, 64271 Darmstadt, Germany) eluted with CH_3CN 0.1% TFA/H_2O 0.1% TFA in a ratio that depended on the characteristics of the compound. All compounds were dissolved in the mobile phase at a concentration of about 0.01 mg/mL and injected through a 20 µL loop. HPLC retention times (tR) were obtained at flow rates of either 1.0 or 1.2 mL/min and the column effluent was monitored using the DAD. The DAD acquired the UV spectra in the range from 190 to 800 nm, and the HPLC chromatogram was recorded at 226, 254, 580 and 660 nm (with 800 nm as the reference wavelength). The purity of the test samples was evaluated as the percentage ratio between the areas of the main peak and of possible impurities at the three wavelengths, and also using a DAD

purity analysis of the chromatographic peak. The purity of all the target compounds was found to be > 95%.

8.1.1 Synthesis of target compounds

Tert-butyl 3-(2-chlorophenyl)-2-(diethoxyphosphoryl)propanoate (85): The reaction was conducted in nitrogen atmosphere. Sodium hydride (60%, 2.13 g, 21.9 eq) was added to a stirred solution of tert-butyl diethylphosphonoacetate (6.17 mL, 26.3 eq) in DMF (40 mL) at 0°C. The reaction mixture was stirred 2 h at room temperature. p-chlorobenzilbromide (2.84 mL, 21.9 eq) was added dropwise at 0°C, and the solution was stirred 2 h at room temperature. The reaction mixture was cooled to 0°C and water was added (20 mL). The solvent was reduced under reduced pressure. The residue was dissolved in diethyl ether and washed with water (2 × 10 mL), brine (15 mL), dried (Na_2SO_4) and concentrated under reduced pressure to give **85** (8.20 g, 99.7%) as a white solid.

Tert-butyl 2-(2-chlorobenzyl)acrylate (86): K_2CO_3 was dissolved in water (80 mL) and added to a stirred solution of **85** (8.25 g, 21.9 eq) and paraformaldehyde (5.25 mL, 175 eq) in water (80 mL). The reaction mixture was heated under reflux for 4 days. The mixture was cooled to room temperature and extracted with EtOAc (3 × 40 mL). The combined organic phases were washed with brine (15 mL), dried (Na_2SO_4), and concentrated under reduced pressure. The crude product was purified by silica gel chromatography (PE/EtOAc 95:5) to give **86** (4.98 g, 90.1%) as a colourless oil. Rf = 0.29 (PE/EtOAc 95:5); MS (ESI): m/z 275/277 $[M + Na]^+$; ^{1}H NMR (300 MHz, $CDCl_3$): δ = 7.36–7.15 (m, 4H, ArH), 6.17 (s, 1H, C=CHH), 5.25 (m, 1H, C=CHH), 3.71 (s, 2H, CH_2), 1.45 (s, 9H, CH3); ^{13}C NMR: (151 MHz, $CDCl_3$): δ = 166.13, 139.88, 136.94, 134.47, 130.92, 129.59, 127.85, 126.83, 125.96, 80.91, 35.47, 28.05.

1-(1-(2-(2-chlorobenzyl)acryloyl)piperidin-4-yl)-1,3-dihydro-2H-benzo[d]imida-

zol-2-one (1): Compound **86** (0.960 g, 3.80 eq) was dissolved in a stirred solution of TFA in DCM (10%, 11.0 mL) at room temperature. After 12 h, the mixture was concentrated under reduced pressure. Crude product from the previous step (0.241 g, 1.23 eq) was dissolved in a stirred solution of **81** (0.399 g, 1.84 eq), DIPEA (0.313 mL, 1.84 eq), HOBt (0.025 g,0.184 eq) and HBTU (0.813 g, 1.84 eq) in DMF (9 mL) at room temperature, and the mixture was stirred overnight. The solvent was evaporated under reduced pressure and a solution of $NaHCO_3$ 10% (15 mL) was added. The mixture was extracted with EtOAc (3 × 10 mL). The combined organic phases were washed with brine (15 mL), dried (Na_2SO_4), and concentrated under reduced pressure. The crude product was purified by silica gel chromatography (DCM/MeOH 98:2) to give **1** (0.223 g, 45.7%) as a white solid. MS (ESI): m/z 396/398 $[M + H]^+$; ^{1}H NMR (300 MHz, $CDCl_3$): δ = 10.00 (s, 1H, NH), 7.37–7.02 (m, 4H, ArH), 6.84–6.88 (m, 1H, C=CHH), 5.22–5.15 (m, 1H, C=CHH), 4.91–4.72 (m, 1H, NCHH), 4.60–4.37 (m, 1H, CH), 4.24–4.02 (m, 1H, NC'HH), 3.81 (d, J = 20.8, 2H, $ArCH_2$), 2.83–2.58 (m, 2H, NCH_2), 2.29–2.02 (m, 2H, $CHCH_2$), 1.95–1.57 (m, 2H, $CHCH_2$); ^{13}C NMR: (151 MHz, $CDCl_3$): δ = 170.54, 155.50, 141.85, 135.61, 134.94, 132.32, 130.12, 129.05, 128,90, 128.53, 127.51, 121.86, 121.38, 116.47, 110.36, 109.88, 50.88, 47.01, 41.62, 38.91, 30.30, 29.35.

General Procedure for the Preparation of Compounds 2–4: The appropriate chlorophenyl carboxylic acid (1 eq) was added to a stirred solution of CDI (1 eq) in DCM (10 mL) at room temperature. After 30 min, 1-(piperidin-4-yl)-2,3- dihydro-1,3-benzodiazol-2-one (1 eq) was added, and the mixture was stirred overnight. The mixture was washed with water (3 × 10 mL), brine (10 mL), dried (Na_2SO_4) and concentrated under reduced pressure.

1-(1-(3-(2-chlorophenyl)propanoyl)piperidin-4-yl)-1,3-dihydro-2H-benzo[d]imidazol-2-one (2): The reaction was run with **82** (0.500 g, 2.71 mmol), CDI (0.439 g, 2.71 mmol) and **81** (0.588 g, 2.71 mmol) in DCM (10 mL). The crude product was purified by silica gel chromatography (DCM/MeOH 95:5) to give **2** (0.820 g, 78.8%) as a white solid. Rf = 0.54 (DCM/MeOH 9:1); mp: 97.3–101.2°C; MS (ESI): m/z 384/386 $[M + H]^+$; ^{1}H NMR (600 MHz, $CDCl_3$): δ = 10.55 (s, 1H, NH), 7.36 (dd, J = 7.9, 1H, ArH3), 7.34 (dd, J = 7.6, 1H, ArH6), 7.24 (t, J = 7.4, 1H, ArH4), 7.19 (t, J = 7.7, 1H, ArH5), 7.18–7.04 (m, 4H, BzImH), 4.92 (d, J = 13.0, 1H, NCHH), 4.54 (tt, J = 12.4, 4.2, 1H, CH), 4.04 (d, J = 13.5, 1H, NC'HH), 3.16 (td, J = 7.9, 2.6, 2H, $ArCH_2$), 3.12 (d, J = 12.3, 1H, NCHH), 2.82–2.64 (m, 2H, $COCH_2$), 2.70 (m, 1H, NC'HH), 2.33–2.22 (m, 2H, CHCHH), 1.89 (t, J = 11.1, 2H, CHCHH).

2-1-(1-(2-chlorobenzoyl)piperidin-4-yl)-1,3-dihydro-2H-benzo[d] imidazol-2-one (3): The reaction was run with **84** (0.100 g, 0.626 mmol), CDI (0.101 g, 0.626 mmol) and **81** (0.140 g, 0.626 mmol) in DCM (5 mL). The crude product was purified by silica gel chromatography (DCM/MeOH 98:2) to give **3** (0.081 g, 36.4%) as a white solid. Rf = 0.21 (DCM/MeOH 95:5); mp: 153.6–158.8°C; MS (ESI): m/z 356/358 $[M + H]^+$; ^{1}H NMR (600 MHz, $CDCl_3$): δ = 10.48 (s, 1H, NH), 7.41 (d, J = 7.0, ArH3), 7.39 (d, J = 7.9, 1H, ArH6), 7.30 (t, J = 7.5, ArH5), 7.22 (t, J = 7.8, ArH4), 7.11–6.95 (m, 4H, BzImH), 4.90 (d, J = 13.3, 1H, NCHH), 4.56 (tt, J = 12.3, 4.2, 1H, CH), 4.05 (d, J = 13.5, NC'HH), 3.92 (m, 2H, $CHCH_2$), 3.21 (t, J = 12.6 Hz, NCHH), 2.74 (t, J = 12.4, NC'HH), 2.32–2.12 (m, 2H, $CHCH_2$), 1.85 (dd, J = 39.6, 12.4, 2H, $COCH_2$). ^{13}C NMR: (151 MHz, $CDCl_3$): δ = 166.82, 154.97, 135.75, 135.64, 130.30, 130.28, 129.75, 128.73, 127.63, 127.31, 121.50, 121.23, 109.96, 109.15, 50.42, 46.40, 41.33, 29.57, 28.86.

1-(1-(2-(2-chlorophenyl)acetyl)piperidin-4-yl)-1,3-dihydro-2H-benzo[d]imidazol-2-one (4): The reaction was run with **83** (0.100 g, 0.586 mmol), CDI (0.095 g, 0.586 mmol) and **81** (0.127 g, 0.586 mmol) in DCM (5 mL). The crude product was purified by silica gel chromatography (DCM/MeOH 95:5) to give **4** (0.176 g, 81.6%) as a white solid. Rf = 0.56 (DCM/MeOH 9:1); mp: 200.3–201.1°C; MS (ESI): m/z 370/372 $[M + H]^+$; ^{1}H NMR (600 MHz, $CDCl_3$): δ = 10.17 (d, J = 5.6, 1H, NH), 7.49–7.27 (m, 4H, ArH), 7.18–7.00 (m, 4H, BzImH), 5.04 (t, J = 15.8, 1H, NCHH), 4.60 (m, CH), 3.61 (d, J = 8.8, NC'HH), 3.35– 3.11 (m, 1H, NCHH), 2.93 (m, 1H, NC'HH), 2.64–2.22 (m, 2H, CHCHH), 2.06–1.70 (m, 2H, CHCHH). ^{13}C NMR: (151 MHz, $CDCl_3$): δ = 168.67, 155.05, 133.75, 133.23, 130.63, 129.56, 128.59, 128.48, 128.11, 127.03, 121.39, 120.97, 109.96, 109.18, 50.27, 45.62, 41.81, 29.38, 28.85.

1-(1-(2-chlorobenzyl)piperidin-4-yl)-1,3-dihydro-2H-benzo[d]imidazol-2-one (5): p-chloro benzylbromide (0.473 g, 2.301 mmol) was added to a stirred solution of **81** (0.500 g, 2.301 mmol) and TEA (0.320 mL, 2.301 mmol) in acetonitrile (10 mL). The reaction mixture was kept at room temperature for 2 h. The mixture was concentrated under reduced pressure. Next, 10% Na2CO3 solution was added (20 mL), and the product was extracted with EtOAc (3 × 25 mL). The combined organic phases were washed with brine, dried (Na_2SO_4), filtered and concentrated under reduced pressure. The crude product was purified by silica gel chromatography (DCM/MeOH 9:1) to give **5** (0.737 g, 93.7%) as a white solid. ^{1}H NMR (600 MHz, $CDCl_3$): δ =7.37 (dd, J = 7.8, 1H, ArH3), 7.31 (dd, J = 7.6, 1H, ArH6), 7.25 (t, J = 7.4, 1H, ArH4), 7.20 (t, J = 7.7, 1H, ArH5), 7.18–7.04 (m, 4H, BzImH), 4.33 (d, J = 13.0, 2H, NCHH), 4.54 (tt, J = 12.4, 4.2, 1H, CH), 3.66 (s,2H, $ArCH_2$), 2.91 (d, J = 12.3, 2H, NCHH),2.33–2.22 (m, 2H, CHCHH), 1.89 (t, J = 11.1, 2H, CHCHH).

1-[3-(2-chlorophenyl)propanol]pyrrolidine-2,5-dione (82a): DCC (0.335 g, 1.625 mmol) and N-hydroxysuccinimide (0.317 g, 2.76 mmol) were added to a stirred solution of 3-(2-chlorophenyl)propanoic acid (0.300 g, 1.625 mmol) in dry THF (7 mL) at 0°C. The reaction mixture was kept at 0°C for 10 min, then stirred at room temperature overnight. The mixture was filtered (3 times) to remove the white solid (DCU), diluted with water (15 mL) and extracted with EtOAc (3 × 15 mL). The combined organic phases were washed with brine (20 mL), dried (Na_2SO_4), filtered and concentrated under reduced pressure. The product was purified by silica gel chromatography (DCM) to give **82a** (0.325 g, 71.1%) as a white solid. Rf = 0.67 (DCM); ^{1}H NMR (300 MHz, $CDCl_3$) δ= 7.31–7.16 (m, ArH), 3.07 (m, 2H, $COCH_2$), 2.08 (s, 2H, $ArCH_2$), 2.72 (s, 4H, $COCH_2CH_2CO$).

General Procedure for the Preparation of Compounds 87 and 88: To a stirred solution of **82a** (1 mmol) in DMF (10 mL), the appropriate amine (1 mmol) and the appropriate base (2 mmol) were added at room temperature. When the reaction was complete (TLC), the mixture was concentrated under reduced pressure. Next, 10% Na2CO3 solution was added (20 mL), and the product was extracted with EtOAc (3 × 25 mL). The combined organic phases were washed with brine, dried (Na_2SO_4), filtered and concentrated under reduced pressure.

Methyl 4-(3-(2-chlorophenyl)propanamido)butanoate (88): The reaction was run with **82a** (0.500 g, 1.77 mmol), methyl 4-aminobutyrate hydrochloride (0.545 g, 3.54 mmol) and triethylamine (0.742 mL, 5.33 mmol) in DMF (6 mL). The crude product was purified by silica gel chromatography (DCM/MeOH 98:2) to give **88** (0.210 g, 41.7%) as a colourless oil. Rf = 0.21 (DCM/MeOH 98:2); MS (ESI): m/z 284/286 $[M + H]^+$; ^{1}H NMR (600 MHz, $CDCl_3$): δ = 7.36–7.14 (m, 4H, ArH), 7, 5.31 (d, J = 0.9, 1H, NH), 3.68 (s, 3H, CH3), 3.27 (q, J = 6.4, 2H, $NHCH_2$), 3.09 (t, J = 7.7, 2H, $ArCH_2$), 2.50 (t, J = 7.6, 2H, $NCOCH_2$), 2.30 (t, J = 7.1, 2H, $OCOCH_2$), 1.79 (p, J = 7.0, 2H, $CH_2CH_2CH_2$).

Ethyl (3-(2-chlorophenyl)propanoyl)glycinate (87): The reaction was run with **82a** (0.156 g, 0.843 mmol), glycine ethyl ester hydrochloride (0.118 g, 0.843 mmol) and triethylamine (0.118 mL, 0.843 mmol) in DMF (3 mL). The crude product was purified

by silica gel chromatography (DCM/MeOH 98:2) to give **87** (0.185 g, 97%). Rf = 0.81 (DCM/MeOH 95:5). ^{1}H NMR (600 MHz, $CDCl_3$): δ = 7.31–7.16 (m, 4H, ArH), 4.09–4.16 (m, 4H), 2.95 (t, J = 7.6, 2H, $ArCH_2$), 1.21 (t, J = 7.8, 3H).

(3-(2-chlorophenyl)propanoyl)glycine (89): Compound **88** (0.185, 0.700 mmol) was dissolved in a stirred solution of aqueous NaOH (2.5 N, 0.730 mL) in EtOH (3 mL). After 2 h, a solution of HCl was added (5 N, 1 mL) and the solvent was evaporated under reduced pressure. The residue was suspended in HCl 0.5 N (10 mL) and filtered to give **89** as a white solid (0.061 g, 36%). ^{1}H NMR (600 MHz, $CDCl_3$): δ = 7.61 (d, J = 7.2, 1H), 7.45–7.10 (m, 3H, ArH), 4.09 (s, 2H, $NHCH_2$), 2.95 (t, J = 7.6, 2H, $ArCH_2$), 2.22 (t, J = 7.6, $NCOCH_2$); ^{13}C NMR: (151 MHz, $CDCl_3$): δ = 176.90, 173.21, 146.87, 133.12, 129.10, 128.31, 128.16, 127.03, 42.79, 35.81, 29.15.

4-(3-(2-chlorophenyl)propanamido)butanoic acid (90): Compound **88** (0.210, 0.740 mmol) was dissolved in a stirred solution of aqueous NaOH (2.5 N, 0.770 mL) in MeOH (15 mL). After 12 h, the mixture's pH was brought to 2 with a solution of HCl (5 N), and the methanol was evaporated under reduced pressure. The acidic aqueous phase was extracted with DCM (4 × 15 mL). The combined organic phases were washed with brine (10 mL), dried (Na_2SO_4) and concentrated under reduced pressure. The crude product was purified by silica gel chromatography (DCM/MeOH 95:5) to give **90** (0.149 g, 74.5%) as a white solid. Rf = 0.15 (DCM/MeOH 95:5); MS (ESI): m/z 268/270 $[M + H]^+$; ^{1}H NMR (600 MHz, $CDCl_3$): δ = 7.45–6.97 (m, 4H, ArH), 4.87 (s, 1H, NH), 3.09 (t, J = 6.8, 2H, $NHCH_2$), 2.95 (t, J = 7.6, 2H, $ArCH_2$), 2.41 (t, J = 7.6, $NCOCH_2$), 2.04 (t, J = 7.3, 2H, $OCOCH_2$), 1.62 (p, J = 7.1, $CH_2CH_2CH_2$); ^{13}C NMR: (151 MHz, $CDCl_3$): δ = 175.90, 173.80, 138.57, 133.85, 130.76, 129.53, 128.06, 127.19, 38.71, 35.86, 31.15, 29.65, 24.75.

General Procedure for the Preparation of Compounds 91 and 6–8: To a stirred solution of the appropriate carboxylic acid (1 mmol) in DMF (2 mL), DIPEA (2 mmol), HOBt (0.15 mmol), HBTU (1.5 mmol) and the appropriate amine (1.1 mmol) were added at room temperature and the mixture was stirred overnight. The solvent was evaporated under reduced pressure and a solution of $NaHCO_3$ 10% (20 mL) was added. The mixture was extracted with EtOAc (3 × 20 mL). The combined organic phases were washed with brine (15 mL), dried (Na_2SO_4) and concentrated under reduced pressure.

Tert-butyl N-3-oxo-3-[4-(2-oxo-2,3-dihydro-1,3 benzodiazol-1-yl)piperidin 1 yl] propyl carbamate (91): The reaction was run using Boc-β-alanine (0.287 g, 1.52 mmol), DIPEA (0.70 mL, 4.14 mmol), HOBt (0.028 g, 0.21 mmol), HBTU (0.915 g, 2.07 mmol) and 1-(piperidin-4-yl)- 2,3-dihydro-1,3-benzodiazol-2-one (0.300 g, 1.38 mmol) in DMF (5 mL). The crude product was purified by silica gel chromatography (PE/EtOAc/MeOH, 7:2.5:0.5) to give **91** (0.330 g, 61.5%) as a white foam. Rf = 0.22 (petroleum ether/EtOAc/MeOH 7:2:1); MS (ESI): m/z 389/391 $[M + H]^+$; ^{1}H NMR (600 MHz, $CDCl_3$): δ = 10.12 (s, 1H, BzImNH), 7.16–7.01 (m, 4H, ArH), 4.85 (d, J = 12.5, 1H, PipNCHH), 4.53 (tt, J = 12.4, 4.1, 1H, CH), 4.01 (q, J = 12.7, 1H PipNC'HH), 3.47 (t, J = 5.2, 2H, $NHCH_2$), 3.18 (t, J = 12.5, 1H, PipNCHH), 2.69 (t, J = 12.6, 1H, PipNC'HH), 2.60 (dt, J = 10.9, 5.6, 2H,

$COCH_2$), 2.48–2.21 (m, 2H, $CHCH_2$), 1.90 (m, 2H, $CHCH_2$), 1.43 (s, 9H, CH3); ^{13}C NMR (151 MHz, $CDCl_3$): δ = 170.20, 156.21, 155.04, 128.88, 128.11, 121.63, 121.35, 110.06, 109.32, 79.35, 50.72, 45.08, 41.45, 36.59, 33.59, 29.73, 28.99, 28.52.

3-(2-chlorophenyl)-N-(2-oxo-2-(4-(2-oxo-2,3-dihydro-1H-benzo[d]imidazol-1-yl) piperidin-1-yl) ethyl)propenamide (6): The reaction was run with **89** (0.061 g, 0.252 mmol), **81** (0.60 g, 0.277 mmol), HBTU (0.167 g, 0.378 mmol), HOBt (0.034 g, 0.025 mmol) and DIPEA (0.129 mL, 0.756 mmol) in DMF (3 mL). The crude product was purified by silica gel chromatography (DCM/MeOH, 95:5) to give **6** as a white solid (0.100 g, 89.8%). Rf = 0.23 (DCM/MeOH 95:5); MS (ESI): m/z 441/443 $[M + H]^+$; ^{1}H NMR (600 MHz, $CDCl_3$): δ = 9.81 (s, 1H, BzImNH), 7.21–7.00 (m, 4H, ArH), 7.02–6.96, (m, 4H, BzImH), 4.85 (d, J = 12.5, PipNCHH), 4.47 (tt, J = 12.2, 4.0, CH), 4.21 (d, J = 8.1, $NHCH_2$), 3.95 (d, J = 12.5, 1H, PipNC'HH), 3.13 (t, J = 12.0, 1H, PipNCHH), 3.07–3.03 (m, 2H, $ArCH_2$), 2.65 (t, J = 12.0, 1H, PipNC'HH), 2.57–2.51 (m, 2H, CHCHH), 2.48 (t, J = 7.8, 2H, $NHCOCH_2$), 2.38–2.23 (m, 2H, CHCHH), ^{13}C NMR: (151 MHz, $CDCl_3$): δ = 172.37, 170.30, 155.80, 154.92, 138.50, 134.02, 130.81, 129.65, 128.99, 127.91, 127.03, 121.70, 121.43, 110.03, 109.25, 50.83, 45.15, 41.55, 40.73, 36.33, 29.80, 29.71, 29.00.

3-(2-chlorophenyl)-N-3-oxo-3-[4-(2-oxo-2,3-dihydro-1,3-benzodiazol-1-yl)piperidin-1-yl] propyl propanamide (7): The reaction was run with **82** (0.093 g, 0.506 mmol), **92** (0.224 g, 0.557 mmol), HBTU (0.336 g, 0.759 mmol), HOBt (0.007 g, 0.051 mmol) and DIPEA (0.258 mL, 1,52 mmol) in DMF (5 mL) at room temperature. The crude product was purified by silica gel chromatography (DCM/MeOH, 95:5) to give **7** as a white solid (0.142 g, 58.2%). Rf = 0.43 (DCM/MeOH 9:1); mp: 114.7–116.2°C; MS (ESI): m/z 455/457 $[M + H]^+$; ^{1}H NMR (600 MHz, $CDCl_3$): δ = 9.85 (s, 1H, BzImNH), 7.25–7.21 (m, 1H, ArH3), 7.18–7.16 (m, 1H, ArH6), 7.08–7.05 (m, 2H, ArH4-5), 7.07–6.93, (s, 4H, BzImH), 4.82 (d, J = 12.6, 1H, PipNCHH), 4.50 (tt, J = 12.3, 4.1, 1H, CH), 3.97 (d, J = 12.5, 1H, PipNC'HH), 3.65–3.49 (m, 2H, $NHCH_2$), 3.16 (t, J = 12.1, 1H, PipNCHH), 3.08 (t, J = 7.8, 2H, $ArCH_2$), 2.69 (t, J = 12.2, 1H, PipNC'HH), 2.58 (dd, J = 9.7, 4.9, 2H, CHCHH), 2.52 (t, J = 7.7, 2H, $NHCOCH_2$), 2.41–2.24 (m, 2H, CHCHH), 1.90 (t, J = 10.8, 2H, $NCOCH_2$); ^{13}C NMR: (151 MHz, $CDCl_3$): δ = 172.32, 170.26, 155.75, 154.88, 138.44, 133.98, 130.74, 129.58, 128.94, 127.83, 126.95, 121.65, 121.38, 109.98, 109.15, 50.72, 45.05, 41.51, 36.26, 35.23, 33.03, 29.73, 29.64, 28.96.

3-(2-chlorophenyl)-N-(4-oxo-4-(4-(2-oxo-2,3-dihydro-1H-benzo[d]imidazol-1-yl) piperidin-1-yl)butyl)propenamide (8): The reaction was run with **90** (0.149 g, 0.551 mmol), **81** (0.132 g, 0.606 mmol), HBTU (0.366 g, 0.824 mmol), HOBt (0.011 g, 0.083 mmol) and DIPEA (0.280 mL, 1.65 mmol) in DMF (5 mL). The crude product was purified by silica gel chromatography (DCM/MeOH 95:5) to give as a rose foam. The product was recrystalised from iPrOH (2 mL) by adding dropwise (iPr)2O to obtain **8** (0.149 g, 74.5%) as a white solid. Rf = 0.51 (DCM/MeOH 9:1); MS (ESI): m/z 467/469 $[M-H]^+$; ^{1}H NMR (600 MHz, $CDCl_3$): δ = 9.95 (s, 1H, BzImNH), 7.43–6.90 (m, 8H, ArH), 4.84 (m, 1H, PipNCHH), 4.49 (t, J = 12.3, CH), 4.01 (m, 1H, PipNC'HH), 3.32 (t, J = 5.8,1H, PipNCHH), 3.18 (m, 2H, $NHCH_2$), 3.09 (t, J = 7.5, 1H, PipNCHH), 2.68 (m, 2H, $ArCH_2$), 2.56 (d, J = 5.9, 2H, CHCHH), 2.44 (m, 2H, $NHCOCH_2$), 2.33 (m, 2H,

$NCOCH_2$), 1.88 (m, 2H, CHCHH), 1.21 (m, 2H, CCH_2C); 13C NMR: (151 MHz, $CDCl_3$): δ = 174.82, 173.25, 156.27, 139.64, 134.93, 131.79, 130.57, 130.53, 129.66, 129.11, 128.22, 122.64, 122.39, 110.58, 52.18, 46.39, 42.65, 39.92, 36.89, 31.26, 30.69, 30.66, 29.95, 26.18.

1-[1-(3-aminopropanoyl)piperidin-4-yl]-2,3-dihydro-1,3-benzodiazol-2-one trifluoroacetate salt (92): Compound **91** (0.330 g, 0.849 mmol) was added to a stirred solution of trifluoracetic acid (0.5 mL, 2,94 mmol) in DCM (5 mL). The reaction mixture was kept at r.t. for 6 h. The solvent was evaporated under reduced pressure and washed 5 times with DCM to strip all the trifluoracetic acid. The residue was dried under reduced pressure to give **92** (0.342 g, 100%) as a white foam. The product was very hygroscopic and, within a few minutes, it became a sticky yellow semisolid. Rf = 0.23 (DCM/MeOH 9:1).

General Procedure for the Preparation of Compounds 97 and 98: p-fluoronitro benezene (1 mmol) was dissolved in a stirred solution of N-Boc alchildi amine (1.1 mmol) and a suspension of fine-powdered K_2CO_3 (2 mmol) in dry DMF under nitrogen gas. The reaction mixture was kept at 70°C overnight. The mixture was concentrated under reduced pressure. Brine (20 mL) was added and the product was extracted with EtOAc. The combined organic phases were washed with brine (15 mL), dried (Na_2SO_4) and concentrated under reduced pressure.

Tert-butyl (3-((2-nitrophenyl)amino)propyl)carbamate (97): The reaction was run with p-fluoro nitrobenezene (0.310 mL, 3.04 mmol), **95** (0.582 g, 3.34 mmol) and K_2CO_3 (0.923 g, 6.68 mmol) in dry DMF under nitrogen gas. The crude product was purified by silica gel chromatography (PE/EtOAc 8:2) to give **97** (0.752 g, 94%) as an orange solid. Rf = 0.22 (PE/EtOAc 8:2); MS (ESI): m/z 496/498 $[M + H]^+$; ^{1}H NMR (300 MHz, $CDCl_3$): δ = 8.15 (d, J = 1.4, 1H, ArH3), 8.05 (s, 1H, ArNH), 7.43 (t, J = 11.4, 1H, ArH5), 6.86 (d, J = 8.6, 1H, ArH6), 6.64 (t, J = 7.8, 1H, ArH4), 4.75 (s, 1H, CONH), 3.30 (dd, J = 12.8, 6.4, 2H, $ArNHCH_2$), 3.20 (q, J = 6.6, 2H, $CONHCH_2$), 1.92 (p, J = 6.8, 2H, CCH_2C), 1.44 (s, 9H, CH3).

Tert-butyl (3-((2-nitrophenyl)amino)ethyl)carbamate (97): The reaction was run with p-fluoroni trobenezene (0.341 mL, 3.24 mmol), **96** (0.675 g, 4.21 mmol) and K_2CO_3 (1.12 g, 8.10 mmol) in dry DMF under nitrogen gas. The crude product was purified by silica gel chromatography (PE/EtOAc 9:1) to give 41 (0.740 g, 81.1%) as an orange solid. Rf = 0.19 (PE/EtOAc 8:2); ^{1}H NMR (300 MHz, $CDCl_3$): δ = 8.18 (d, J = 1.5, 1H, ArH3), 8.05 (s, 1H, ArNH), 7.45 (t, J = 8.6, 1H, ArH5), 6.94 (d, J = 8.6, 1H, ArH6), 6.68 (t, J = 7.8, 1H, ArH4), 4.82 (s, 1H, CONH), 3.59–3.33 (m, 4H, NCH_2), 1.42 (m, 11H, CCH_2C, CH3).

General Procedure for the Preparation of Compounds 99 and 100 The appropriate p-nitroaniline derivatives (1 mmol) were dissolved in a stirred suspension of Pd/C (10%, 0.1 mmol) in the reaction solvent. The reaction mixture was kept overnight under hydrogen atmosphere (1 atm). The suspension was filtered and concentrated under reduced pressure.

Tert-butyl (3-((2-aminophenyl)amino)propyl)carbamate (99): The reaction was run with **97** (0.727 g, 2.46 mmol) and Pd/C (10%, 0.073 g) in MeOH (10 mL) under atmospheric H_2. The crude product was purified by silica gel chromatography (PE/EtOAc 7:3) to give **99** (0.553 g, 85.0%) as a violet solid. Rf = 0.24 (PE/EtOAc 1:1); ^{1}H NMR (300 MHz, $CDCl_3$): δ = 6.90–6.60 (m, 4H, ArH), 4.71 (s, 1H, ArNHC), 3.41 (s, 2H, $ArNH_2$), 3.30 (dd, J = 12.8, 6.4, 2H, $CONHCH_2$), 3.20 (t, J = 6.6, 2H, $ArNHCH_2$), 1.85 (p, J = 6.6, 2H, CCH_2C), 1.47 (s, 9H, CH3); ^{13}C NMR: (75 MHz, $CDCl_3$): δ = 156.56, 137.85, 134.82, 120.97, 119.11, 116.89, 112.30, 79.75, 41.87, 38.78, 30.16, 28.82.

Tert-butyl (3-((2-aminophenyl)amino)ethyl)carbamate (100): the reaction was run with **98** (0.740 g, 2.63 mmol) and Pd/C (10%, 0.073 g) in dry THF (10 mL) under atmospheric H_2. The crude product was purified by silica gel chromatography (PE/EtOAc 7:3) to give **100** (0.560 g, 85.0%) as a violet solid. Rf = 0.29 (PE/EtOAc 1:1).

General Procedure for the Preparation of compounds 101 and 102: The appropriate p-diaminobenzene (1 mmol) derivatives were added to a stirred solution of CDI (1.1 mmol) in THF. The reaction was kept at room temperature overnight. The reaction mixture was concentrated under reduced pressure. The residue was dissolved in DCM and washed with water (2 × 15 mL), with brine (15 mL), dried (Na_2SO_4) and concentrated under reduced pressure.

Tert-butyl (3-(2-oxo-2,3-dihydro-1H-benzo[d]imidazol-1-yl)propyl) carbamate (101): The reaction was run with **99** (0.538 g, 2.03 mmol) and CDI (0.365 g, 2.25 mmol) in THF (45 mL). The crude product was purified by silica gel chromatography (DCM/MeOH 98:2 and PE/EtOAc 6:4) to give **101** (0.385 g, 65.3%) as a dark yellow solid. Rf = 0.12 (PE/EtOAc 1:1); MS (ESI): m/z 292 $[M + H]^+$; ^{1}H NMR (300 MHz, $CDCl_3$): δ = 10.55 (s, 1H, BzImNH), 7.22–6.95 (m, 4H, ArH), 5.57 (s, 1H, NH), 4.01 (t, J = 6.4, 2H NCH_2), 3.16 (dd, J = 12.3, 6.2, 2H, $NHCH_2$), 1.94 (p, J = 6.4, 2H, CCH_2C), 1.47 (s, 9H, CH3); ^{13}C NMR: (75 MHz, $CDCl_3$): δ = 156.61, 156.61, 130.28, 128.55, 122.16, 121.86, 110.29, 108.29, 79.56, 38.14, 37.39, 28.85, 28.58.

Tert-butyl (3-(2-oxo-2,3-dihydro-1H-benzo[d]imidazol-1-yl)ethyl)carbamate (102): The reaction was run with **100** (0.568 g, 2.23 mmol) and CDI (0.361 g, 2.23 mmol) in THF (10 mL). The crude product was purified by silica gel chromatography (PE/EtOAc 6:4 to 5:4.5:0.5) to give **102** (0.292 g, 47.3%) as a white solid. Rf = 0.58 (DCM/MeOH 9:1); MS (ESI): m/z 278 [MH+]; ^{1}H NMR (300 MHz, $CDCl_3$): δ = 9.59 (s, 1H, BzImNH), 7.43–6.90 (m, 4H, ArH), 4.11 (q, J = 7.1, 2H, NCH_2), 3.09 (t, J = 7.5, 2H, $NHCH_2$), 1.21 (s, 9H, CH3); ^{13}C NMR: (75 MHz, $CDCl_3$): δ = 156.17, 155.76, 130.70, 127.91, 121.74, 121.63, 109.57, 108.21, 79.60, 40.56, 39.70, 28.52.

1-(3-aminopropyl)-1,3-dihydro-2H-benzo[d]imidazol-2-one (103): Compound **101** (0.292 g, 1.05 mmol) was dissolved in a stirred solution of TFA/DCM (10%, 5.5 mL) at room temperature. After 4 h, the reaction mixture was concentrated under reduced pressure to give **103** (0.191 g, 62.5%) as a white foam. MS (ESI): m/z 192 $[M + H]^+$; ^{1}H

NMR (300 MHz, $CDCl_3$): δ = 7.12–7.02 (m, 4H, ArH), 3.85 (t, J = 6.7, NCH_2), 2.90 (m, 2H, NH_2CH_2), 1.99 (m, 2H, CCH_2C).

1-(3-aminoethyl)-1,3-dihydro-2H-benzo[d]imidazole-2-one (104): Compound **102**
(0.337 g, 1.16 mmol) was dissolved in a stirred solution of TFA/DCM (10%, 8.8 mL) at room temperature. After 3 h, the reaction mixture was concentrated under reduced pressure to give **104** (0.191 g, 62.5%) as a white-yellow foam. ^{1}H NMR (600 MHz, MeOD): δ = 7.16–7.05 (m, 4H, ArH), 4.17 (t, J = 5.9, 2H, NCH_2), 3.30 (dd, J = 11.0, 5.0, 2H, NH_2CH_2). ^{13}C NMR: (75 MHz, MeOD): δ = ^{13}C NMR (151 MHz, MeOD) δ 155.87, 129.76, 128.57, 121.96, 121.38, 109.44, 107.52, 38.41, 38.19.

General Procedure for the Preparation of Compounds 9 and 10: To a stirred solution of **82a** (1 mmol) in DMF (10 mL), the appropriate amine (1 mmol) and the appropriate base (2 mmol) were added at room temperature. When the reaction was complete (TLC), the mixture was concentrated under reduced pressure. Na2CO3 10% solution was added (20 mL), and the product was extracted with EtOAc (3 × 25 mL). The combined organic phases were washed with brine, dried (Na_2SO_4), filtered and concentrated under reduced pressure.

3-(2-chlorophenyl)-N-(2-(2-oxo-2,3-dihydro-1H-benzo[d]imidazol-1-yl)ethyl) propanamide (9): The reaction was run with **82a** (0.100 g, 0.354 mmol), **104** (0.097 g, 0.354 mmol) and DIPEA (0.088 mL, 0.532 mmol) in DMF (3 mL). The crude product was purified by silica gel chromatography (DCM/MeOH 95:5) to give **9** (0.118 g, 86.4%) as a white solid. Rf = 0.21 (DCM/MeOH 95:5); MS (ESI): m/z 366/368 [M+Na]+ ; ^{1}H NMR (300 MHz, $CDCl_3$): δ = 10.75 (s, 1H, BzImNH), 7.97 (t, J = 5.9, 1H, ArH), 7.35–6.83 (m, 7H, ArH), 3.99 (s, 1H, NH), 3.71 (t, J = 6.1, 2H, NCH_2), 3.22–3.16 (m, 2H, $NHCH_2$), 2.72 (t, J = 7.2, 2H, $ArCH_2$), 2.17 (t, J = 7.0, 2H); 13C NMR: (75 MHz, $CDCl_3$): δ = 172.17, 155.09, 139.40, 133.68, 131.42, 131.30, 130.03, 129.11, 128.82, 128.14, 121.56, 121.29, 109.56, 108.32, 40.31, 38.10, 35.79, 29.44.

3-(2-chlorophenyl)-N-(3-(2-oxo-2,3-dihydro-1H-benzo[d]imidazol-1-yl)propyl) propanamide (10): The reaction was run with **82a** (0.130 g, 0.458 mmol), **104** (0.140 g, 0.458 mmol) and DIPEA (0.116 mL, 0.687 mmol) in DMF (5 mL). The crude product was purified by silica gel chromatography (DCM/MeOH 97:3) to give **10** (0.141 g, 85.9%) as a white solid. Rf = 0.27 (DCM/MeOH 98:2); MS (ESI): m/z 358/360 [MH+]; ^{1}H NMR (300 MHz, $CDCl_3$): δ = 10.40 (s, 1H, BzImNH), 7.26–6.90 (m, 8H, ArH), 4.73 (s, 1H, NH), 3.73 (t, J = 5.9, $NHCH_2$), 3.13 (m, 2H, NCH_2), 3.05 (m, 2H, $COCH_2$); 2.52 (t, J = 7.7, 2H, $ArCH_2$), 1.79 (m, 2H, CCH_2C); ^{13}C NMR: (75 MHz, $CDCl_3$): δ = 172.83, 156.50, 138.64, 134.30, 131.17, 130.09, 129.93, 128.42, 128.23, 127.32, 122.41, 122.07, 110.38, 108.34, 37.88, 36.69, 36.02, 30.24, 27.81.

Tert-butyl 2-oxo-2,3-dihydro-1H-benzo[d]imidazole-1-carboxylate (105a) Benzimidazolone (2.5 g, 18.6 mmol) was dissolved in dry DMF (45 mL) under nitrogen atmosphere. NaH (60%, 0.818 g, 20.5 mmol) was added portionwise to the solution at 0°C.

(Boc)2O (0.406 g, 18.6 mmol) was dissolved in DMF (10 mL) and added dropwise in the reaction mixture and stirred at room temperature overnight. The mixture was concentrated under reduced pressure. Water (100 mL) was added, and the product was extracted with EtOAc (5 × 50 mL). The combined organic phases were washed with brine (15 mL), dried (Na_2SO_4) and concentrated under reduced pressure. The residue was purified by silica gel chromatography (PE/EtOAc 7:3) to give **105a** (3.74 g, 85.9%) as a white solid. Rf = 0.21 (PE/EtOAc 1:1); ^{1}H NMR (600 MHz, $CDCl_3$): δ = 10.45 (s, 1H, BzImNH), 7.25–6.85 (m, 4H, BzImH), 1.45 (s, 9H, CH3). ^{13}C NMR: (75 MHz, $CDCl_3$): δ = 158.85, 155.79, 130.14, 128.11, 122.13, 121.58, 110.09, 107.95, 82.89, 28.09.

Tert-butyl 3-(3-bromopropyl)-2-oxo-2,3-dihydro-1H-benzo[d]imidazole-1-carboxylate (105): Compound **105a** (1.00 g, 4.27 mmol) was added to a stirred solution of dibromopropane (4.35 mL, 42.7 mmol), fine-powdered K_2CO_3 (2.95 g, 21,35 mmol) and KI (0.070 g, 0.425 mmol) in ACN (20 mL). The reaction mixture was kept at room temperature overnight. The solvent was evaporated under reduced pressure, saturated NH4Cl (20 mL) was added and the product was extracted with DCM (6 × 20 mL). The combined organic phases were washed with brine (15 mL), dried (Na_2SO_4) and concentrated under reduced pressure. The residue was purified by silica gel chromatography (PE/EtOAc 9:1) to give **105** (0.998 g, 66.2%) as a white solid. Rf = 0.57 (PE/EtOAc 7:3); ^{1}H NMR (600 MHz, $CDCl_3$): δ = 7.82 (d, J = 7.7, 1H, BzImH), 7.20 (t, J = 7.7, 1H, BzImH), 7.12 (d, J = 14.5, 1H, BzImH), 7.07 (d, J = 7.9, 1H, BzImH), 4.00 (t, J = 6.8, 2H, NCH_2), 3.43 (t, J = 6.4, 2H, $BrCH_2$), 2.31 (p, J = 6.5, 2H, CCH_2C), 1.66 (s, 9H, CH3); ^{13}C NMR: (151 MHz, $CDCl_3$): δ = 151.14, 148.87, 129.44, 126.25, 124.14, 122.36, 114.67, 107.62, 84.91, 39.62, 31.03, 30.35, 28.19.

17. Tert-butyl 3-(3-bromopropyl)-2-oxo-2,3-dihydro-1H-benzo[d]imidazole-1-carboxylate (106): Compound **105** (1.00 g, 4.27 mmol) was added to a stirred solution of dibromopropane (4.35 mL, 42.7 mmol), fine-powdered K_2CO_3 (2.95 g, 21,35 mmol) and KI (0.070 g, 0.425 mmol) in ACN (20 mL). The reaction mixture was kept at room temperature overnight. The solvent was evaporated under reduced pressure, saturated NH4Cl (20 mL) was added and the product was extracted with DCM (6 × 20 mL). The combined organic phases were washed with brine (15 mL), dried (Na_2SO_4) and concentrated under reduced pressure. The residue was purified by silica gel chromatography (PE/EtOAc 9:1) to give **106** (0.998 g, 66.2%) as a white solid. Rf = 0.57 (PE/EtOAc 7:3); ^{1}H NMR (600 MHz, $CDCl_3$): δ = 7.82 (d, J = 7.7, 1H, BzImH), 7.20 (t, J = 55 7.7, 1H, BzImH), 7.12 (d, J = 14.5, 1H, BzImH), 7.07 (d, J = 7.9, 1H, BzImH), 4.00 (t, J = 6.8, 2H, NCH_2), 3.43 (t, J = 6.4, 2H, $BrCH_2$), 2.31 (p, J = 6.5, 2H, CCH_2C), 1.66 (s, 9H, CH3); ^{13}C NMR: (151 MHz, $CDCl_3$): δ = 151.14, 148.87, 129.44, 126.25, 124.14, 122.36, 114.67, 107.62, 84.91, 39.62, 31.03, 30.35, 28.19.

Tert-butyl 3-(3-(3-(2-chlorophenyl)-N-methylpropanamido)propyl)-2-oxo-2,3-dihydro-1H-benzo[d]imidazole-1-carboxylate (107): Compound **82** (0.056 g, 0.304 mmol) was dissolved in a solution of CDI (0.049 g, 0.304 mmol) in DCM (3 mL). After 30 min, **106** (0.093 g, 0.304mmol) was added, and the mixture was stirred overnight at room temperature. The reaction mixture was washed with $NaHCO_3$ 10% (3 × 15 mL),

brine (50 mL), dried (Na_2SO_4) and concentrated under reduced pressure. The residue was purified by silica gel chromatography (DCM/MeOH 97:3) to give **107** (0.081 g, 56.1%) as a white solid. Rf = 0.39 (DCM/MeOH 95:5); ^{1}H NMR (600 MHz, $CDCl_3$): δ = 7.39–7.02 (m, 4H, ArH), 3.97 (t, J = 7.2, 2H, BzImNCH$_2$), 3.53 (t, J = 7.2, 2H, NCH$_2$), 3.09–3.02 (m, 2H, COCH$_2$), 2.97 (s, 3H, CH3), 2.67 (dd, J = 14.5, 6.4, 2H, ArCH$_2$), 2.09–1.96 (m, 2H, CCH$_2$C), 1.66 (s, 9H, CH3).

3-(2-chlorophenyl)-N-methyl-N-(3-(2-oxo-2,3-dihydro-1H-benzo[d] imidazole-1-yl)propyl)propenamide (11): Compound **107** (0.080 g, 0.169 mmol) was dissolved in TFA (1 mL) and stirred 1 h at room temperature. TFA was evaporated under reduced pressure and the residue was dissolved in DCM. The solution was washed with saturated $NaHCO_3$ (2 × 10 mL), dried (Na_2SO_4) and concentrated under reduced pressure. The residue was purified by silica gel chromatography (DCM/MeOH 95:5) to give **11** (0.035 g, 55.5%) as a white solid. Rf = 0.45 (DCM/MeOH 95:5); ^{1}H NMR (600 MHz, $CDCl_3$): δ = 9.97 (s, 1H, NH), 7.34–7.05 (m, 4H, ArH), 3.90 (t, J = 7.3, 2H, BzImNCH$_2$), 3.48 (t, J = 7.3, 2H, NCH$_2$), 3.07–3.01 (m, 2H, COCH$_2$), 2.95 (s, 3H, CH3), 2.67 (dd, J = 14.5, 6.4, 2H, ArCH$_2$), 2.07–1.92 (m, 2H, CCH$_2$C); ^{13}C NMR: (151 MHz, $CDCl_3$): δ = 173.62, 160.55, 138.10, 133.87, 130.96, 129.63, 129.57, 129.50, 128.14, 127.43, 127.24, 127.19, 116.02, 108.64, 45.98, 38.94, 35.84, 33.27, 29.97, 29.63.

Tert-butyl (1-(3-(2-chlorophenyl)propanoyl)piperidin-4-yl)carbamate (108): A solution of thionyl chloride (1.20 mL, 16.3 mmol) in DCM (5 mL) was added dropwise over 15 min in a solution of **82** (2.0 g, 10.83 mmol) and DMF (0.100 mL) in dry DCM (33 mL) at 0°C under nitrogen atmosphere. The reaction mixture was kept 2 h at room temperature under nitrogen atmosphere. The solvent was evaporated under reduced pressure. The residue was dissolved in a solution of DIPEA (3.70 mL, 21.7 mmol) in DCM (30 mL), and a solution of tert-butyl piperidin-4-ylcarbamate (2.39 g, 11.9 mmol) was added dropwise at 0°C. The mixture was stirred for 3h at room temperature. The reaction mixture was washed with $NaHCO_3$ 10% (3 × 15 mL), brine (50 mL), dried (Na_2SO_4) and concentrated under reduced pressure. The residue was purified by silica gel chromatography (PE/EtOAc 7:3 to PE/EtOAc/MeOH 5:3:2) to give **108** (3.42 g, 86.3%) as a white solid. MS (ESI): m/z 389/391 [M+Na]+ ; ^{1}H NMR (600 MHz, $CDCl_3$): δ = 7.31 (dd, J = 7.8, 1.5, 1H, ArH3), 7.27–7.21 (m, 1H, ArH6), 7.14 (dtd, J = 18.8, 7.4, 1.7, 2H, ArH4-5), 4.48 (s, 1H, NH), 3.74 (d, J = 13.2, 1H, NCHH), 3.65–3.56 (m, 1H, CH), 3.04 (t, J = 7.9, 2H, ArCH$_2$), 2.99–2.97 (m, 1H, NC'HH), 2.69 (t, J = 12.6, 2H, NCH$_2$), 2.60 (td, J = 7.7, 3.7, 2H, OCCH$_2$), 1.89 (d, J = 12.7, 2H, CHCH$_2$), 1.41 (s, 9H, CH3), 1.26–1.08 (m, 2H, CHCH$_2$); ^{13}C NMR: (151 MHz, $CDCl_3$): δ = 170.45, 155.15, 138.80, 133.94, 131.03, 129.60, 127.91, 127.08, 79.64, 47.90, 44.45, 33.05, 32.17, 29.84, 28.47.

Phenyl-N-(1-(3-(2-chlorophenyl)propanoyl)piperidin-4-yl)-N'-cyanocarbamimidate (109): Compound **108** (3.30 g, 8.99 mmol) was dissolved in a stirred solution of TFA (7.00 mL) in DCM (40 mL). The reaction mixture was kept at room temperature overnight. The mixture was concentrated under reduced pressure. The product was dissolved in HCl 1 N (40 mL) and washed with diethyl ether (2 × 25 mL). The aqueous phase was basified with NaOH pellets to pH 12 and extracted with DCM (5 × 20 mL). The

combined organic phases were washed with brine, dried (Na_2SO_4), filtered and concentrated under reduced pressure. The product obtained (2.4 g, 8.99 mmol) was dissolved in a stirred solution of diphenyl cyanocarbonimidate (2.36 g, 9.89 mmol) in DCM (20 mL). After 1 h the solvent was evaporated under reduced pressure. The residue was purified by silica gel chromatography (petroleum ether/EtOAc/MeOH 6.5:3:0.5 to 6:3:1) to give **109** (3.40 g, 96.0%) as a white foam. Rf = 0.61 (DCM/MeOH 95:5); MS (ESI): m/z 425/427 $[M + H]^+$; ^{1}H NMR (600 MHz, $CDCl_3$): δ = 7.35–7.14 (m, 9H, ArH), 6.34 (s, 1H, NH), 4.94 (d, J = 14.6, 1H, OCH_2), 3.75 (s, 1H, NHCHH), 3.68–3.53 (m, 1H, CH), 3.02–2.97 (m, 1H, NHC'HH), 2.95 (d, J = 11.4, 1H, NHCHH), 2.89 (t, J = 7.8, 2H, $ArCH_2$), 2.65 (t, J = 12.2, 1H, NHC'HH), 2.55 (dd, J = 15.8, 7.5, 2H, $OCCH_2$), 1.80 (s, 2H, $CHCH_2$), 1.16–0.96 (m, 1H, $CHCH_2$); ^{13}C NMR: (151 MHz, $CDCl_3$): δ = 170.54, 170.33, 159.16, 140.94, 138.40, 136.13, 133.74, 130.79, 129.50, 129.11, 128.49, 128.37, 128.26, 127.87, 127.14, 126.97, 126.21, 118.10, 48.76, 45.79, 44.00, 40.28, 34.83, 32.85, 32.27, 31.50, 29.66.

1-(1-(3-(2-chlorophenyl)propanoyl)piperidin-4-yl)-2-cyano-3-methylguanidine (12): Compound **109** (0.600 g, 1.46 mmol) was dissolved in a solution of ethanolic ethylamine (33%, 2.72 mL, 29.2 mmol) and stirred 1.5 h at room temperature. The reaction mixture was cooled to 0°C and filtered to isolate **12** (0.450 g, 88.6%) as a white solid. Rf = 0.35 (DCM/MeOH 95:5); mp: 208.6–210.0°C; MS (ESI): m/z 348/350 $[M + H]^+$; ^{1}H NMR (600 MHz, $CDCl_3$): δ = 7.29–7.24 (m, 1H, ArH3), 7.18 (dd, J = 7.3, 1.8, 1H, ArH6), 7.15–7.11 (m, 1H, ArH5), 7.09 (td, J = 7.6, 2.0, 1H, ArH4), 4.47 (d, J = 13.6, 1H, NCHH), 3.76 (d, J = 15.0, 1H, CH), 3.72 (s, 1H, NC'HH), 2.96 (dd, J = 8.0, 2.5, 2H, $ArCH_2$), 2.94 (d, J = 9.8, 1H, NCHH), 2.74 (s, 3H, CH3), 2.58 (d, J = 8.1, 1H, NC'HH), 2.54–2.56 (m, 2H, $OCCH_2$), 1.86 (dd, J = 28.1, 12.5, 2H, $CHCH_2$), 1.22 (dqd, J = 64.3, 12.4, 4.2, 2H, $CHCH_2$); ^{13}C NMR: (151 MHz, $CDCl_3$): δ = 171.10, 159.70, 138.29, 133.77, 130.77, 129.58, 128.02, 127.11, 119.00, 48.91, 44.65, 40.94, 33.03, 32.45, 31.44, 29.70, 28.23

1-benzyl-3-(1-(3-(2-chlorophenyl)propanoyl)piperidin-4-yl)-2-cyanoguanidine (13): Compound **109** (0.200 g, 0.487 mmol) was dissolved in a solution of benzylamine (0.265 mL, 2.43 mmol) in iPrOH (2 mL) and stirred for 24 h at room temperature. The solvent was evaporated under reduced pressure. The residue was dissolved in DCM (20 mL), washed with $NaHCO_3$ 10% (3 × 15 mL), brine (50 mL), dried (Na_2SO_4) and concentrated under reduced pressure. The residue was purified by silica gel chromatography (DCM to DCM/MeOH 95:5) to give **13** (0.170 g, 81.9%) as a white solid; ^{1}H NMR (600 MHz, $CDCl_3$): δ = 7.35–7.14 (m, 9H, ArH), 6.34 (s, 2H, $NHCH_2Ar$), 4.94 (d, J = 14.6, 1H, NCHH), 3.75 (s, 1H, CH), 3.68–3.53 (m, 1H, NC'HH), 2.95 (d, J = 11.4, 1H, NCHH), 2.89 (t, J = 7.8, 2H, $ArCH_2$), 2.65 (t, J = 12.2, 1H, NC'HH), 2.55 (dd, J = 15.8, 7.5, 2H, $OCCH_2$), 1.85–1.75 (m, 2H, $CHCH_2$), 1.15–0.95 (m, 2H, $CHCH_2$); ^{13}C NMR: (151 MHz, $CDCl_3$): δ = 170.54, 170.33, 159.16, 140.94, 138.40, 136.13, 133.74, 130.79, 129.50, 129.11, 128.49, 128.37, 128.26, 127.87, 127.14, 126.97, 126.21, 118.10, 48.76, 45.79, 44.00, 40.28, 34.83, 32.85, 32.27, 31.50, 29.66.

Tert-butyl 4-(1H-benzo[d]imidazol-1-yl)piperidine-1-carboxylate (111): 110 (0.500 g, 1.79 mmol) was dissolved to a stirred suspension of benzimidazole (0.211 g, 1.79

mmol) and K_2CO_3 (0.49 g, 3.58 mmol) in DMF (2 mL). The mixture was heated under reflux for 2 days. The reaction mixture was concentrated under reduced pressure. The residue was dissolved in EtOAc and washed with water (2 × 15 mL), brine (15 mL), dried (Na_2SO_4) and concentrated under reduced pressure. The crude product was purified by silica gel chromatography (DCM/MeOH 95:5) to give **111** (0.101 g, 18.7%) as a yellow oil. Rf = 0.74 (DCM/MeOH 95:5).

1-(piperidin-4-yl)-1H-benzo[d]imidazole, trifluoroacetate salt (115): Compound **111** (0.081 g, 0.270 mmol) was dissolved in a stirred solution of TFA/DCM (10%, 4.4 mL) at room temperature. After 2 h, the reaction mixture was concentrated under reduced pressure to give **115** (0.084 g, 99.6%) as a white foam. Rf = 0.08 (DCM/MeOH 95:5 + NH3). MS (ESI): m/z 202 $[M + H]^+$; ^{1}H NMR (600 MHz, MeOD): δ = 9.58 (s, 1H, BzH_2), 8.11–8.02 (m, 1H, BzH4), 7.91–7.83 (m, 1H, BzH7), 7.73–7.63 (m, 2H, BzH5-6), 3.73–3.59 (m, 2H, NCH_2), 3.36–3.31 (m, 2H, CH), 2.61–2.49 (m, 2H, $CHCH_2$), 2.47–2.37 (m, 2H, $CHCH_2$); ^{13}C NMR: (151 MHz, MeOD): δ = 139.26, 131.36, 130.62, 127.15, 126.66, 114.80, 112.97, 52.89, 42.89, 28.02.

1-(4-(1H-benzo[d]imidazol-1-yl)piperidin-1-yl)-3-(2-chlorophenyl)propan-1-one (14): Compound **115** (0.084g, 0.270 mmol) was added to a stirred solution of **82a** (0.076 g, 0.270 mmol) and DIPEA (0.138 mL, 0.811 mmol) in DMF (1 mL). The mixture was kept at room temperature overnight. The reaction mixture was concentrated under reduced pressure. Water (10 mL) was added, and the product was extracted with EtOAc (3 × 25 mL). The combined organic phases were washed with brine, dried (Na_2SO_4), filtered and concentrated under reduced pressure. The crude product was purified by silica gel chromatography (DCM/MeOH 97:3) to give **14** (0.083 g, 83.6%) as a colourless oil. Rf = 0.23 (DCM/MeOH 97:3). MS (ESI): m/z 368/370 $[M + H]^+$; ^{1}H NMR (600 MHz, $CDCl_3$): δ = 7.96 (s, 1H, BzH_2), 7.81–7.77 (m, 1H, ArH3), 7.39–7.14 (m, 7H, BzH, ArH), 4.92–4.86 (m, 1H, NCHH), 4.37 (tt, J = 12.0, 3.9, 1H, CH), 4.05–3.97 (m, 1H, NC'HH), 3.13 (m, 3H, NCHH, $ArCH_2$), 2.81–2.60 (m, 3H, NC'HH, $COCH_2$), 2.14 (dd, J = 31.0, 12.2, 2H, $CHCH_2$), 1.88 (qd, J = 12.5, 4.4, CHCHH), 1.65 (qd, J = 12.5, 4.3, 1H, CHCHH); ^{13}C NMR: (151 MHz, $CDCl_3$): δ = 170.63, 143.35, 140.12, 138.59, 133.98, 132.97, 131.30, 129.72, 128.11, 127.11, 123.21, 122.71, 120.59, 109.95, 53.70, 44.94, 41.15, 32.80, 32.65, 31.90, 29.96.

Tert-butyl 4-((2-nitrophenyl)amino)piperidine-1-carboxylate (112): 1-fluoro-2-nitrobenzene (0.756 mL, 7.08 mmol) was dissolved in a stirred solution of tert-butyl 4-aminopiperidine-1-carboxylate (1.99 g, 9.92 mmol) and a suspension of fine powdered K_2CO_3 (2.16 g, 15.6 mmol) in dry DMF (5 mL) under nitrogen gas. The reaction mixture was kept at 70°C overnight. The mixture was concentrated under reduced pressure. Brine (20 mL) was added, and the product was extracted with EtOAc. The combined organic phases were washed with brine (15 mL), dried (Na_2SO_4) and concentrated under reduced pressure. The crude product was purified by silica gel chromatography (PE/EtOAc 9:1 to PE/EtOAc/MeOH 8.5:1:0.5) to give **112** (2.20 g, 96%) as an orange solid.

Tert-butyl 4-((2-aminophenyl)amino)piperidine-1-carboxylate (113):
Compound **112** (2.00 g, 6.22 mmol) was dissolved in a stirred suspension of Pd/C (10%, (10%, 0.660 g, 0.62 mmol) in the methanol (40 mL) under atmospheric pressure of H_2. The suspension was filtered and concentrated under reduced pressure. The crude product was purified by silica gel chromatography (DCM to DCM/MeOH 99:1) to give **113** (1.79 g, 99.0%) as a violet solid, stored under nitrogen atmosphere.

Tert-butyl 4-(2-(cyanoimino)-2,3-dihydro-1H-benzo[d]imidazol-1-yl)piperidine-1-carboxylate (114): Compound **113** (0.300 g, 1.03 mmol) was dissolved to a stirred solution of diphenyl cyanocarbonimidate (0.245 g, 1.03 mmol) and DIPEA (0.350 mL, 2.06 mmol) in ACN (24 mL). The reaction was heated under reflux and nitrogen atmosphere overnight. The reaction mixture was cooled to 0°C and filtered to isolate **114** (0.218 g, 62.3%) as a white solid. Rf = 0.35 (DCM/MeOH 97:3). MS (ESI): m/z 342 $[M + H]^+$; ^{13}C NMR: (151 MHz, $CDCl_3$): δ = 154.72, 153.28, 129.39, 129.18, 122.87, 122.54, 118.46, 110.84, 110.52, 80.27, 52.35, 28.66, 28.18.

N-(1-(piperidin-4-yl)-1,3-dihydro-2H-benzo[d] imidazol-2-ylidene)cyanamide (116): Compound **114** (0.218 g, 0.639 mmol) was dissolved in a stirred solution of TFA/DCM (10%, 11.0 mL) at room temperature. After 5 h, the reaction mixture was concentrated under reduced pressure. $NaHCO_3$ was added, and the product was extracted with DCM (5 × 15 mL). The combined organic phases were washed with brine, dried (Na_2SO_4), filtered and concentrated under reduced pressure to give **116** (0.130 g, 84.4%) as a white-yellow solid.

N-(1-(1-(3-(2-chlorophenyl)propanoyl)piperidin-4-yl)-1,3-dihydro-2H-benzo[d] imidazol-2-ylidene)cyanamide (15): Compound **82** (0.184 g, 0.539 mmol) was dissolved in solution of CDI (0.087 g, 0.539 mmol) in DCM (3 mL). After 300 , a solution of **116** (0.093 g, 0.304mmol) and DIPEA (0.458 mL, 2.69 mmol) in DCM (2 mL) was added to the reaction mixture and stirred overnight at room temperature. The reaction mixture was washed with water (3 × 15 mL), brine (50 mL), dried (Na_2SO_4) and concentrated under reduced pressure. The residue was purified by silica gel chromatography (DCM/MeOH 95:5) to give **15** (0.080 g, 36.4%) as a white solid. Rf = 0.25 (DCM/MeOH 95:5); MS (ESI): m/z 409/411 [MH+]; ^1H NMR (600 MHz, DMSO-d6): δ = 7.43–7.38 (m, 4H, ArH), 7.29–7.06 (m, 4H, BzH), 4.79 (d, J = 13.0, 1H, NCHH), 4.64–4.58 (m, 1H, CH), 4.03 (d, J = 13.7, 1H, NC'HH), 3.10 (t, J = 12.8, 1H, NCHH), 2.95 (t, J = 7.6, 2H, $ArCH_2$), 2.76–2.72 (m, 1H, NC'HH), 2.71–2.60 (m, 2H, $COCH_2$), 2.23 (tt, J = 12.5, 7.8, 1H, CHCHH), 2.10 (qd, J = 12.7, 4.6, 1H, CHC'HH), 1.77 (d, J = 12.1, 2H, $CHCH_2$); ^{13}C NMR: (151 MHz, DMSO-d6): δ = 172.58, 170.03, 162.86, 139.26, 133.50, 131.35, 131.31, 129.70, 128.51, 127.80, 122.21, 112.00, 52.55, 44.94, 41.23, 40.57, 36.33, 32.60, 29.19, 21.60.

1-(3-(2-chlorophenyl)propanoyl)-1,3-dihydro-2H-benzo[d]imidazol-2-one (16):
Compound **82** (1 g, 5.42 mmol) was dissolved in SOCl2 (5 mL) and heated under reflux for 1 h. Meanwhile, in a second flask, the 1,3-dihydro-2H-benzo[d]imidazol-2-one (726 mg, 5.42 mmol) and sodium hydride 60% dispersion in mineral oil (217 mg, 5.42 mmol) were dissolved in DMF and stirred at room temperature for 1h. Solvent was evaporated

from flask one and the formed acyl chloride was dissolved in dry DMF, slowly transferred in the reaction mixture of flask 2 and stirred for 3 h at room temperature. The solvent was evaporated under reduced pressure. Extraction was performed with ethyl acetate (3 × 50 mL) and a saturated solution of ammonium chloride (50 mL). The combined organic phases were washed with brine (150 mL), dried (Na_2SO_4) and concentrated under reduced pressure. The crude product was purified by silica gel chromatography (petroleum ether/ethyl acetate 9:1 to 7:3) to give **16** as a white solid. Rf = 0.40 (petroleum ether/ethyl acetate/MeOH 8:1.5:0.5). ^{1}H NMR (600 MHz, $CDCl_3$) δ 11.37 (s, 1H, NH), 7.97 (d, J = 7.9 Hz, 1H, 30ArH), 7.42–7.36 (m, 2H, 40 , 70BzImH), 7.29–7.11 (m, 3H, 40 , 50 , 60ArH), 7.09–6.97 (m, 2H, 50 , 60 BzImH), 3.34 (t, J = 7.6 Hz, 2H, $COCH_2CH_2$), 3.05 (t, J = 7.5 Hz, 2H, $COCH_2CH_2$).

General Procedure for Compounds 17, 18 and 117–119: Compound **16** (1 mmol) and the appropriate base (2 mmol) were dissolved in THF. The appropriate α-bromoacetate ester, acrylate ester or acetonitrile (2.5 mmol) was added. The reaction mixture was stirred at room temperature overnight. The solvent was concentrated under vacuum.

Ethyl 2-(3-(3-(2-chlorophenyl)propanoyl)-2-oxo-2,3-dihydro-1H-benzo[d]imidazol-1-yl) acetate (17): The reaction was run with **16** (150 mg, 0.499 mmol), ethyl bromoacetate (208 mg, 1.24 mmol) and DBU (150 µL, 0.997 mmol) in THF (5 mL). After completion, the reaction mixture was extracted with DCM (3 × 10 mL) and HCl 0.5N (10 mL). The combined organic phases were washed with brine (30 mL), dried (Na_2SO_4) and concentrated under reduced pressure to give **17** as a white solid (147mg, 76.2%). Rf = 0.25 (petroleum ether/ethyl acetate 95:5). ^{1}H NMR (600 MHz, $CDCl_3$) δ = 8.23 (d, J = 7.9 Hz, 1H, 30ArH), δ = 7.34 (m, J = 7.6 Hz, 2H, 40 , 50ArH), δ = 7.23–7.10 (m, 4H, BzImH), δ = 6.85 (d, J = 7.6 Hz, 1H, 60ArH), δ = 4.57 (s, 2H, NCH_2COOEt), 4.23 (q, J = 7.0 Hz, 2H, OCH_2CH3), δ = 3.50 (t, J = 7.6 Hz, 2H, $COCH_2CH_2$), δ = 3.21 (t, J = 7.6 Hz, 2H, $COCH_2CH_2$), δ = 1.27 (t, J = 7.0 Hz, 3H, OCH_2CH3).

Ethyl 2-(3-(3-(2-chlorophenyl)propanoyl)-2-oxo-2,3-dihydro-1H-benzo[d]imidazol-1-yl)propanoate (18): Compound **16** (120 mg, 0.400 mmol) was dissolved in a solution of DBU (120 µL, 0.800 mmol) in ethyl acrylate (1 mL). After completion, the reaction mixture was extracted with DCM (3 × 10 mL) and HCl 0.5N (10 mL). The combined organic phases were washed with brine (30 mL), dried (Na_2SO_4) and concentrated under reduced pressure to give **18** as a white solid (112 mg, 70.8%). Rf = 0.62 (petroleum ether/ethyl acetate 9:1). ^{1}H NMR (600 MHz, $CDCl_3$) δ = 8.23 (d, J = 7.9 Hz, 1H, 30ArH), 7.34 (m, J = 7.6 Hz, 2H, 40 ,50ArH), 7.21 (t, J = 7.8 Hz, 1H, ArH), 7.17 (t, J = 7.5 Hz, 1H, ArH) 7.23–7.10 (m, 2H, BzImH), 7.05 (d, J = 7.6 Hz, 1H, ArH), 4.11 (t, J = 7.1 Hz, 2H, CH_2CH3), 4.10–4.07 (m, 2H, NCH_2COOEt), 3.53–3.43 (m, 2H, $ArCH_2$), 3.19 (t, J = 7.7 Hz, 2H, CH_2COOEt), 2.75 (t, J = 7.0 Hz, 2H, CH_2COON), 1.19 (t, J = 7.2 Hz, 3H, CH3). ^{13}C NMR (151 MHz, $CDCl_3$), δ = 172.49, 170.94, 152.03, 138.21, 134.13, 130.75, 129.55, 129.45, 127.82, 126.93, 126.32, 124.65, 122.84, 115.90, 107.81, 61.08, 37.16, 37.09, 32.61, 28.04, 14.14.

Tert-butyl 2-(3-(3-(2-chlorophenyl)propanoyl)-2-oxo-2,3-dihydro-1H-benzo[d] imidazol-1-yl) acetate (117): The reaction was run with **16** (160 mg, 0.532 mmol) and sodium hydride (21.3 mg, 0.532 mmol) in THF (2 mL) and DMF (1 mL) under nitrogen atmosphere at 0°C. The reaction mixture was stirred at room temperature for 2 h. Tert-butyl bromoacetate (79 µL, 0.532 mmol) was added dropwise and the reaction mixture was stirred for 1 h at room temperature. Solvents were evaporated, water was added (15 mL) and the mixture was extracted with DCM (3 × 15 mL), washed with brine, dried (Na_2SO_4) and concentrated under reduced pressure. The crude product was purified by silica gel chromatography (DCM/petroleum ether 5:5 to 6:4) to give **117** as a white solid (100 mg, 45.2%). Rf = 0.22 (petroleum ether/ethyl acetate 7:3). ^{1}H NMR (600 MHz, $CDCl_3$) δ = 8.21 (d, J = 7.8 Hz, 1H, 3'ArH), δ = 7.40–7.27 (m, J = 7.8 Hz, 2H, 4',5'ArH), δ = 7.22–7.03 (m, 4H, BzImH), δ = 6.83 (d, J = 7.7 Hz, 1H, 6'ArH), δ = 4.46 (s, 2H, NCH_2CO), δ = 3.55–3.42 (t, 2H, $COCH_2CH_2$), δ = 3.20 (t, J = 7.7 Hz, 2H, $COCH_2CH_2$), 1.45 (s, 9H, OCC3H9). ^{13}C NMR (151 MHz, $CDCl_3$) δ = 172.53, 166.19, 152.30, 138.26, 134.19, 130.80, 129.60, 127.87, 127.00, 126.38, 124.74, 123.18, 116.08, 107.53, 83.31, 77.42, 77.20, 76.99, 42.88, 37.20, 29.81, 28.09.

2-(3-(3-(2-chlorophenyl)propanoyl)-2-oxo-2,3-dihydro-1H-benzo[d]imidazol-1-yl)acetonitrile (118): Compound **16** (100 mg, 0.333 mmol) was dissolved in dry DMF (3 mL). Sodium hydride 60% dispersion in mineral oil was added and the reaction mixture stirred for 1 h at room temperature. Bromoacetonitrile was then added (35 µL, 0.499 mmol) and the reaction mixture stirred for 2 h. The mixture was diluted with water (5 mL) and extracted with DCM (3 × 10 mL), washed with brine (30 mL), dried (Na_2SO_4) and concentrated under reduced pressure. The crude product was purified by silica gel chromatography (petroleum ether/ethyl acetate 8:2) to give **118** as a solid (60 mg, 54.5%). Rf = 0.21 (petroleum ether/ethyl acetate 9:1). ^{1}H NMR (600 MHz, $CDCl_3$) δ = 8.24 (d, J = 7.9 Hz, 1H, 3'ArH), δ = 7.34 (td, J = 7.5, 1.3 Hz, 2H,4',5'ArH), δ = 7.30 (td, J = 7.7, 0.8 Hz, 1H,6'ArH), δ = 7.24 (td, J = 7.9, 1.0 Hz, 1H, 4'BzImH), δ = 7.21–7.13 (m, 2H,50 , 60BzImH), δ = 7.12–7.06 (m, 1H, 70BzImH), δ = 4.76 (s, 2H, NCH_2CN), δ = 3.48 (t, J = 7.7 Hz, 2H, $COCH_2CH_2$), δ = 3.21 (t, J = 7.6 Hz, 2H, $COCH_2CH_2$). ^{13}C NMR (151 MHz, $CDCl_3$) δ = 172.21, 151.33, 137.97, 134.19, 130.86, 129.71, 128.05, 127.68, 127.07, 126.46, 125.27, 124.31, 116.51, 113.23, 107.70, 77.37, 77.16, 76.95, 37.23, 28.82, 28.09.

Tert-butyl 2-(3-(3-(2-chlorophenyl)propanoyl)-2-oxo-2,3-dihydro-1H-benzo-[d] imidazol-1-yl) prop anoate (119): Compound **16** (110 mg, 0.366 mmol) was dissolved in a solution of DBU (109 µL, 0.732 mmol) in t-Butyl acrylate (1 mL). After completion, the reaction mixture was extracted with DCM (3 × 10 mL) and NH4Cl (Saturated solution, 10 mL). The combined organic phases were washed with brine (30 mL), dried (Na_2SO_4) and concentrated under reduced pressure. The crude product was purified by silica gel chromatography (Petroleum ether/Ethyl Acetate 95:5 to 9:1) to give **119** as a white solid (97.3 mg, 62.1%). Rf= 0.62 (petroleum ether/ethyl acetate 9:1). ^{1}H NMR (600 MHz, $CDCl_3$) δ = 8.19 (t, J = 10.7 Hz, 1H, ArH), 7.21 (t, J = 7.7 Hz, 1H, ArH), 7.18 (t, J = 7.3 Hz, 1H, ArH), 7.16–7.10 (m, 2H, ArH), 7.05 (d, J = 7.8 Hz, 1H), 4.09 (t, J = 7.2 Hz, 2H, NCH_2), 3.49 (t, J = 7.7 Hz, 2H, $ArCH_2$), 3.20 (t, J = 7.7 Hz, 2H, CH_2CON), 2.67 (t, J = 7.2 Hz, 2H, CH_2COOt-Bu), 1.38 (s, 9H, CH3).13C NMR (151 MHz, $CDCl_3$),

δ = 172.59, 170.17, 152.06, 138.25, 134.17, 130.78, 129.60, 129.50, 127.85, 126.97, 126.36, 124.68, 122.87, 115.94, 107.92, 81.53, 37.20, 33.82, 28.09, 28.06.

2-(3-(3-(2-chlorophenyl)propanoyl)-2-oxo-2,3-dihydro-1H-benzo[d]-imidazol-1-yl)acetic acid (19): Compound **117** (100 mg, 0.291 mmol) was dissolved in DCM (2ml), and trifluoroacetic acid (185 µL, 2.41mmol) was added and the reaction stirred at room temperature overnight. Solvent was evaporated under reduced pressure and the obtained solid was washed with iced DCM to give **19** as a white solid (102.1 mg, 98.2%). Rf = 0.25 (DCM/MeOH 8:2); MS (ESI): m/z 359/361 [MH+]; ^{1}H NMR (600 MHz, $CDCl_3$) δ = 8.21 (d, J = 7.8 Hz, 1H, 3'ArH), δ = 7.40–7.27 (m, J = 7.8 Hz, 2H, 4',5'ArH), δ = 7.22–7.03 (m, 4H, BzImH), δ = 6.83 (d, J = 7.7 Hz, 1H, 6'ArH), δ = 4.46 (s, 2H, NCH_2CO), δ = 3.55–3.42 (t, 2H, $COCH_2CH_2$), δ = 3.20 (t, J = 7.7 Hz, 2H, $COCH_2CH_2$). ^{13}C NMR (151 MHz, $CDCl_3$) δ = 172.53, 166.19, 152.30, 138.26, 134.19, 130.80, 129.60, 127.87, 127.00, 126.38, 124.74, 123.18, 116.08, 107.53, 83.31, 77.42, 77.20, 76.99, 42.88, 37.20, 29.81.

1-((2H-tetrazol-5-yl)methyl)-3-(3-(2-chlorophenyl)propanoyl)-1,3-dihydro-2H-benzo[d]imidazol-2-one (21): Compound **118** (60 mg, 0.177 mmol) was dissolved in dry DMF (2 mL). Sodium azide (35 mg, 0.530 mmol) and ammonium chloride (9.5mg, 0.177mmol) were added, and the reaction mixture was stirred at 120°C for 2 h. The solvent was evaporated under reduced pressure. Extraction was performed with ethyl acetate (3 × 10 mL) and a saturated ammonium chloride aqueous solution (10 mL). The combined organic phases were washed with brine (30 mL), dried (Na_2SO_4) and concentrated under reduced pressure. The crude product was purified by silica gel chromatography (petroleum ether/ethyl acetate/methanol 80:15:5) to give **21** as a white solid (45 mg, 66.1%). Rf = 0.13 (petroleum ether/ethyl acetate 7:3).

2-(3-(3-(2-chlorophenyl)propanoyl)-2-oxo-2,3-dihydro-1H-benzo[d]- imidazol-1-yl)propionic acid (20): Compound **119** (100 mg) was dissolved in a solution of trifluoroacetic acid (0.7 mL) in DCM (7 mL), and the mixture was stirred at room temperature overnight. Solvent was evaporated under reduced pressure. The crude product was purified by silica gel chromatography (DCM/MeOH 97:3) to give **20** as a white solid (87 mg, 99.5%). Rf = 0.51 (DCM/MeOH 9:1). ^{1}H NMR (600 MHz, $CDCl_3$) δ = 8.17 (d, J = 7.9 Hz, 1H, ArH), 7.31 (dd, J = 7.8, 1.2 Hz, 2H, ArH), 7.19 (t, J = 7.6 Hz, 1H, ArH), 7.16 (t J = 7.4 Hz, 1H, ArH), 7.14–7.09 (m, 2H, ArH), 7.04 (d, J = 7.8 Hz, 1H, ArH), 4.09 (t, J = 7.1 Hz, 2H, NCH_2), 3.46 (t, J = 7.7 Hz, 2H, $ArCH_2$), 3.18 (t, J = 7.7 Hz, 2H, CH_2CON), 2.75 (t, J = 7.1 Hz, 2H, CH_2COOH). 13C NMR (151 MHz, $CDCl_3$) δ = 173.96, 172.62, 152.13, 138.15, 134.11, 130.75, 129.57, 129.38, 127.86, 126.97, 126.31, 124.72, 122.95, 115.95, 107.88, 77.37, 77.16, 76.95, 37.17, 36.96, 32.20, 28.04.

N-(2-chlorophenethyl)-2-nitroaniline (120): 2-(2-chlorophenyl)ethan-1-amine (0.649 mL, 4.61 mmol) was added to a stirred solution of 2-fluoronitrobenzene (0.373 mL, 3.54 mmol) and K_2CO_3 in DMF (3 mL). The reaction was kept under nitrogen atmosphere at 70°C for 18h. The solvent was evaporated under reduced pressure. The residue was dissolved in DCM (20 mL) and washed with water (3 × 20 mL). The crude product was purified by silica gel chromatography (Pe/EtOAc 9:1) to give **120** as an orange solid (978

mg, 99.5%). Rf = 0.58 (Pe/EtOAc 9:1). ^{1}H NMR (600 MHz, $CDCl_3$) δ = 8.16 (dd, J = 8.5, 1.5 Hz, 1H, ArH), 7.44–7.41 (m, 1H, ArH), 7.38 (dd, J = 7.7, 1.5 Hz, 1H, ArH, 7.27 (dd, J = 7.2, 1.7 Hz, 1H, ArH), 7.24–7.18 (m, 2H, ArH), 6.91 (d, J = 7.9 Hz, 1H, ArH), 6.65–6.63 (m, 1H, ArH), 3.60 (t, J = 7.2 Hz, 2H, NCH_2), 3.14 (t, J = 7.2 Hz, 2H, $ArCH_2$)

N-(2-chlorophenethyl)benzene-1,2-diamine (121): Compound **120** (0.93 g, 3.66 mmol) was dissolved in a stirred suspension of Pd/C (10%, 0.358 g, 0.34 mmol) in methanol (20 mL) under atmospheric pressure of H_2. The suspension was filtered and concentrated under reduced pressure. The crude product was purified by silica gel chromatography (PE/EtOAc 9:1) to give **121** (764 mg, 92.0%) as a white solid. Rf = 0.21 (Pe/EtOAc 9:1). ^{1}H NMR (600 MHz, $CDCl_3$) δ = 7.39–7.37 (m, 1H), 7.34–7.31 (m, 1H), 7.27–7.18 (m, 3H), 6.85–6.77 (m, 2H), 6.75–6.72 (m, 1H), 3.41 (t, J = 7.2 Hz, 2H, NCH_2), 3.00 (t, J = 7.2 Hz, 2H, $ArCH_2$).

1-(2-chlorophenethyl)-1,3-dihydro-2H-benzo[d]imidazol-2-one (122): CDI (1.05 g, 6.49 mmol) was added to a stirred solution of **121** (0.80 mg, 3.24 mmol) in DCM (50mL). After monitoring the end of the reaction (TLC), the solution was washed with water (3 × 20 mL). The organic solvent was evaporated under reduced pressure. The crude product was purified by silica gel chromatography (Pe/EtOAc 7:3) to give **122** as a white solid (170 mg, 78.0%). Rf = 0.39 (Pe/EtOAc/MeOH 8:1.5:0.5). ^{1}H NMR (600 MHz, DMSO-D6) δ = 10.78 (s, 1H, BzImNH), 7.36–7.34 (m, 1H, ArH), 7.24–7.18 (m, 3H, ArH), 6.94–6.90 (m, 4H, ArH), 3.98 (t, J = 7.2 Hz, 2H, NCH_2), 3.03 (t, J = 7.2 Hz, 2H, $ArCH_2$).

Ethyl 2-(3-(2-chlorophenethyl)-2-oxo-2,3-dihydro-1H-benzo[d]imidazol-1-yl) acetate (22): Compound **122** (200 mg, 0.733 mmol) was dissolved in a solution of DBU (0.219 µL, 1.466 mmol) and ethyl 2-bromoacetate (0.163 mL, 1.47 mmol) in dry THF (5 mL). After completion, water (10 mL) was added, and the product was extracted with DCM (3 × 10 mL). The combined organic phases were washed with brine (30 mL), dried (Na_2SO_4) and concentrated under reduced pressure. The crude product was purified by silica gel chromatography (Pe/EtOAc 8:2) to give **22** as a white solid (190 mg, 73.2%). Rf = 0.53 (Pe/EtOAc/MeOH 8:1.5:0.5). ^{1}H NMR (600 MHz, $CDCl_3$) δ = 7.29 (d, J = 1.7 Hz, 1H), 7.28–7.33 (m, 2H), 7.25 (d, J = 1.7 Hz, 1H), 7.23 (d, J = 2.1 Hz, 1H), 7.18–7.26 (m, 1H), 6.85–6.84 (m, 2H), 4.86–4.83 (m, 2H), 3.72 (t, J = 6.5 Hz, 2H), 2.97 (m, 4H), 1.84–1.82 (m, 3H).

Tert-butyl 2-(3-(2-chlorophenethyl)-2-oxo-2,3-dihydro-1H-benzo[d]imidazol-1-yl) acetate (123): Compound **122** (100 mg, 0.367 mmol) was dissolved in a solution of DBU (0.110 µL, 0.733 mmol) and tert-butyl 2-bromoacetate (0.108 mL, 0.733 mmol) in dry THF (3 mL). After completion, water (10 mL) was added, and the product was extracted with DCM (3 × 10 mL). The combined organic phases were washed with brine (30 mL), dried (Na_2SO_4) and concentrated under reduced pressure. The crude product was purified by silica gel chromatography (Pe/EtOAc 8:2) to give **123** as a white solid (102 mg, 75.1%). Rf = 0.50 (Pe/EtOAc/MeOH 8:1.5:0.5).). ^{1}H NMR (600 MHz, $CDCl_3$) δ = 8.25–8.35 (m, 2H), 7.65 (d, J = 7.5 Hz, 1H), 7.41–7.50 (m, 2H), 7.21–7.10 (m, 3H), 4.59 (t, J = 7.1 Hz, 2H), 4.05 (q, J = 7.9 Hz, 2H), 3.32 (t, J = 6.5 Hz, 2H), 2.89 (t, J = 7.1

Hz, 4H), 2.61 (t, J = 7.9 Hz, 4H), 1.38 (t, J = 7.8 Hz, 3H). ^{13}C NMR (151 MHz, $CDCl_3$) δ = 166.8, 154.1, 135.8, 134.2, 131.5, 129.6, 128.9, 128.7, 128.4, 127.2, 121.8, 121.4, 107.9, 107.8, 43.1, 43.0, 41.0, 34.8, 32.8, 28.1

2-(3-(2-chlorophenethyl)-2-oxo-2,3-dihydro-1H-benzo[d]imidazol-1-yl)acetic acid (23): Compound **123** (100 mg) was added in a stirred solution of TFA (0.300 mL) in DCM (3 mL). After 18 h, the solvents were evaporated under reduced pressure. The crude product was purified by preparative HPLC (ACN/H_2O 6:4) to give **23** as a white solid (45 mg, 50.5%). Rf = 0.12 (DCM/MeOH 9:1). ^{1}H NMR (600 MHz, DMSO-D6) δ = 7.37 (d, J = 7.2 Hz, 1H), 7.27 (d, J = 6.9 Hz, 1H), 7.19 (t, J = 7.6 Hz, 2H), 7.09–7.12 (m, 1H), 7.01–6.98 (m, 3H), 4.04 (t, J = 7.1 Hz, 2H), 3.04 (t, J = 7.1 Hz, 2H), 2.46 (s, 3H). ^{13}C NMR (151 MHz, DMSO-D6) δ = 170.2, 153.9, 138.8, 136.2, 133.7, 131.9, 129.8, 129.3, 127.9, 126.9, 121.6, 121.4, 108.7, 108.1, 40.7, 34.4, 32.2.

General Procedure for the Preparation of compounds 24, 26 and 28: 3-(2-chlorophenyl)propanoic acid (1 mmol) was added to a stirred solution of CDI (1 mmol) (5mmol) in DCM. The reaction was stirred at room temperature for 30'. The appropriate piperidine derivative was added, and the mixture stirred for 18 h. The reaction mixture was concentrated under reduced pressure. The residue was dissolved in DCM and washed with water (2 × 15 mL), brine (15 mL), dried (Na_2SO_4) and concentrated under reduced pressure.

Ethyl 4-(3-(2-chlorophenyl)propanoyl)piperidine-1-carboxylate (24): The reaction was run with 3-(2-chlorophenyl)propanoic acid (1.00 g, 5.42 mmol), CDI (0.88 g, 5.42 mmol), and ethyl 4-carboxypiperidine (0.834 mL, 5.42 mmol) in DCM (20 mL). The crude product was purified by silica gel chromatography (PE/EtOAc 7:3) to give **24** (1.45 g, 80.7%) as a colourless oil solid. Rf = 0.28 (PE/EtOAc 7:3); ^{1}H NMR (600 MHz, $CDCl_3$) δ7.31 (d, J = 7.7 Hz, 1H), 7.26 (d, J = 7.4 Hz, 1H), 7.16 (t, J = 7.4 Hz, 1H), 7.13 (t, J = 7.5 Hz, 1H), 4.40 (d, J = 12.5 Hz, 1H), 4.11 (q, J = 7.1 Hz, 2H), 3.76 (d, J = 12.7 Hz, 1H), 3.05 (t, J = 7.9 Hz, 2H), 3.01 (t, J = 10.0 Hz, 1H), 2.78 (t, J = 11.5 Hz, 1H), 2.61 (dd, J = 12.6, 7.4 Hz, 2H), 2.46 (tt, J = 10.7, 4.0 Hz, 1H), 1.86 (dd, J = 35.4, 12.1 Hz, 2H), 1.54 (dd, J = 40.2, 10.1 Hz, 2H), 1.23 (t, J = 7.1 Hz, 3H). ^{13}C NMR (151 MHz, $CDCl_3$) δ174.10, 170.30, 138.70, 133.79, 130.88, 129.45, 127.75, 126.95, 60.55, 44.77, 41.00, 40.91, 32.97, 29.69, 28.31, 27.79, 14.14.

Ethyl 3-(3-(2-chlorophenyl)propanoyl)piperidine-1-carboxylate (26): The reaction was run with 3-(2-chlorophenyl)propanoic acid (1.00 g, 5.42 mmol), CDI (0.88 g, 5.42 mmol), and ethyl 3-carboxypiperidine (0.834 mL, 5.42 mmol) in DCM (20 mL). The crude product was purified by silica gel chromatography (PE/EtOAc 7:3) to give **26** (1.25 g, 70.4%) as a colourless oil solid. Rf = 0.28 (PE/EtOAc 7:3); ^{1}H NMR (600 MHz, $CDCl_3$) δ7.31 (d, J = 7.8 Hz, 2H), 7.28 – 7.23 (m, 2H), 7.19 – 7.10 (m, 4H), 4.11 (q, J = 7.1 Hz, 5H), 3.05 (t, J = 7.9 Hz, 4H), 2.98 – 2.88 (m, 2H), 2.66 (s, 4H), 1.99 (s, 2H), 1.68 (s, 4H), 1.22 (t, J = 7.2 Hz, 6H).

3-(3-(2-chlorophenyl)propanoyl)piperidine-1-carboxamide (28): The reaction was run with 3-(2-chlorophenyl)propanoic acid (1.00 g, 5.42 mmol), CDI (0.88 g, 5.42 mmol), and 3-piperidincarboxamide (0.834 mL, 5.42 mmol) in DCM (20 mL). The crude product was purified by silica gel chromatography (PE/EtOAc 7:3) to give **28** (0.89 g, 45.7%) as a colourless oil solid. Rf = 0.28 (PE/EtOAc 7:3); ^{1}H NMR (600 MHz, DMSO-D6) δ8.10-8.02 (m, 2H), 7.38 (t, J = 4.5 Hz, 1H), 7.28-7.23 (m, 2H), 3.99 (s, 1H), 3.80 (d, J = 4.8 Hz, 1H), 3.17-3.05 (m, 2H), 2.55 (d, J = 9.3 Hz, 2H), 2.46 (d, J = 3.8 Hz, 3H). ^{13}C NMR (151 MHz, DMSO-D6) δ171.9, 167.9, 167.8, 134.7, 134.3, 132.7, 129.8, 129.2, 127.6, 55.7, 50.5, 40.5, 37.1, 36.2.

4-(3-(2-chlorophenyl)propanoyl)piperidine-1-carboxylic acid (25): Compound **24** (1.28, 3.93 mmol) was dissolved in a stirred solution of aqueous NaOH (2.5 N, 4 mL) in ethanol (15 mL). After 12 h, the mixture was acidified with HCl 1 N (10 mL), and the ethanol was evaporated under reduced pressure. The acidic aqueous phase was extracted with DCM (4 × 15 mL). The combined organic phases were washed with brine (10 mL), dried (Na_2SO_4) and concentrated under reduced pressure. The crude product was purified by silica gel chromatography (DCM/MeOH 95:5) to give **25** (1.16 g, 99.4%) as a white solid. ^{1}H NMR (600 MHz, $CDCl_3$) δ7.31 (d, J = 7.7 Hz, 1H), 7.26 (d, J = 7.4 Hz, 1H), 7.16 (t, J = 7.4 Hz, 1H), 7.13 (t, J = 7.5 Hz, 1H), 4.40 (d, J = 12.5 Hz, 1H), 3.76 (d, J = 12.7 Hz, 1H), 3.05 (t, J = 7.9 Hz, 2H), 3.01 (t, J = 10.0 Hz, 1H), 2.78 (t, J = 11.5 Hz, 1H), 2.61 (dd, J = 12.6, 7.4 Hz, 2H), 2.46 (tt, J = 10.7, 4.0 Hz, 1H), 1.86 (dd, J = 35.4, 12.1 Hz, 2H), 1.54 (dd, J = 40.2, 10.1 Hz, 2H). ^{13}C NMR (151 MHz, $CDCl_3$) δ174.10, 170.30, 138.70, 133.79, 130.88, 129.45, 127.75, 126.95, 60.55, 41.00, 40.91, 32.97, 29.69, 28.31, 27.79.

3-(3-(2-chlorophenyl)propanoyl)piperidine-1-carboxylic acid (27): Compound **26** (0.298, 0.921 mmol) was dissolved in a stirred solution of aqueous NaOH (2.5 N, 1 mL) in MeOH (5 mL). After 12 h, the mixture was acidified with HCl 1 N (10 mL), and the methanol was evaporated under reduced pressure. The acidic aqueous phase was extracted with DCM (4 × 15 mL). The combined organic phases were washed with brine (10 mL), dried (Na_2SO_4) and concentrated under reduced pressure. The crude product was purified by silica gel chromatography (DCM/MeOH 95:5) to give **27** (0.194 g, 74.5%) as a white solid. ^{1}H NMR (600 MHz, DMSO-d6) δ7.32 (dd, J = 23.6, 7.0 Hz, 4H), 7.19 (ddd, J = 15.1, 12.2, 5.4 Hz, 4H), 4.76 – 3.53 (m, 14H), 3.46 (s, 2H), 3.30 (dd, J = 13.5, 8.6 Hz, 1H), 3.01 (td, J = 9.7, 4.7 Hz, 1H), 2.96 – 2.81 (m, 5H), 2.71 – 2.50 (m, 5H), 2.49 – 2.43 (m, 4H), 2.33 (td, J = 8.3, 4.0 Hz, 1H), 2.19 (tt, J = 10.7, 3.9 Hz, 1H), 1.93 – 1.75 (m, 2H), 1.61 (ddd, J = 16.7, 14.1, 6.5 Hz, 2H), 1.58 – 1.40 (m, 2H), 1.32 – 1.13 (m, 2H). ^{13}C NMR (151 MHz, DMSO-d6) δ174.83, 174.77, 170.07, 139.16, 139.05, 133.43, 131.21, 129.59, 128.38, 127.67, 48.30, 48.16, 48.02, 47.88, 47.74, 47.10, 45.65, 43.61, 41.76, 41.11, 40.08, 39.95, 39.82, 39.68, 39.55, 39.41, 39.28, 32.68, 32.53, 29.18, 27.25, 27.09, 25.03, 23.98.

General procedure for the preparation of compounds 124–127: To a stirred solution of the appropriate carboxylic acid (1 mmol) in DMF (5 mL), DIPEA (2 mmol), HOBt (0.15 mmol), HBTU (1.5 mmol) and the appropriate amine (1.1 mmol) were added at room temperature and the mixture was stirred overnight. The solvent was evaporated under reduced pressure and a solution of $NaHCO_3$ 10% (20 mL) was added. The mixture

was extracted with EtOAc (3 × 20 mL). The combined organic phases were washed with brine (15 mL), dried (Na_2SO_4) and concentrated under reduced pressure.

Benzoyl (1-(3-(2-chlorophenyl)propanoyl)piperidine-4-carbonyl)alaninate (124): The reaction was run using alanine benzoyl ester (0.18 g, 1.52 mmol), DIPEA (0.70 mL, 4.14 mmol), HOBt (0.03 g, 0.21 mmol), HBTU (0.92 g, 2.07 mmol) and **25** (0.300 g, 1.38 mmol) in DMF (5 mL). The crude product was purified by silica gel chromatography (PE/EtOAc/MeOH, 7:2.5:0.5) to give **124** (0.330 g, 61.5%) as a white foam. Rf = 0.22 (petroleum ether/EtOAc/MeOH 7:2:1); ^{1}H NMR (500 MHz, DMSO) δ7.32 - 7.18 (m, 8H), 7.11 (s, 1H), 5.31 – 5.27 (m, 2H), 4.35 (s, 1H), 3.58 – 3.53 (m, 2), 3.26 – 3.21 (m, 2H), 2.96 – 2.92 (m, 2H), 2.63 – 2.59 (m, 2H), 2.49 (s, 1H), 1.94 – 1.90 (m, 2H), 1.78 – 1.74 (m, 2H), 1.49 – 1.36 (m, 2H). ^{13}C NMR (151 MHz, $CDCl_3$) δ175.3, 173.6, 171.5, 146.9, 136.1, 133.0, 129.2, 128.9, 128.7, 127.6, 127.3, 127.1, 127.0, 126.7, 126.5, 66.4, 52.4, 44.5, 44.1, 38.8, 32.9, 30.1, 29.6, 26.3, 17.3.

t-butyl (1-(3-(2-chlorophenyl)propanoyl)piperidine-4-carbonyl)phenylalaninate (125): The reaction was run using phenylalanine t-butyl ester (0.287 g, 1.52 mmol), DIPEA (0.70 mL, 4.14 mmol), HOBt (0.028 g, 0.21 mmol), HBTU (0.915 g, 2.07 mmol) and **25** (0.300 g, 1.38 mmol) in DMF (5 mL). The crude product was purified by silica gel chromatography (PE/EtOAc/MeOH, 7:2.5:0.5) to give **124** (0.330 g, 75.5%) as a white foam. Rf = 0.22 (petroleum ether/EtOAc/MeOH 7:2:1); ^{1}H NMR (600 MHz, $CDCl_3$) δ9.16 (d, J = 147.0 Hz, 1H), 7.35 – 7.27 (m, 1H), 7.27 – 7.05 (m, 10H), 6.13 (d, J = 38.4 Hz, 1H), 4.90 – 4.76 (m, 1H), 4.56 – 4.41 (m, 1H), 3.77 (t, J = 17.4 Hz, 1H), 3.22 (dt, J = 33.1, 16.6 Hz, 1H), 3.15 – 3.07 (m, 1H), 3.03 (t, J = 7.7 Hz, 2H), 2.97 – 2.84 (m, 1H), 2.63 (dd, J = 13.9, 5.9 Hz, 2H), 2.60 (d, J = 14.5 Hz, 1H), 2.35 – 2.22 (m, 1H), 1.82 – 1.62 (m, 2H), 1.58 – 1.33 (m, 2H), 1.32 (s, 9H, CH3).

t-butyl (1-(3-(2-chlorophenyl)propanoyl)piperidine-3-carbonyl)glycinate (126): The reaction was run using glycine t-butyl ester (0.910 g, 3.76 mmol), DIPEA (0.90 mL, 7.16 mmol), HOBt (0.048 g, 0.36 mmol), HBTU (2.04 g, 5.73 mmol) and **27** (0.660 g, 3.58 mmol) in DMF (5 mL). The crude product was purified by silica gel chromatography (DCM/MeOH, 99:1) to give **124** (0.330 g, 61.5%) as a white foam. Rf = 0.24 (petroleum ether/EtOAc/MeOH 7:2:1); ^{1}H NMR (600 MHz, CHLOROFORM-D) δ7.97 (s, 0H), 7.32-7.10 (m, 4H), 4.08 (td, J = 7.2, 2.1 Hz, 1H), 3.87-3.85 (m, 2H), 3.05-3.00 (m, 2H), 2.91 (d, J = 2.1 Hz, 2H), 2.84 (d, J = 1.0 Hz, 2H), 2.64-2.58 (m, 2H), 2.00 (t, J = 2.4 Hz, 2H), 1.40-1.44 (9H), 1.22 (qd, J = 4.8, 2.2 Hz, 2H). ^{13}C NMR (151 MHz, CHLOROFORM-D) δ172.9, 172.7, 171.2, 171.0, 170.6, 168.9, 162.6, 138.8, 138.7, 133.9, 131.1, 130.9, 129.6, 127.9, 127.1, 60.4, 46.3, 42.0, 36.6, 33.1, 28.1, 27.6, 24.6, 14.3.

Benzoyl (1-(3-(2-chlorophenyl)propanoyl)piperidine-3-carbonyl)alaninate (127): The reaction was run using alanine benzoyl ester (0.242 g, 1.35 mmol), DIPEA (0.43 mL, 2.70 mmol), HOBt (0.08 g, 0.14 mmol), HBTU (0.77 g, 2.03 mmol) and **27** (0.400 g, 1.35 mmol) in DMF (5 mL). The crude product was purified by silica gel chromatography (PE/EtOAc/MeOH, 7:2.5:0.5) to give **124** (0.330 g, 61.5%) as a white foam. Rf = 0.22 (petroleum ether/EtOAc/MeOH 7:2:1); ^{1}H NMR (500 MHz, DMSO) δ7.32 - 7.18 (m, 8H),

7.11 (s, 1H), 5.31 – 5.27 (m, 2H), 4.35 (s, 1H), 3.58 – 3.53 (m, 2), 3.26 – 3.21 (m, 2H), 2.96 – 2.92 (m, 2H), 2.63 – 2.59 (m, 2H), 2.49 (s, 1H), 1.94 – 1.90 (m, 2H), 1.78 – 1.74 (m, 2H), 1.49 – 1.36 (m, 2H). ^{13}C NMR (151 MHz, $CDCl_3$) δ175.3, 173.6, 171.5, 146.9, 136.1, 133.0, 129.2, 128.9, 128.7, 127.6, 127.3, 127.1, 127.0, 126.7, 126.5, 66.4, 52.4, 44.5, 44.1, 38.8, 32.9, 30.1, 29.6, 26.3, 17.3.

(1-(3-(2-chlorophenyl)propanoyl)piperidine-4-carbonyl)phenylalanine (30):
Compound **125** (90 mg) was dissolved in a solution of trifluoroacetic acid (2 mL) in DCM (5 mL), and the mixture was stirred at room temperature overnight. Solvent was evaporated under reduced pressure. The crude product was purified by silica gel chromatography (DCM/MeOH 97:3) to give **30** as a white solid (60 mg, 74.4%). Rf = 0.51 (DCM/MeOH 9:1). ^{1}H NMR (600 MHz, $CDCl_3$) δ9.16 (d, J = 147.0 Hz, 1H), 7.35 – 7.27 (m, 1H), 7.27 – 7.05 (m, 10H), 6.13 (d, J = 38.4 Hz, 1H), 4.90 – 4.76 (m, 1H), 4.56 – 4.41 (m, 1H), 3.77 (t, J = 17.4 Hz, 1H), 3.22 (dt, J = 33.1, 16.6 Hz, 1H), 3.15 – 3.07 (m, 1H), 3.03 (t, J = 7.7 Hz, 2H), 2.97 – 2.84 (m, 1H), 2.63 (dd, J = 13.9, 5.9 Hz, 2H), 2.60 (d, J = 14.5 Hz, 1H), 2.35 – 2.22 (m, 1H), 1.82 – 1.62 (m, 2H), 1.58 – 1.33 (m, 2H). ^{13}C NMR (151 MHz, $CDCl_3$) δ174.04, 174.00, 173.80, 171.43, 138.28, 135.97, 135.92, 133.84, 131.02, 129.65, 129.50, 128.62, 128.14, 127.22, 77.35, 77.14, 76.93, 52.99, 52.93, 45.34, 45.28, 42.61, 41.52, 37.36, 32.97, 29.91, 28.82, 28.49, 28.09.

(1-(3-(2-chlorophenyl)propanoyl)piperidine-3-carbonyl)glycine (31):
Compound **126** (1.4 mg) was dissolved in a solution of trifluoroacetic acid (1.5 mL) in DCM (15 mL), and the mixture was stirred at room temperature overnight. Solvent was evaporated under reduced pressure. The crude product was purified by silica gel chromatography (DCM/MeOH 97:3) to give **31** as a white solid (1.3 mg, 99.1%). Rf = 0.48 (DCM/MeOH 9:1). ^{1}H NMR (600 MHz, $CDCl_3$) δ7.31 (d, J = 7.6 Hz, 1H), 7.27 – 7.19 (m, 1H), 7.19 – 7.08 (m, 2H), 5.27 (s, 6H), 4.60 (s, 1H), 4.13 (d, J = 18.1 Hz, 1H), 4.00 (d, J = 18.2 Hz, 1H), 3.72 (d, J = 12.2 Hz, 1H), 3.45 (s, 1H), 3.02 (s, 3H), 2.83 (s, 1H), 2.66 (s, 2H), 2.53 (s, 1H), 1.87 (d, J = 15.6 Hz, 2H), 1.71 (d, J = 10.6 Hz, 1H), 1.29 (dd, J = 47.9, 38.8 Hz, 1H). ^{13}C NMR (151 MHz, CHLOROFORM-D) δ173.2, 172.4, 171.7, 138.1, 133.9, 131.0, 129.6, 128.1, 127.2, 53.6, 46.8, 45.6, 42.8, 41.7, 33.1, 29.7, 26.5, 24.9.

1-(3-(2-chlorophenyl)propanoyl)piperidine-4-carbonyl)alanine (29): Compound **124** (0.26 g, 0.57 mmol) was dissolved in a stirred suspension of Pd/C (10%, 0.061 g, 0.06 mmol) in the methanol (5 mL) under atmospheric pressure of H_2. The suspension was filtered and concentrated under reduced pressure. The crude product was purified by silica gel chromatography (DCM to DCM/MeOH 99:1) to give **29** (0.13 g, 62.1%) as a white solid. ^{1}H NMR (600 MHz, DMSO-d6) δ8.20 (d, J = 7.1 Hz, 1H), 7.23 (d, J = 7.8 Hz, 1H), 7.20 (d, J = 6.9 Hz, 2H), 7.13 (t, J = 7.0 Hz, 1H), 4.31 (d, J = 13.1 Hz, 1H), 4.20 (p, J = 7.2 Hz, 1H), 3.82 (d, J = 10.1 Hz, 1H), 3.57 (s, 3H), 2.92 (s, 1H), 2.76 (t, J = 7.8 Hz, 2H), 2.57 (d, J = 8.1 Hz, 2H), 2.46 (s, 2H), 2.36 (t, J = 11.3 Hz, 1H), 1.62 (t, J = 13.9 Hz, 2H), 1.38 (d, J = 12.1 Hz, 1H), 1.30 (d, J = 6.7 Hz, 1H), 1.22 (d, J = 7.3 Hz, 3H). ^{13}C NMR (151 MHz, DMSO-d6) δ174.88, 174.43, 173.74, 170.16, 142.00, 128.91, 128.73, 126.34, 52.32, 47.93, 44.88, 41.73, 41.05, 34.55, 31.34, 29.24, 28.39, 17.39.

1-(3-(2-chlorophenyl)propanoyl)piperidine-3-carbonyl)alanine (32): Compound **127** (0.17 g, 0.37 mmol) was dissolved in a stirred suspension of Pd/C (10%, 0.08 g, 0.04 mmol) in the methanol (5 mL) under atmospheric pressure of H_2. The suspension was filtered and concentrated under reduced pressure. The crude product was purified by silica gel chromatography (DCM to DCM/MeOH 99:1) to give **32** (38 mg, 28.0%) as a white solid. ^{1}H NMR (600 MHz, CHLOROFORM-D) δ7.94-8.07 (m, 2H), 7.13-7.32 (m, 4H), 4.45-4.71 (m, 1H), 3.46-3.77 (m, 1H), 3.12-3.42 (m, 1H), 2.75-3.09 (m, 2H), 2.58-2.75 (m, 2H), 1.60-1.95 (m, 2H), 1.37-1.50 (m, 2H), 1.15-1.41 (m, 1H). ^{13}C NMR (151 MHz, CHLOROFORM-D) δ176.3, 175.9, 172.7, 128.7, 128.7, 128.5, 128.5, 126.5, 126.4, 53.5, 48.5, 45.7, 43.0, 42.5, 27.0, 24.9, 18.6, 17.7.

t-butyl 2-((2-chlorophenil)(hydroxy)methyl)acrylate (128): To a stirred solution of 2-clorobenzaldeide (4.00 g; 28.46 mmol) in CH_3CN (9.3 mL) t-butyl acrylate (9.3 mL, 84.89 mmol) and water (54 mL) were added. DABCO (3.2 g; 28.46 mmol) was added to the solution and the mixture was stirred for 7 days at room temperature. The mixture was diluted with CH_2Cl_2 (30 mL) and extracted with HCl 1N (3 x 30 mL), washed with saturated NaCl (30 mL), dried (Na_2SO_4) and the solvent was evaporated under reduced pressure. The crude product was purified by silica gel chromatography (PE/EtOAc 9/1) to give **128** as a colourless oil (5.42 g; yield 38 %). Rf=0,29 (PE/EtOAc 9:1); MS (ESI): m/z 269 [MH+]; ^{1}H NMR (600 MHz,$CDCl_3$): δ7.51 (dd, J=7.7, 1.6 Hz, 1H, ArH), 7.35 (dd, J=7.9, 1.2 Hz, 1H, ArH), 7.28 (d, J=7.6, 1.1 Hz, 1H, ArH), 7.25–7.23 (d, 1H, ArH), 6.25 (s, 1H, C=CH), 5.93 (s, 1H, OH-CH), 5.53 (s, 1H, C=CH), 1.43 (s, 9H, CH3), 1.25 (s, 1H,OH).

t-butyl 2-(acetossi(2-chlorophenyl)methyl)acrilate (129): A solution of acetic anhydride (0,509 g; 4,99 mmol) in DCM (2) was added drop-wise over 30' to a solution of compound **128** (1,00 g; 4,16 mmol) and DMAP (102 mg, 0,831 mmol) in CH_2Cl_2 (10 mL) at 0°C. The reaction was stirred at room temperature for 2h. The mixture was washed with HCl 1N (3 x 15 mL), saturated solution of NaCl (15 mL), dried (Na_2SO_4) and the solvent was evaporated under reduced pressure. The crude product was purified by silica gel chromatography (PE/EtOAc 9:1) to give **129** (0,783 g; yield 80%) as a colourless oil. Rf=0,57 (PE/EtOAc 9:1); MS (ESI): m/z 311 [MH+]; ^{1}H NMR (600 MHz,$CDCl_3$): δ= 7.39–7.37 (m, 1H, ArH), 7.33–7.30 (m, 1H, ArH), 7.27–7.25 (m, 1H, ArH), 7.25–7.23 (m, 1H, ArH), 7.00 (s, 1H), 6.37 (s, 1H, C=CH), 5.51 (s, 1H, C=CH), 2.11 (s, 3H, O=C-CH3), 1.37 (s, 9H,C-CH3). ^{13}C NMR (150 MHz,$CDCl_3$):δ=169.29, 164.19, 139.94, 135.86, 133.94, 129.89, 129.72, 128.63, 126.99, 126.38, 81.75, 70.37, 28.01, 21.00.

t-butyl (2S,3S)-3-(2-chlorophenyl)-3-idrossi-2-(phenylsulfanilmethyl)propanoate (130): Compound **129** (0,200 g; 0,831 mmol) was added to a stirred solution of DABCO (0,190 g; 1,69 mmol) and thiophenol (0,103 mL; 0,997 mmol) in THF (15 mL) under N_2 atmosphere. The mixture stirred at 20 °C for 18h. The solvent was evaporated under reduced pressure. The residue was resuspended in DCM (30 mL) and mixture was washed with HCl 1N (3 x 30 mL), saturated solution of NaCl (30 mL), dried (Na_2SO_4) and the solvent was evaporated under reduced pressure. The crude product was purified by silica gel chromatography (PE/EtOAc 95/5 to PE/EtOAc 9/1) to give **130** as a colourless

oil (219 mg, yield 76%) Rf=0,71 (PE/EtOAc 95:5); MS (ESI): m/z 361/362 [MH+]; ^{1}H NMR (600 MHz,$CDCl_3$): δ=7.71 (s, 1H, C=CH), 7.36 (dd, J=8.0, 1.2 Hz, 1H, ArH), 7.31 (t, J=1.7 Hz, 1H, ArH), 7.30–7.29 (m, 2H, ArH), 7.24–7.21 (m, 1H, ArH), 7.21 (dt, J=2.2, 1.2 Hz, 1H, ArH), 7.19 (dd, J=9.5, 4.3, 2.9 Hz, 2H, ArH), 7.17–7.16 (m, 1H, ArH), 3.86 (d, J=2.6 Hz, 2H, CH_2), 1.53 (s, 9H, C-CH3). ^{13}C NMR (150 MHz,$CDCl_3$):δ= 165.36, 136.79, 135.90, 134.11, 133.58, 132.07, 130.86, 130.11, 129.64, 129.46, 128.79, 126.67, 126.56, 81.52, 32.50, 28.02.

(Z)-t-butyl 3-(2-chlorophenyl)-2-((cyloexylthio)methyl)acrilate (131):
Compound **130** (0,050 g; 0,177 mmol) was added to a stirred solution of TEA (0,037 mL; 0,265 mmol) and Cycloexylmercaptane (0,027 mL; 0.230 mol) in DCM (5 mL) under N_2 atmosphere. The mixture stirred at 60 °C for 18h. After cooling to room temperature, a solution of HCl 1N (15 mL) was added and the product was extracted with EtOAc (3 x 15 mL), washed with saturated solution of NaCl (15 mL), dried (Na_2SO_4) and the solvent was evaporated under reduced pressure. The crude product was purified by silica gel chromatography (PE/EtOAc 98/2) to give **131** (0,0234 g; yield 66%) as a white solid. Rf= 0,57 (PE/EtOAc 95:5); MS (ESI): m/z 367/368 [MH+]; ^{1}H NMR (600 MHz, $CDCl_3$): δ= 7.65 (s, 1H, C=CH), 7.54–7.51 (m, 1H, ArH), 7.40 (ddd, J=7.4, 4.4, 1.7 Hz, 1H, ArH), 7.30–7.25 (m, 2H, ArH), 3.48 (s, 2H, C-CH_2-S), 2.59–2.52 (m, 1H, S-CH-(CH_2)2), 1.75 (t, J=10.4 Hz, 2H), 1.66 (t, J=10.0 Hz, 2H), 1.55 (s, 9H), 1.40–1.23 (m, 2H), 1.23–1.19 (m, 2H), 1.15 (d, J=9.3 Hz, 2H). ^{13}C NMR (150 MHz, $CDCl_3$):δ= 166.29, 135.75, 134.30, 134.22, 133.54, 130.67, 129.76, 129.70, 126.79, 81.44, 43.83, 33.63, 28.25, 26.87, 26.22, 25.92.

(Z)-3-(2-chlorophenyl)-2-((phenylthio)methyl)acrylic acid (132): Compound **130** (100 mg) was added in a stirred solution of TFA (0.300 mL) in DCM (3 mL). After 18 h, the solvents were evaporated under reduced pressure. To give **132** as a white solid (78 mg, 92.4%). Rf = 0.12 (DCM/MeOH 9:1). Mp: 97,6-99,9 °C; MS/ESI negativa m/z: 303-305 [M-H]-; ^{1}H NMR ($CDCl_3$): δ, 12,36 (br, 1H, COOH); 7,98 (s, 1H, C=CH); 7,39-7,20 (m, 9H, ArH); 3,93 (s, 2H, CH_2S); ^{13}C NMR ($CDCl_3$): δ172,6; 140,2; 135,3; 134,4; 133,0; 131,2; 130,3; 130,1; 129,7; 129,6; 128,9; 127,0; 126,7; 32,0.

(Z)-3-(2-chlorophenyl)-2-((cyloexylthio)methyl)acrylic acid (133): Compound **148** (100 mg) was added in a stirred solution of TFA (0.300 mL) in DCM (3 mL). After 18 h, the solvents were evaporated under reduced pressure to give **133** as a white solid (82 mg, 94.2%). Rf = 0.12 (DCM/MeOH 9:1). MS/ESI negativa: 309-311 [M-H]-; ^{1}H NMR ($CDCl_3$): δ, 10,42 (br, 1H, COOH); 7,97 (s, 1H, C=CH); 7,65-7,28 (m, 4H, ArH); 3,58 (s, 2H, CH_2S); 2,60-2,58 (m, 1H, CH); 1,84-1,21 (m, 10H, cyloexyle); ^{13}C NMR ($CDCl_3$): δ, 172,4; 139,0; 134,3; 133,5; 130,9; 130,5; 130,2; 129,7; 126,8; 43,9; 33,3; 26,2; 26,1; 25,8.

General procedure for the synthesis of 33–41: To a stirred solution of the substituted acrylic or propionic acid derivatives (0,100 g; 0,33 mmol) in DMF (5 mL), DIPEA (0,111 mL; 0,66 mmol), HOBt (4,43 mg; 0,03 mmol) e HBTU (0,187 g; 0,49 mmol) were added and the mixture was stirred for 30'. Ethyl nipecotate (0,050 mL; 0,33 mmol) was added and the reaction was stirred at room temperature for 18h. The mixture was diluted

with diethyl eter (15 mL), washed with HCl 1N (3 x 15 mL), saturated solution of NaCl (15 mL), dried (Na_2SO_4) and the solvent was evaporated under reduced pressure. The crude product was purified by silica gel chromatography (PE/EtOAc 9/1 e poi PE/EtOAc 8/2).

ethyl (Z)-1-(3-(2-chlorophenyl)-2-((phenylthio)methyl)acryloyl)piperidine-4-carboxylate (33): Compound **33** was isolated as a white solid (0,100 g; yield: 69%). Purity (HPLC) 96%; eluent CH_3CN/H_2O + 0,1% CF_3COOH, 70/30; flux 1,0 mL/min; tR= 8,558. Rf= 0,75. (PE/EtOAc/MeOH 7,5:2:0,5); MS (ESI) m/z: 444-446 [M+H]+; ^{1}H NMR (DMSO-D6, 80 °C): δ, 7,47–7,46 (m, 1H, Ar-H); 7,35-7,33 (m, 3H, Ar-H); 7,16-7,08 (m, 5H, Ar-H); 6,61 (s, 1H, C=CH); 4,20-4,18 (m, 1H, CH-pip); 4,04 (q, J= 7,1 Hz; 2H, O-CH_2); 3,91-3,86 (m, 2H, S-CH_2); 3,08-2,93 (m, 2H, N-CH_2pip); 2,44 (m, 2H, CH_2pip); 1,96-1,94 (m, 1H, CH_2pip); 1,66–1,57 (m, 2H, CH_2pip); 1,41-1,39 (m, 1H, CH_2pip); 1,23 (t, J= 7,1 Hz; 3H, CH3). ^{13}C NMR ($CDCl_3$): δ, 172,6; 169,6; 135,3; 134,4; 133,4; 130,5; 129,65; 129,58; 129,2; 129,0; 128,5; 128,4, 126,8; 126,0; 60,7; 48,2*; 43,9; 41,3; 31,8; 27,7*; 24,8*; 14,3. *Peak split due to rotamers.

ethyl (Z)-1-(3-(2-chlorophenyl)-2-((phenylthio)methyl)acryloyl)piperidine-3-carboxylate (35): Compound **35** was isolated as a white solid (0,100 g; yield: 69%). Purity (HPLC) 96%; eluent CH_3CN/H_2O + 0,1% CF_3COOH, 70/30; flux 1,0 mL/min; tR= 8,558. Rf= 0,75. (PE/EtOAc/MeOH 7,5:2:0,5); MS (ESI) m/z: 444-446 [M+H]+; ^{1}H NMR (DMSO-D6, 80 °C): δ, 7,47–7,46 (m, 1H, Ar-H); 7,35-7,33 (m, 3H, Ar-H); 7,16-7,08 (m, 5H, Ar-H); 6,61 (s, 1H, C=CH); 4,20-4,18 (m, 1H, CH-pip); 4,04 (q, J= 7,1 Hz; 2H, O-CH_2); 3,91-3,86 (m, 2H, S-CH_2); 3,08-2,93 (m, 2H, N-CH_2pip); 2,44 (m, 2H, CH_2pip); 1,96-1,94 (m, 1H, CH_2pip); 1,66–1,57 (m, 2H, CH_2pip); 1,41-1,39 (m, 1H, CH_2pip); 1,23 (t, J= 7,1 Hz; 3H, CH3). ^{13}C NMR ($CDCl_3$): δ, 172,6; 169,6; 135,3; 134,4; 133,4; 130,5; 129,65; 129,58; 129,2; 129,0; 128,5; 128,4, 126,8; 126,0; 60,7; 48,2*; 43,9; 41,3; 31,8; 27,7*; 24,8*; 14,3. *Peak split due to rotamers.

(Z)-1-(3-(2-chlorophenyl)-2-((phenylthio)methyl)acryloyl)piperidine-3-carboxyamide (37): The reaction was run using piperidine-3-carbossammide (0,390 g; 0,390 mmol). The crude product was purified by silica gel chromatography (CH_2Cl_2/EtOAc 8:2) to give **37** (0,110 g; yield 75%) as a white solid. Mp: 60,5 – 61,4 °C; MS (ESI) m/z: 415-417 [M+H]+; ^{1}H NMR ($CDCl_3$) δ, 7,37 (s, 1H); 7,28-7,24 (m, 3H); 7.09-6,99 (m, 5H); 6,58 (s, 1H); 5,87 (s, 1H); 3,99-3,98 (m, 3H); 3,64-3,10 (m, 2H); 2,60-2,44 (m, 1H); 1,97-1,95 (m, 1H); 1,83-1,67 (m, 1H); 1,46 (d, 2H, J = 48,5 Hz); ^{13}C NMR ($CDCl_3$) δ, 175,1; 170,1; 135,0; 134,1; 133,8; 133,1; 130,3; 129,5; 129,4; 129,0; 128,8; 128,1; 126,7; 125,9; 48,1; 44,1; 41,7; 31,4; 27,2; 24,6.

ethyl (Z)-1-(3-(2-chlorophenyl)-2-((cyloexylthio)methyl)acryloyl)piperidine-4-carboxylate (40): Compound **40** was isolated as a white solid (0,199 g; yield 70%). Purity (HPLC): 96%; eluent CH_3CN/H_2O + 0,1% CF_3COOH, 70/30; flux 1,0 mL/min; tR=17,767. Rf= 0,5 (PE/EtOAc/MeOH 8/1,5/0,5); MS (ESI) m/z: 450-452 [M+H]+; ^{1}H NMR ($CDCl_3$): δ, 7,42–7,38 (m, 3H, Ar-H); 7,38–7,34 (m, 3H, Ar-H); 7,29 (dd, J= 7,4; 1,1 Hz, 1H, Ar-H); 7,19 (td, J= 7,7; 1,6 Hz, 1H, Ar-H); 6;56 (s, 2H, C=CH); 5,56–5,06

(m, 3H, CH_2); 4,16 (q, J= 7,1 Hz, 5H, CH_2); 3,58 (s, 4H, S-CH_2); 3,20 (m, 2H, CHpip); 2,59 (m, 4H, CH_2); 2,50–2,44 (m, 4H, CH_2); 2,00 (d, J= 11,6 Hz, 4H, CH_2); 1,91 (m, 6H, CH3); 1,67 (s, 4H, CH_2); 1,54 (m, 4H, CH_2); 1,25 (m, 14H, CH_2).

ethyl (Z)-1-(3-(2-chlorophenyl)-2-((cyloexylthio)methyl)acryloyl)piperidine-3-carboxylate (41): Compound **41** was isolated as a white solid (0,052 g; yield 64%). Purity (HPLC): 89%; eluent CH_3CN/H_2O + 0,1% CF_3COOH, 80/20; flux 1,0 mL/min; tR= 11,690. Rf= 0,5 (PE/EtOAc/MeOH 8/1,5/0,5); MS (ESI) m/z: 450-452 [M+H]+; ^{1}H NMR ($CDCl_3$): δ, 7,41 (dd, J=7,6; 1,6 Hz, 1H, Ar-H); 7,31–7,25 (m, 3H, Ar-H); 6,59 (s, 1H, C=CH); 4,65 (s, 2H, CH_2); 4,19 (m, 3H, CH_2); 3,62 (t, J= 14,2 Hz, 2H, CH_2); 3,19 (m, 2H, CH_2); 2,64 (m, 2H, CH_2); 2,45 (s, 1H, CH_2); 2,28–2,11 (m, 1H, S-CH), 1,88–1,82 (m, 1H, CH); 1,61 (d, J= 5,5 Hz, 3H, CH_2); 1,52 (d, J= 16,4 Hz, 2H, CH_2); 1,26 (t, J= 7.0 Hz, 3H, CH3); 1,12 (m, 5H, CH_2). ^{13}C NMR ($CDCl_3$): δ, 173,0; 171,4; 134,9; 134,4; 134,0; 131,0; 129,8; 129,7; 127,8; 127,2; 61,1; 47,9; 45,6; 43,0; 41,6; 35,4; 33,5; 27,9; 26,4; 26,0; 22,2; 14,6.

acido (Z)-1-(3-(2-chlorophenyl)-2-((phenylthio)methyl)acryloyl)piperidine-4-carbossilico (34): A solution of NaOH 2,5M (1.14 mL) was added to a stirred solution of **33** (0.107 g; 0.24 mmol) in dioxane (2 mL). The mixture stirred at 20 °C for 18h. The mixture was washed with HCl 1N (3 x 15 mL), saturated solution of NaCl (15 mL), dried (Na_2SO_4) and the solvent was evaporated under reduced pressure. The crude product was purified by silica gel chromatography (CH_2Cl_2/MeOH 95/5) to give **34** as a pale yellow oil (0,062 g; yield 95.8%). Purity (HPLC): 98,6%; eluent CH_3CN/H_2O + 0,1% CF_3COOH, 60/40; flux 1,0 mL/min; tR= 6,416. Rf= 0,3 (DCM/MeOH 95/5); MS (ESI) negativa m/z: 414-416 [M-H]-; ^{1}H NMR (CD3OD): δ, 8,81 (t, J=8,5 Hz, 1H, ArH); 8,74–8,69 (m, 3H, ArH); 8,51–8,44 (m, 3H, ArH); 8,42–8,32 (m, 2H, ArH); 7,97 (s, 1H, C=CH); 5,69 (d, J=10,7 Hz, 1H, CH); 5,35 (d, J=13,1 Hz, 3H, Pip-H); 4,64 (s, 2H, S-CH_2); 4,33–3,62 (m, 1H, Pip-H); 3,35–2,87 (m, 4H, Pip-H). ^{13}C NMR (CD3OD): δ, 176,8; 170,3; 134,9; 134,2; 134,0; 133,2; 130,4; 129,7; 129,4; 129,3; 128,8; 128,6; 126,8; 126,0; 41,3; 40,6; 30,9; 27,7.

Acido (Z)-1-(3-(2-chlorophenyl)-2-((phenylthio)methyl)acryloyl)piperidine-3-carbossilico (36): A solution of NaOH 2,5M (0,500 mL) was added to a stirred solution of **35** (0,047 g; 0,110 mmol) in dioxane (1 mL). The mixture stirred at 20 °C for 18h. The mixture was washed with HCl 1N (3 x 15 mL), saturated solution of NaCl (15 mL), dried (Na_2SO_4) and the solvent was evaporated under reduced pressure. The crude product was purified by silica gel chromatography (CH_2Cl_2/MeOH 95/5) to give **36** as a white solid (0,042 g; yield 62.3%). Purity (HPLC): 98% eluent CH_3CN/H_2O + 0,1% CF_3COOH, 60/40; flux 1,0 mL/min; tR=7,303. Rf= 0,2 (DCM/MeOH 95/5); MS (ESI) negativa m/z: 414-416 [M-H] -; ^{1}H NMR (CD3OD): δ, 7,70 (s, 1H, ArH); 7,47 (d, J=12,1 Hz, 2H, ArH); 7,34 (d, J=12,4 Hz, 2H, ArH); 7,28–7,17 (m, 4H, ArH); 7,09 (s, 1H, C=CH); 4,07 (s, 1H, CH); 3,68 (s, 2H, S-CH_2); 3,62 (t, J=5,9 Hz, 3H, Pip-H); 3,41-3,15 (m, 2H, Pip-H); 2,29-1,87 (m, 3H, Pip-H). ^{13}C NMR (CD3OD): δ, 178,0; 170,2; 134,0; 133,2; 131,8; 130,4; 129,5; 129,4; 129,3; 129,1; 128,9; 128,6; 126,7; 125,9; 39,4; 31,8; 31,6; 29,6; 27,1; 22,6.

t-butyl 2-(2-chlorobenzyl)-3-(phenylthio)propanoate (134): Compound **86** (0,350 g; 1,45 mmol) was added to a stirred solution of DABCO (0,326 g; 2,91 mmol) and thiophenol (0,358 mL; 3,49 mmol) in THF (15 mL) under N_2 atmosphere. The mixture stirred at 20 °C for 18h. The solvent was evaporated under reduced pressure. The residue was resuspended in DCM (30 mL) and mixture was washed with HCl 1N (3 x 30 mL), saturated solution of NaCl (30 mL), dried (Na_2SO_4) and the solvent was evaporated under reduced pressure. The crude product was purified by silica gel chromatography (PE/EtOAc 98:2) to give **134** as a colourless oil (0,247 g; yield 77%). MS/CI (isobutane) m/z: 335-337 [M+1]+; ^{1}H NMR ($CDCl_3$): δ, 7,44-7,07 (m, 9H, ArH); 4,03 (q, J = 7,1 Hz, 2H, CH_2CH3); 3,37-2,92 (m, 5H, H alifatici); 1,12 (t, J = 7,1 Hz, 3H, CH_2CH3). ^{13}C NMR ($CDCl_3$): δ, 174,0; 136,6; 136,0; 134,6; 131,7; 130,2; 130,0; 129,4; 128,6; 127,2; 126,8; 61,1; 45,9; 36,1, 35,9; 14,5.

t-butil 2-(2-chlorobenzyl)-3-(cyloexylthio) propanoate (135): Compound **86** (1,06 g, 4,19 mmol) was added to a stirred solution of DBU (2,18 mL, 14,69 mmol) e Cycloexylmercaptane (1,16 mL, 11,75 mmol) in DCM (11 mL) under N_2 atmosphere. The mixture stirred at 20 °C for 18h. The mixture was washed with HCl 1N (3 x 15 mL), saturated solution of NaCl (15 mL), dried (Na_2SO_4) and the solvent was evaporated under reduced pressure. The crude product was purified by silica gel chromatography (PE/DCM 8:2) to give **135** (544 mg, yield 35,1%). Rf= 0.6 (PE/DCM 7:3); MS (ESI): m/z 369 [MH+];^{1}H NMR (600 MHz,$CDCl_3$): δ= 7.33 (d, J=3.6 Hz, 1H, ArH), 7.26–7.20 (m, 1H, ArH), 7.14 (t, J=7.3 Hz, 2H, , ArH), 3.08–3.01 (m, 1H, CH_2-CH-CH_2), 2.97–2.86 (m, 2H, CH_2), 2.79 (dd, J=12.5, 8.0 Hz, 1H, S-CH), 2.69–2.58 (m, 2H, CH_2), 1.91 (d, J=12.9 Hz, 2H,CH_2), 1.73 (s, 2H, CH_2), 1.59 (d, J=10.6 Hz, 2H), 1.33 (s, 9H, CH3), 1.30–1.20 (m, 4H, Cy-H). ^{13}C NMR (150 MHz, $CDCl_3$): δ= 173.58, 137.04, 134.52, 131.77, 129.86, 128.27, 126.93, 81.16, 47.04, 44.13, 36.27, 33.92, 32.45, 28.33, 26.42, 26.17

2-(2-chlorobenzyl)-3-(phenylthio) propanoic acid (136): Compound **134** (1,08 g 2,99 mmol) was added to a stirred solution of TFA (6 mL, 78,35 mmol) in DCM (60 mL) and the mixture stirred at 20 °C for 18h. The mixture was washed with H_2O (2x15 mL), brine (15 mL), dried (Na_2SO_4) and the solvent was evaporated under reduced pressure to give **136** (812 mg, 89% di yield) as a white solid. MS (ESI): m/z 305/307 [MH-]; ^{1}H NMR (600 MHz $CDCl_3$):δ= 8.45 (s, 1H, OH), 6.93–6.90 (m, 1H, Ar-H), 6.87 (t, J=1.7 Hz, 1H, Ar-H), 6.85 (t, J=1.6 Hz, 1H, Ar-H), 6.83 (d, J=1.7 Hz, 1H, Ar-H), 6.81 (dd, J=8.1, 1.7 Hz, 1H, Ar-H), 6.79–6.76 (m, 1H, Ar-H), 6.76 (t, J=1.7 Hz, 1H, Ar-H), 6.75 (s, 1H, Ar-H), 6.75–6.72 (m, 1H, Ar-H), 2.81–2.76 (m, 1H, CH), 2.69 (dd, J=9.2, 4.6 Hz, 2H, CH_2), 2.68–2.64 (m, 2H, CH_2). ^{13}C NMR (150 MHz, $CDCl_3$):δ= 179.49, 135.84, 135.27, 134.37, 131.41, 130.15, 129.87, 129.14, 128.49, 127.03, 126.76, 45.38, 35.39, 35.22.

2-(2-chlorobenzyl)-3-(cyloexylthio) propanoic acid (137): Compound **135** (522 mg, 1,42 mmol) was added to a stirred solution of TFA (3 mL, 39.6 mmol) in DCM (30 mL)and the mixture stirred at 20 °C for 18h. The mixture was washed with H_2O di HCl 1N (15 mL x 2), brine (15 mL), dried (Na_2SO_4) and the solvent was evaporated under reduced pressure to give **137** as a white solid. (348 mg, yield: 79%). MS (ESI): m/z 311/313 [MH-]; ^{1}H NMR (600 MHz,$CDCl_3$): δ= 8.52 (s, 1H, OH) 7.34 (dd, J=5.5, 3.6 Hz,

1H, Ar-H), 7.26–7.21 (m, 1H, Ar-H), 7.17 (dd, J=5.6, 3.5 Hz, 2H, Ar-H), 3.14–3.06 (m, 2H CH-CH_2), 3.03 (dd, J=13.4, 6.2 Hz, 1H, CH), 2.82 (dd, J=13.2, 7.6 Hz, 1H, CH-CHb), 2.71 (dd, J=13.1, 4.7 Hz, 1H CH-CHa), 2.63 (s, 1H, S-CH), 1.94–1.81 (m, 2H, Cy-H), 1.73 (s, 2H, Cy-H), 1.58 (d, J=10.3 Hz, 2H, Cy-H), 1.31–1.16 (m, 4H, Cy-H). ^{13}C NMR (150 MHz, $CDCl_3$):δ= 179.71, 136.21, 134.30, 131.48, 129.83, 128.39, 127.00, 46.03, 44.04, 35.45, 33.61, 31.34, 26.18, 25.91.

ethyl 1-(2-(2-chlorobenzyl)-3-(phenylthio)propanoyl)piperidine-4-carboxylate (38): Compound **136** (0,140 g; 0,46 mmol) was added to a solution of DIPEA (0,157 mL; 0,92 mmol), HOBt (6,21 mg; 0,05 mmol) e HBTU (0,261 g; 0,69 mmol) in DMF (7,00 mL). The mixture was stirred at 20°C for 30'. Ethyl isonipecotate (0,070 mL; 0,46 mmol) was added, and the mixture stirred at 20 °C for 18h. The mixture was diluted with diethyl eter (15 mL), washed with HCl 1N (3 x 15 mL), saturated solution of NaCl (15 mL), dried (Na_2SO_4) and the solvent was evaporated under reduced pressure. The crude product was purified by silica gel chromatography (PE/EtOAc 9/1 to PE/EtOAc 8/2), to give **38** as a colourless oil (0,126 g; yield 62%). Purity (HPLC) >99%; eluent CH_3CN/H_2O + 0,1% CF_3COOH, 60/40; flux 1,0 mL/min; tR= 16,019. Rf= 0,23 (DCM/EtOAc 98/2); MS (ESI) m/z: 446-448 [M+H]+; ^{1}H NMR ($CDCl_3$): δ, 7,86–6,66 (m, 9H, ArH); 4,44–4,00 (m, 2H, CH_2); 3,59–3,25 (m, 2H, CH_2); 3,30–2,91 (m, 2H, CH_2); 2,88–2,44 (m, 1H, CH); 2,25 (dd, J = 12,2; 9,6 Hz, 1H, CH); 2,16 (s, 6H, CH_2); 1,77–1,30 (m, 2H, CH_2); 1,26–1,08 (m, 3H, CH3). ^{13}C NMR ($CDCl_3$): δ, 174,0; 171,9; 135,9; 132,2; 132,0; 129,7; 129,1; 129,0; 128,9; 127,2; 127,0; 126,2; 60,7; 45,3; 41,6; 39,9; 37,4; 36,2; 27,9; 14,3.

ethyl 1-(2-(2-chlorobenzyl)-3-(phenylthio)propanoyl)piperidine-3-carboxylate (39): Compound **136** (0,146 g; 0,48 mmol) was added to a solution of DIPEA (0,163 mL; 0,96 mmol), HOBt (6,47 mg; 0,05 mmol) e HBTU (0,273 g; 0,72 mmol) in DMF (7,3 mL). The mixture was stirred at 20°C for 30'. Ethyl nipecotate (0,075 mL; 0,48 mmol) was added, and the mixture stirred at 20 °C for 18h. The mixture was diluted with diethyl eter (15 mL), washed with HCl 1N (3 x 15 mL), saturated solution of NaCl (15 mL), dried (Na_2SO_4) and the solvent was evaporated under reduced pressure. The crude product was purified by silica gel chromatography (PE/EtOAc 9/1 to PE/EtOAc 8/2), to give **39** as a colourless oil (68 mg; yield 32%). ^{1}H NMR ($CDCl_3$): δ, 7,33–7,22 (m, 7H, ArH); 7,22–7,09 (m, 11H, ArH); 4,58 (m, 2H, CH_2); 4,14–3,96 (m, 4H, CH_2); 3,64 (d, J=13,5 Hz, 2H, CH_2); 3,46 (m, 2H, CH_2); 3,32 (m, 2H, CH); 3,17–3,01 (m, 4H, CH_2); 3,02–2,90 (m, 2H, CH); 2,67–2,55 (m, 2H, CH_2); 2,41–2,26 (m, 2H, CH_2); 2,22–2,14 (m, 2H, CH_2); 2,07–1,90 (m, 2H, CH_2); 1,78–1,59 (m, 2H, CH_2); 1,47–1,28 (m, 4H, CH_2); 1,25–1,18 (m, 6H, CH3). ^{13}C NMR ($CDCl_3$): δ, 173,41; 172,94, 172,37; 172,22; 136,85; 136,47; 136,15; 136,10; 134;35; 134,24; 132,47; 132,00; 129,87; 129,83; 129,34; 129,27; 128,68; 128,64; 127,25; 127,17; 126,9; 126,44; 126,11; 60,94; 60,83; 47,50; 46,41; 44,22; 42,83; 42,33; 41,64; 40,18; 40,13; 37,73; 37,59; 36,62; 35,34; 27,87; 27,51; 24,88; 24,78; 14,50; 14,47.

ethyl 1-(2-(2-chlorobenzyl)-3-(cyloexylthio)propanoyl)piperidine-4-carboxylate (41): Compound **137** (0,330 g; 1,06 mmol) was added to a solution of DIPEA (0,359 mL; 2,11 mmol), HOBt (0,014 g; 0,11 mmol) e HBTU (0,599 g; 1,58 mmol) in DMF (16 mL). The mixture was stirred at 20°C for 30'. Ethyl isonipecotate (0,164 mL; 1,06 mmol) was

added, and the mixture stirred at 20 °C for 18h. The mixture was diluted with diethyl eter (15 mL), washed with HCl 1N (3 x 15 mL), saturated solution of NaCl (15 mL), dried (Na_2SO_4) and the solvent was evaporated under reduced pressure. The crude product was purified by silica gel chromatography (PE/EtOAc 9/1 to PE/EtOAc 8/2), to give **41** as a pale yellow oil (0,298 g; yield 65%). Purity (HPLC): 89%; eluent CH_3CN/H_2O + 0,1% CF_3COOH, 80/20; flux 1,0 mL/min; tR= 11,690. Rf= 0,5 (PE/EtOAc/MeOH 8/1,5/0,5); MS (ESI) m/z: 450-452 [M+H]+; ^{1}H NMR ($CDCl_3$): δ, 7,41 (dd, J=7,6; 1,6 Hz, 1H, Ar-H); 7,31–7,25 (m, 3H, Ar-H); 6,59 (s, 1H, C=CH); 4,65 (s, 2H, CH_2); 4,19 (m, 3H, CH_2); 3,62 (t, J= 14,2 Hz, 2H, CH_2); 3,19 (m, 2H, CH_2); 2,64 (m, 2H, CH_2); 2,45 (s, 1H, CH_2); 2,28–2,11 (m, 1H, S-CH), 1,88–1,82 (m, 1H, CH); 1,61 (d, J= 5,5 Hz, 3H, CH_2); 1,52 (d, J= 16,4 Hz, 2H, CH_2); 1,26 (t, J= 7.0 Hz, 3H, CH3); 1,12 (m, 5H, CH_2). ^{13}C NMR ($CDCl_3$): δ, 173,0; 171,4; 134,9; 134,4; 134,0; 131,0; 129,8; 129,7; 127,8; 127,2; 61,1; 47,9; 45,6; 43,0; 41,6; 35,4; 33,5; 27,9; 26,4; 26,0; 22,2; 14,6.

ethyl 1-(2-(2-chlorobenzyl)-3-(cyloexylthio)propanoyl)piperidine-3-carboxylate (43): Compound **137** (0,330 g; 1,06 mmol) was added to a solution of DIPEA (0,359 mL; 2,11 mmol), HOBt (0,014 g; 0,11 mmol) and HBTU (0,599 g; 1,58 mmol) in DMF (16 mL). The mixture was stirred at 20°C for 30'. Ethyl nipecotate (0,164 mL; 1,06 mmol) was added, and the mixture stirred at 20 °C for 18h. The mixture was diluted with diethyl eter (15 mL), washed with HCl 1N (3 x 15 mL), saturated solution of NaCl (15 mL), dried (Na_2SO_4) and the solvent was evaporated under reduced pressure. The crude product was purified by silica gel chromatography (PE/EtOAc 9/1 to PE/EtOAc 8/2), to give **43** as a pale yellow oil (0,279 g; yield 59%). Purity (HPLC) >99%; eluent CH_3CN/H_2O + 0,1% CF_3COOH, 80/20; flux 1,0 mL/min; tR=13,237. Rf= 0,33 (PE/EtOAc 8/2); MS (ESI) m/z: 452-454 [M+H]+; ^{1}H NMR ($CDCl_3$): δ, 7,32 (t, J= 6,8 Hz, 1H, ArH); 7,23 (d, J= 32,3 Hz, 1H, ArH); 7,15 (d, J= 3,0 Hz, 2H, ArH); 4,77–4,36 (m, 1H, CH); 4,11 (s, 2H, CH_2); 4,02–3,59 (m, 1H, CH); 3,41 (t, J= 37,6 Hz, 1H, CH); 3,24–2,82 (m, 4H, CH_2); 2,76–2,27 (m, 5H, CH_2); 2,18–1,99 (m, 1H); 1,90 (dd, J= 46,7; 33,2 Hz, 2H, CH_2); 1,84–1,64 (m, 3H, CH_2); 1,57 (t, J= 25,2 Hz, 2H, CH_2); 1,53–1,38 (m, 2H, CH_2); 1,30–1,27 (m, 3H, CH_2); 1,25 (d, J= 6,8 Hz, 3H, CH3). ^{13}C NMR ($CDCl_3$): δ, 173,2; 172,4; 136,9; 134,2; 132,3; 131,8; 128,3; 126,9; 60,8; 47,9; 46,4; 44,5; 41,5; 37,7; 33,9; 33,6; 33,4; 27,2; 26,2; 25,9; 24,3; 14,3.

N'-hydroxy-2-(3-(trifluoromethyl)phenyl)acetimidamide) (138): 3-trifluoromethyl phenyl acetonitrile (1g, 5.40mmol), hydroxylamine hydrochloride (777mg, 11.88mmol) and TEA(1.73ml, 12.42mmol) were dissolved in EtOH 96% (15ml) and heated at 75°C overnight. Evaporation of solvent under reduced pression. Extraction with ethyl acetate (6x50ml) and basic (pH=8) aqueous solution of NaOH (2.5N, 50ml). The combined organic phases were washed with brine (30ml), dried (Na_2SO_4) and concentrated under reduced pressure to give **138** as white solid (1.03g, 87.5%). Rf = 0.15 (petroleum ether/ethyl acetate 8:2). ^{13}C NMR (151 MHz, $CDCl_3$) δ=135.25, 132.96, 130.06, 130.38 (q, J = 32.1 Hz, CF3C), 126.06 – 124.34 (m, J = 3.9 Hz, CF3CCH), 124.27 (q, J = 271.3 Hz, CF3), 117.46, 44.16.

Methyl 4-(3-(3-(trifluoromethyl)benzyl)-1,2,4-oxadiazol-5-yl)benzoate (44):
Compound **138** (500mg, 2.28mmol) was dissolved in toluene (50ml) then methyl 4-fromyl benzoate (930mg, 2.51mmol) and PTSA (45mg, 0.229mmol) were added and heated under reflux for 24 hours with a Dean-Stark apparatus. The reaction mixture was stirred at room temperature for 3 hours. Evaporation of solvent under reduced pression. Extraction with DCM (3x50ml) and water (50ml). The combined organic phases were washed with brine (150ml), dried (Na_2SO_4) and concentrated under reduced pressure. The crude product was purified by silica gel chromatography (petroleum ether /ethyl acetate 95:5) and then crystallized from ethanol to give **44** as a white solid (130mg, 15.2%). Rf=0.23 (petroleum ether/ethyl acetate 9:1). ^{1}H NMR (600 MHz, $CDCl_3$) δ=8.17 (d, J = 1.7 Hz, 4H,ArH), δ=7.64 (s, 1H,2'CF3ArH), δ=7.57 (d, J = 7.6 Hz, 1H4'CF3ArH), δ=7.53 (d, J = 7.8 Hz, 1H,6'CF3ArH), δ=7.46 (t, J = 7.7 Hz, 1H, 5'CF3ArH), δ=4.20 (s, 2H, CH_2), δ=3.95 (s, 3H, CH3). ^{13}C NMR (151 MHz, $CDCl_3$) δ=175.25, 169.77, 166.11, 136.36, 133.93, 132.59, 131.21 (q, J = 32.1 HzCF3C), 130.37, 129.36, 128.25, 127.78, 126.01 (d, J = 3.9 Hz, CF3C2'CH), 124.31 (q, J = 6.9, 3.7 Hz, CF3C4'CH), 124.11 (q, J = 272.2 Hz,CF3), 52.70, 32.34.

4-(3-(3-(trifluoromethyl)benzyl)-1,2,4-oxadiazol-5-yl)benzoic acid (45):
Compound **44** (10mg, 0.028mmol) and a solution of LiOH 1M (1.38µl, 0.138mmol) were dissolved in THF (300µl) and stirred overnight at room temperature. HCl 1N was then added to the reaction mixture (100µl) causing the formation of a white solid that was filtered under vacuum after the addiction of water (100 µl). The obtained solid was washed with cool water to give INF206 as a white solid (5mg, 63.1%). The compound was analysed via UHPLC (MP: acetonitrile/water 0.1%TFA 70:30, rate 1ml/min, SP: LiChrosphere C18 Merck (4.6 x 25 mm, 5 um)). Rt= 9.165 min, purity 100%. ^{1}H NMR (600 MHz, $CDCl_3$) δ=8.17 (d, J = 1.7 Hz, 4H), 7.64 (s, 1H), 7.57 (d, J = 7.6 Hz), 7.53 (d, J = 7.8 Hz, 1H), 7.46 (t, J = 7.7 Hz, 1H), 4.20 (s, 2H). ^{13}C NMR (151 MHz, $CDCl_3$) δ=175.25, 169.77, 166.11, 136.36, 133.93, 132.59, 131.21 (q, J = 32.1), 130.37, 129.36, 128.25, 127.78, 126.01, 124.31 (d, J = 6.9 Hz), 124.11 (q, J = 272.2 Hz), 52.70.

Methyl-4-(N'-hydroxycarbamimidoyl) benzoate (139): Methyl-4-cianobenzoate (500mg, 3.10mmol), hydroxylamine hydrochloride (473mg, 6.82mmol) and TEA(0.995ml, 7.13mmol) were dissolved in EtOH 96% (7ml) and heated under reflux for 3h. Evaporation of solvent under reduced pression. The crude product was purified by silica gel chromatography (DCM/MEOH 98:2 to 95:5) to give **139** a white crystalline solid (530mg, 87.2%). Rf=0.22 (DCM/MeOH 98:2). ^{1}H NMR (600 MHz, $CDCl_3$) δ8.01 (dd, J = 8.5, 1.9 Hz, 2H,3'5'ArH), 7.65 (dd, J = 8.5, 1.9 Hz, 2H, 2'6'ArH), 3.88 (s, 3H, OCH3), 2.73 (br, 2H, NH_2).

Methyl 4-(5-(3-(trifluoromethyl)benzyl)-1,2,4-oxadiazol-3-yl)benzoate (47): 3-trifluoromethylphenyl acetonitrile (289mg, 1.41mmol) and CDI(228mg, 1.41mmol) were dissolved in THF (3ml) and stirred at room temperature for 1h before adding **139** (250mg, 1.29 mmol). The reaction mixture was stirred at room temperature for 3 hours. Evaporation of solvent under reduced pression. The obtained white solid was dissolved in acetic acid and heat under reflux overnight. Extraction with DCM (3x20ml) and a 10% aqueous

carbonate solution (20ml). The combined organic phases were washed with brine (30ml), dried (Na_2SO_4) and concentrated under reduced pressure. The crude product crystallized from ethanol to give INF209 a white crystalline solid (255mg, 54.6%). Rf=0.21 (petroleum ether/ethyl acetate 9:1). ^{1}H NMR (600 MHz, $CDCl_3$) δ=8.19 – 8.09 (m, 4H, EtOOCArH), δ=7.59 (dd, J = 53.9, 46.0 Hz, 4H, CF3ArH), δ=4.37 (s, 2H, CH_2), δ=3.95 (s, 3H, OCH3).

2-(2-chlorophenyl) acetohydrazide (140): the reaction was run with 2-chlorophenyl acetic acid (**83**, 1g, 5.86mmol) and CDI (1.046g, 6.45 mmol) in THF (15ml) for 1 hour. Hydrazine monohydrate (0.440 g, 8.79mmol) was added, with subsequently formation of a white solid. Mixture was stirred overnight at room temperature. The crude product was purified by silica gel chromatography (DCM/MeOH 95:5) to give **140** as a white opalescent solid. (0.920g, 85.2%). Rf= 0.18 (DCM/MeOH from 98:2 to 95:5). ^{1}H NMR (600 MHz, $CDCl_3$) δ=7.37 – 7.33 (m, 1H, 6'ArH), δ=7.31 – 7.28 (m, 1H, 3'ArH), δ=7.24 – 7.19 (m, 2H, 4',5'ArH), δ= 3.63 (s, 2H,CH_2), δ=2.66 – 2.51 (m, 2H, NH_2). ^{13}C NMR (151 MHz, $CDCl_3$) δ= 170.81, 134.38, 132.21, 131.71, 129.80, 129.11, 127.38, 127.33, 39.31.

5-(2-chlorobenzyl)-1,3,4-oxadiazol-2(3H)-one (141): Compound **140** (0.630g, 3.42 mmol) and CDI (0.610g, 3.76 mmol) were dissolved in dry THF (60ml) and stirred overnight at room temperature under nitrogen atmosphere. Evaporation of solvents under reduced pression and extraction with acid water (pH=5, 25ml) and ethyl acetate (3x20ml). The combined organic phases were washed with brine (25ml), dried (Na_2SO_4) and concentrated under reduced pressure. The crude product was purified by silica gel chromatography (DCM/MEOH 99:1 to 95:5) to give 6, a white crystalline solid (648mg, 90.3%). Rf=0.20 (DCM/MeOH 98:2). ^{1}H NMR (600 MHz, $CDCl_3$) δ=9.76 (s, 1H, NH), δ=7.44 – 7.36 (m, 1H, 6'ArH), δ=7.33 – 7.27 (m, 1H, 3'-ArH), δ=7.27 – 7.21 (m, 2H, 4',5' ArH), δ=4.02 (s, 2H, CH_2). ^{13}C NMR (151 MHz, $CDCl_3$) δ=155.85, 155.61, 134.39, 131.16, 130.74, 130.01, 129.54, 127.40, 30.78.

General procedure for the synthesis of compounds 43, 48, 50, 52 and 53: Compound **141** (1 mmol) was dissolved in THF and cooled to 0°C, DBU (1.5 mmol) was added and after 30 minutes the desired bromo derivate was added to the reaction mixture thus forming a white precipitate. The reaction mixture was then stirred at room temperature for 4 hours. Liquid phase was transferred in another flask and concentrated under vacuum. Extraction with ethyl acetate (3x10ml) and water (10ml). The combined organic phases were washed with brine (30ml), dried (Na_2SO_4) and concentrated under reduced pressure.

Ethyl 2-(5-(2-chlorobenzyl)-2-oxo-1,3,4-oxadiazol-3(2H)-yl)acetate (48): The reaction was run with compound **141** (100 mg, 0.475mmol), DBU (142 µl, 0.950mmol) and ethyl 2-bromoacetate (78 uL, 0.712 mmol) in THF (2mL). The crude product was purified by silica gel chromatography (petroleum ether/ethyl acetate 95:5 to 85:15) to give **48**, a yellowish oil (100mg, 70.9%). Rf = 0.25(petroleum ether/ethyl acetate 8:2). ^{1}H NMR (600 MHz, $CDCl_3$) δ=7.43 – 7.40 (m, 1H, 6'ArH), δ=7.32 (m, J = 6.6, 3.1 Hz, 1H, 3'ArH), δ=7.29 – 7.26 (m, 2H, 4',5'ArH), δ=4.44 (s, 2H,NCH_2), δ=4.24 (t, J = 7.2 Hz, 2H, OCH_2), δ=4.05 (s, 2H, $ArCH_2$), δ=1.28 (t, J = 7.2 Hz, 3H, OCH_2CH3). ^{13}C NMR (151 MHz,

$CDCl_3$) δ=166.69, 154.38, 154.17, 134.43, 131.11, 130.77, 130.00, 129.52, 127.40, 62.24, 46.79, 30.82, 14.19.

t-butyl 2-(5-(2-chlorobenzyl)-2-oxo-1,3,4-oxadiazol-3(2H)-yl)acetate (50): The reaction was run with compound **141** (300 mg, 1.42mmol), DBU (318 µl, 2.13mmol) and tert-butyl bromoacetate (555mg, 2.84mmol) in THF (6ml). The crude product was purified by silica gel chromatography (petroleum ether/ethyl acetate 95:5 to 90:10) to give (**50**, a white solid (340mg, 74.0%). Rf= 0.23 (petroleum ether/ethyl acetate 9:1). ^{1}H NMR (600 MHz, $CDCl_3$) δ7.42 – 7.39 (m, 1H, 6'ArH), 7.34 – 7.29 (m, 1H, 3'ArH), 7.27 (m, J = 4.4, 2.9 Hz, 1H, 4'ArH), 7.25 (m, J = 3.9, 3.5 Hz, 2H, 5'ArH), 4.33 (s, 2H, NCH_2), 4.04 (s, 2H,CH_2), 1.46 (s, 9H, OCC_3H_9).

2-(5-(2-chlorobenzyl)-2-oxo-1,3,4-oxadiazol-3(2H)-yl)acetatonitrile (142): The reaction was run with compound **141** (500 mg, 1.42mmol), DBU (390 µl, 2.61mmol) and 2-bromoacetonitrile (248 µl, 3.56 mmol) in THF (6ml). The crude product was purified by silica gel chromatography (petroleum ether/ethyl acetate 8:2) to give (**142**, a white solid (540 mg, 91.2%). Rf= 0.45 (petroleum ether/ethyl acetate 7:3). ^{1}H NMR (600 MHz, $CDCl_3$) δ7.42 – 7.39 (m, 1H, 6'ArH), 7.34 – 7.29 (m, 1H, 3'ArH), 7.27 (m, J = 4.4, 2.9 Hz, 1H, 4'ArH), 7.25 (m, J = 3.9, 3.5 Hz, 2H, 5'ArH), 4.33 (s, 2H, NCH_2), 4.04 (s, 2H,CH_2).

Ethyl 4-((5-(2-chlorobenzyl)-2-oxo-1,3,4-oxadiazol-3(2H)-yl)methyl)benzoate (52): The reaction was run with compound **141** (300 mg, 1.42mmol), DBU (318µl, 2.13mmol) and ethyl (2-bromomethyl)benzoate (690mg, 2.84mmol) in THF (6ml). The crude product was purified by silica gel chromatography (petroleum ether/ethyl acetate 95:5) to give **52**, a white solid (340mg, 64.3%). Rf= 0.22 (petroleum ether/ethyl acetate 9:1) ^{1}H NMR (600 MHz, $CDCl_3$) δ=8.06 – 7.21 (m, 8H, ArH), δ=4.88 (s, 2H, NCH_2), δ=4.37 (q, J = 7.1 Hz, 2H, OCH_2), δ=4.00 (s, 2H, CH_2), δ=1.39 (t, J = 7.2 Hz, 3H, OCH_2CH3). ^{13}C NMR (151 MHz, $CDCl_3$) δ=166.21, 154.18, 153.89, 139.70, 134.37, 131.10, 130.76, 130.57, 130.17, 129.98, 129.47, 128.05, 127.34, 53.54, 49.12, 30.85, 14.40.

5-(2-chlorobenzyl)-3-(4-methoxybenzyl)-1,3,4-oxadiazol-2(3H)-one (53): The reaction was run with compound **141** (200mg, 0.950mmol), 4-metoxy benzyl alcohol (118l, 0.95mmol) and triphenylphosphine (310 µl, 1.42mmol) in THF at 0°C under nitrogen atmosphere, then DIAD (279 µl, 1.42mmol) was slowly added to the reaction mixture. The reaction mixture was stirred for 4 hours before evaporating solvent under vacuum. The crude product was purified by silica gel chromatography (petroleum ether/ethyl acetate 95:5 to 90:10) to give **53**, a white solid (250mg, 79.9%). Rf= 0.17 (petroleum ether/ethyl acetate 9:1). MS(ESI) m/z 353.4/355.4 [MNa+]. ^{1}H NMR (600 MHz, $CDCl_3$) δ=7.50 – 6.76 (m, 8H, ArH), δ=4.76 (s, 2H, NCH_2), δ=3.98 (s, 2H, CH_2), δ=3.79 (s, 3H, OCH3). ^{13}C NMR (151 MHz, $CDCl_3$) δ=159.74, 153.94, 153.82, 134.40, 131.07, 131.02, 129.98, 129.85, 129.40, 127.33, 127.19, 114.29, 55.41, 49.13, 30.82.

2-(5-(2-chlorobenzyl)-2-oxo-1,3,4-oxadiazol-3(2H)-yl)acetic acid (49):

Compound **50** (50mg, 0.154mmol) was dissolved in DCM (1.2ml), trifluoroacetic acid (117µl, 1.54mmol) was added and the reaction stirred at room temperature overnight.

Extraction with DCM (3x15ml) and water (15ml). Collected organic phases were washed with brine (15ml), dried (Na_2SO_4) and concentrated under reduced pressure. The crude product was purified by silica gel chromatography (DCM/MeOH 95:5) to give **49** as a transparent liquid (27 mg, 63.3%). ^{1}H NMR (600 MHz, DMSO-D6) δ7.47-7.42 (m, 2H), 7.34-7.32 (m, 2H), 4.43 (s, 2H), 4.10 (s, 2H). ^{13}C NMR (151 MHz, DMSO-D6) δ169.0, 154.3, 134.0, 132.3, 131.7, 130.1, 130.1, 128.1, 47.1, 30.4.

2-(5-(2-chlorobenzyl)-2-oxo-1,3,4-oxadiazol-3(2H)-yl)methyltetrazole (51):
Compound **142** (400mg, 1.60 mmol) was dissolved in a solution of sodium azide (156 mg, 2.40 mmol) and ammonium chloride (86 mg, 1.60 mmol) in DMF (5 ml), and the reaction stirred at room temperature for 18 h. Extraction with DCM (3x15ml) and water (15ml). Collected organic phases were washed with brine (15ml), dried (Na_2SO_4) and concentrated under reduced pressure. The crude product was purified by silica gel chromatography (DCM/MeOH 95:5) to give **51** as a white solid (145 mg, 91%). ^{1}H NMR (600 MHz, CHLOROFORM-D) δ7.97 (s, 1H), 7.36-7.20 (m, 4H), 5.24 (s, 2H), 3.99 (s, 2H). ^{13}C NMR (151 MHz, CHLOROFORM-D) δ163.3, 154.9, 153.7, 134.3, 131.2, 130.5, 129.9, 129.5, 127.4, 39.8, 37.0, 31.9, 30.7.

1-(2-chlorobenzoyl)pyrrolidine-2,5-dione (143): the reaction was run with 2-chloro benzoic acid (500mg, 3.19mmol), N-hydroxysuccinimide (551mg, 4.79mmol) and N,N'-dicyclohexyl carbodiimide (658mg, 3.19mmol) in THF(10ml) at 0°C for ten mitutes, mixture was then stirred at room temperature overnight. The suspension was filtered under vacuum and concentrated under reduced pression. Liquid phases collected were extracted with ethyl acetate (3x50ml) and water(50ml). Combined organic phases were washed with brine (150ml), dried (Na_2SO_4) and concentrated under reduced pressure. The crude product was purified by silica gel chromatography (petroleum ether/ethyl acetate 8:2) to give **143** as a white opalescent solid (500mg, 66.1%). Rf=0.15 (petroleum ether/ ethyl acetate 8:2). ^{1}H NMR (600 MHz, $CDCl_3$) δ8.14 – 8.06 (m, 1H, 6'ArH), 7.59 – 7.50 (m, 2H, 3'4'ArH), 7.42 – 7.37 (m, 1H,5'ArH), 2.91 (br, 4H, $NHSCH_2CH_2$). ^{13}C NMR (151 MHz, $CDCl_3$) δ169.15, 160.24, 135.71, 134.78, 132.53, 131.74, 127.10, 124.59, 25.78.

ethyl 1-(5-amino-1,3,4-thiadiazol-2-yl)piperidine-3-carboxylate (144): 2-amino-5-bromo1,3,4-thiadiazole (300mg, 1.67mmol), ethyl nipecotate (284 µl, 1.83mmol) and DIPEA (1.42ml, 8.35mmol) were dissolved in DMF (6ml) and stirred at 80°C for one hour before evaporating solvent under vacuum. The mixture was extracted with ethyl acetate(3x30ml) and water(30ml). Combined organic phases were washed with brine (90ml), dried (Na_2SO_4) and concentrated under reduced pressure. The crude product was purified by silica gel chromatography (DCM/MeOH 98:2 to 97:3) to give **144** as a white solid (318mg, 74.5%). Rf= 0.12 (petroleum ether/ethyl acetate 7:3). MS(ESI) m/z 257.4/259.4 [MH+] ^{1}H NMR (600 MHz, $CDCl_3$) δ5.08 (s, 2H, NH_2), 4.11 (q, J = 7.1 Hz, 2H, OCH_2), 3.83 (dd, J = 12.9, 4.0 Hz, 1H, 2'PyrH), 3.56 (dd, J = 13.2, 3.5 Hz, 1H, 2'PyrH), 3.18 (dd, J = 12.8, 10.1 Hz, 1H, 6'PyrH), 3.11 – 3.03 (m, 1H, 6'PyrH), 2.66 – 2.55 (m, 1H, 3'PyrH), 2.08 – 1.97 (m, 1H, 4'PipH), 1.75 (dd, J = 8.9, 3.9 Hz, 1H,4'PipH), 1.70 – 1.57 (m, 2H, 5'PipH), 1.23 (t, J = 7.2 Hz, 3H, OCH_2CH3). ^{13}C NMR (151 MHz, $CDCl_3$) δ173.11, 165.69, 160.53, 60.83, 51.89, 50.39, 40.69, 26.96, 23.59, 14.28.

ethyl N-(5-amino-1,3,4-thiadiazol-2-yl)-N-methylglycinate (145): 2-amino-5-bromo1,3,4-thiadiazole (300mg, 1.67mmol), ethyl N-methylglicinate hydrochloride (281 mg, 1.83mmol) and DIPEA (1.08ml, 8.35mmol) were dissolved in DMF (7ml) and stirred at 80°C for one hour before evaporating solvent under vacuum. The mixture was extracted with ethyl acetate(3x30ml) and water(30ml). Combined organic phases were washed with brine (90ml), dried (Na_2SO_4) and concentrated under reduced pressure. The crude product was purified by silica gel chromatography (DCM/MeOH 98:2) to give **145** as a white solid (416mg, 80.4%). Rf= 0.33 (DCM/MeOH 95:5). ^{1}H NMR (600 MHz, DMSO-D6) δ6.41 (s, 2H), 4.10 (s, 2H), 4.11-4.07 (m, 4H), 3.63-3.58 (m, 2H), 3.13 (qd, J = 7.3, 4.2 Hz, 2H), 2.97 (s, 2H), 1.18 (td, J = 7.1, 4.6 Hz, 3H). ^{13}C NMR (151 MHz, DMSO-D6) δ162.9, 161.0, 54.1, 53.6, 42.4, 41.0, 17.3, 13.0

ethyl N-(5-amino-1,3,4-thiadiazol-2-yl)-N-benzylglycinate (146): 2-amino-5-bromo1,3,4-thiadiazole (500mg, 2.78mmol), ethyl N-benzylglicinate (573 µl, 3.06mmol) and DIPEA (0.92ml, 5.55mmol) were dissolved in DMF (6ml) and stirred at 80°C for one hour before evaporating solvent under vacuum. The mixture was extracted with ethyl acetate(3x30ml) and water(30ml). Combined organic phases were washed with brine (90ml), dried (Na_2SO_4) and concentrated under reduced pressure. The crude product was purified by silica gel chromatography (petroleum ether/ethyl acetate/methanol 7:2.5:0.5) to give **146** as a white solid (712mg, 77.6%). Rf= 0.12 (petroleum ether/ethyl acetate 7:3). ^{1}H NMR (600 MHz, ACETONITRILE-D3) δ7.89 (s, 2H), 7.34-7.27 (m, 5H), 5.34 (s, 2H), 4.53 (s, 2H), 4.10 (q, J = 7.1 Hz, 2H), 1.17 (t, J = 7.2 Hz, 3H). ^{13}C NMR (151 MHz, ACETONITRILE-D3) δ169.6, 163.7, 162.5, 160.4, 136.9, 128.7, 127.9, 127.8, 61.0, 57.3, 51.9, 35.7, 30.5, 13.6.

General procedure for the synthesis of compounds 54, 55 and 56: the desired heterocyclic amino derivate (1 mmol), compound **143** (1 mmol), and DIPEA (1 mmol) were dissolved in DMF at 100°C and stirred overnight. The reaction mixture was extracted with ethyl acetate (3x30 ml) and sodium bicarbonate saturated solution (30ml). The collected organic phases were washed with brine (90ml), dried (Na_2SO_4) and concentrated under reduced pressure.

ethyl 1-(5-(2-chlorobenzamido)-1,3,4-thiadiazol-2-yl)piperidine-3-carboxylate (54): The reaction was run with **144** (100mg, 0.390mmol), **143** (92.4mg, 0.390 mmol), and DIPEA (66µl, 0.390mmol). The crude product was purified by silica gel chromatography (petroleum ether/ethyl acetate 7:3 to 6:4) to give **54** as a white solid (130mg, 84.9%). Rf= 0.18 (DCM/MeOH 99:1). MS(ESI) m/z 395.4/397.4 [MH+]. ^{1}H NMR (600 MHz,$CDCl_3$) δ=7.78 (dd, J = 7.4, 1.7 Hz, 1H, 6'ArH), 7.41 (dddd, J = 19.9, 14.6, 7.6, 1.4 Hz, 3H, 3'4'5'ArH), 4.18 (q, J = 7.1 Hz, 2H,OCH_2), 3.96 (dd, J = 13.1, 3.9 Hz, 1H, 2'PipH), 3.63 (m, J = 13.2 Hz, 1H, 2'PipH), 3.19 (dd, J = 13.0, 10.4 Hz, 1H, 6'PipH), 3.13 – 3.07 (m, 1H, 6'PipH), 2.60 (tt, J = 10.5, 3.9 Hz, 1H, 3'PipH), 2.15 – 2.07 (m, 1H,4'PipH), 1.78 (dd, J = 9.4, 3.8 Hz, 1H, 4'PipH), 1.74 – 1.59 (m, 2H, 5'PipH), 1.29 (t, J = 7.1 Hz, 3H, OCH_2CH3). ^{13}C NMR (151 MHz, $CDCl_3$) δ=172.97, 167.78, 164.15, 151.86, 132.80, 132.14, 130.65, 130.59, 127.15, 60.90, 50.94, 50.07, 40.55, 27.10, 23.65, 14.36.

ethyl N-methyl-N-(5-(2-chlorobenzamido)-1,3,4-thiadiazol-2-yl)glycinate (55): The reaction was run with **145** (250mg, 0.975mmol), **143** (231mg, 0.975 mmol), and DIPEA (165µl, 0.975mmol). The crude product was purified by silica gel chromatography (petroleum ether/ethyl acetate 7:3 to 6:4) to give **55** as a white solid (325mg, 81.9%). Rf= 0.18 (DCM/MeOH 99:1). ^{1}H NMR (600 MHz, DMSO-D6) δ12.67 (s, 1H), 7.63-7.44 (m, 4H), 4.33-4.30 (m, 2H), 4.15-4.12 (m, 2H), 3.15-3.12 (m, 3H), 1.21 (t, J = 7.2 Hz, 4H). ^{13}C NMR (151 MHz, DMSO-D6) δ169.2, 134.2, 132.0, 130.3, 129.8, 129.5, 127.2, 60.7, 53.2, 40.4, 14.1.

ethyl N-benzyl-N-(5-(2-chlorobenzamido)-1,3,4-thiadiazol-2-yl)glycinate (56): The reaction was run with **146** (500mg, 2.61 mmol), **143** (408mg, 2.61 mmol), and DIPEA (66µl, 0.390mmol). The crude product was purified by silica gel chromatography (petroleum ether/ethyl acetate 7:3 to 6:4) to give **56** as a white solid (618mg, 82.3%). Rf= 0.41 (petroleum ether/ethyl acetate/methanol 7:3). ^{1}H NMR (600 MHz, CHLOROFORM-D) δ7.77 (d, J = 7.6 Hz, 1H), 7.42 (d, J = 7.9 Hz, 1H), 7.39-7.31 (m, 5H), 7.28 (d, J = 7.2 Hz, 2H), 4.65 (s, 2H), 4.20 (q, J = 7.1 Hz, 2H), 4.07 (s, 2H), 1.27 (t, J = 7.1 Hz, 3H). ^{13}C NMR (151 MHz, CHLOROFORM-D) δ169.0, 167.3, 164.0, 151.4, 135.3, 132.6, 132.1, 132.0, 130.5, 130.5, 128.9, 128.2, 127.9, 127.0, 61.4, 56.8, 50.7, 14.2.

8.1.2 Biochemistry

Cells and Treatments Human myelomonocytic THP-1 cells were cultured in RPMI 1640 medium (Aurogene, Rome, Italy) supplemented with fetal bovine serum (10%; Aurogene), L-glutamine (2 mM; Aurogene), penicillin (100 IU/mL; Aurogene) and streptomycin (100 mg/mL; Aurogene). Cell culture medium was replaced every 2-3 days, and the cultures were maintained at 37°C and 5% CO_2 in a fully humidified incubator. The day before each experiment, cells were plated in 48-well culture plates (90.000 cells/well) and were differentiated by treatment with PMA (50 nM, 24 h; Sigma-Aldrich). PMA-differentiated THP-1 cells were washed twice with phosphate-buffered saline (PBS) and primed with LPS (10 µg/mL, 4 h; Sigma-Aldrich) in serum-free medium. Cells were then incubated with compounds dissolved in medium containing 0.1% DMSO for 1 h and cell death was triggered with ATP (5 mM, 90 min; Sigma-Aldrich). MCC950 (Sigma-Aldrich batch #45216 and batch #85021 and from Crysdot (product n. CD31002496; OS05876-18070932) was used in the experiments.

LDH Release Measurement Cell death was quantified by using the CytoTox 96 non-radioactive cytotoxicity assay (Promega Corporation, Madison, MI, USA): LDH activity was determined in differentiated THP-1 supernatant, after 1.5 h from ATP treatment, by measuring absorbance using the Victor X4 (PerkinElmer, Waltham, MA, USA) at λ = 490 nm. Cell death was expressed according to the manufacture's instruction.

IL-1β Release IL-1β release was quantified in differentiated THP-1 supernatant, obtained as previously described, using Human IL-1β Uncoated ELISA kit (Invitrogen, MA, USA), according to the manufacture's instruction.

Cytotoxicity Assay THP-1 were plated in 96-wells culture plates (15.000 cells/well) and were treated with increasing concentrations (0.1–100 µM) of each compound. Cell viability was measured at 72 h by the MTT assay, a colorimetric assay based on the conversion of the water-soluble 3-(4,5-dimethylthiazol-2-yl)- 2,5-diphenyltetrazolium bromide (MTT; Sigma-Aldrich) to an insoluble purple formazan by actively respiring cells. The formazan concentration was determined by measuring absorbance in the Victor X4 at a $\lambda = 570$ nm.

Cloning, mutagenesis, protein Expression and purification For recombinant protein expression of the C-terminal domain of the human Gasdermin-D (GSDMD), cDNA encoding the full-length GSDMD were cloned into a pET vector with an N-terminal X 6 His-SUMO tag (pET-SUMO-hGSDMD, Addgene plasmid # 111559). cDNA was isolated with Miniprep (PureLink Quick Plasmid Miniprep Kit, Invitrogen) and sequenced using T7reverse primers. Isolated cDNA was mutated using Q5 Site-directed mutagenesis kit (New England Biolabs inc.). The DNA was amplified with primers designed for the deletion of the bases coding for the N-terminal domain of GSDMD (GSDMD-NT) and the insertion of the bases coding for TEV protease site on the new N-terminal of the GSDMD-CT domain. Forward primer: 5'-gaa aac ctg tat ttt cag ggc ggg gtc cct gcg gag ggg -3, Reverse Primer: 5'-acc acc aat ctg ttc tct gtg agc ctc aat aat atc -3'. After KLD reaction, NEB 5-alpha Competent E. coli (New England Biolabs, NEB#C2987) were transformed and incubated overnight at 37°C in Kanamycin LB media. The manipulated cDNA was isolated with PureLink Quick Plasmid Miniprep standard procedure and sequenced using T7reverse primers. Manipulated cDNA was transformed in BL-21* competent cells. Transformed BL-21* were grown at 37°C in 2 L of LB Kanamycin media and protein expression was induced (OD = 0.62) at 20°C overnight with IPTG (0.75 mM solution). Cells were harvested and lysed in a FF6 wash buffer (20 mM phosphate buffer, 500 mM NaCl, 0.02% NaN3) adding lysozyme, Triton 100x 25%, freezing at -80°C and thawing. DNAse was added to the solution and the recombinant SUMO-HisTag GSDMD-CT in the cleared cell lysate were purified by affinity chromatography on HisTrap fast flow 5 mL column (Sigma Aldrich). Elution fractions containing the GSDMD-CT protein were pooled, incubated with TEV protease, and dialysed at 4°C. A second HisTrap affinity chromatography was run to remove uncleaved protein, the His-SUMO tag, the His-tagged TEV protease and aspecific binders. GSDMD-CT was isolated in solution with an overall yield of 43 mg/L of LB colture.

Expression of ^{15}N- and ^{13}C-labelled proteins For the recombinant expression of the ^{15}N- and ^{13}C-labelled proteins, similar procedures described for unlabelled protein were followed. The manipulated cDNA was transformed in BL-21* competent cells. Transformed BL-21* were grown at 37°C in 1 L of LB Kanamycin media. When OD was around 0.8, cells were harvested by centrifugation at moderate speed (5 minutes at 5000 rpm). Pellet was washed with M9 media (2 x 300 mL). M9 medium was prepared according to literature procedures.[130] Cell were suspended in 1L of M9 media, formulated with NH_4Cl ^{15}N-NH_4Cl and glucose or ^{13}C-glucose for the expression of ^{15}N and or ^{13}C labelled version of GSDMD. After 1 h, protein expression was induced at 20°C overnight with IPTG (0.75 mM solution). Purification followed the same strategy described before. ^{15}N-GSDMD-CT was isolated in solution with an overall yield of 21 mg/L of M9 colture. ^{15}N^{13}C-GSDMD-CT double labelled protein was isolated in 11 mg/L of minimal media colture.

SDS Page analysis of proteins The homogeneity and purity GSDMD were checked by NuPAGE 4-12 bis-tris gel electrophoresis (4% stacking and 12.5% separating gels). Protein samples were added of 5 µL of denaturing SDS buffer, heated at 100°C for 5 min and loaded to the gel. Electrophoresis was run at room temperature for 35 min at 200 V, 120 mA, 25W. The gel was stained with InstaBlue treatment (1 h) followed by water washing.

protein NMR sample preparation, data collection and assignment NMR samples were prepared in a buffer of 20 mM phosphate (Na_2HPO_4 and NaH_2PO_4), pH 7.2, 50 mM sodium chloride, 2 mM DTT and 0.02% NaN3 with a protein concentration of 0.8 mM for assignment and 100–200 µM for titrations. Backbone and sidechain assignment of the domain was obtained from a combination of 3D HNCACB, (H)C(CCO)NH, HNCO, HN(CA)CO, 15N and 13C resolved 3D NOESY-HSQCs and a HCCH-TOCSY experiment recorded at 800 MHz on Bruker Avance spectrometers at 35 °C. Spectra were processed with Topspin 4.0.6 (Bruker) and all assignments were performed with CCPN analysis 2.4.[131]

Circular dichroism UV and Circular Dichroism (CD) spectra of 100 µg/ml samples were measured on the Applied Photophysics Chirascan Plus spectrometer (Leatherhead, UK). Quartz Suprasil rectangular cuvettes (Hellma UK and Starna Scientific Ltd) were employed. The instrument was flushed continuously with pure evaporated nitrogen throughout the experiment. The following parameters were employed: Wavelength Range 260-190nm, Spectral Bandwidth 2nm, Stepsize 1nm, Time per point 1.36s, Pathlength 0.5 mm. The UV and CD spectra were buffer baseline subtracted and measured at 23°C. Where appropriate the CD spectra were smoothed with a window factor of 4 using the Savitzky-Golay method for better presentation. Data processing were done using APL Prodata Viewer v4.2.15 and spectra presentation using Origin V6. The signal ($mdeg$) was converted to molar ellipticity (θ) using equation 8.1:

$$\theta = \frac{mdegM}{CL10} \tag{8.1}$$

in which M is the molecular weight, L is the path length of the cell in centimeters, and C is the concentration of the protein in g/L.

For the thermal ramping, The far-UV CD spectra of each sample were first recorded at 23°C, cooled to 6oC then heated to high temperature (94°C), then cooled to 23°C after heating. The multi–wavelength melting profiles monitored at ε (260-190nm) were recorded during the heating (6 to 94°C) process. The instrument was equipped with a Quantum NorthWest TC125 Peltier unit set to change temperature from 6 to 94°C at 1°C per minute rate with a 2°C step size. A 1.36s and time-per-point CD measurement time (total scan time = 2minutes per spectrum) and 1nm step-size were employed in the 260-190nm with a 2nm Spectral Bandwidth. A 0.5mm rectangular cell pathlength was used. The temperatures were measured directly with a thermocouple probe in the sample solution and buffer baseline auto-subtracted. Melting temperatures were determined from the derivative CD vs Temperature spectra and fitted using a Levenberg–Marquardt algorithm (LMA) on the van't Hoff isochore. (Global 3, Global Analysis for T-ramp Version 1.2 built 1786, Applied Photophysics Ltd, 2007-2012).

NMR screening data collection Samples were prepared by combining ligand stock solution in DMSO, protein in phosphate buffer (20 mM phosphate (Na_2HPO_4 and NaH_2PO_4), pH 7.2, 50 mM sodium chloride, 2 mM DTT and 0.02% NaN3), 10% D_2O to a final volume of 600 µL. Group A) Ligand 1 mM, protein 50 µM, phosphate buffer 460.8 µL, D_2O 60 µL, 1% DMSO. Group B) Ligand 0.5 mM, protein 25 µM, phosphate buffer 534 µL, D_2O 60 µL, 10% DMSO. Spectra were acquired with a 600 MHz AVANCE NEO spectrometer equipped with a triple resonance cryoprobe with 1H/13C/15N channels and a SampleJet for automation (all Bruker, UK). For each sample, STD spectra were acquired by applying the Bruker pulse sequence *stddiffesgp.3*, for saturation transfer difference with shaped pulse train for saturation on f2 channel alternating between on- and off-resonance, with spoil sequence to destoy unwanted magnetization, water suppression using excitation sculpting with gradients, and with spinlock to suppress protein signals. The on-resonance frequency was -0.23 ppm and the off-resonance frequency -40.0 ppm. A total saturation time of 1 s, 2 s, or 4 s was employed, with 8 scans. Each sample was maintained at a temperature of 25 °C during the NMR spectrum acquisition.

8.1.3 Animals

SAMP8 (Senescence-Accelerated Mouse-Prone 8) mice (2 months old, 20–25 g body weight), a spontaneous genetic model of AD, and their control strain SAMR1 (Senescence-Accelerated Mouse-Resistant 1) (2 months old, 20–25 g body weight) were purchased from ENVIGO Srl (San Pietro al Natisone UD, Italy) and employed throughout the study. The animals were fed with standard laboratory chow and tap water ad libitum, and were not employed for at least 1 week after their delivery to the laboratory. They were housed, one in a cage, in temperature-controlled rooms on a 12-h light cycle at 22–24 °C and 50–60% humidity. Standard diet (Altromin International, Germany; SD, TD.2018) provided 3.1 kcal/g, of which 18% as fats, 24% as proteins and 58% as carbohydrates. The feeding behaviour (frequency and amount) was assessed until the day before the sacrifice. At the end of study, animals were euthanised. Animals were housed, three in a cage, in temperature-controlled rooms on a 12-h light cycle at 22–24 °C and 50–60% humidity. Their care and handling were in accordance with the provisions of the European Community Council Directive 210/63/UE, recognised and adopted by the Italian Government. The experiments were approved by the Ethical Committee for Animal Experimentation of the University of Pisa and by the Italian Ministry of Health on february 25th 2016 (Authorisation No. 198/2016-PR). The SAMP8 mouse is one of the accelerated senescence strains that develops spontaneously early learning and memory deficits, with similar features to those observed in AD. Of note, the SAMP8 mouse displays the main clinical and pathophysiological features to those observed in AD patients, including Aβ 1–40 or 1–42 proteins in hippocampal granules, hyperphosphorylation of tau protein, increase in α-syn, presenilin, oxidative damage, glutamate levels, and nNOS, along with the decrease in ChAT activity. SAMP8 and SAMR1 animals at four, six and eight months of age were subjected to Morris Water Maze (MWM) test in order to evaluate alterations of cognitive functions from the initial phases of early learning and memory deficiencies until the full development of AD. The day after the evaluation of cognitive and motor performances, animals were employed for the assessment of faecal output, as described below. One hour after the evaluation of faecal output, SAMP8 and SAMR1 animals at six months of age were euthanised

and colonic specimens were dissected and processed for functional experiments and other assays, as described below.

Male Sprague–Dawley rats (200–250 g body weight) were used throughout the study. The animals were fed standard laboratory chow and tap water ad libitum and were not employed for at least 1 week after their delivery to the laboratory. They were housed, three in a cage, in temperature-controlled rooms on a 12-h light cycle at 22–24 °C and 50–60% humidity. Their care and handling were in accordance with the provisions of the European Community Council Directive 86-609, recognized and adopted by the Italian Government. All efforts were made to minimize animals' suffering and to reduce the number of animals used.

Evaluation of Cognitive Functions MWM test: The MWM uses a round pool (90 cm in diameter and 60 cm in height) filled with opaque water (26 ± 1 °C temperature). The pool was divided into four quadrants of equal area, designated arbitrarily as northeast (NE), southeast (SE), southwest (SW) and northwest (NW). A circular platform (10 cm diameter and 30 cm height) was placed in the centre of one quadrant. All external clues were constant for the spatial orientation of mice. A camera mounted directly above the centre of the round pool monitored animal movements. The camera image was digitalised and fed to a computerised tracking system that monitored and stored animal movements. The MWM test consists of visible-platform acquisition training, hidden-platform training, and probe trial as previously reported. The platform was in the same location for both visible-platform training and hidden platform training. In the acquisition training, the escape latency was assessed for each animal (time required to reach the platform). Mice were placed on the platform for 15 s before being released into the water. Mice were allowed to swim and find the visible platform within 60 s. Each animal was subjected to sessions of four trials every day for 2 days. After the daily trial, mice were returned to their home cages for resting. In the hidden-platform training, performed by submerging the platform 1.5 cm below the surface of the water, escape latency was evaluated over the next 5 days. Each animal was subjected to sessions of four trials every day. Finally, on the eighth day, the platform was removed from the tank for the probe trial. The number of target crossings the number of entries into the target quadrant, the time spent in the target quadrant where the platform was placed, the swimming speed and swim distance were assessed in 60 s. Data were expressed as raw values.

Induction of colitis For acute experimental colitis induction, C57BL/6 mice were treated with 2.5% DSS or saline in their drinking water for 9 days. During the experiment, body weight, stool, and body posture were monitored daily to assess the DAI (Cooper et al., 1993; Alex et al., 2009). The DAI is the combined score of weight loss compared with initial weight, stool consistency, and bleeding. The details are as follows: (a) weight loss (0 point none, 1 point 1–5% weight loss, 2 points 5–10% weight loss, 3 points 10–15% weight loss, and 4 points more than 15% weight loss), (b) stool consistency or diarrhea (0 point normal, 2 points loose stools, and 4 points watery diarrhea), and (c) bleeding (0 point no bleeding, 2 points slight bleeding, and 4 points gross bleeding). Mice were euthanized at the indicated time points, and the colon was immediately collected for colon length measurement, colon explant culture, colon Western blot analysis, and histological analysis.

List of Abbreviations

Aβ	amyloid-β
ACN	acetonitrile
AD	Alzheimer's disease
AGE	Advanced glycation end product
AIM2	Absent In Melanoma 2
ALRs	AIM2-Like Receptors
ASC	Apoptosis-associated speck-like protein containing a CARD
BIR	Baculovirus Inhibitor of apoptosis protein Repeat
BRET	Bioluminescence Resonance Energy Transfer
C5aR	Complement component 5a Receptor
CAPS	Cryopyrin-associated periodic fever syndrome
CARD	Caspase Activation and Recruitment Domain
Casp-1	Caspase-1
CD36	Cluster of differentiation 36
CDI	carbonyldiimidazole
CIITA	class II major histocompatibility complex transactivator
CINCA	Chronic Infantile Neurological Cutaneous and Articular syndrome
CNS	Central nervous system
DABCO	1,4-diazabicyclo[2.2.2]ottane
DAMPs	Danger-Associated Molecular Patterns
DBU	1,8-diazabicyclo[5.4.0]undec-7-ene
DCC	dicyclohexylcarbodiimide

DIPEA	diisopropylethylamine
DSS	dextrane sodium sulphate
DUBs	deubiquitinating enzyme
EAE	Experimental autoimmune encephalomyelitis
FADD	Fas-associated protein with death domain
FBX	F-box (protein)
FCAS	Familial cold auto-inflammatory syndrome
FFA	Free fatty acid
FIIND	function to find domain
FISNA	Fish-specific NACHT associated
FKLC	Palmoplantar carcinoma and familial keratosis lichenoides chronica
GSDMD	Gasdermin-D
GSDMD-CT	Gasdemin-D C-terminal domain
GSDMD-NT	Gasdemin-D N-terminal domain
HBTU	N,N,N',N'-Tetramethyl-O-(1H-benzotriazol-1-yl)uronium hexafluorophosphate
HD1	Helical domain 1
HD2	Helical domain 2
HOBt	hydroxybenzotriazole
IKK	Inhibitor of NF-κB kinase
IL	Interleukin
IL-18BP	IL-18 binding protein
IL-1R	IL-1 Receptor
IPTG	isopropyl β-D-1-thiogalactopyranoside
IRAK	Interleukin-1 receptor-associated kinase 1
JNK1	Jun N-terminal kinase-1
LDH	lactate dehydrogenase
LPS	Lipopolysaccharides
LPS	lipopolysaccharide

LRR	Leucine-Rich Repeats
MAMPs	Microbe-Associated Molecular Patterns
MAPKKK	mitogen-activated protein kinase kinase kinase
MAVS	Mitochondrial antiviral-signalling protein
MS	Multiple sclerosis
MWS	Muckle-Wells syndrome
MyD88	Myeloid differentiation primary response protein 88
NACHT	NAIP, CIITA, HET-E, and TP1-containing domain
NAFLD	Non-alcoholic fatty liver disease
NAIAD	NLRP1 associated autoinflammation with arthritis and dyskeratosis
NASH	Nonalcoholic steatohepatitis
NBD	Nucleotide-Binding Domain
NBD	Nucleotide-binding domain
NEK7	NIMA-related kinase 7
NHS	N-hydroxysuccinimide
$NLRP3^{PYD}$	PYD domain of NLRP3
NLRs	Nucleotide-binding domain and Leucine-rich repeat Receptors
NOMID	Neonatal-onset multisystem inflammatory disease
oxLDL	Oxidised low density lipoprotein
P2X7R	P2X7 receptors
PAMPs	Pathogen-Associated Molecular Patterns
PD	Parkinson's disease
PMA	phorbol myristate acetate
PP2A	Protein phosphatase 2A
PRRs	Pattern Recognition Receptors
PtdIns4P	Phosphatidylinositol 4-phosphate
$PTPN_22$	Protein tyrosine phosphatase nonreceptor type 22
PTSA	p-Toluen sulfonic acid

PYD	Pyrin Domain
RAGE	Receptor for AGE
RIPK1	Receptor-interacting serine/threonine-protein kinase 1
ROS	Reactive oxygen species
S1P	Sphingosine-1-phosphate
S1PR1	S1P receptor 1
SAA	Serum amyloid A
SCAN4	Syndrome of enterocolitis and auto-inflammation associated with mutation NLRC4
SFA	Saturated fatty acid
STAND	Signal transduction ATPases with numerous domains
STD	Saturation-Transfer Difference
TAK1	TGF-β-activated kinase 1
TEA	triethylamine
TGN	trans-Golgi network
TLR	Toll-like receptor
TNFR	tumor-necrosis factor receptor
TRIF	TIR-domain-containing adapter-inducing interferon-β
TRIM31	Tripartite motif containing 31
waterLOGSY	Water-Ligand Observed via Gradient SpectroscopY
WHD	Winged-helix domain

Bibliography

(1) Huang, Y.; Xu, W.; Zhou, R. NLRP3 inflammasome activation and cell death. *Cell Mol Immunol* **2021**, *18(9)*, 2114–2127, DOI: https://doi.org/10.1038/s41423-021-00740-6.

(2) Gong, T.; Liu, L.; Jiang, W.; Zhou, R. DAMP-sensing receptors in sterile inflammation and inflammatory diseases. *Nat Rev Immunol* **2020**, *20(2)*, 95–112, DOI: https://doi.org/10.1038/s41577-019-0215-7.

(3) Martinon, F.; Burns, K.; Tschopp, J. The inflammasome: a molecular platform triggering activation of inflammatory caspases and processing of proIL-1beta. *Mol Cell* **2002**, *10(2)*, 417–426.

(4) Lamkanfi, M.; Dixit, V. M. Mechanisms and Functions of Inflammasomes. *Cell* **2014**, *157(5)*, 1013–1022, DOI: https://doi.org/10.1016/j.cell.2014.04.007.

(5) Tuladhar, S.; Kanneganti, T.-D. NLRP12 in innate immunity and inflammation. *Mol Aspects Med* **2020**, *76*, 100887, DOI: https://doi.org/10.1016/j.mam.2020.100887.

(6) Sharma, M.; de Alba, E. Structure, Activation and Regulation of NLRP3 and AIM2 Inflammasomes. *Int J Mol Sci* **2021**, *22(2)*, 872, DOI: https://www.mdpi.com/1422-0067/22/2/872.

(7) Man, S. M.; Kanneganti, T.-D. Regulation of inflammasome activation. *Immunol Rev* **2015**, *265(1)*, 6–21, DOI: https://doi.org/10.1111/imr.12296.

(8) MacDonald, J. A.; Wijekoon, C. P.; Liao, K.-C.; Muruve, D. A. Biochemical and structural aspects of the ATP-binding domain in inflammasome-forming human NLRP proteins. *IUBMB Life* **2013**, *65(10)*, 851–862, DOI: https://doi.org/10.1002/iub.1210.

(9) Ju Young, B.; Hyun Ho, P. Crystal Structure of NALP3 Protein Pyrin Domain (PYD) and Its Implications in Inflammasome Assembly. *J Biol Chem* **2011**, *286(45)*, 39528–39536, DOI: https://doi.org/10.1074/jbc.M111.278812.

(10) Oroz, J.; Barrera-Vilarmau, S.; Alfonso, C.; Rivas, G.; de Alba, E. ASC Pyrin Domain Self-associates and Binds NLRP3 Protein Using Equivalent Binding Interfaces. *J Biol Chem* **2016**, *291(37)*, 19487–19501, DOI: https://doi.org/10.1074/jbc.M116.741082.

(11) Jumper, J. et al. Highly accurate protein structure prediction with AlphaFold. *Nature* **2021**, *596(7873)*, 583–589, DOI: https://doi.org/10.1038/s41586-021-03819-2.

(12) Andreeva, L.; David, L.; Rawson, S.; Shen, C.; Pasricha, T.; Pelegrin, P.; Wu, H. NLRP3 cages revealed by full-length mouse NLRP3 structure control pathway activation. *Cell* **2021**, DOI: https://doi.org/10.1016/j.cell.2021.11.011.

(13) Hochheiser, I. V.; Pilsl, M.; Hagelueken, G.; Moecking, J.; Marleaux, M.; Brinkschulte, R.; Latz, E.; Engel, C.; Geyer, M. Structure of the NLRP3 decamer bound to the cytokine release inhibitor CRID3. *Nature* **2022**, *604*, 184–189, DOI: https://doi.org/10.1038/s41586-022-04467-w.

(14) Sharif, H.; Wang, L.; Wang, W. L.; Magupalli, V. G.; Andreeva, L.; Qiao Qiand Hauenstein, A. V.; Wu, Z.; Núñez, G.; Mao, Y.; Wu, H. Structural mechanism for NEK7-licensed activation of NLRP3 inflammasome. *Nature* **2019**, *570(7761)*, 338–343, DOI: https://doi.org/10.1038/s41586-019-1295-z.

(15) Tapia-Abellán, A.; Angosto-Bazarra, D.; Alarcón-Vila, C.; Baños, M. C.; Hafner-Bratkovič, I.; Oliva, B.; Pelegrín, P. Sensing low intracellular potassium by NLRP3 results in a stable open structure that promotes inflammasome activation. *Sci Adv* **2021**, *7(38)*, eabf4468, DOI: https://doi.org/10.1126/sciadv.abf4468.

(16) Sandall, C. F.; Ziehr, B. K.; MacDonald, J. A. ATP-Binding and Hydrolysis in Inflammasome Activation. *Molecules* **2020**, *25(19)*, DOI: https://doi.org/10.3390/molecules25194572.

(17) Zhang, L.; Chen, S.; Ruan, J.; Wu, J.; Tong, A. B.; Yin, Q.; Li, Y.; David, L.; Lu, A.; Wang, W. L.; Marks, C.; Ouyang, Q.; Zhang, X.; Mao, Y.; Wu, H. Cryo-EM structure of the activated NAIP2-NLRC4 inflammasome reveals nucleated polymerization. *Science* **2015**, *350(6259)*, 404–409, DOI: https://www.science.org/doi/10.1126/science.aac5789.

(18) Maharana, J.; Panda, D.; De, S. Deciphering the ATP-binding mechanism(s) in NLRP-NACHT 3D models using structural bioinformatics approaches. *PloS one* **2018**, *12(13)*, 1–17, DOI: https://doi.org/10.1371/journal.pone.0209420.

(19) Kelley, N.; Jeltema, D.; Duan, Y.; He, Y. The NLRP3 Inflammasome: An Overview of Mechanisms of Activation and Regulation. *Int J Mol Sci* **2019**, *20(13)*, DOI: https://doi.org/10.3390/ijms20133328.

(20) Gritsenko, A.; Green, J. P.; Brough, D.; Lopez-Castejon, G. Mechanisms of NLRP3 priming in inflammaging and age related diseases. *Cytokine Growth Factor Rev.* **2020**, *55*, 15–25, DOI: https://doi.org/10.1016/j.cytogfr.2020.08.003.

(21) Tezcan, G.; Martynova, E. V.; Gilazieva, Z. E.; McIntyre, A.; Rizvanov, A. A.; Khaiboullina, S. F. MicroRNA Post-transcriptional Regulation of the NLRP3 Inflammasome in Immunopathologies. *Fron Pharmacol* **2019**, *10*, 451, DOI: https://doi.org/10.3389/fphar.2019.00451.

(22) Hoss, F.; Mueller, J. L.; Rojas Ringeling, F.; Rodriguez-Alcazar, J. F.; Brinkschulte, R.; Seifert, G.; Stahl, R.; Broderick, L.; Putnam, C. D.; Kolodner, R. D.; Canzar, S.; Geyer, M.; Hoffman, H. M.; Latz, E. Alternative splicing regulates stochastic NLRP3 activity. *Nat Comm* **2019**, *10(1)*, DOI: https://doi.org/10.1038/s41467-019-11076-1.

(23) Blasiak, J.; Wei, M.; Wang, L.; Wu, T.; Xi, J.; Han, Y.; Yang, X.; Zhang, D.; Fang, Q.; Tang, B. NLRP3 Activation Was Regulated by DNA Methylation Modification during *Mycobacterium tuberculosis* Infection. *Biomed Res Int* **2016**, DOI: https://doi.org/10.1155/2016/4323281.

(24) Muñoz-Planillo, R.; Kuffa, P.; Martínez-Colón, G.; Smith, B. L.; Rajendiran, T. M.; Núñez, G. K^+ Efflux Is the Common Trigger of NLRP3 Inflammasome Activation by Bacterial Toxins and Particulate Matter. *Immunity* **2013**, *38(6)*, 1142–1153, DOI: https://doi.org/10.1016/j.immuni.2013.05.016.

(25) Brough, D.; Le Feuvre, R. A.; Wheeler, R. D.; Solovyova, N.; Hilfiker, S.; Rothwell, N. J.; Verkhratsky, A. Ca^{2+} Stores and Ca^{2+} Entry Differentially Contribute to the Release of IL-1β and IL-1α from Murine Macrophages. *J Immunol* **2003**, *170(6)*, 3029–3036, DOI: https://doi.org/10.4049/jimmunol.170.6.3029.

(26) Katsnelson, M. A.; Rucker, L. G.; Russo, H. M.; Dubyak, G. R. K^+ Efflux Agonists Induce NLRP3 Inflammasome Activation Independently of Ca^{2+} Signaling. *J Immunol* **2015**, *194(8)*, 3937–3952, DOI: https://doi.org/10.4049/jimmunol.1402658.

(27) Lawlor, K. E.; Vince, J. E. Ambiguities in NLRP3 inflammasome regulation: Is there a role for mitochondria? *Biochim Biophys Acta* **2014**, *596()*, 1433–1440, DOI: https://doi.org/10.1016/j.bbagen.2013.08.014.

(28) Hornung, V.; Bauernfeind, F.; Halle, A.; Samstad, E. O.; Kono, H.; Rock, K. L.; Fitzgerald, K. A.; Latz, E. Silica crystals and aluminum salts activate the NALP3 inflammasome through phagosomal destabilization. *Nat Immunol* **2008**, *9(8)*, 847–856, DOI: https://doi.org/10.1038/ni.1631.

(29) Dostert, C.; Guarda, G.; Romero, J. F.; Menu, P.; Gross, O.; Tardivel, A.; Suva, M.-L.; Stehle, J.-C.; Kopf, M.; Stamenkovic, I.; Corradin, G.; Tschopp, J. Malarial Hemozoin Is a Nalp3 Inflammasome Activating Danger Signal. *PLOS ONE* **2009**, *4*, 1–10, DOI: https://doi.org/10.1371/journal.pone.0006510.

(30) Dekker, C.; Mattes, H.; Wright, M.; Boettcher, A.; Hinniger, A.; Hughes, N.; Kapps-Fouthier, S.; Eder, J.; Erbel, P.; Stiefl, N.; Mackay, A.; Farady, C. J. Crystal Structure of NLRP3 NACHT Domain With an Inhibitor Defines Mechanism of Inflammasome Inhibition. *J Mol Biol* **2021**, *433(24)*, 4701–4711, DOI: https://doi.org/10.1016/j.jmb.2021.167309.

(31) Guo, C. et al. Cholesterol Homeostatic Regulator SCAP-SREBP2 Integrates NLRP3 Inflammasome Activation and Cholesterol Biosynthetic Signaling in Macrophages. *Immunity* **2018**, *49(5)*, 842–856.e7, DOI: https://doi.org/10.1016/j.immuni.2018.08.021.

(32) Duncan, J. A.; Bergstralh, D. T.; Wang, Y.; Willingham, S. B.; Ye, Z.; Zimmermann, A. G.; Ting, J. P.-Y. Cryopyrin/NALP3 binds ATP/dATP, is an ATPase, and requires ATP binding to mediate inflammatory signaling. *PNAS* **2007**, *104(19)*, 583–589, DOI: https://doi.org/10.1073/pnas.0611496104.

(33) Wang, L.; Sharif, H.; Vora, S. M.; Zheng, Y.; Wu, H. Structures and functions of the inflammasome engine. *J Allergy Clin Immunol* **2021**, *147(6)*, 2021–2029, DOI: https://doi.org/10.1016/j.jaci.2021.04.018.

(34) Li, Y.; Fu, T.-M.; Lu, A.; Witt, K.; Ruan, J.; Shen, C.; Wu, H. Cryo-EM structures of ASC and NLRC4 CARD filaments reveal a unified mechanism of nucleation and activation of caspase-1. *PNAS* **2018**, *115(43)*, 10845–10852, DOI: https://doi.org/10.1073/pnas.1810524115.

(35) Lu, A.; Magupalli, V. G.; Ruan, J.; Yin, Q.; Atianand, M. K.; Vos, M. R.; Schröder, G. F.; Fitzgerald, K. A.; Wu, H.; Egelman, E. H. Unified Polymerization Mechanism for the Assembly of ASC-Dependent Inflammasomes. *Cell* **2014**, *156(6)*, 1193–1206, DOI: https://doi.org/10.1016/j.cell.2014.02.008.

(36) Lu, A.; Li, Y.; Schmidt, F. I.; Yin, Q.; Chen, S.; Fu, T.-M.; Tong, A. B.; Ploegh, H. L.; Mao, Y.; Wu, H. Molecular basis of caspase-1 polymerization and its inhibition by a new capping mechanism. *Nat Struct Mol Biol* **2016**, *23(5)*, 416–425, DOI: https://doi.org/10.1038/nsmb.3199.

(37) Of Pro-Caspases by Oligomerization, A. A. Xiaolu Yang and Howard Y Chang and David Baltimore. *Mol Cell* **1998**, *1(2)*, 319–325, DOI: https://doi.org/10.1016/S1097-2765(00)80032-5.

(38) D'Souza, C. A.; Heitman, J.

(39) Yu, P.; Zhang, X.; Liu, N.; Tang, L.; Peng, C.; Chen, X. Pyroptosis: mechanisms and diseases. *Signal Transduct Target Ther* **2021**, *6(1)*, 128, DOI: https://doi.org/10.1038/s41392-021-00507-5.

(40) Xia, S.; Zhang, Z.; Magupalli, V. G.; Pablo, J. L.; Dong, Y.; Vora, S. M.; Wang, L.; Fu, T.-M.; Jacobson, M. P.; Greka, A.; Lieberman, J.; Ruan, J.; Wu, H. Gasdermin D pore structure reveals preferential release of mature interleukin-1. *Nature* **2021**, *593(7860)*, 607–611, DOI: https://doi.org/10.1038/s41586-021-03478-3.

(41) Liu, Z.; Wang, C.; Yang, J.; Zhou, B.; Yang, R.; Ramachandran, R.; Abbott, D. W.; Xiao, T. S. Crystal Structures of the Full-Length Murine and Human Gasdermin D Reveal Mechanisms of Autoinhibition, Lipid Binding, and Oligomerization. *Immunity* **2019**, *51(1)*, 43–49.e4, DOI: https://doi.org/10.1016/j.immuni.2019.04.017.

(42) Wang, K.; Sun, Q.; Zhong, X.; Zeng, M.; Zeng, H.; Shi, X.; Li, Z.; Wang, Y.; Zhao, Q.; Shao, F.; Ding, J. Structural Mechanism for GSDMD Targeting by Autoprocessed Caspases in Pyroptosis. *Cell* **2020**, *180(5)*, 941–955.e20, DOI: https://doi.org/10.1016/j.cell.2020.02.002.

(43) Huang, Y.; Xu, W.; Zhou, R. NLRP3 inflammasome activation and cell death. *Cell Mol Immunol* **2021**, *18(9)*, 2114–2127, DOI: https://doi.org/10.1038/s41423-021-00740-6.

(44) Diamond, C. E.; Khameneh, H. J.; Brough, D.; Mortellaro, A. Novel perspectives on non-canonical inflammasome activation. *Immunotargets Ther* **2015**, *4*, 131–141, DOI: https://doi.org/10.2147/ITT.S57976.

(45) Shi, J.; Zhao, Y.; Wang, Y.; Gao, W.; Ding, J.; Li, P.; Hu, L.; Shao, F. Inflammatory caspases are innate immune receptors for intracellular LPS. *Nature* **2021**, *514(7521)*, 187–192, DOI: https://doi.org/10.1038/nature13683.

(46) Chu, L. H.; Indramohan, M.; Ratsimandresey, R. A.; Gangopadhyay, A.; Morris, E. P.; Monack, D. M.; Dorfleutner, A.; Stehlik, C. The oxidized phospholipid oxPAPC protects from septic shock by targeting the non-canonical inflammasome in macrophages. *Nat Comm* **2018**, *9(1)*, 996, DOI: https://doi.org/10.1038/s41467-018-03409-3.

(47) Gaidt, M. M.; Ebert, T. S.; Chauhan, D.; Schmidt, T.; Schmid-Burgk, J. L.; Rapino, F.; Robertson, A. A.; Cooper, M. A.; Graf, T.; Hornung, V. Human Monocytes Engage an Alternative Inflammasome Pathway. *Immunity* **2016**, *44(4)*, 833–846, DOI: https://doi.org/10.1016/j.immuni.2016.01.012.

(48) Zhang, M.; Kenny, S. J.; Ge, L.; Xu, K.; Schekman, R. Translocation of interleukin-1β into a vesicle intermediate in autophagy-mediated secretion. *eLife* **2015**, *4*, e11205, DOI: https://doi.org/10.7554/eLife.11205.

(49) Dupont, N.; Jiang, S.; Pilli, M.; Ornatowski, W.; Bhattacharya, D.; Deretic, V. Autophagy-based unconventional secretory pathway for extracellular delivery of IL-1β. *EMBO J* **2011**, *30(23)*, 4701–4711, DOI: https://doi.org/10.1038/emboj.2011.398.

(50) Song, N.; Li, T. Regulation of NLRP3 Inflammasome by Phosphorylation. *Front Immunol* **2018**, *9*, 2305, DOI: https://doi.org/10.3389/fimmu.2018.02305.

(51) Gong, Y.-N.; Wang, X.; Wang, J.; Yang, Z.; Li, S.; Yang, J.; Liu, L.; Lei, X.; Shao, F. Chemical probing reveals insights into the signaling mechanism of inflammasome activation. *Cell Res* **2010**, *20(12)*, 1289–1305, DOI: https://doi.org/10.1038/cr.2010.135.

(52) Martin, B. N. et al. IKKα negatively regulates ASC-dependent inflammasome activation. *Nat Comm* **2014**, *5(1)*, 4977–4991, DOI: https://doi.org/10.1038/ncomms5977.

(53) Stutz, A.; Kolbe, C.-C.; Stahl, R.; Horvath, G. L.; Franklin, B. S.; van Ray, O.; Brinkschulte, R.; Geyer, M.; Meissner, F.; Latz, E. NLRP3 inflammasome assembly is regulated by phosphorylation of the pyrin domain. *J Exp Med* **2017**, *214(6)*, 1725–1736, DOI: https://doi.org/10.1084/jem.20160933.

(54) Sharma, M.; de Alba, E. Structure, Activation and Regulation of NLRP3 and AIM2 Inflammasomes. *Int J Mol Sci* **2021**, *22(2)*, 872, DOI: https://doi.org/10.3390/ijms22020872.

(55) Lopez-Castejon, G.; Luheshi, N. M.; Compan, V.; High, S.; Whitehead, R. C.; Flitsch, S.; Kirov, A.; Prudovsky, I.; Swanton, E.; Brough, D. Deubiquitinases Regulate the Activity of Caspase-1 and Interleukin-1β Secretion via Assembly of the Inflammasome. *J Biol Chem* **2013**, *288(4)*, 2721–2733, DOI: https://doi.org/10.1074/jbc.M112.422238.

(56) Lopez-Castejon, G. Control of the inflammasome by the ubiquitin system. *FEBS Journal* **2020**, *287(1)*, 11–26, DOI: https://doi.org/10.1111/febs.15118.

(57) Han, S.; Lear, T. B.; Jerome, J. A.; Rajbhandari, S.; Snavely, C. A.; Gulick, D. L.; Gibson, K. F.; Zou, C.; Chen, B. B.; Mallampalli, R. K. Lipopolysaccharide Primes the NALP3 Inflammasome by Inhibiting Its Ubiquitination and Degradation Mediated by the SCF^{FBXL2} E3 Ligase. *J Biol Chem* **2015**, *290(29)*, 18124–18133, DOI: https://doi.org/10.1074/jbc.M115.645549.

(58) Humphries, F.; Bergin, R.; Jackson, R.; Delagic, N.; Wang, B.; Yang, S.; Dubois, A. V.; Ingram, R. J.; Moynagh, P. N. The E3 ubiquitin ligase Pellino2 mediates priming of the NLRP3 inflammasome. *Nat Commun* **2018**, *9(1)*, 1560, DOI: https://doi.org/10.3390/ijms22020872.

(59) Paik, S.; Kim, J. K.; Silwal, P.; Sasakawa, C.; Jo, E.-K. An update on the regulatory mechanisms of NLRP3 inflammasome activation. *Cell Mol Immunol* **2021**, *18(5)*, 1141–1160, DOI: https://doi.org/10.1038/s41423-021-00670-3.

(60) Zhou, Q.; Aksentijevich, I.; Wood, G. M.; Walts, A. D.; Hoffmann, P.; Remmers, E. F.; Kastner, D. L.; Ombrello, A. K. Brief Report: Cryopyrin-Associated Periodic Syndrome Caused by a Myeloid-Restricted Somatic NLRP3 Mutation. *Arthritis Rheumatol* **2015**, *67(9)*, 2482–2486, DOI: https://doi.org/10.1002/art.39190.

(61) Altaf, A.; Qu, P.; Zhao, Y.; Wang, H.; Lou, D.; Niu, N. NLRP3 inflammasome in peripheral blood monocytes of acute coronary syndrome patients and its relationship with statins. *Coron Artery Dis* **2015**, *26(5)*, 1473–5830, DOI: https://doi.org/10.1097/MCA.0000000000000255.

(62) Peng, K.; Liu, L.; Wei, D.; Lv, Y.; Wang, G.; Xiong, W.; Wang, X.; Altaf, A.; Wang, L.; He, D.; Wang, H.; Qu, P. P2X7R is involved in the progression of atherosclerosis by promoting NLRP3 inflammasome activation. *J Int Mol Med* **2015**, *35(5)*, 1179–1188, DOI: https://doi.org/10.3892/ijmm.2015.2129.

(63) Liu, W.; Yin, Y.; Zhou, Z.; He, M.; Dai, Y. OxLDL-induced IL-1beta secretion promoting foam cells formation was mainly via CD36 mediated ROS production leading to NLRP3 inflammasome activation. *Inflamm Res* **2014**, *63*, 33–43, DOI: https://doi.org/10.1007/s00011-013-0667-3.

(64) Lee, H.-M.; Kim, J.-J.; Kim, H. J.; Shong, M.; Ku, B. J.; Jo, E.-K. Upregulated NLRP3 Inflammasome Activation in Patients With Type 2 Diabetes. *Diabetes* **2013**, *62(1)*, 194–204, DOI: https://doi.org/10.2337/db12-0420.

(65) Szekanecz, Z.; Szamosi, S.; Kovács, G. E.; Kocsis, E.; Benkő, S. The NLRP3 inflammasome - interleukin 1 pathway as a therapeutic target in gout. *Arch Biochem Biophys* **2019**, *670*, 82–93, DOI: https://doi.org/10.1016/j.abb.2019.01.031.

(66) Zhen, Y.; Zhang, H. NLRP3 Inflammasome and Inflammatory Bowel Disease. *Front Immunol* **2019**, *10*, 276, DOI: https://doi.org/10.3389/fimmu.2019.00276.

(67) Zhang, Y.; Zhao, Y.; Zhang, J.; Yang, G. Mechanisms of NLRP3 Inflammasome Activation: Its Role in the Treatment of Alzheimer's Disease. *Neurochem Res* **2020**, *45(11)*, 2560–2572, DOI: https://doi.org/10.1007/s11064-020-03121-z.

(68) Gao, L.; Dong, Q.; Song, Z.; Shen, F.; Shi, J.; Li, Y. NLRP3 inflammasome: a promising target in ischemic stroke. *Inflamm Res* **2017**, *66(1)*, 17–24, DOI: https://doi.org/10.1007/s00011-016-0981-7.

(69) Govindarajan, V.; de Rivero Vaccari, J. P.; Keane, R. W. Role of inflammasomes in multiple sclerosis and their potential as therapeutic targets. *J Neuroinflammation* **2020**, *17(1)*, 260, DOI: https://doi.org/10.1186/s12974-020-01944-9.

(70) Haque, M. E.; Akther, M.; Jakaria, M.; Kim, I.-S.; Azam, S.; Choi, D.-K. Targeting the microglial NLRP3 inflammasome and its role in Parkinson's disease. *Mov Disord* **2020**, *35(1)*, 20–33, DOI: https://doi.org/10.1002/mds.27874.

(71) Ralston, J. C.; Lyons, C. L.; Kennedy, E. B.; Kirwan, A. M.; Roche, H. M. Fatty Acids and NLRP3 Inflammasome–Mediated Inflammation in Metabolic Tissues. *Annu Rev Nutr* **2017**, *37(1)*, 77–102, DOI: https://doi.org/10.1146/annurev-nutr-071816-064836.

(72) Wang, H.; Lv, C.; Wang, S.; Ying, H.; Weng, Y.; Yu, W. NLRP3 Inflammasome Involves in the Acute Exacerbation of Patients with Chronic Obstructive Pulmonary Disease. *Inflammation* **2018**, *41(4)*, 1321–1333, DOI: https://doi.org/10.1007/s10753-018-0780-0.

(73) Hugh, T. A critical role for the NLRP3 inflammasome in NASH. *Nat Rev Gastroenterol Hepatol* **2017**, *14(4)*, 197, DOI: https://doi.org/10.1038/nrgastro.2017.21.

(74) Awad, F.; Assrawi, E.; Louvrier, C.; Jumeau, C.; Georgin-Lavialle, S.; Grateau, G.; Amselem, S.; Giurgea, I.; Karabina, S.-A. Inflammasome biology, molecular pathology and therapeutic implications. *Pharmacol Ther* **2018**, *187*, 133–149, DOI: https://doi.org/10.1016/j.pharmthera.2018.02.011.

(75) Chen, Q.-L.; Yin, H.-R.; He, Q.-Y.; Wang, Y. Targeting the NLRP3 inflammasome as new therapeutic avenue for inflammatory bowel disease. *Biomed Pharmacother* **2021**, *138*, 111442, DOI: https://doi.org/10.1016/j.biopha.2021.111442.

(76) Wang, L.; Hauenstein, A. V. The NLRP3 inflammasome: Mechanism of action, role in disease and therapies. *Mol Asp Med* **2020**, *76*, 100889, DOI: https://doi.org/.

(77) Libby, P.; Loscalzo, J.; Ridker, P. M.; Farkouh, M. E.; Hsue, P. Y.; Fuster, V.; Hasan, A. A.; Amar, S. Inflammation, Immunity, and Infection in Atherothrombosis: JACC Review Topic of the Week. *J Am Coll Cardiol* **2018**, *72(17)*, 2071–2081, DOI: https://doi.org/10.1016/j.jacc.2018.08.1043.

(78) Martinon, F.; Petrilli, V.; Mayor, A.; Tardivel, A.; Tschopp, J. Gout-associated uric acid crystals activate the NALP3 inflammasome. *Nature* **2006**, *440(7081)*, 237–241, DOI: https://doi.org/10.1038/nature04516.

(79) Hotamisligil, G. S. Inflammation, metaflammation and immunometabolic disorders. *Nature* **2017**, *542(7640)*, 177–185, DOI: https://doi.org/10.1038/nature21363.

(80) Heneka, M. T.; McManus, R. M.; Latz, E. Inflammasome signalling in brain function and neurodegenerative disease. *Nat Rev Neurosci* **2018**, *19(10)*, 610–621, DOI: https://doi.org/10.1038/s41583-018-0055-7.

(81) Heneka, M. T.; Golenbock, D. T.; Latz, E. Innate immunity in Alzheimer's disease. *Nat Immunol* **2015**, *16(3)*, 229–236, DOI: https://doi.org/10.1038/ni.3102.

(82) Venegas, C. et al. Microglia-derived ASC specks cross-seed amyloid-β in Alzheimer's disease. *Nature* **2017**, *552(7685)*, 355–361, DOI: https://doi.org/10.1038/nature25158.

(83) Daniele, S. G.; Béraud, D.; Davenport, C.; Cheng, K.; Yin, H.; Maguire-Zeiss, K. A. Activation of MyD88-dependent TLR1/2 signaling by misfolded α-synuclein, a protein linked to neurodegenerative disorders. *Sci Signal* **2015**, *8(376)*, ra45, DOI: https://doi.org/10.1126/scisignal.2005965.

(84) Keane, R. W.; Dietrich, W. D.; de Rivero Vaccari, J. P. Inflammasome proteins as biomarkers of multiple sclerosis. *Front Neurol* **2018**, *9*, 135, DOI: https://doi.org/10.3389/fneur.2018.00135.

(85) Van Gorp, H.; Van Opdenbosch, N.; Lamkanfi, M. Inflammasome-Dependent Cytokines at the Crossroads of Health and Autoinflammatory Disease. *Cold Spring Harb perspect biol* **2019**, *11:a028563*, DOI: https://doi.org/10.1101/cshperspect.a028563.

(86) Chauhan, D.; Vande Walle, L.; Lamkanfi, M. Therapeutic modulation of inflammasome pathways. *Immunol Rev* **2020**, *297(1)*, 123–138, DOI: https://doi.org/10.1111/imr.12908.

(87) Comparative study of Interleukin-18 (IL-18) serum levels in adult onset Still's disease (AOSD) and systemic onset juvenile idiopathic arthritis (sJIA) and its use as a biomarker for diagnosis and evaluation of disease activity. *BMC Rheumatol* **2019**, *3(1)*, 4, DOI: https://doi.org/10.1186/s41927-019-0053-z.

(88) Bahia, M. S.; Kaur, M.; Silakari, P.; Silakari, O. Interleukin-1 receptor associated kinase inhibitors: potential therapeutic agents for inflammatory-and immune-related disorders. *Cell Signall* **2015**, *27(6)*, 1039–1055, DOI: https://doi.org/10.1016/j.cellsig.2015.02.025.

(89) Buckley, G. M.; Ceska, T. A.; Fraser, J. L.; Gowers, L.; Groom, C. R.; Higueruelo, A. P.; Jenkins, K.; Mack, S. R.; Morgan, T.; Parry, D. M.; Pitt, W. R.; Rausch, O.; Richard, M. D.; Sabin, V. IRAK-4 inhibitors. Part II: A structure-based assessment of imidazo[1,2-a]pyridine binding. *Bioorg Med Chem Lett* **2008**, *18(11)*, 3291–3295, DOI: https://doi.org/10.1016/j.bmcl.2008.04.039.

(90) Bednash, J. S.; Mallampalli, R. K. Regulation of inflammasomes by ubiquitination. *Cell Mol Immunol* **2016**, *13(6)*, 722–728, DOI: https://doi.org/10.1038/cmi.2016.15.

(91) Liang, Z.; Damianou, A.; Di Daniel, E.; Kessler, B. M. Inflammasome activation controlled by the interplay between post-translational modifications: emerging drug target opportunities. *Cell Commun Signal* **2021**, *19(1)*, 1–12, DOI: https://doi.org/10.1186/s12964-020-00688-6.

(92) Song, H.; Zhao, C.; Yu, Z.; Li, Q.; Yan, R.; Qin, Y.; Jia, M.; Zhao, W. UAF1 deubiquitinase complexes facilitate NLRP3 inflammasome activation by promoting NLRP3 expression. *Nat Comm* **2020**, *11(1)*, 1–11, DOI: https://doi.org/10.1038/s41467-020-19939-8.

(93) Akther, M.; Haque, M. E.; Park, J.; Kang, T.-B.; Lee, K.-H. NLRP3 Ubiquitination – A New Approach to Target NLRP3 Inflammasome Activation. *Int J Mol Sci* **2021**, *22(16)*, 9790, DOI: https://doi.org/10.3390/ijms22168780.

(94) Zhao, K.; Zhang, Y.; Xu, X.; Liu, L.; Huang, L.; Luo, R.; Li, J.; Zhang, N.; Lu, B. Acetylation is required for NLRP3 self-aggregation and full activation of the inflammasome. *Biorxiv* **2019**, DOI: https://doi.org/10.1101/2019.12.31.891556.

(95) Rodgers, M. A.; Bowman, J. W.; Fujita, H.; Orazio, N.; Shi, M.; Liang, Q.; Amatya, R.; Kelly, T. J.; Iwai, K.; Ting, J., et al. The linear ubiquitin assembly complex (LUBAC) is essential for NLRP3 inflammasome activation. *J Exp Med* **2014**, *211(7)*, 1333–1347, DOI: https://doi.org/10.1084/jem.20132486.

(96) Lin, Y.-C.; Huang, D.-Y.; Wang, J.-S.; Lin, Y.-L.; Hsieh, S.-L.; Huang, K.-C.; Lin, W.-W. Syk is involved in NLRP3 inflammasome-mediated caspase-1 activation through adaptor ASC phosphorylation and enhanced oligomerization. *J Leukoc Biol* **2015**, *97(5)*, 825–835, DOI: https://doi.org/10.1189/jlb.3HI0814-371RR.

(97) Liu, X.; Pichulik, T.; Wolz, O.-O.; Dang, T.-M.; Stutz, A.; Dillen, C.; Garcia, M. D.; Kraus, H.; Dickhöfer, S.; Daiber, E., et al. Human NACHT, LRR, and PYD domain–containing protein 3 (NLRP3) inflammasome activity is regulated by and potentially targetable through Bruton tyrosine kinase. *Journal of Allergy and Clinical Immunology* **2017**, *140(4)*, 2017, DOI: https://doi.org/10.1016/j.jaci.2017.01.017.

(98) Mangan, M. S.; Olhava, E. J.; Roush, W. R.; Seidel, H. M.; Glick, G. D.; Latz, E. Targeting the NLRP3 inflammasome in inflammatory diseases. *Nat Rev Drug Disc* **2018**, *17(8)*, 588–606, DOI: https://doi.org/10.1038/nrd.2018.97.

(99) Liu, A.; Gao, X.; Zhang, Q.; Cui, L. Cathepsin B inhibition attenuates cardiac dysfunction and remodeling following myocardial infarction by inhibiting the NLRP3 pathway. *Mol Med Rep* **2017**, *16(5)*, 7873, DOI: https://doi.org/10.3892/mmr.2013.1507.

(100) Perregaux, D. G.; McNiff, P.; Laliberte, R.; Hawryluk, N.; Peurano, H.; Stam, E.; Eggler, J.; Griffiths, R.; Dombroski, M. A.; Gabel, C. A. Identification and characterization of a novel class of interleukin-1 post-translational processing inhibitors. *J Pharmacol Exp Ther* **2001**, *299(1)*, 187–197, DOI: https://jpet.aspetjournals.org/content/299/1/187.

(101) Coll, R. C.; Robertson, A. A.; Chae, J. J.; Higgins, S. C.; Muñoz-Planillo, R.; Inserra, M. C.; Vetter, I.; Dungan, L. S.; Monks, B. G.; Stutz, A., et al. A small-molecule inhibitor of the NLRP3 inflammasome for the treatment of inflammatory diseases. *Nat Med* **2015**, *21(3)*, 248–255, DOI: https://doi.org/10.1038/nm.3806.

(102) Coll, R. C.; Hill, J. R.; Day, C. J.; Zamoshnikova, A.; Boucher, D.; Massey, N. L.; Chitty, J. L.; Fraser, J. A.; Jennings, M. P.; Robertson, A. A., et al. MCC950 Directly Targets the NLRP3 ATP-Hydolysis Motif for Inflammasome Inhibition. *Nat Chem Biol* **2019**, *15(6)*, 556–559, DOI: https://doi.org/10.1038/s41589-019-0277-7.

(103) Tapia-Abellán, A.; Angosto-Bazarra, D.; Martinez-Banaclocha, H.; de Torre-Minguela, C.; Cerón-Carrasco, J. P.; Pérez-Sánchez, H.; Arostegui, J. I.; Pelegrin, P. MCC950 closes the active conformation of NLRP3 to an inactive state. *Nat Chem Biol* **2019**, *15(6)*, 560–564, DOI: https://doi.org/10.1038/s41589-019-0278-6.

(104) O'neill, L.; Coll, R.; Cooper, M.; Robertson, A.; Schroder, K. Sulfonylureas and related compounds and use of same. *Patent EP 3,259,253 and US 10,538,487* **2019**.

(105) Cooper, M.; Miller, D.; Macleod, A.; Thom, S.; St-Gallay, S.; Shannon, J. Sulfonylureas and sulfonylthioureas as NLRP3 Inhibitors. *US Patent App. 16/638,700* **2021**.

(106) Harrison, D.; Watt, A. P.; Bock, M. G. Sulphonyl urea derivatives as nlrp3 inflammasome modulators. *US Patent App. 16/955,284* **2021**.

(107) Marchetti, C.; Toldo, S.; Chojnacki, J.; Mezzaroma, E.; Liu, K.; Salloum, F. N.; Nordio, A.; Carbone, S.; Mauro, A. G.; Das, A., et al. Inhibition of the NLRP3 Inflammasome Preserves Cardiac Function After Ischemic and Nonischemic Injury in the Mouse. *J Cardiovasc Pharmacol* **2015**, *66(1)*, 1–8, DOI: https://doi.org/10.1097/FJC.0000000000000247.

(108) Fulp, J.; He, L.; Toldo, S.; Jiang, Y.; Boice, A.; Guo, C.; Li, X.; Rolfe, A.; Sun, D.; Abbate, A., et al. Structural Insights of Benzenesulfonamide Analogues as NLRP3 Inflammasome Inhibitors: Design, Synthesis, and Biological Characterization. *J Med Chem* **2018**, *61(12)*, 5412–5423, DOI: https://doi.org/10.1021/acs.jmedchem.8b00733.

(109) Yin, J.; Zhao, F.; Chojnacki, J. E.; Fulp, J.; Klein, W. L.; Zhang, S.; Zhu, X. NLRP3 Inflammasome Inhibitor Ameliorates Amyloid Pathology in a Mouse Model of Alzheimer's Disease. *Mol Neurobiol* **2018**, *55(3)*, 1977–1987, DOI: https://doi.org/10.1007/s12035-017-0467-9.

(110) Guo, C.; Fulp, J. W.; Jiang, Y.; Li, X.; Chojnacki, J. E.; Wu, J.; Wang, X.-Y.; Zhang, S. Development and Characterization of a Hydroxyl-Sulfonamide Analogue, 5-Chloro-N-[2-(4-hydroxysulfamoyl-phenyl)-ethyl]-2-methoxy-benzamide, as a Novel NLRP3 Inflammasome Inhibitor for Potential Treatment of Multiple Sclerosis. *ACS Chem Neurosci* **2017**, *8(10)*, 2194–2201, DOI: https://doi.org/10.1021/acschemneuro.7b00124.

(111) Jiang, Y.; He, L.; Green, J.; Blevins, H.; Guo, C.; Patel, S. H.; Halquist, M. S.; McRae, M.; Venitz, J.; Wang, X.-Y., et al. Discovery of Second-Generation NLRP3 Inflammasome Inhibitors: Design, Synthesis, and Biological Characterization. *J Med Chem* **2019**, *62(21)*, 9718–9731, DOI: https://doi.org/10.1021/acs.jmedchem.9b01155.

(112) Jiang, H.; He, H.; Chen, Y.; Huang, W.; Cheng, J.; Ye, J.; Wang, A.; Tao, J.; Wang, C.; Liu, Q., et al. Identification of a selective and direct NLRP3 inhibitor to treat inflammatory disorders. *J Exp Med* **2017**, *214(11)*, 3219–3238, DOI: https://doi.org/10.1084/jem.20171419.

(113) Chen, Y.; He, H.; Jiang, H.; Li, L.; Hu, Z.; Huang, H.; Xu, Q.; Zhou, R.; Deng, X. Discovery and optimization of 4-oxo-2-thioxo-thiazolidinones as NOD-like receptor (NLR) family, pyrin domain-containing protein 3 (NLRP3) inhibitors. *Bioorg Med Chem Lett* **2020**, *30(7)*, 127021, DOI: https://doi.org/10.1016/j.bmcl.2020.127021.

(114) Cocco, M.; Garella, D.; Di Stilo, A.; Borretto, E.; Stevanato, L.; Giorgis, M.; Marini, E.; Fantozzi, R.; Miglio, G.; Bertinaria, M. Electrophilic warhead-based design of compounds preventing NLRP3 inflammasome-dependent pyroptosis. *J Med Chem* **2014**, *57(24)*, 10366–10382, DOI: https://doi.org/10.1021/jm501072b.

(115) Cocco, M.; Miglio, G.; Giorgis, M.; Garella, D.; Marini, E.; Costale, A.; Regazzoni, L.; Vistoli, G.; Orioli, M., et al. Design, Synthesis, and Evaluation of Acrylamide Derivatives as Direct NLRP3 Inflammasome Inhibitors. *Chem Med Chem* **2016**, *11(16)*, 1790–1803, DOI: https://doi.org/10.1002/cmdc.201600055.

(116) Cocco, M.; Pellegrini, C.; Martinez-Banaclocha, H.; Giorgis, M.; Marini, E.; Costale, A.; Miglio, G.; Fornai, M.; Antonioli, L.; Lopez-Castejon, G., et al. Development of an Acrylate Derivative Targeting the NLRP3 Inflammasome for the Treatment of Inflammatory Bowel Disease. *J Med Chem* **2017**, *60(9)*, 3656–3671, DOI: https://doi.org/10.1021/acs.jmedchem.6b01624.

(117) Wannamaker, W.; Davies, R.; Namchuk, M.; Pollard, J.; Ford, P.; Ku, G.; Decker, C.; Charifson, P.; Weber, P.; Germann, U. A., et al. (S)-1-((S)-2-{[1-(4-amino-3-chloro-phenyl)-methanoyl]-amino}-3, 3-dimethyl-butanoyl)-pyrrolidine-2-carboxylic acid ((2R, 3S)-2-ethoxy-5-oxo-tetrahydro-furan-3-yl)-amide (VX-765), an orally available selective interleukin (IL)-converting enzyme/caspase-1 inhibitor, exhibits potent anti-inflammatory activities by inhibiting the release of IL-1β and IL-18. *J Pharmacol Exp Ther* **2007**, *321(2)*, 509–516, DOI: https://doi.org/10.1124/jpet.106.111344.

(118) Flores, J.; Noël, A.; Foveau, B.; Lynham, J.; Lecrux, C.; LeBlanc, A. C. Caspase-1 inhibition alleviates cognitive impairment and neuropathology in an Alzheimer's disease mouse model. *Nat Comm* **2018**, *9(1)*, 1–14, DOI: https://doi.org/10.1038/s41467-018-06449-x.

(119) Li, S.; Wu, Y.; Yang, D.; Wu, C.; Ma, C.; Liu, X.; Moynagh, P. N.; Wang, B.; Hu, G.; Yang, S. Gasdermin D in peripheral myeloid cells drives neuroinflammation in experimental autoimmune encephalomyelitis. *J Exp Med* **2019**, *11(216)*, 2562–2581, DOI: https://doi.org/10.1084/jem.20190377.

(120) Rathkey, J. K.; Zhao, J.; Liu, Z.; Chen, Y.; Yang, J.; Kondolf, H. C.; Benson, B. L.; Chirieleison, S. M.; Huang, A. Y.; Dubyak, G. R., et al. Chemical disruption of the pyroptotic pore-forming protein gasdermin D inhibits inflammatory cell death and sepsis. *Sci Immunol* **2018**, *26(3)*, DOI: https://doi.org/10.1126/sciimmunol.aat2738.

(121) Hu, J. J.; Liu, X.; Zhao, J.; Xia, S.; Ruan, J.; Luo, X.; Kim, J.; Lieberman, J.; Wu, H. Identification of pyroptosis inhibitors that target a reactive cysteine in gasdermin D. *BioRxiv* **2018**, DOI: https://doi.org/10.1101/365908.

(122) Sollberger, G.; Choidas, A.; Burn, G. L.; Habenberger, P.; Di Lucrezia, R.; Kordes, S.; Menninger, S.; Eickhoff, J.; Nussbaumer, P.; Klebl, B., et al. Gasdermin D plays a vital role in the generation of neutrophil extracellular traps. *Sci Immunol* **2018**, *3(26)*, DOI: https://doi.org/sciimmunol.aar6689.

(123) Shi, Y.; Lv, Q.; Zheng, M.; Sun, H.; Shi, F. NLRP3 inflammasome inhibitor INF39 attenuated NLRP3 assembly in macrophages. *Int Immunopharmacol* **2021**, *92*, 107358, DOI: https://doi.org/10.1016/j.intimp.2020.107358.

(124) Liao, K.-C.; Sandall, C. F.; Carlson, D. A.; Ulke-Lemee, A.; Platnich, J. M.; Hughes, P. F.; Muruve, D. A.; Haystead, T. A.; MacDonald, J. A. Application of immobilized ATP to the study of NLRP inflammasomes. *Arch Biochem Biophys* **2019**, *670*, 104–115, DOI: https://doi.org/10.1016/j.abb.2018.12.031.

(125) Gastaldi, S.; Boscaro, V.; Gianquinto, E.; Sandall, C. F.; Giorgis, M.; Marini, E.; Blua, F.; Gallicchio, M.; Spyrakis, F.; MacDonald, J. A.; Bertinaria, M. Chemical Modulation of the 1-(Piperidin-4-yl)-1,3-dihydro-2H-benzo[d]imidazole-2-one Scaffold as a Novel NLRP3 Inhibitor. *Molecules* **2021**, *26(13)*, 3975, DOI: https://doi.org/10.3390/molecules26133975.

(126) Pellegrini, C.; Daniele, S.; Antonioli, L.; Benvenuti, L.; D'Antongiovanni, V.; Piccarducci, R.; Pietrobono, D.; Citi, V.; Piragine, E.; Flori, L., et al. Prodromal intestinal events in Alzheimer's disease (AD): colonic dysmotility and inflammation are associated with enteric AD-related protein deposition. *Int J Mol Sci* **2020**, *21(10)*, 3523, DOI: https://doi.org/10.3390/ijms21103523.

(127) Kim, J.; Lee, H.-j.; Park, S. K.; Park, J.-H.; Jeong, H.-R.; Lee, S.; Lee, H.; Seol, E.; Hoe, H.-S. Donepezil Regulates LPS and Aβ-Stimulated Neuroinflammation through MAPK/NLRP3 Inflammasome/STAT3 Signalingl. *Int J Mol Sci* **2021**, *22(19)*, 10637, DOI: https://doi.org/10.3390/ijms221910637.

(128) Takada-Takatori, Y.; Nakagawa, S.; Kimata, R.; Nao, Y.; Mizukawa, Y.; Urushidani, T.; Izumi, Y.; Akaike, A.; Tsuchida, K.; Kume, T. Donepezil modulates amyloid precursor protein endocytosis and reduction by up-regulation of SNX33 expression in primary cortical neurons. *Sci Rep* **2019**, *9(1)*, 1–11, DOI: https://doi.org/10.1038/s41598-019-47462-4.

(129) Yoshiyama, Y.; Kojima, A.; Ishikawa, C.; Arai, K. Anti-inflammatory action of donepezil ameliorates tau pathology, synaptic loss, and neurodegeneration in a tauopathy mouse model. *J Alzheimers Dis* **2010**, *22(1)*, 295–306, DOI: https://doi.org/10.3233/JAD-2010-100681.

(130) Marley, J.; Lu, M.; Bracken, C. A method for efficient isotopic labeling of recombinant proteins. *J Biomol NMR* **2001**, *20(1)*, 71–75, DOI: https://doi.org/10.1023/A:1011254402785.

(131) Vranken, W. F.; Boucher, W.; Stevens, T. J.; Fogh, R. H.; Pajon, A.; Llinas, M.; Ulrich, E. L.; Markley, J. L.; Ionides, J.; Laue, E. D. The CCPN data model for NMR spectroscopy: development of a software pipeline. *Proteins: structure, function, and bioinformatics* **2005**, *59(4)*, 687–696, DOI: https://doi.org/10.1002/prot.20449.

(132) Mori, S.; Abeygunawardana, C.; Johnson, M. O.; Vanzijl, P. C. Improved sensitivity of HSQC spectra of exchanging protons at short interscan delays using a new fast HSQC (FHSQC) detection scheme that avoids water saturation. *J Magn Reson Ser B* **1995**, *1(108)*, 94–98, DOI: https://doi.org/10.1006/jmrb.1995.1109.

(133) Gutmans, D. S.; Whittaker, S. B.; Asiani, K.; Atkinson, R. A.; Oregioni, A.; Pfuhl, M. Controlling the dynamics of the Nek2 leucine zipper by engineering of "kinetic" disulphide bonds. *PLOS one* **2019**, *14(2)*, e0210352, DOI: https://doi.org/10.1371/journal.pone.0210352.

(134) Wittekind, M. HNCACB, a highsensitivity 3D NMR experiment to correlate amide-proton and nitrogen resonances with the α-carbon and β-carbon resonances in proteins. *J Magn Reson Ser B* **1993**, *101*, 214–217.

(135) Montelione, G. T.; Lyons, B. A.; Emerson, S. D.; Tashiro, M. An efficient triple resonance experiment using carbon-13 isotropic mixing for determining sequence-specific resonance assignments of isotopically-enriched proteins. *J Am Chem Soc* **1992**, *27(114)*, 10974–10975, DOI: https://doi.org/10.1021/ja00053a051.

(136) Zhang, O.; Kay, L. E.; Olivier, J. P.; Forman-Kay, J. D. Backbone 1H and 15N resonance assignments of the N-terminal SH3 domain of drk in folded and unfolded states using enhanced-sensitivity pulsed field gradient NMR techniques. *J Biomol NMR* **1994**, *4(6)*, 845–858, DOI: https://doi.org/10.1007/BF00398413.

(137) Sali, A.; Blundell, T. L. Comparative protein modelling by satisfaction of spatial restraints. *J Mol Biol* **1993**, *234(3)*, 779–815, DOI: https://doi.org/10.1006/jmbi.1993.1626.

(138) MacKerell Jr, A. D.; Bashford, D.; Bellott, M.; Dunbrack Jr, R. L.; Evanseck, J. D.; Field, M. J.; Fischer, S.; Gao, J.; Guo, H.; Ha, S., et al. All-atom empirical potential for molecular modeling and dynamics studies of proteins. *J Phys Chem B* **1998**, *102(18)*, 3586–3616, DOI: https://doi.org/10.1021/jp973084f.

(139) Abraham, M. J.; Murtola, T.; Schulz, R.; Pall, S.; Smith, J. C.; Hess, B.; Lindahl, E. GROMACS: High performance molecular simulations through multi-level parallelism from laptops to supercomputers. *SoftwareX* **2015**, *1*, 19–25, DOI: https://doi.org/10.1016/j.softx.2015.06.001.

(140) Da Silva, T. U.; Pougy, K. d. C.; Albuquerque, M. G.; da Silva Lima, C. H.; Machado, S. d. P. Development of parameters compatible with the CHARMM36 force field for [Fe4S4] 2+ clusters and molecular dynamics simulations of adenosine-5'-phosphosulfate reductase in GROMACS 2019. *J Biomol Struct Dyn* **2020**, 1–11, DOI: https://doi.org/10.1080/07391102.2020.1847687.

(141) Izadi, S.; Anandakrishnan, R.; Onufriev, A. V. Building water models: a different approach. *J Phys Chem Lett* **2014**, *5(21)*, 3863–3871, DOI: https://doi.org/10.1021/jz501780a.

(142) Ross, G. A.; Rustenburg, A. S.; Grinaway, P. B.; Fass, J.; Chodera, J. D. Biomolecular simulations under realistic macroscopic salt conditions. *J Phys Chem B* **2018**, *122(21)*, 5466–5486, DOI: https://doi.org/10.1021/acs.jpcb.7b11734.

(143) Golo, V.; Shaitan, K. Dynamic attractor for the Berendsen thermostat an the slow dynamics of biomacromolecules. *Biofizika* **2002**, *47(4)*, 611–617.

(144) Tuble, S. C.; Anwar, J.; Gale, J. D. An approach to developing a force field for molecular simulation of martensitic phase transitions between phases with subtle differences in energy and structure. *J Am Chem Soc* **2004**, *126(1)*, 396–405, DOI: https://doi.org/10.1021/ja0356131.

(145) Darden, T.; York, D.; Pedersen, L. Particle mesh Ewald: An $Nlog(N)$ method for Ewald sums in large systems. *J Chem Phys* **1993**, *98(12)*, 10089–10092, DOI: https://doi.org/10.1063/1.464397.

(146) Hess, B.; Bekker, H.; Berendsen, H. J.; Fraaije, J. G. LINCS: a linear constraint solver for molecular simulations. *J Comp Chem* **1997**, *18(12)*, 1463–1472, DOI: https://doi.org/10.1002/(SICI)1096-987X(199709)18:12<1463::AID-JCC4>3.0.CO;2-H.

(147) Pall, S.; Hess, B. A flexible algorithm for calculating pair interactions on SIMD architectures. *Comp Phys Comm* **2013**, *184(12)*, 2641–2650, DOI: https://doi.org/10.1016/j.cpc.2013.06.003.

(148) Jones, G.; Willett, P.; Glen, R. C.; Leach, A. R.; Taylor, R. Development and validation of a genetic algorithm for flexible docking. *J Mol Biol* **1997**, *267(3)*, 727–748, DOI: https://doi.org/10.1006/jmbi.1996.0897.

(149) Korb, O.; Stutzle, T.; Exner, T. E. Empirical scoring functions for advanced protein-ligand docking with PLANTS. *J Chem Inf Model* **2009**, *49(1)*, 84–96, DOI: https://doi.org/10.1021/ci800298z.

(150) Vanommeslaeghe, K.; Hatcher, E.; Acharya, C.; Kundu, S.; Zhong, S.; Shim, J.; Darian, E.; Guvench, O.; Lopes, P.; Vorobyov, I., et al. CHARMM general force field: A force field for drug-like molecules compatible with the CHARMM all-atom additive biological force fields. *J Comp Chem* **2010**, *31(4)*, 671–690, DOI: https://doi.org/10.1002/jcc.21367.

(151) Bhunia, A.; Bhattacharjya, S.; Chatterjee, S. Applications of saturation transfer difference NMR in biological systems. *Drug Discov Today* **2012**, *17(9-10)*, 505–513, DOI: https://doi.org/10.1016/j.drudis.2011.12.016.

(152) Dalvit, C.; Fogliatto, G.; Stewart, A.; Veronesi, M.; Stockman, B. WaterLOGSY as a method for primary NMR screening: practical aspects and range of applicability. *J Biomol NMR* **2001**, *21(4)*, 349–359, DOI: https://doi.org/10.1023/A:1013302231549.

(153) Davis, D.; Perlman, M.; London, R. Direct measurements of the dissociation-rate constant for inhibitor-enzyme complexes via the T1ρ and T2 (CPMG) methods. *J Magn Reson Ser B* **1994**, *3(104)*, 266–275, DOI: https://doi.org/10.1006/jmrb.1994.1084.

(154) Mureddu, L.; Vuister, G. W. Simple high-resolution NMR spectroscopy as a tool in molecular biology. *FEBS* **2019**, *286(11)*, 2035–2'41, DOI: https://doi.org/10.1111/febs.14771.